



Wright, Michael (2014) Higgs production in association with a Z Boson at the LHC. PhD thesis.

<http://theses.gla.ac.uk/5754/>

Copyright and moral rights for this thesis are retained by the author

A copy can be downloaded for personal non-commercial research or study, without prior permission or charge

This thesis cannot be reproduced or quoted extensively from without first obtaining permission in writing from the Author

The content must not be changed in any way or sold commercially in any format or medium without the formal permission of the Author

When referring to this work, full bibliographic details including the author, title, awarding institution and date of the thesis must be given.



University  
of Glasgow | Experimental  
Particle Physics

**Higgs Production  
in Association with a  
 $Z$  Boson at the LHC**

*Michael Wright*

University of Glasgow

A thesis submitted for the degree of

Doctor of Philosophy

at the University of Glasgow

School of Physics and Astronomy

University of Glasgow

*July 2014*

## Abstract

The associated  $Z$  vector boson production rate of the Standard Model Higgs boson has been measured in decays into two  $b$  quarks, with the  $Z$  boson decaying into an electron or muon pair in the ATLAS detector at the Large Hadron Collider (LHC). The associated  $Z$  vector boson production cross section in the Standard Model is almost two orders of magnitude smaller than the dominant Higgs boson production cross section from gluon fusion. Proton-proton collision data at a centre-of-mass energy of 8 TeV delivered by the LHC with the ATLAS detector corresponding to an integrated luminosity of  $13 \text{ fb}^{-1}$  has been analysed. A Higgs boson produced via associated production with a  $Z$  vector boson is excluded with a 95% confidence level in a mass range between 110 to 130 GeV at 6 to 11 times the Standard Model cross section, respectively.

## Acknowledgements

I would like to begin by thanking Prof. Tony Doyle and the Glasgow Particle Physics Group for accepting me as a PhD student and supporting me through the past years. In particular I would like to thank Tony Doyle for his guidance and wisdom throughout this unique, wonderful and testing period in my life. In addition, I would like to thank Christopher Collins-Tooth and Richard St. Denis, for their in-depth knowledge and discussions over the years.

I am very thankful for those at CERN and the HSG5 group who supported me through the long days and nights, when first setting limits for the group and to Graham Stewart who helped me obtain my authorship.

I would like to also thank all my friends in the Glasgow and CERN office, who not only made the experience of my PhD intellectually stimulating, but also fun at the same time. Special thanks goes out to my good friends Donnchadha Quilty, William Breaden Madden, Nicolas Edwards, Genevieve Steele and Alistair Gemmell, who made the bad days into good days and the good days into great days.

Lastly, I would like to thank my wife Kimberley Wright, who has suffered and given the most. Without her support, love and help, none of this would be possible. I love you deeply and always.

## **Declaration**

This thesis represents work completed from September 2009 to July 2014 in the Experimental Particle Physics group in the School of Physics and Astronomy at the University of Glasgow. The work presented in Chapter 5 is my own, except where stated in the text.

# Contents

<b>Abstract</b>	<b>ii</b>
<b>Acknowledgements</b>	<b>iii</b>
<b>Declaration</b>	<b>iv</b>
<b>1 Introduction</b>	<b>1</b>
<b>2 Theoretical Foundations</b>	<b>3</b>
2.1 Elementary Particles in The Standard Model . . . . .	4
2.1.1 Fermions - Matter Particles . . . . .	4
2.1.2 Bosons - Force Carriers . . . . .	7
2.2 The Standard Model . . . . .	9
2.2.1 Quantum Electrodynamics (QED) . . . . .	10
2.2.2 Quantum Chromodynamics (QCD) . . . . .	11
2.2.3 Electroweak Theory . . . . .	13
2.2.4 Spontaneous Symmetry Breaking . . . . .	14
2.2.5 Theoretical Mass Constraints . . . . .	18
2.3 Higgs Production in Proton-Proton Collisions . . . . .	21

2.3.1	Phenomenology (Proton-Proton Scattering) . . . . .	22
2.3.2	Production of the Higgs Boson at the LHC . . . . .	27
2.3.3	Decays of the Higgs Boson . . . . .	31
2.3.4	Simulation of Event Generation . . . . .	33
2.4	Experimental Constraints . . . . .	35
2.5	Summary . . . . .	38
<b>3</b>	<b>The LHC and the ATLAS Experiment</b>	<b>39</b>
3.1	The Large Hadron Collider . . . . .	39
3.2	The ATLAS Detector . . . . .	45
3.2.1	Overview . . . . .	45
3.2.2	Co-ordinate System . . . . .	48
3.2.3	Inner Detector . . . . .	49
3.2.4	Calorimeter . . . . .	52
3.2.5	Muon System . . . . .	57
3.2.6	Trigger System . . . . .	58
3.2.7	Luminosity Measurements . . . . .	59
3.2.8	Simulation of the ATLAS Detector . . . . .	60
3.2.9	Summary . . . . .	61
<b>4</b>	<b>Event Reconstruction</b>	<b>62</b>
4.1	Data Quality . . . . .	63
4.2	Reconstruction of Charged Track Particles . . . . .	63
4.3	Reconstruction of the Primary Vertex . . . . .	66
4.4	Electrons . . . . .	69

4.4.1	Electron Reconstruction . . . . .	69
4.4.2	Electron Identification . . . . .	70
4.4.3	Scale Factors and Energy Corrections . . . . .	74
4.5	Muons . . . . .	74
4.5.1	Muon Reconstruction and Identification . . . . .	74
4.5.2	Muon Scale Factors and Energy Corrections . . . . .	78
4.6	Jets . . . . .	78
4.6.1	Jet Reconstruction . . . . .	78
4.6.2	Jet Calibration . . . . .	82
4.6.3	Jet Selection . . . . .	84
4.6.4	Jet Energy Resolution . . . . .	87
4.7	b-tagging . . . . .	89
4.7.1	b-tagging Algorithms . . . . .	89
4.7.2	b-tagging Uncertainty . . . . .	92
4.8	Missing Transverse Energy Reconstruction . . . . .	92
4.9	Trigger . . . . .	96
4.9.1	Muon Trigger . . . . .	97
4.9.2	Electron Trigger . . . . .	97
4.10	Summary . . . . .	98
<b>5</b>	<b><math>H \rightarrow b\bar{b}</math> in Associated Production with a <math>Z \rightarrow l^+l^-</math> Vector Boson</b>	<b>99</b>
5.1	Introduction . . . . .	99
5.2	Simulation and Data Samples . . . . .	100
5.3	Object Selection . . . . .	108

5.3.1	Muons . . . . .	108
5.3.2	Electrons . . . . .	111
5.3.3	Jets . . . . .	112
5.3.4	$b$ -jets . . . . .	113
5.3.5	Missing transverse energy . . . . .	114
5.4	Event Selection . . . . .	114
5.5	Background Estimation . . . . .	118
5.5.1	Estimation of the Multijet Background . . . . .	118
5.5.2	Estimation of the Top Background . . . . .	124
5.5.3	Estimation of the $Z + jets$ Background . . . . .	135
5.6	Control Regions . . . . .	156
5.6.1	Pretag Control Region . . . . .	156
5.6.2	1-tag Control Region . . . . .	167
5.7	Systematic Uncertainties . . . . .	177
5.7.1	Theoretical Uncertainties on the ZH Signal . . . . .	177
5.7.2	Modelling of the $Z+jets$ Background . . . . .	178
5.7.3	Impact of Systematic Uncertainties . . . . .	183
5.8	Results . . . . .	186
5.8.1	Signal Region . . . . .	186
5.8.2	Extraction of the Limit on $ZH \rightarrow l^+l^-b\bar{b}$ Production . . . . .	196
5.8.3	Summary . . . . .	202
<b>6</b>	<b>Conclusion</b>	<b>204</b>
<b>References</b>		<b>206</b>

# Chapter 1

## Introduction

The Standard Model successfully describes the interactions between elementary particles using local gauge symmetry. The predictions made by the model have been experimentally tested in many precise experiments, without any contradictions from the model being observed. The Standard Model allows us to explain the masses of the gauge bosons mediating the weak interaction and the fermion masses by the Higgs Mechanism, which was developed by Englert, Brout [1] and Higgs [2], as well as Hagen, Guralnik and Kibble [3]. The Higgs mechanism predicts a massive scalar particle called the Higgs boson, which couples to all massive Standard Model particles. A description of the Higgs boson and its properties is found in Chapter 2.

The Large Hadron Collider (LHC) at CERN, is designed to collide proton beams with a centre-of-mass energy of 14 TeV and was constructed to find the Higgs boson, which is an essential step in verifying the Higgs mechanism. The collider has been operating since autumn 2009 with an ongoing interruption for an energy upgrade. In 2012 each proton beam energy reached 4 TeV, with an integrated luminosity of 21

$\text{fb}^{-1}$  of data collected. Another  $5 \text{ fb}^{-1}$  of data was collected in 2011, with a centre-of-mass energy of 7 TeV. The design energy is expected to be reached with the start up of the LHC in 2015. The data used in this thesis has been recorded at the ATLAS<sup>1</sup> detector. The detector and the LHC accelerator system is discussed in greater detail in Chapter 3. The reconstruction of particles, jets and physics objects needed for the analysis are discussed in Chapter 4.

In July 2012 the full available datasets were used in the ATLAS [4] and CMS<sup>2</sup> [5] experiments to discover a Higgs boson candidate at a mass of  $125.5 \pm 0.6 \text{ GeV}$  [6] and  $125.7 \pm 0.4 \text{ GeV}$  [7], respectively. This thesis focuses on the measurement of the production of the Higgs boson through associated production with a  $Z$  vector boson, where the Higgs boson decays to two bottom quarks and the  $Z$  vector boson decays into an electron or muon pair, i.e.  $ZH \rightarrow e^+e^-b\bar{b}$  or  $ZH \rightarrow \mu^+\mu^-b\bar{b}$ . There are different processes that contribute to the background of this channel, with the dominant backgrounds coming from the  $Z$  boson and top-quark-pair production, as well as Drell-Yan processes. The background expectations from Monte-Carlo simulations have been corrected using control measurements. The event selection, background determinations and results for the analysis are presented in Chapter 5, with a summary of the thesis given in Chapter 6.

---

<sup>1</sup>ATLAS: A Toroidal LHC ApparatuS

<sup>2</sup>CMS: Compact Muon Solenoid

# Chapter 2

## Theoretical Foundations

The Standard Model [8] is a quantum field theory with a particular set of fields and gauge symmetries that allow us to accurately describe the particles and forces that exist in our universe. The interactions of these fields with Standard Model particles are discussed in the following chapter.

We begin by introducing the current known set of elementary particles and the forces that act upon them, followed by an overview of the Standard Model and spontaneous breaking of the electroweak symmetries that give rise to massive vector bosons and fermions. The theoretical predictions for the Higgs boson production cross sections and branching ratios at hadron colliders are also discussed, with an overview of the discovery of the Higgs boson candidate and the measured properties at the ATLAS and CMS experiments in the LHC.

## 2.1 Elementary Particles in The Standard Model

The known physical world is currently best described by the Standard Model. In its simplest terms, the Standard Model describes the interactions of fundamental particles. The Standard model currently describes all known particles and three out of the four known fundamental interactions – electromagnetic, weak and strong. Particles in the Standard Model are categorised by their spin, with particles either having a half-integer or integer spin. The half-integer spin particles are called fermions and obey Fermi-Dirac statistics and the Pauli exclusion principle. Fermions are also matter particles. The integer spin particles are called bosons and obey Bose-Einstein statistics, which allows similar particles to occupy the same quantum state. The fundamental interactions between fermions is propagated by bosons.

### 2.1.1 Fermions - Matter Particles

Fermions are categorised into two groups, quarks and leptons. Quarks have a baryon number  $B = \frac{1}{3}$ , whereas the leptons have a lepton number  $L = 1$ . Quarks and leptons both consist of three families or generations, each consisting of two particles. Figure 2.1 shows the quark and lepton families with some of their properties.

The first generation of quarks consists of an up quark ( $u$ ), with an electric charge of  $\frac{2}{3}$  and a down quark ( $d$ ), with an electric charge of  $-\frac{1}{3}$ . The second generation consists of the strange quark ( $s$ ) and charm quark ( $c$ ), which have an electric charge of  $\frac{2}{3}$  and  $-\frac{1}{3}$  respectively. Similarly, the third generation of quarks, bottom ( $b$ ) and top ( $t$ ) have electric charges of  $\frac{2}{3}$  and  $-\frac{1}{3}$  respectively. The differences in the three generations of quarks can be seen in the quark masses, with the up quark being

the lightest quark at a predicted mass of  $2.3^{+0.7}_{-0.5}$  MeV<sup>1</sup> and the top quark being the heaviest at  $173.29 \pm 0.95$  GeV. Quarks can also be separated by their colour charge, such that each quark can have a colour charge of red, green or blue.

The lepton doublet is composed of an electrically charged lepton with a corresponding chargeless neutrino. The first generation of leptons consists of an electron ( $e$ ) with an electron neutrino ( $\nu_e$ ). The second generation of leptons comprises of a muon ( $\mu$ ) with a muon neutrino ( $\nu_\mu$ ) and the third generation is composed of a tau ( $\tau$ ) and a tau neutrino ( $\nu_\tau$ ). Similar to the quark families, the lepton families also increase in mass with each generation.

The quark and lepton generations each have anti-particles with opposite electric charge. The quark families can be made up from quark and anti-quark pairs called mesons or three quarks called baryons.

---

<sup>1</sup>Quarks cannot be directly measured due to asymptotic freedom. The quark masses can however be measured indirectly via the constituents mass and subtracting the gluon QCD binding energy

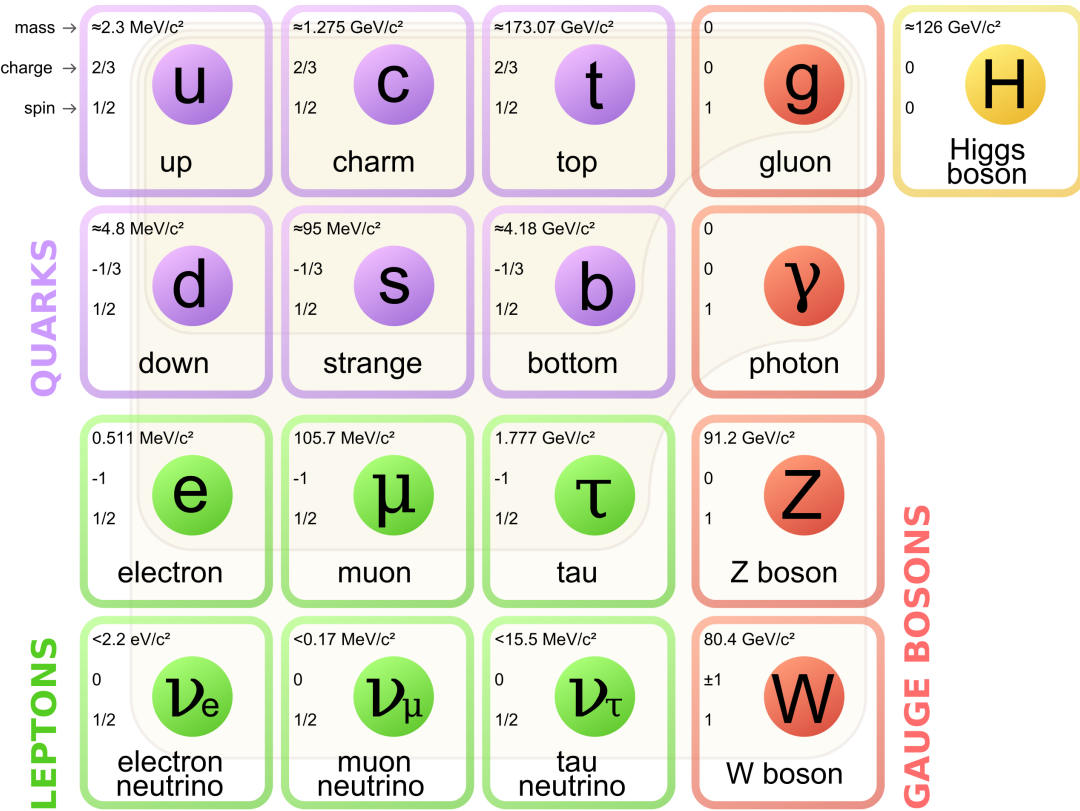


Figure 2.1: Elementary particles in the Standard Model. The three generations of quarks and leptons with the boson force carriers. Taken from [9].

## 2.1.2 Bosons - Force Carriers

Integer spin particles called bosons mediate the interactions of fermions by absorption and emission. The interactions can be split into four fundamental forces, electromagnetic, strong, weak and gravity. The electromagnetic force binds electrons to nuclei and causes oppositely charged particles to attract over an infinite range. The electromagnetic force is mediated by the photon ( $\gamma$ ). The strong force holds nuclei together and is the strongest force of the four. However, the strong force has a short range and partons must be close to one another to be effected by it. The strong force is mediated by eight massless gluons ( $g$ ). The weak force governs decays of unstable particles, such as mesons and is about 100,000 times weaker than the electromagnetic force, due to the massive  $W$  and  $Z$  particles that mediate the weak force and constrain its range. The last of the four fundamental forces is gravity and is responsible for galaxy formation and giving physical objects weight. Gravity is the weakest of all the forces and is negligible at the energy scales in particle physics. An overview of the particles in the Standard Model is summarised in Table 2.1.

Table 2.1: Overview of the Standard Model particles, where  $J$  denotes the spin and  $P$  the parity of the particle. The masses of the particles are taken from [6, 10].

	Name	Symbol	Charge	Mass
Fermions	Electron neutrino	$\nu_e$	0	< 2 eV
	Electron	$e$	-1	0.511 MeV
	Muon neutrino	$\nu_\mu$	0	< 0.12 MeV
	Muon	$\mu$	-1	105.7 MeV
	Tau neutrino	$\nu_\tau$	0	< 18.2 MeV
	Tau	$\tau$	-1	1.777 GeV
Quarks	Up	$u$	+2/3	$2.3^{+0.7}_{-0.5}$ MeV
	Down	$d$	-1/3	$4.8^{+0.5}_{-0.3}$ MeV
	Strange	$s$	+2/3	$95 \pm 5$ MeV
	Charm	$c$	-1/3	$1.275 \pm 0.025$ GeV
	Bottom	$b$	+2/3	$4.18 \pm 0.03$ GeV
	Top	$t$	-1/3	$173.29 \pm 0.95$ GeV
Bosons	Gluon	$g$	0	0
	Photon	$\gamma$	0	0
	$W$ boson	$W^\pm$	$\pm 1$	$80.385 \pm 0.015$ GeV
	$Z$ boson	$Z^0$	0	$91.1876 \pm 0.0021$ GeV
Scalar	Higgs boson	$H$	0	$125.6^{+0.5}_{-0.6}$ GeV

## 2.2 The Standard Model

The Standard Model is a quantum field theory in the local gauge symmetric group

$$SU(3) \otimes SU(2) \otimes U(1), \quad (2.1)$$

where  $SU(3)$  represents the strong interaction and  $SU(2) \otimes U(1)$  represents the electroweak interaction [11]. The quantum field theory is used to determine the properties of the interactions between fundamental particles discussed in Section 2.1 and has been verified in many experiments. From the time of writing, there has been no significant deviation found from the Standard Model and all particles described by the model have been observed. However, the model does not provide predictions for gravity and other unexplained phenomena.

The fundamental interactions of particles in the Standard Model are described by the local quantum gauge fields, which can be summarised by:

- **Quantum electrodynamics (QED)** [12], which describes the interactions between electrically charged particles and is mediated by a massless photon. The electromagnetic interaction is defined by the Abelian  $U(1)$  gauge symmetry.
- **The electroweak interaction** [13], which describes the electromagnetic interaction using the Glashow-Salam-Weinberg theory, which predicts the interactions to be mediated by a massive  $W^+, W^-$  or  $Z^0$  boson in the non-Abelian  $SU(2) \otimes U(1)$  gauge symmetry.
- **Quantum chromodynamics (QCD)** [14], which describes the strong inter-

action between colour charged quarks and is mediated by eight massless gluons carrying different combinations of colour and anti-colour. The strong interaction is defined by the non-Abelian  $SU(3)$  gauge symmetry.

### 2.2.1 Quantum Electrodynamics (QED)

Quantum electrodynamics describes the interactions of all quantum electromagnetic interactions that consist of charged fermions, with the electromagnetic field carried by the photon. A quantum electromagnetic interaction is shown in Figure 2.2, where an electron-positron pair annihilates, producing a photon, which decays into a muon-anti-muon pair. The strength of the interaction is determined by the coupling constant ( $\alpha$ ), which is associated to each vertex. The corresponding coupling constant increases with the increase in energy. The vertex is the building block of the QED process and is represented in Figure 2.2, as a Feynman diagram [15]. Feynman diagrams that have the smallest possible number of vertices for a given process are referred to as tree-level or leading order. Higher degrees of accuracy for the process can be found by using higher order diagrams, which are summed together over all possible internal states. The higher order diagrams produce a more detailed picture of the QED process and improve our understanding of the physics process (see Section 2.3.4).

A Lagrangian formalism is used to describe the interactions between fermions in the Standard Model, such that it describes the action involved in a Lagrangian acting on the fermion fields. The process of the non-interacting fermion fields is described by the Dirac Lagrangian [16]. In 1954 the Yang-Mills theory [17] proposed the idea that the quanta of the underlying field must involve the exchange of a massless

vector boson (photon field) to maintain gauge invariance. The gauge invariance of the physical system results in a local gauge transformation that conserves the electric charge of a fermion. A local gauge transformation in QED is represented under the  $U(1)$  group, which is a unitary matrix of dimension  $1 \times 1$ . The symmetry groups can be extended in the same principle to explain the strong and weak interactions.

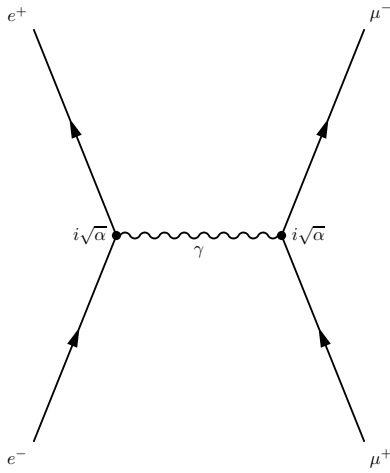


Figure 2.2: Leading order Feynman diagram of electron-positron annihilation and muon-anti-muon pair production.

### 2.2.2 Quantum Chromodynamics (QCD)

Quantum Chromodynamics (QCD) is a quantum field theory that describes the strong interaction. The strong force couples to colour charge and only exists between quarks and coloured gluons. Figure 2.3 shows a QCD interaction vertex, involving quarks emitting a gluon. The local gauge group  $SU(3)$  with the unitary group of  $3 \times 3$  matrices with determinant one, refers to QCD and the strong interaction. The three dimensional matrices in the group are due to the three quark colours, which lead to

the quark fields transforming in the vector space of colour. The local gauge invariance of the Dirac Lagrangian is maintained by eight massless vector fields, which represent the corresponding eight gluons, with the ninth gluon being a non-physical singlet that acts on all quarks equally.

The  $SU(3)$  group is said to be a non-Abelian group, as the generators do not commute, leading to gluons carrying colour charge and self-interaction. The self-interaction of the gluons in the QCD Lagrangian leads to gluons coupling other gluons, which does not happen in QED, as the photon does not carry electric charge. Gluon self-coupling leads to both quark anti-quark loops and gluon-gluon loops that contribute to higher order processes. The quark anti-quark loops lead to a net reduction in the coupling strength with an increase in distance. However, gluon-gluon loops lead to an increase in the coupling strength with an increase in distance, which overcomes the quark anti-quark loops reductions. The net effect of the coupling strength is an increase with increasing distance; due to there being more gluons and therefore more gluon-gluon loop contributions. A consequence of asymptotic freedom is that no free quarks or gluons are observed in nature. The only observed QCD particles found in nature are the colourless hadrons - baryons and mesons.

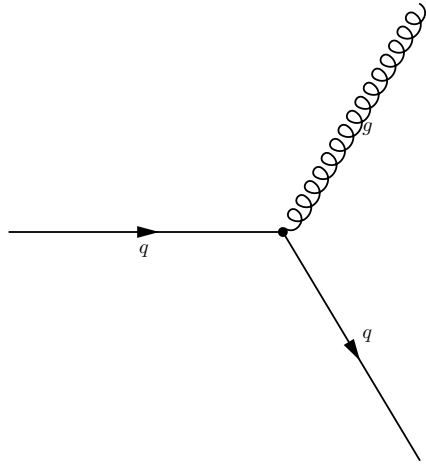


Figure 2.3: Leading order Feynman diagram of the emission of a gluon from a quark.

### 2.2.3 Electroweak Theory

The electroweak interaction is a unification of the electromagnetic and weak force in the gauge symmetric group  $SU(2) \otimes U(1)$ , which was introduced by Glashow, Salam and Weinberg [13]. The successful unification under the  $SU(2) \otimes U(1)$  gauge group showed that the two components of the electromagnetic and weak force can be considered as a single force at large energies. The gauge group preserves local invariance by requiring four massless fields, which correspond to the massless  $W_\mu^a$  ( $a = 1, 2, 3$ ) vector fields of weak isospin from the  $SU(2)$  group and the massless  $B_\mu^0$  vector field of weak hypercharge from the  $U(1)$  group. The observed  $W_\mu^\pm$ ,  $Z_\mu$  and  $A_\mu$  (photon) boson fields are related to the massless vector fields by the transformations shown in Equation 2.2

$$W_\mu^\pm = \frac{1}{\sqrt{2}}(W_\mu^1 \mp iW_\mu^2), \quad (2.2a)$$

$$Z_\mu = W_\mu^3 \cdot \cos \theta_W - B_\mu^0 \cdot \sin \theta_W, \quad (2.2b)$$

$$A_\mu = W_\mu^3 \cdot \sin \theta_W + B_\mu^0 \cdot \cos \theta_W, \quad (2.2c)$$

where the rotation angle  $\theta_W$  is the weak mixing angle. Due to the  $SU(2)$  gauge group being non-Abelian, self-interaction between the  $W$  and  $Z$  bosons takes place and allows the bosons to couple to each other. However, photon-photon coupling does not take place, as the  $U(1)$  group is Abelian and the absence of self-coupling in QED is maintained.

#### 2.2.4 Spontaneous Symmetry Breaking

A unified theory of all the fundamental forces apart from gravity are defined by a local gauge group  $SU(3) \otimes SU(2) \otimes U(1)$  and the associated Standard Model Lagrangian. To conserve the local gauge symmetries in the gauge groups, the vector fields must be massless. However, experiments have shown that the  $W^\pm$ ,  $Z$  and fermions all have a mass.

The mechanism of spontaneous electroweak symmetry breaking first introduced independently by Higgs [2], Englert and Brout [1], as well as Guralnik, Hagen and Kibble [3, 18], provides a solution to why we observe massive particles, while maintaining the massless fields. The mechanism is more commonly known as the Higgs mechanism and introduces a complex scalar field  $\Phi$ , which is represented by  $\Phi = (\Phi_1 + i\Phi_2)/\sqrt{2}$ . The Lagrangian describing the system for a scalar particle is described in Equation 2.3

$$\mathcal{L} = \mathcal{T} - \mathcal{V} = (\partial_\nu \Phi^*)(\partial^\nu \Phi) - (\mu^2 \Phi^* \Phi + \lambda(\Phi^* \Phi)^2), \quad (2.3)$$

where  $\mathcal{T}$  is the kinetic energy,  $\mathcal{V}$  is the potential energy and  $\mu$  and  $\lambda$  are free parameters. To preserve invariance under global gauge transformation of the  $U(1)$  group, the Lagrangian must have a vacuum state with positive and finite energy. Due to this constraint  $\lambda$  must be a positive value, which leads to two solutions for  $\mu^2$ . Figure 2.4 shows the potential of the field for  $\lambda \geq 0$ , where  $\mu^2 \geq 0$  or  $\mu^2 \leq 0$ . When  $\mu^2 \geq 0$ ,  $\Phi$  is self-interacting with coupling  $\lambda$ , giving a ground state vacuum expectation of  $\Phi = 0$ , therefore the Higgs field has no energy to give the gauge bosons mass. However, when  $\mu^2 \leq 0$  the potential no longer has  $\Phi = 0$ , instead there is a radial excitation of the potential shown in Figure 2.4, which is more commonly known as the Mexican hat potential. The maximum potential occurs at  $\Phi = 0$ , with the minimum potential found at all points on the projected circle, as shown in Figure 2.4. The projected circle has a radius  $\nu$  in the  $\phi_1 - i\phi_2$  plane, leading to Equation 2.4, which has an infinite number of ground states.

$$\Phi_1^2 + i\Phi_2^2 = \nu^2, \quad (2.4)$$

Equation 2.5 shows a solution for the location of the minima,  $\Phi^{min}$ ,

$$\Phi^{min} = e^{i\theta} \sqrt{\frac{\mu^2}{2\lambda}}, \quad (2.5)$$

where  $0 \leq \theta \leq 2\pi$  is the angle around the  $\mathcal{V}$  axis. The invariance of the gauge group  $U(1)$  is broken when we choose a value for  $\theta$ , as a transformation in  $U(1)$  does not exist in the same energy state and breaks the symmetry, leading to a non-zero vacuum expectation value. If we take the minimum of the potential to be at  $\theta = 0$ , we find the minimum of the field to be

$$\Phi^{min} = \frac{\nu}{\sqrt{2}}, \quad (2.6)$$

which is the scalar field in the vacuum and the selected gauge. The excitations from the chosen gauge has zero energy in many quantum states, leading to massless particles and fields with zero expectation values. Equation 2.7 is a scalar field that satisfies this requirement

$$\Phi = \frac{1}{\sqrt{2}}\left(\frac{\mu}{\lambda} + \mathcal{H} + i\phi\right), \quad (2.7)$$

where both  $\mathcal{H}$  and  $\phi$  have zero vacuum expectation values. The scalar field from Equation 2.7 leads to a potential shown in Equation 2.8, where the field  $\mathcal{H}$  has a mass term and the field  $\phi$  does not. The  $\phi$  field represents the massless particles called the Goldstone bosons.

$$\mathcal{V} = \mu^2 \mathcal{H}^2 + \mu^2 \sqrt{\lambda} (\mathcal{H}^3 + \phi^2 \mathcal{H}) + \frac{\lambda}{4} (\mathcal{H}^4 + \phi^4 + 2\mathcal{H}^2 \phi^2) + \frac{\mu^4}{4\lambda} \quad (2.8)$$

The field  $\phi$  is a result of a Goldstone's theorem [19] and transforms the vacuum

into many other degenerate minimum energy states, which are not consistent with the original choice of gauge shown in Equation 2.5. Due to this inconsistency we say that the Goldstone bosons are 'unphysical', with their degrees of freedom used to create a new third degree of freedom, which is used to turn the massless gauge bosons of  $SU(2) \otimes U(1)$  into massive gauge bosons. The example above only shows one Goldstone boson, but in fact there are four, due to the complex scalar field  $\phi$  being a doublet, such that

$$\Phi = \sqrt{\frac{1}{2}} \begin{pmatrix} \Phi^+ \\ \Phi^0 \end{pmatrix} = \begin{pmatrix} \Phi_3 + i\Phi_4 \\ \Phi_1 + i\Phi_2 \end{pmatrix} \quad (2.9)$$

The four extra degrees of freedom are given to the massive scalar bosons  $W^\pm$ ,  $Z^0$  and  $H$  the Higgs boson. The photon remains massless, as it does not break the symmetry, due to it not holding any charge and allowing it to remain locally invariant under a gauge transform. The masses of the weak gauge bosons are given by

$$m_W = \frac{\nu g}{2} = m_z \cos \theta_W, \quad (2.10)$$

where  $g$  is the gauge coupling strength of the  $SU(2)$  group. The Higgs boson mechanism allows coupling between the Higgs boson  $H$  and the weak vector bosons  $V = W, Z$  with a coupling strength defined by

$$g_{HVV} = -2i \frac{m_V^2}{\nu} \quad \text{and} \quad g_{HHVV} = -2i \frac{m_V^2}{\nu^2} \quad (2.11)$$

Fermions acquire their mass through Yukawa couplings with a strength  $g_f$ , which is proportional to the fermions mass and is not predicted by the Standard Model. The coupling strength for a fermion is defined by

$$g_f = im_f \frac{\sqrt{2}}{\nu} \quad (2.12)$$

The Higgs boson mass is also not predicted by the Standard Model and is defined by

$$m_H = \sqrt{2\lambda\nu^2}, \quad (2.13)$$

where the self-interaction strength  $\lambda$  must be greater than zero for spontaneous symmetry breaking to take place, which requires the Higgs boson to be massive.

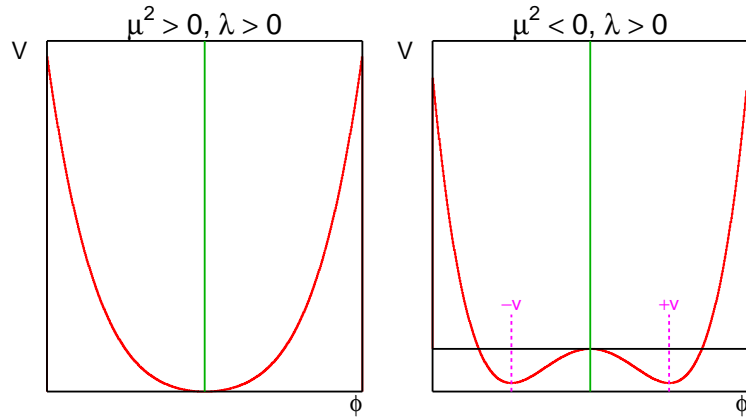


Figure 2.4: The potential of  $\mathcal{V}$  for a complex scalar field when  $\lambda \geq 0$  and  $\mu^2 > 0$  or  $\mu^2 \leq 0$ .

### 2.2.5 Theoretical Mass Constraints

The Standard Model (SM) defines four types of gauge vector bosons ( $W, Z, \gamma$  and gluon), with twelve types of fermions (six leptons and six quarks). The SM also predicts that the Higgs boson is responsible for the masses of all particles, but the theory

itself does not predict a Higgs boson mass. However, several theoretical techniques have been derived that define possible boundaries for the value of the Higgs boson mass, such as unitarity and vacuum stability, which are described below.

## Unitarity

Unitarity in the SM requires the total scattering probability of a process to be less than one and is calculated by integrating over all contributing Feynman diagrams. The electroweak theory violates unitarity due to its assumption of point-like interactions. However, by introducing massive bosons one can resolve this issue at low energy. At higher energy longitudinal components of the vector bosons violate unitary at tree level for some processes. The  $W^+W^- \rightarrow W^+W^-$  process is one such example and has a probability  $P_{WW \rightarrow WW} = \sigma_{WW \rightarrow WW}/\sigma_{Total} \geq 1$ , which is unphysical. Unitarity can be restored by the introduction of Higgs exchange diagrams, adding to the overall scattering probability [20]. Feynman diagrams of some of the possible Higgs exchanges are shown in Figure 2.5. The Higgs exchange also allows an upper bound of the Higgs boson mass to be calculated using,

$$m_{H^0}^2 \leq \frac{8\pi^2\nu^2}{2\ln(\Lambda^2)/\nu^2}, \quad (2.14)$$

where  $\Lambda$  is the cut-off energy scale for a stable vacuum.

## Vacuum Stability

The top quarks Yukawa coupling is larger than the Higgs self-coupling, which leads to a smaller Higgs mass compared to the top quark. However, by having a low Higgs mass for large couplings between the top and weak boson, a global minimum at a

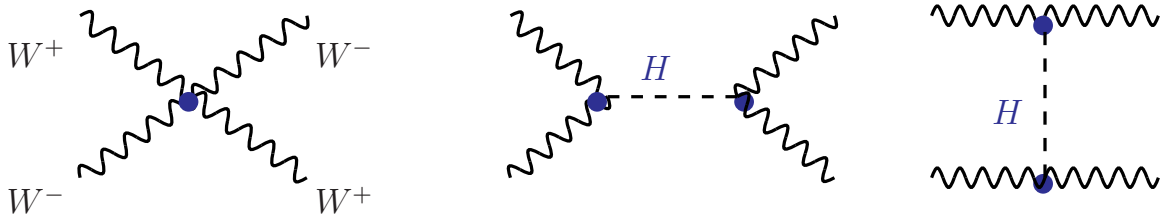


Figure 2.5: Leading order Feynman diagrams contributing to the  $W^+W^- \rightarrow W^+W^-$  process.

large energy is produced for the Higgs potential and leads to an unstable vacuum and prevents spontaneous symmetry breaking. To overcome this, an appropriate cut-off energy scale  $\Lambda$  is selected, such that the vacuum remains stable [21]. If we select a  $\Lambda \approx 1 \text{ TeV}$  (at the electroweak scale) the mass range of the Higgs boson is found to be within  $50 \leq m_H \leq 800 \text{ GeV}$ . The combined effects of the Higgs self-coupling being smaller than the top quarks Yukawa coupling and vacuum stability is shown in Figure 2.6, where the allowed Higgs mass range varies as a function of the cut-off energy scale. The bands from Figure 2.6 represent the upper and lower limits of the theoretical uncertainties of the Higgs mass and were derived using a top mass of  $m_t = 175 \pm 6 \text{ GeV}$ , with a strong coupling constant of  $\alpha_s = 0.118 \pm 0.002$

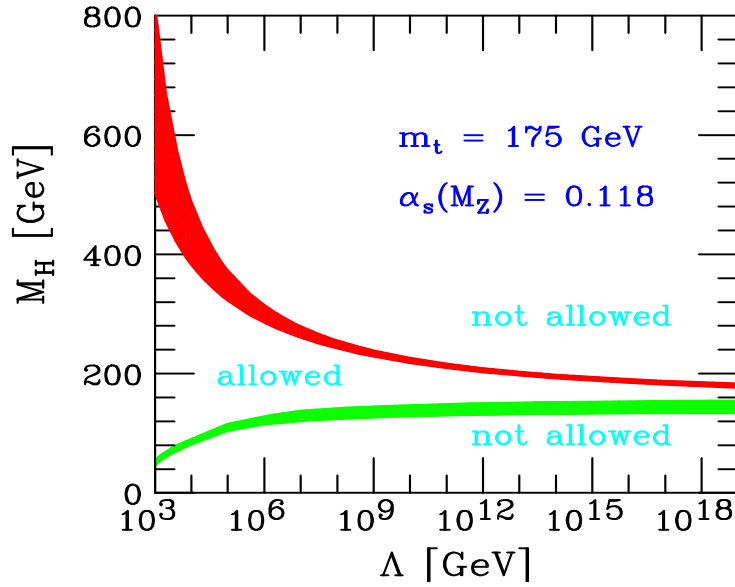


Figure 2.6: Theoretical upper and lower limits on the mass of the Higgs boson as a function of cut-off energy scale  $\Lambda$ . Taken from [20].

## 2.3 Higgs Production in Proton-Proton Collisions

In the following section theoretical predictions of the Higgs boson production and decay in a proton-proton collision are discussed (for a more detailed account see [22]).

In Section 2.3.1 the processes of interest that take place between proton constituents and the residual processes from these constituents are discussed. This is followed by the main mechanisms of the Higgs boson production in Section 2.3.2 and the most important Higgs boson decays in Section 2.3.3. The event generators used to predict the differential cross sections and decay rates for signal and background process are also discussed in Section 2.3.4.

### 2.3.1 Phenomenology (Proton-Proton Scattering)

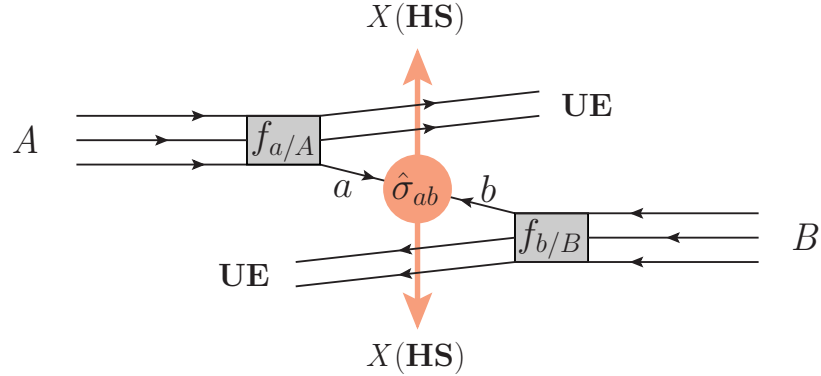


Figure 2.7: Proton-Proton scattering factorised into the hard scattering (HS) process  $ab \rightarrow X$  with cross section  $\hat{\sigma}_{ab \rightarrow X}$  and soft scatter process leading to the underlying event (UE). The functions  $f_{a/A}$  and  $f_{b/B}$  refer to the Parton Distribution Functions (PDF), which are experimentally determined and describe the momentum distribution of the quarks and gluons inside the proton.

Protons are fermions and in its simplest terms consists of three valence quarks, with two up quarks and one down quark, which are held together by the strong force, mediated by gluons. The proton, made up of partons, consists of virtual quark-antiquark pairs called sea quarks, which form when a gluon colour field splits. Collisions from two partons are classified as either soft or hard depending on the momentum transfer in the collision. The softer processes in the collision are more dominant and take place between the hard event. The soft process is however less understood, as perturbation theory breaks down for QCD calculations at smaller energy, due to the small-divisor problem. The soft interaction of the proton-proton collision is also known as the underlying event. Figure 2.7 shows a proton-proton interaction

between two protons A and B, with the process factorised into hard and soft. The hard process  $ab \rightarrow X$ , where  $a$  and  $b$  are two partons in the final state  $X$ , has a cross section  $\hat{\sigma}_{ab \rightarrow X}$ , which only takes into account the hard scatter and does not account for soft and fragmentation terms. The total proton scattering cross section for the hard scatter  $\sigma_{AB}$  is defined by,

$$\sigma_{AB} = \int dx_a dx_b f_{a/A}(x_a, \mu_F) f_{b/B}(x_b, \mu_F) \hat{\sigma}_{ab \rightarrow X}, \quad (2.15)$$

where the function  $f_{a/A}(x_a, \mu_F^2)$  is the Parton Distribution Function (PDF), which is dependent on the parton momentum fraction,

$$x_a = \frac{p_a}{E_{beam}}, \quad (2.16)$$

and the factorisation scale  $\mu_F$ .

QCD perturbative corrections must also be considered in the calculation. One such correction, coming from collinear gluon radiation, can lead to large logarithmic terms. These terms can be absorbed by the PDF, due to the factorisation scale  $\mu_F$ , which describes the energy scale separating the hard and soft processes.

The perturbative calculation of the hard scatter, neglecting soft and fragmentation terms, can be expressed by the strong coupling constant  $\alpha_s$ , which depends heavily on the renormalisation scale  $\mu_R$  of a given process,

$$\hat{\sigma}_{ab \rightarrow X} = \hat{\sigma}_0 + \alpha_s(\mu_R^2) \hat{\sigma}_1 + \alpha_s^2(\mu_R^2) \hat{\sigma}_2 + \alpha_s^3(\mu_R^2) \hat{\sigma}_3 + \dots, \quad (2.17)$$

where the leading order terms come from  $\hat{\sigma}_0$  and  $\hat{\sigma}_1$ , next-to-leading-order terms come from  $\hat{\sigma}_2$  and next-to-next-leading-order terms come from  $\hat{\sigma}_3$ . The cross sections can be accurately calculated for proton-proton scattering by combining Equations 2.17 and 2.15. Figure 2.10 summarises some of the next-to-leading order perturbative cross sections for a number of processes as a function of the centre-of-mass energy, while Figure 2.9 shows the inclusive Higgs boson cross section as a function of the Higgs mass at leading-order (LO), next-to-leading-order (NLO) and next-to-next-to-leading-order (NNLO). From Figure 2.9 we can see that higher-order corrections make large contributions to the cross section of the Higgs boson.

The dependency of the calculated cross sections largely depends on the two scales  $\mu_F$  and  $\mu_R$ . These scales are usually chosen to be equal to the momentum transfer of the hard event, such that  $\mu_F = \mu_R = Q$ . At higher order calculations the cross section is less dependent to these scale factors. In fact, if all the terms in the perturbation series were calculated there would be no dependence on  $\mu_F$  and  $\mu_R$ . However, such calculations do not exist and uncertainties are assigned to the predicted cross sections by varying  $\mu_F$  and  $\mu_R$  [23].

The PDFs dependence on  $\mu_F$  and the parton momentum  $x_{a/b}$  is calculated through theoretical [24] and experimental analysis, respectively. The two PDFs used in the presented thesis are the CT10 [25] and CTEQ6L1 [26]. The CT10 PDF for different quark flavours and gluons is shown in Figure 2.8, where it can be seen that the gluons have less momentum fraction on average than the valence quarks.

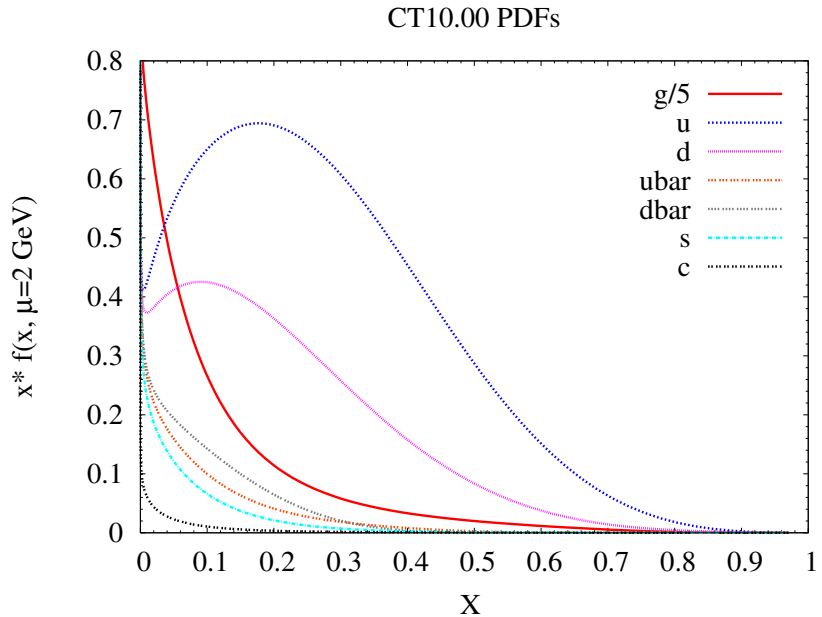


Figure 2.8: Parton distribution functions determined from CT10 for a factorisation scale  $\mu_F = 2$  GeV. Taken from [25].

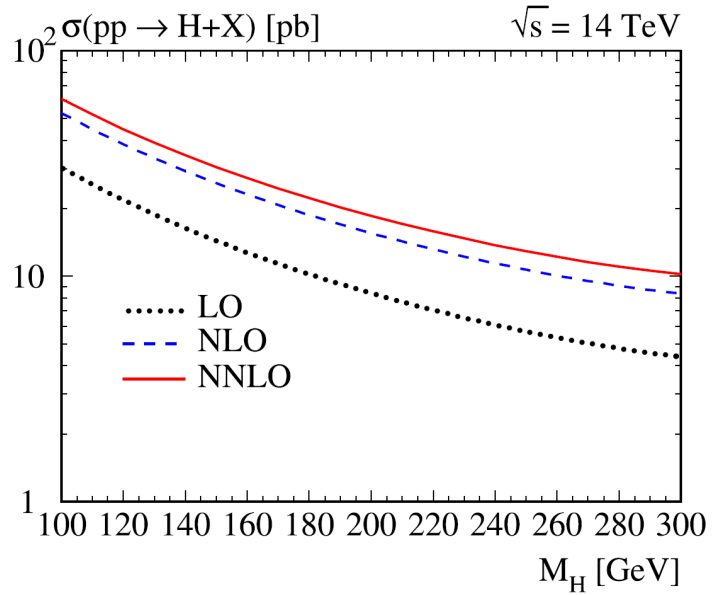


Figure 2.9: Inclusive Higgs boson cross section for proton-proton collisions as a function of Higgs boson mass. Taken from [27].

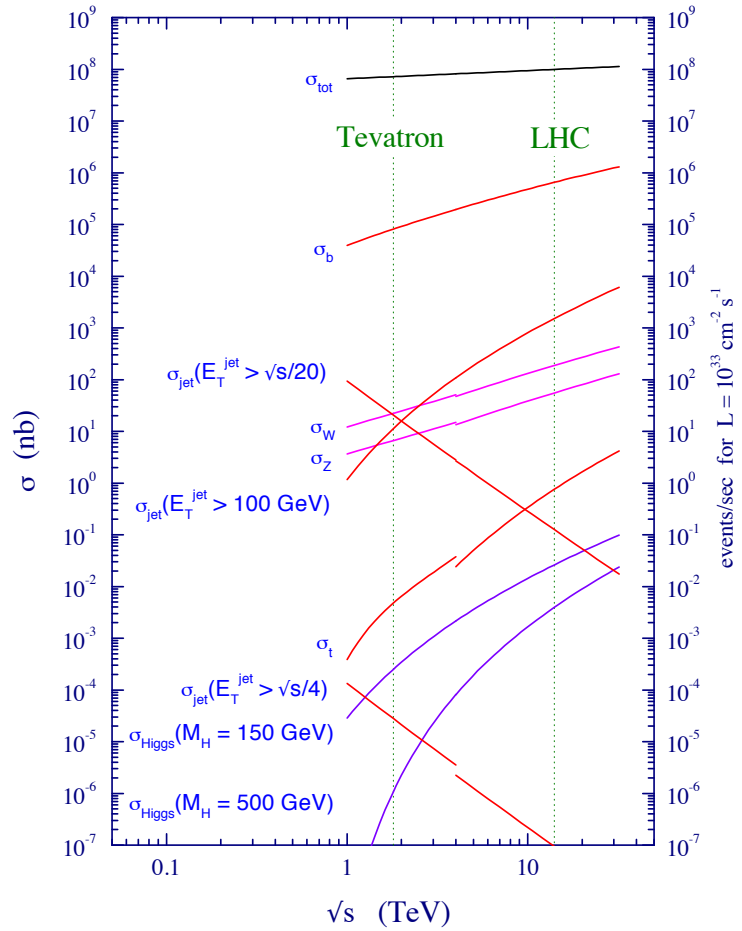


Figure 2.10: Next-to-leading-order cross sections and expected number of events for an integrated luminosity of  $L = 10^{33} \text{ s}^{-1} \text{ cm}^{-2}$  for Standard Model processes in proton-proton (LHC) and proton-anti-proton (Tevatron) collisions, as a function of the centre-of-mass-energy  $\sqrt{s}$ . Taken from [27].

### 2.3.2 Production of the Higgs Boson at the LHC

The Standard Model Higgs boson is produced through a number of production mechanisms, which are highlighted in Figure 2.11. A summary of the most dominant production mechanisms is summarised in Table 2.2, with the associated predicted cross section at a centre-of-mass-energy of  $\sqrt{s} = 8$  TeV for a Higgs boson mass of  $m_H = 125$  GeV. From Table 2.2, we can see that the dominant production mechanism is via gluon fusion ( $ggF$ ) that occurs through quark loops. The next dominant production process is from vector boson fusion ( $VBF$ ) and has an order of magnitude in difference with the  $ggF$  cross section. The cross sections from associated pair production ( $VH$ ) with vector bosons, where  $V = W$  or  $Z$ , is also further reduced by a factor of two for  $WH$  and four for  $ZH$ , when comparing with  $VBF$  production. Finally, the production mechanism of the Higgs boson in association with a top-quark-pair is again reduced and occurs less frequently than all the other productions in Table 2.2.

The production mechanism cross section for the Higgs boson is dependent on the chosen mass for the Higgs. Figure 2.12a shows the cross section as a function of the Higgs boson mass for the various production modes. The relationship shown in Figure 2.12a, shows the cross section rapidly decreasing for an increase in the Higgs boson mass for all production mechanisms (the cross section is calculated using the method described in [28]). The  $ggF$  cross section calculation uses NNLO in QCD [29], with NLO electroweak (EW) corrections [30] and next-to-next-to-leading logarithmic (NNLL) terms. The  $VBF$  cross section has been calculated using the full NLO QCD and EW corrections [31]. The cross section for associated vector boson production has been calculated using NLO QCD and NNLO corrections [32, 33],

while NLO EW corrections have also been considered. Lastly, the  $t\bar{t}H$  production has been calculated only in NLO QCD. The uncertainties shown in Table 2.2 and bands in Figure 2.12a, are calculated from uncertainties in the PDFs and choices in factorisation and normalisation [28, 34].

Table 2.2: The Higgs boson production mechanisms at the LHC, with their cross sections calculated at a centre-of-mass energy of  $\sqrt{s} = 8$  TeV for a Higgs boson mass of  $m_H = 125$  GeV [35].

Production Mechanism	Cross Section [pb] ( $m_H = 125$ GeV)	Figure
$gg \rightarrow H$	$19.52^{+2.87}_{-2.87}$	2.12a
$qq \rightarrow qqH$	$1.58^{+0.04}_{-0.05}$	2.12b
$qq \rightarrow WH$	$0.70^{+0.03}_{-0.03}$	2.12c
$qq \rightarrow ZH$	$0.39^{+0.02}_{-0.02}$	2.12d
$gg \rightarrow t\bar{t}H$	$0.13^{+0.02}_{-0.02}$	2.12e

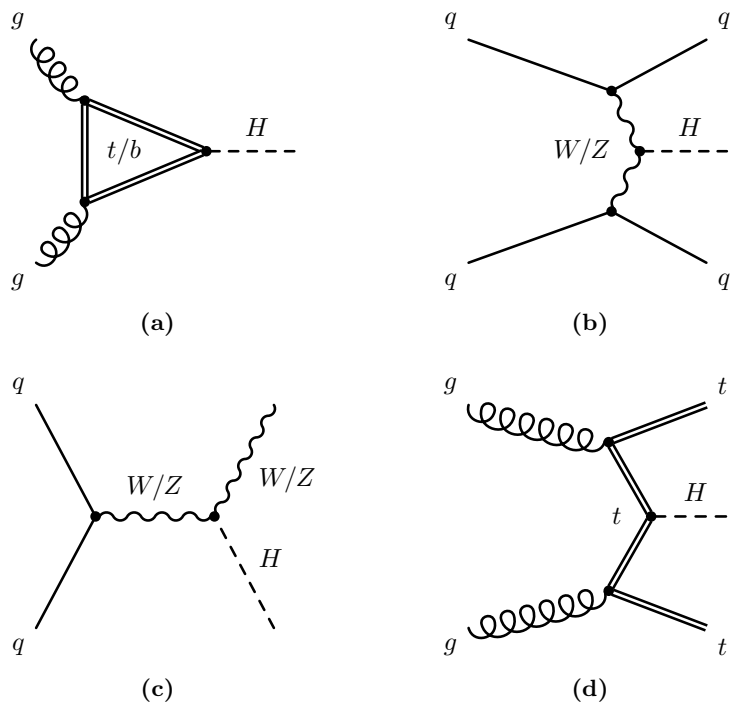


Figure 2.11: Leading order Feynman diagrams for Higgs boson production modes (a) gluon fusion ( $ggF$ ), (b) weak vector boson fusion ( $VBF$ ), (c) associated production with  $W$  and  $Z$  bosons and (d) associated production with a top-quark-pair ( $ttH$ ).

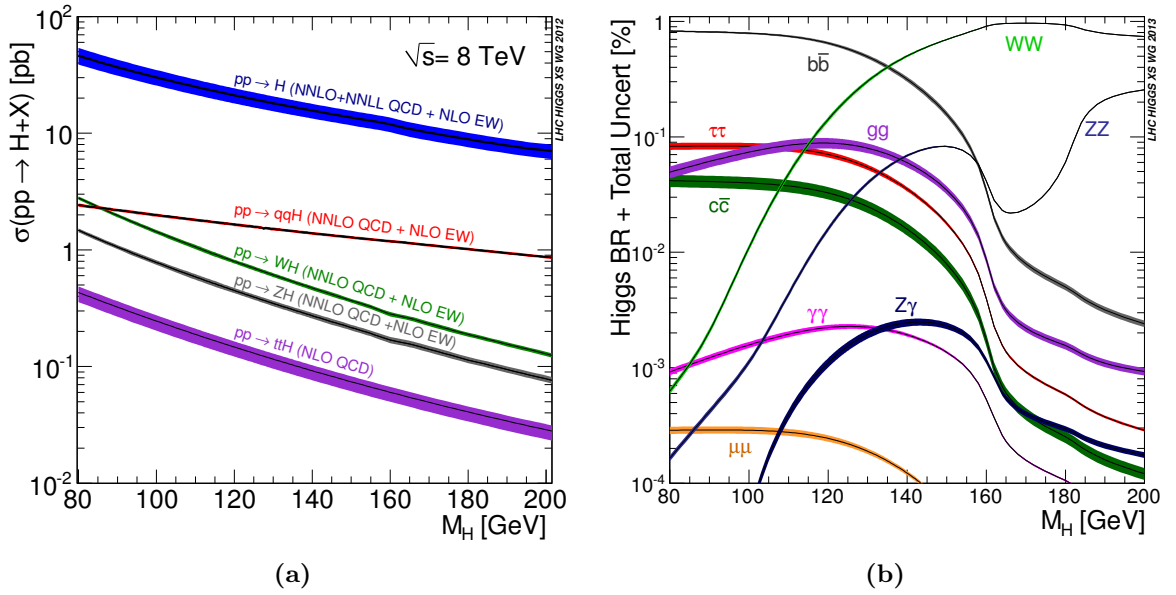


Figure 2.12: Theoretical predictions for (a) Higgs boson production cross section for proton-proton collisions at  $\sqrt{s} = 8$  TeV and (b) Higgs boson branching ratios for the most significant decay channels as a function of the Higgs boson mass  $m_H$ . The bands in (a) and (b) indicate the uncertainties of the predicted measurement. Taken from [35].

### 2.3.3 Decays of the Higgs Boson

The Higgs boson decays into a vast number of decay modes, with the Standard Model Higgs boson favouring decays to heavy vector bosons and fermions. Table 2.3 shows a list of the most favourable decay modes and are ordered by their branching fractions for a Higgs boson mass of  $m_H = 125$  GeV. At a Higgs boson mass of  $m_H = 125$  GeV the Higgs prefers to decay into a b-quark pair, followed closely by decays into two bosons. The  $H \rightarrow gg$  decay process, which predominantly occurs via heavy quark loops, like that seen in  $ggF$  production (see Figure 2.12a) is another favourable decay mode at  $m_H = 125$  GeV.

The search for the Higgs boson is however not only dependent on the branching fraction of the decaying Higgs, but also the final state signature and the cross section of the background candidates. Hence,  $b$  and  $c$  quarks, gluons, hadronic decays of  $W$  and  $Z$  bosons are all less sensitive final states, when compared to leptons in the hadron collider.

The Higgs boson decay widths and branching ratios are computed using the *HDECAY* [36] program for all channels. Higher-order QCD and electroweak corrections are taken into account if available. The uncertainties in the branching fraction calculations are detailed in [35] and calculate the uncertainties from the input parameters  $\alpha_s$  and  $m_c$ ,  $m_b$  and  $m_t$  due to missing higher-order corrections.

Table 2.3: The branching fractions calculations for the main Higgs boson decay modes for a Higgs boson mass of  $m_H = 125$  GeV. Errors are shown in percentages to emphasise the relative accuracy of the measured branching fraction [35].

Decay Mode	Branching fraction ( $m_H = 125$ GeV)	Figure
$H \rightarrow b\bar{b}$	$5.77 \cdot 10^{-1} \begin{array}{l} +3.2\% \\ -3.3\% \end{array}$	2.13c
$H \rightarrow WW$	$2.15 \cdot 10^{-1} \begin{array}{l} +4.3\% \\ -4.2\% \end{array}$	2.13b
$H \rightarrow gg$	$8.57 \cdot 10^{-2} \begin{array}{l} +10.2\% \\ -10.0\% \end{array}$	2.13a
$H \rightarrow c\bar{c}$	$2.91 \cdot 10^{-2} \begin{array}{l} +12.2\% \\ -12.2\% \end{array}$	2.13c
$H \rightarrow \tau\bar{\tau}$	$6.32 \cdot 10^{-2} \begin{array}{l} +5.7\% \\ -5.7\% \end{array}$	2.13c
$H \rightarrow ZZ$	$2.64 \cdot 10^{-2} \begin{array}{l} +4.3\% \\ -4.2\% \end{array}$	2.13b
$H \rightarrow \gamma\gamma$	$2.28 \cdot 10^{-3} \begin{array}{l} +5.0\% \\ -4.9\% \end{array}$	2.13a
$H \rightarrow \mu\bar{\mu}$	$2.20 \cdot 10^{-4} \begin{array}{l} +6.0\% \\ -5.9\% \end{array}$	2.13c

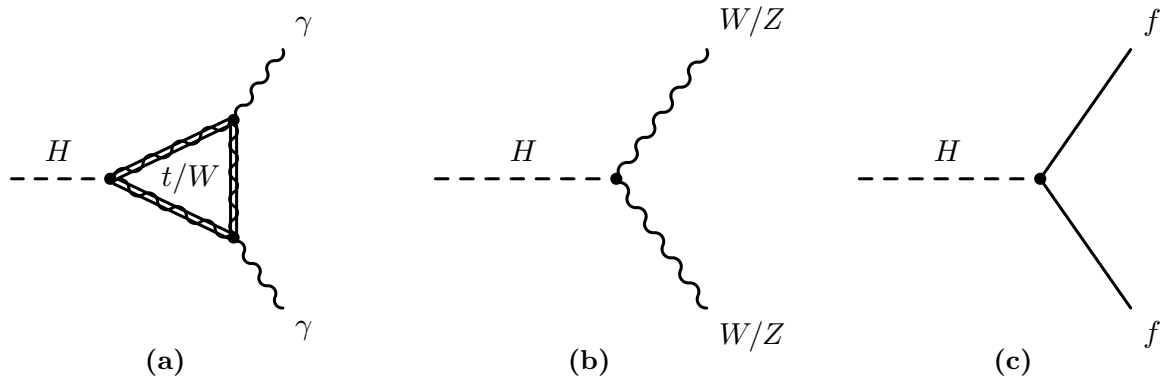


Figure 2.13: Leading-order Feynman diagrams for the main decay modes of the Standard Model Higgs boson.

### 2.3.4 Simulation of Event Generation

Simulated events allow us to compare our theoretical understanding of proton-proton collisions with data. The simulation starts with hard scattered events at the parton-level and uses the highest-order matrix element (ME) calculations available. Once the ME has been calculated, parton decays are modelled using parton shower (PS) algorithms, which simulate higher-order processes that the ME does not account for, such as initial and final state gluon radiation. A more detailed discussion on the Monte-Carlo event generation is described in [37].

The hadronisation of final state partons is modelled using Monte-Carlo methods, such as the Lund String Model [38]. The model parameters are tuned using electron-positron annihilation data and allow the process to be analysed in a clean environment, minimising the systematic impact.

The underlying event is also simulated using Monte-Carlo methods, with the model parameters tuned with data. Additional modelling of pile-up events is also taken into consideration and discussed in more detail in Section 3.1. The analysis presented uses several Monte-Carlo generators to simulate signal and background processes. Table 2.4 shows an overview of the generators used for the simulation of the hard and soft processes in the event simulation.

The *POWHEG* generator is used to simulate next-to-leading order signal processes, while the *ALPGEN* generator uses leading order ME calculations combined with the MLM scheme to match parton shower contributions from the *HERWIG* simulator. The generators used to simulate the hard scatter also need to model Parton Distribution Functions (PDF) and take them as inputs into the model. The

*ALPGEN* and *PYTHIA 6/8* generators use the PDF set of CTEQ6L1 [25], whereas *POWHEG* and *MC@NLO* generators us the PDF set of CT10 [26].

Table 2.4: Monte-Carlo event generators used in the presented analysis, where HS indicates the hard scattering process; had. indicates hadronisation; PS indicates parton shower; UE+PU indicates underlying and pile-up event modelling and All indicates the full event description.

	Generator	Application	Remarks
NLO	<i>POWHEG</i> [39]	HS	
	<i>MC@NLO</i> [40]	HS	
LO	<i>ALPGEN</i> [41]	HS	Combined with <i>HERWIG</i> and <i>JIMMY</i>
	<i>ACERMC</i> [42]	HS	
	<i>SHERPA</i> [43]	All	Includes higher-order electroweak corrections
	<i>PYTHIA 6/8</i> [44]	had.,PS, UE+PU	
	<i>HERWIG</i> [45]	had.,PS	
	<i>JIMMY</i> [46]	UE+PU	Combined with <i>HERWIG</i>

## 2.4 Experimental Constraints

In this section we will look at the direct and indirect experimental constraints that have been placed on the Standard Model Higgs boson. The direct limits that have been derived from the LEP experiment at CERN [47, 48, 49] and the Tevatron experiment at Fermilab [50, 51] will be shown. The indirect limits derived from precision measurements of the electroweak parameters will also be shown. Lastly, an overview of the LHC’s 2012 discovery will be briefly discussed.

The precision electroweak tests have allowed an upper limit to be derived for the Higgs boson mass, where a combination of LEP and Tevatron data has been used to constrain the Higgs boson mass to be less than 186 GeV at a 95% CL [52]. Figure 2.14 (blue band plot) shows a  $\chi^2$  best fit to all the electroweak precision tests as a function of the Higgs boson mass. The minimum of the  $\chi^2$  fit shows the best matching value for the Higgs mass, which has a minimum at  $m_H = 80^{+36}_{-26} \text{ GeV}$ .

The direct searches of the Higgs boson from LEP and Tevatron have also allowed lower and upper limits to be derived for the Higgs boson. The LEP experiment successfully placed a lower limit on the Higgs boson mass of up to 114.4 GeV at a 95% CL [52]. The main Higgs production mechanism that was analysed at LEP was the Higgs-strahlung process, which radiates a virtual  $Z$  boson,  $e^+e^- \rightarrow Z^* \rightarrow ZH$ . The Tevatron experiment also produced combined results on the Higgs boson mass, which excluded a mass range between  $90 < m_H < 109 \text{ GeV}$  and  $149 < m_H < 184 \text{ GeV}$  (see Figure 2.15). The main Higgs production mechanism at the Tevatron collider was associated production with a vector boson, where  $p\bar{p} \rightarrow VH$ , with  $V = W^\pm, Z$ . Due to the wider mass range of the Tevatron the main decay channels of the Higgs

boson included vector boson pairs, such as  $H \rightarrow ZZ$  and  $H \rightarrow W^+W^-$ .

The discovery of the new particle at the LHC, was produced by a combined result from the ATLAS [4] and CMS [5] experiments on July 4th 2012. The experiments observed a significant excess of events, which were compatible with the expectation of the Standard Model Higgs boson, with a mass of  $\sim 125$  GeV. The results were taken from a dataset with  $5 \text{ fb}^{-1}$  at  $\sqrt{s} = 7 \text{ TeV}$  and  $5.8 \text{ fb}^{-1}$  at  $\sqrt{s} = 8 \text{ TeV}$ . Figure 2.16 shows an excess above the Standard Model background only hypothesis at a mass of  $\sim 125$  GeV, while all other mass regions have been excluded.

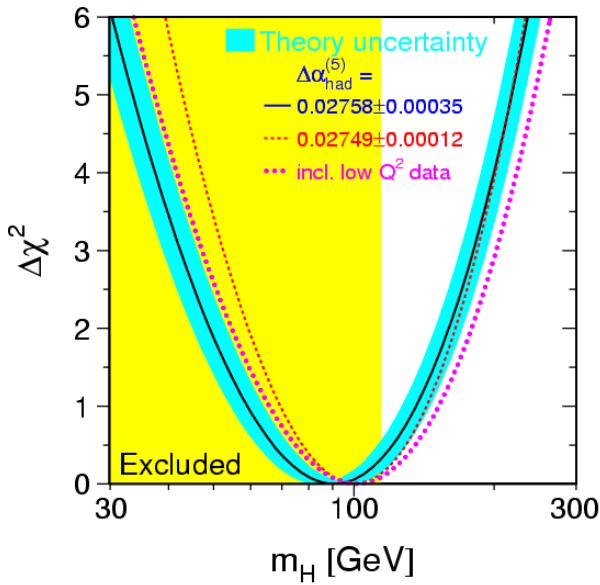


Figure 2.14: A  $\Delta\chi^2$  eighteen parameter fit of the electroweak precision measurements as a function of the Higgs boson mass  $m_H$ . Taken from [52].

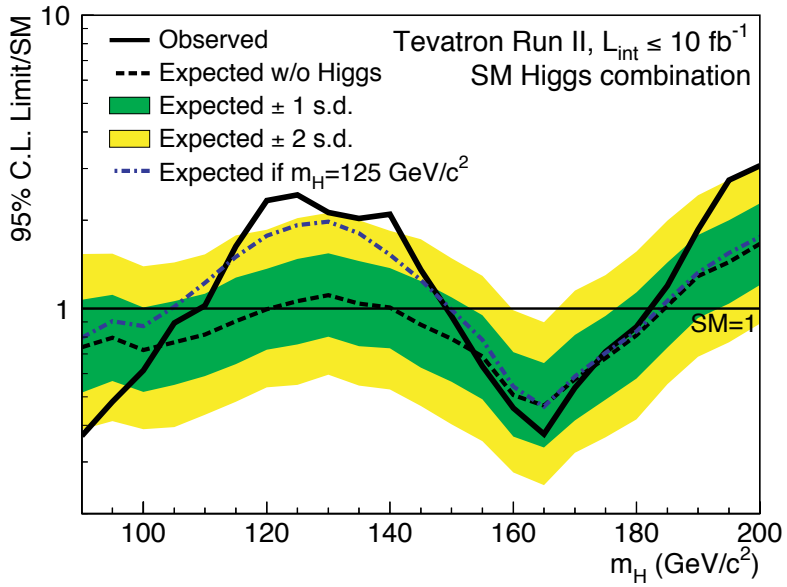
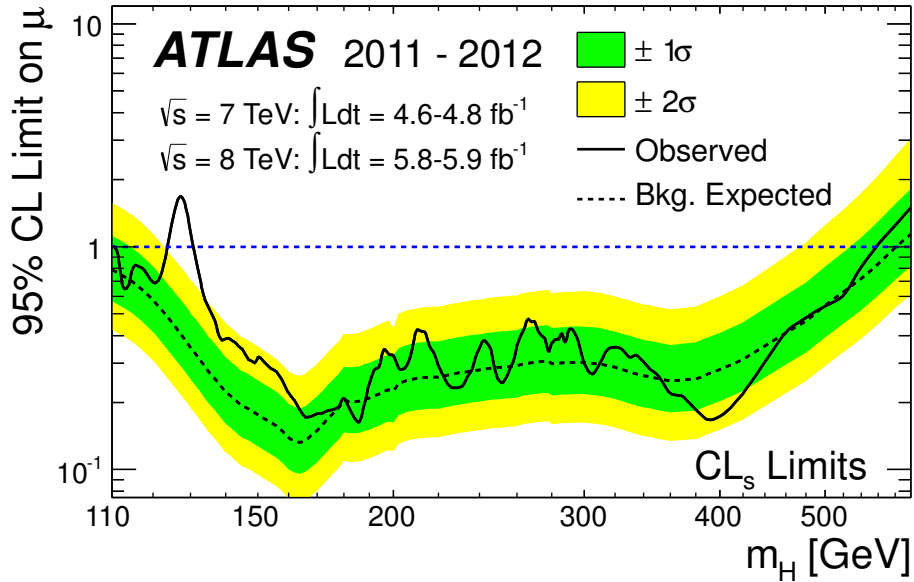


Figure 2.15: Observed and expected 95% CL upper production limits expressed as a multiple of the Standard Model cross section as a function of Higgs boson mass for the combined CDF and D0 searches in all decay modes. Taken from [53].



The most sensitive decays found at the ATLAS experiment are the two photon [54] and two  $Z$  boson [55] decays, which show a combined discovery-level signal significance of over six standard deviations, when combined with the CMS [56] results. The two experiments have also precisely measured the invariant mass of the Higgs boson, with a mass of  $m_H = 125.5 \pm 0.6$  GeV [6] and  $m_H = 125.7 \pm 0.4$  GeV [7], from the ATLAS and CMS experiments respectively. Evidence of the Higgs boson has also been shown from the decay of the Higgs boson into two  $W$  bosons [57] and two  $\tau$  leptons [58]. These channels have shown a significance of four standard deviations over the signal significance. Currently the Higgs boson decay mode to  $H \rightarrow b\bar{b}$  [59], which is the main focus of this thesis, has found no significant evidence of the Higgs boson particle. However, new studies that supersede the presented analysis have shown new promising results [60].

## 2.5 Summary

The Standard Model has allowed us to successfully describe the actions of the current set of known fundamental particles. In this chapter we have focused our attention on the electroweak sector of the theory, where spontaneous symmetry breaking allows us to describe the mass symmetry of the vector bosons that carry the fundamental forces. The Higgs Mechanism postulates that there must exist a remnant Higgs boson. The Higgs boson has many production and decay modes in the Standard Model, with a discovery potential in several mass regions. It has been shown however, by experiments at LEP, Tevatron and CERN that there was in fact a small window in which there was a possible Higgs boson candidate. The discovery on July 4th 2012 at CERN, gave evidence of a Higgs boson candidate at an invariant mass of  $\sim 125$  GeV.

# Chapter 3

## The LHC and the ATLAS Experiment

### 3.1 The Large Hadron Collider

The Large Hadron Collider (LHC) [61] is the world’s largest and most energetic particle collider. Over 10,000 scientists and engineers from over 100 countries helped construct the LHC from 1998 to 2008. The two ring superconducting collider was installed in the already existing  $\sim 27$  km Large Electron Positron (LEP) tunnel, which has eight straight sections and eight arcs lying from  $\sim 45$  m to  $\sim 170$  m below the surface and crosses the Swiss-French border near Geneva.

The collider tunnel contains two parallel beam pipes, which can contain either protons or lead ions. The protons are supplied to the LHC through an injector chain [63] that starts at the Linac 2 linear accelerator accelerating the protons from source to 50 MeV. The protons are then received by the Proton Booster, which accelerates

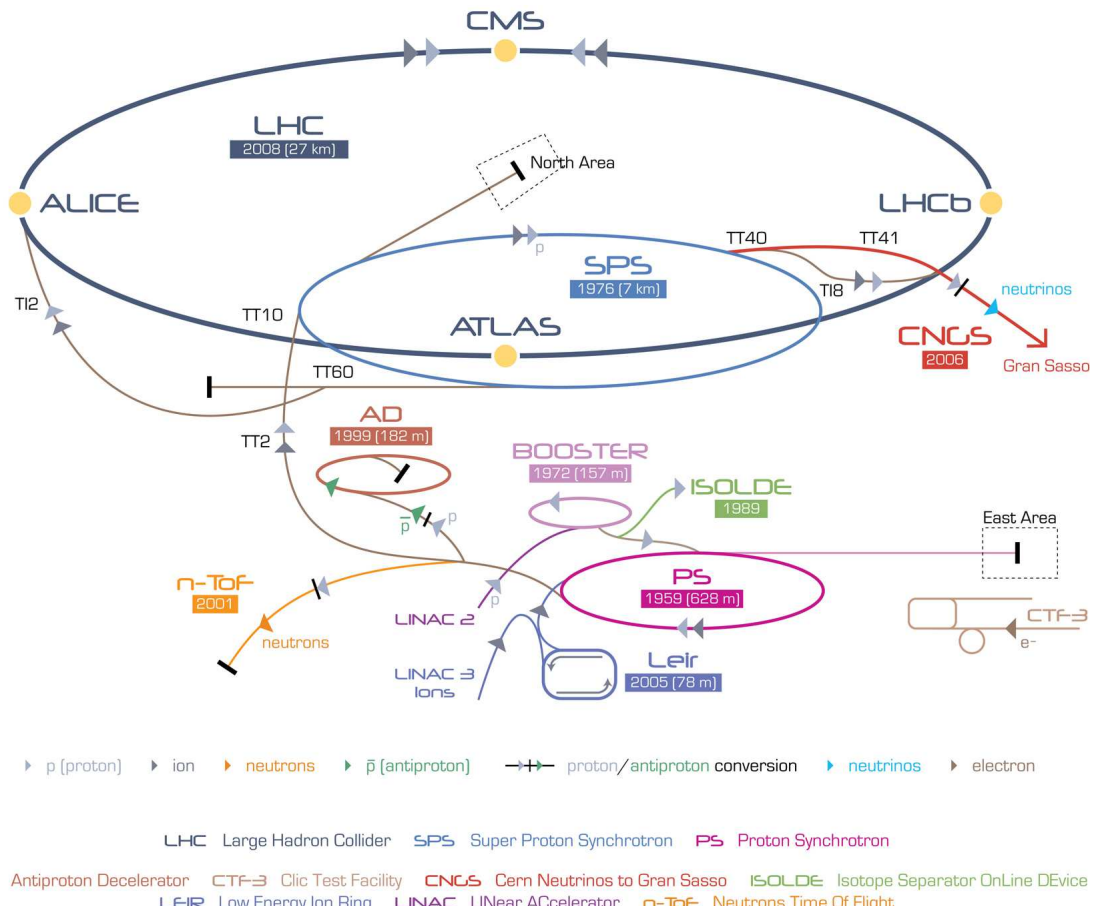


Figure 3.1: CERN accelerator complex. Image taken from [62]

the protons up to  $\sim 1.4$  GeV. From here the protons are injected into the Proton Synchrotron (PS), accelerating the protons to  $\sim 25$  GeV. The PS injects the protons into the Super Proton Synchrotron (SPS), the last stage in the injection chain before the protons are injected into the LHC. The protons enter the LHC from the SPS at 450 GeV, where the LHC can accelerate the protons using radio frequency (RF) cavities to an energy of 7 TeV per beam for collisions at four interaction points where ATLAS, CMS, LHCb and the ALICE experiments are housed. The beam pipe is stored in a cryostat, maintaining a temperature of 1.9 K, allowing superconducting magnets at a magnetic field of  $\sim 8.33$  T to be used for bending the beam around the ring. During full intensity the LHC is designed to hold 2808 bunches with a bunch spacing of 25 ns - each bunch will contain approximately  $\sim 10^{11}$  protons. Currently the bunches have a spacing of 50 ns allowing for 1380 bunches to collide at 4 TeV per beam. The beams are brought to collision with a small crossing angle of  $150 - 200 \mu\text{rad}$  to avoid parasitic collisions.

The geometrical properties of the colliding bunches and the machine's parameters can allow us to express the luminosity in the equation below.

$$L = \frac{N_b^2 n_b f_{rev} \gamma_r F}{4\pi \epsilon_n \beta^*}, \quad (3.1)$$

where  $N_b$  denotes the number of particles per bunch,  $n_b$  the number of bunches per beam,  $f_{rev}$  the revolution frequency,  $\gamma_r$  the relativistic gamma factor,  $\epsilon_n$  the normalised transverse beam emittance,  $\beta^*$  the beta function of the collision point and  $F$  the reduction factor due to the crossing angle at the interaction point (IP):

$$F = \left( 1 + \left( \frac{\theta_c \sigma_z}{2\sigma^*} \right)^2 \right)^{-\frac{1}{2}}, \quad (3.2)$$

where  $\theta_c$  is the crossing angle at the IP,  $\sigma_z$  the RMS of the bunch length and  $\sigma^*$  is the RMS of the transverse beam size at the IP - see Table 3.1 for beam parameters.

In addition to the instantaneous luminosity we can calculate the number of pile-up<sup>1</sup> events expected per bunch crossing based on the rate definition in Eq. ??.

$$R = \sigma_{MB} \cdot \mathcal{L} \cdot \frac{\Delta_{tbc}}{1 - f_{empty}}, \quad (3.3)$$

where  $\Delta_{tbc}$  is the time interval between two bunch crossings and  $f_{empty}$  is the fraction of empty bunches. During the data taking periods from 2010 to 2012 in-depth analysis of the detector performance was carried out. Figures 3.2 show the number of colliding bunches, delivered luminosity, peak pile-up and number of interactions per bunch crossing. Throughout 2010 pile-up mainly consisted of in-time pile-up<sup>2</sup>. The strategy to correct for in-time pile-up was to apply an event-by-event calorimeter correction to the recorded signal in data [64]. In comparison 2011 and 2012 have seen an increase in out-of-time<sup>3</sup> pile-up due to the increase in beam energy and smaller bunch spacing. To correct for out-of-time pile-up an event-by-event correction that only considered particles coming from the collision of interest were considered [64].

---

<sup>1</sup>Pile-up is defined as having more than one collision per crossing.

<sup>2</sup>In-time pile-up refers to multiple interactions within the same bunch crossing.

<sup>3</sup>Out-of-time pile-up refers to the bunch spacing being shorter than the detector response time.

Table 3.1: LHC beam parameters.

Parameter	Nominal	2011	2012
LHC circumference	27 km	-	-
beam energy	7 TeV	3.5 TeV	4 TeV
dipole magnetic field strength	8.33 T	-	-
dipole magnet temperature	1.9 K	$\sim$ 1.9 K	$\sim$ 1.9 K
particles per bunch	$1.15 \times 10^{11}$	$1.5 \times 10^{11}$	$1.6 \times 10^{11}$
bunches per beam	2808	1380	1380
bunch crossing frequency	40 MHz	20 MHz	20 MHz
bunch spacing	25 ns	50 ns	50 ns
amplitude function, $\beta^*$	0.5 m	1.0m	0.6 m
emittance, $\epsilon_n$	3.75 $\mu\text{m}$	1.9 – 2.3 $\mu\text{m}$	1.7 – 3.0 $\mu\text{m}$
luminosity ( $\text{cm}^{-2}\text{s}^{-1}$ )	$1 \times 10^{34}$	$3.6 \times 10^{33}$	$7.7 \times 10^{33}$

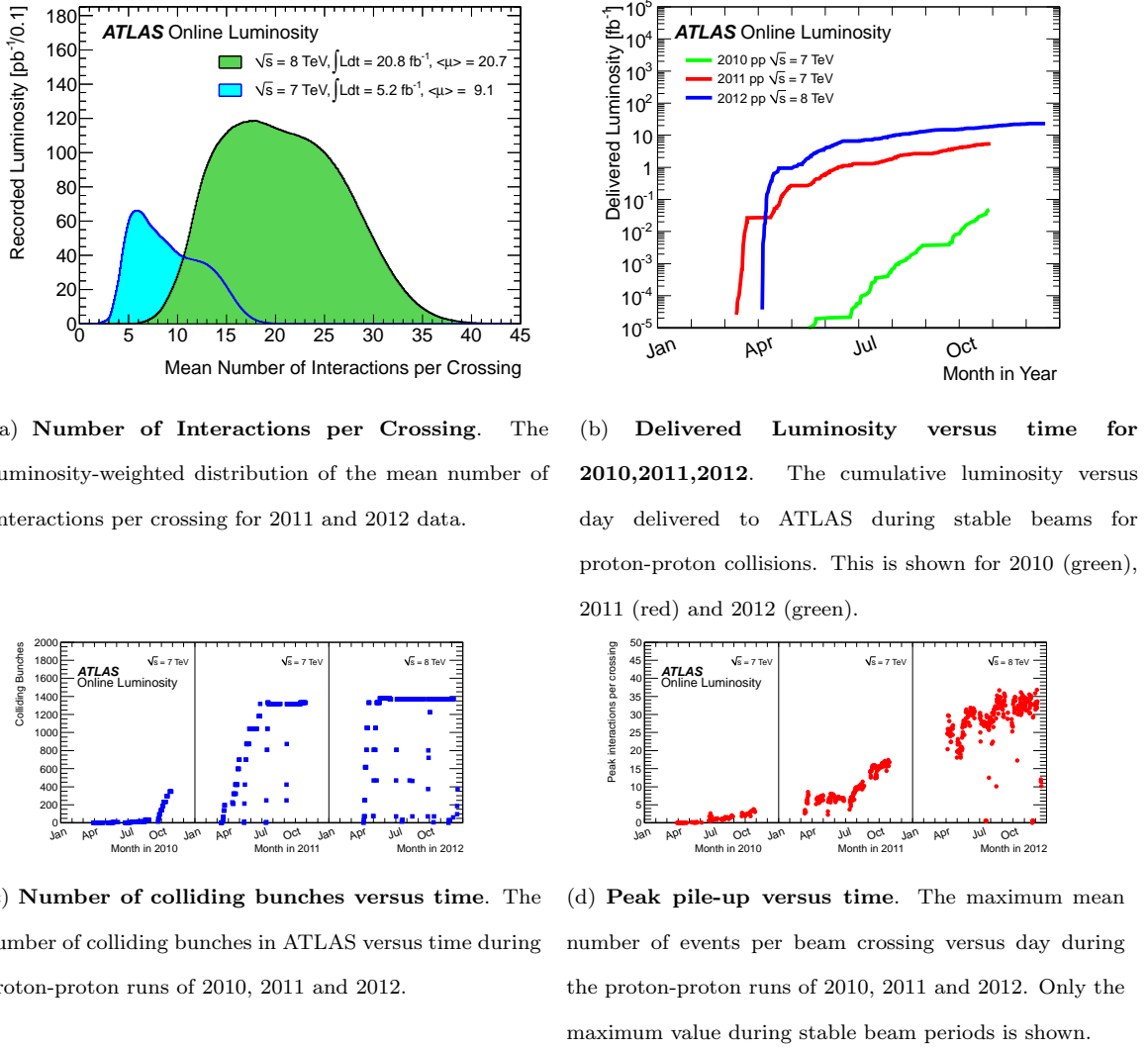


Figure 3.2: ATLAS luminosity measurement [65].

## 3.2 The ATLAS Detector

### 3.2.1 Overview

The ATLAS (**A** Toroidal **L**H**C** **A**pparatus) general purpose detector located at the LHC Intersection Point 1 started operations in autumn 2007 when the last piece of the complex structure (shown in Figure 3.3) was installed in the cavern 100 m below the surface. The high radiation doses and interaction rates delivered by the LHC collider create an inhospitable environment for the detector to operate. In spite of the difficult operating conditions, the search for the Higgs boson and other new physics phenomena require the detector to have a broad array of requirements, which include:

- Large acceptance in pseudo-rapidity and almost full azimuthal angle covered.
- Small charged particle resolution and high reconstruction efficiency in the inner detector.
- High precision impact parameter reconstruction for  $b$ -jet and  $\tau$ -jet identification.
- Exceptional electromagnetic (EM) calorimeter performance to identify and measure electron and photon energies, complemented with a full-coverage of the hadronic calorimeter for accurate measurements of jet and missing transverse energy.
- Accurate muon identification and momentum resolution for a wide range of momenta - especially for high  $p_T$  muons.

- Fast, efficient and flexible trigger system that can select events of interest in the presence of low transverse momentum objects and large backgrounds.

The ATLAS detector spans a length of 44 m along the beam axis and reaches a height of 25 m. The detector has 6 different detector subsystems and 2 magnetic subsystems. The subsystem closest to the interaction point in the detector is the inner detector, which is surrounded by a 2 T solenoid magnetic field. The coverage of the inner detector is  $|\eta| < 2.5$ , which is discussed in Section 3.2.2. The next layer of the detector consists of a LAr electromagnetic calorimeter covering a range up to  $|\eta| < 3.2$ . The hadronic calorimeter situated behind the EM calorimeter covers a range  $|\eta| < 1.7$  in the scintillator-tiles to  $|\eta| > 1.5$  in the LAr end-caps. The forward LAr calorimeters provide EM and hadronic energy measurements and extend the pseudo-rapidity coverage up to  $|\eta| = 4.9$ . The muon system has a coverage of  $|\eta| > 2.7$  and surrounds the calorimeter with three high precision tracking chambers [66].

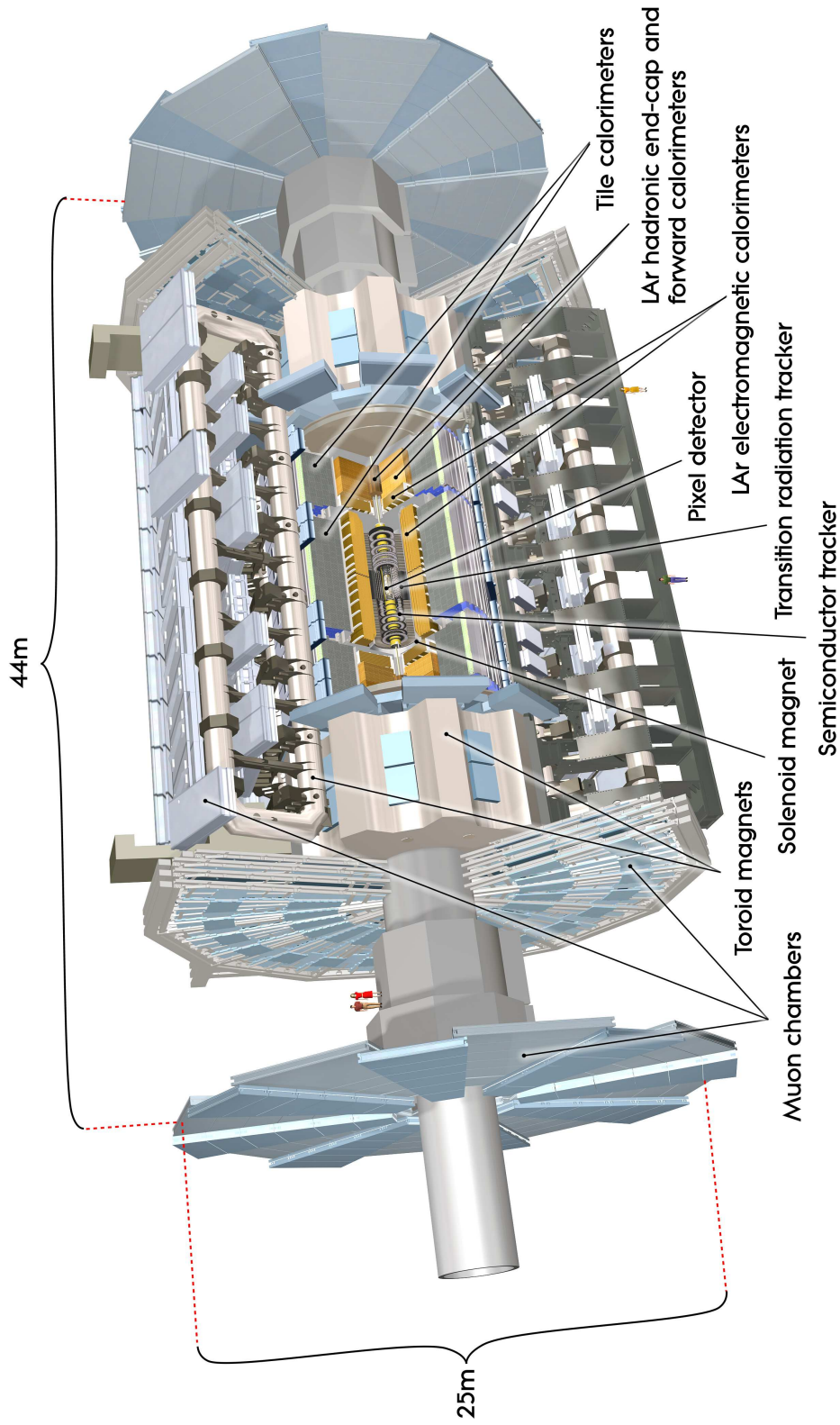


Figure 3.3: The schematic of the ATLAS detector

### 3.2.2 Co-ordinate System

The ATLAS co-ordinate system is centred around the interaction point and set along the beam axis in the  $z$  direction, while  $x$  in the transverse plane points positively to the centre of LHC ring and  $y$  points upwards from the detector perpendicular to both the  $x$  and  $z$  axes. Due to the cylindrical geometry of the detector, polar co-ordinates  $(R, \theta, \phi)$  have been defined. The angle  $\theta$  is defined as the measured angle from the beam axis and the azimuthal angle  $\phi$  defined in the  $x - y$  plane around the  $z$ -axis, with respect to the  $x$ -axis. The angle  $\theta$  can be used to derive the Lorentz invariant measure of position in the detector - more commonly known as pseudorapidity ( $\eta$ ).

The *Rapidity* is defined:

$$y = \frac{1}{2} \ln \frac{E + p_z}{E - p_z}, \quad (3.4)$$

Where  $E$  is the energy and  $p_z$  is the beam axis momentum component.

The pseudorapidity can be shown to equal Equation 3.4 when the speed of the particle is close to the speed of light and  $E \gg M$ .

$$\eta = \ln \tan \left( \frac{\theta}{2} \right). \quad (3.5)$$

The distance between two objects in the detector can be defined in the  $\eta - \phi$  plane.

$$\Delta R = \sqrt{\Delta\eta^2 + \Delta\phi^2}, \quad (3.6)$$

where  $\Delta\eta$  is the difference in pseudorapidity and  $\Delta\phi$  is the difference in the azimuthal angles of the two objects.

When considering the transverse quantities in the detector such as transverse momentum  $p_T$ , transverse energy  $E_T$  and missing transverse energy  $E_T^{miss}$ , we define these in the  $x - y$  plane.

### 3.2.3 Inner Detector

The Inner Detector (ID) is the innermost part of the detector sitting a few centimetres from the beam axis and covering a region of  $|\eta| < 2.5$ . The 2 T solenoid magnet that overlooks the ID is used to reconstruct charged tracks by combining energy hits deposited in the high-resolution semiconductor pixel and silicon microstrip detectors (SCT), at high radii hits from the Transition Radiation Tracker (TRT) is used. To minimise multiple particle scattering and to avoid degradation of the momentum resolution, the optimum amount of material was used in the detector. The complete layout of the ID is illustrated in figures shown in Figure 3.4.

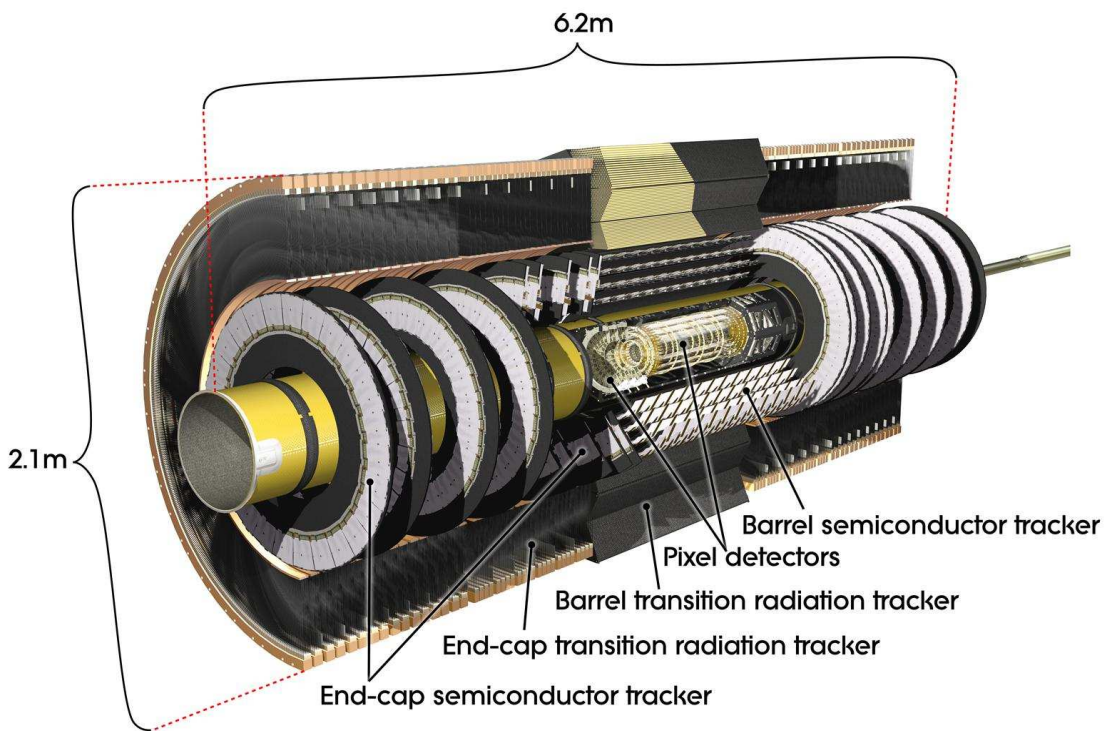


Figure 3.4: The schematic of the ATLAS Inner Detector.

## Pixel detector

The ID provides precision tracking by arranging the tracking detector (pixels and SCT) on cylinders around the beam axis and end-caps located on disks perpendicular to the beam axis. The silicon pixel detectors are segmented in  $R - \phi$  and  $z$ , with the minimum pixel size in  $R - \phi \times z$  of  $50 \times 400 \mu\text{m}^2$ , which achieves an accuracy in the barrel region of  $10 \mu\text{m}$  in  $R - \phi$  and  $115 \mu\text{m}$  in  $z$ . The end-cap region has an intrinsic accuracy of  $10 \mu\text{m}$  in  $R - \phi$  and  $115 \mu\text{m}$  in  $\phi$ . When a charged track hits the ID there is an energy deposit typically seen in the first three pixel layers. The layers must be positioned as close to the interaction point as possible to achieve a low impact parameter resolution, which is vital for efficient b-jet identification. The closest layer, named the b-layer is found 50.5 mm from the interaction point.

## Semiconductor Tracker (SCT)

The SCT is a silicon strip detector, with four barrel layers and two endcaps consisting of nine disks each. The barrel layers are made from 2112 separate modules, while the endcap consists of 988 modules. The SCT is made from two layers of single sided p-in-n silicon that allows charged particles to pass through to the depletion region at the centre of the junction, which produces electron hole pairs leading to a current and a signal that can be read out.

A SCT module consists of 768 strips, with a length of 6.4 cm at a pitch of  $80\mu\text{m}$ . The strips from the barrel layer run parallel with the beam axis on one side, while in the endcap, they run along the  $R$  direction. The other layer of the the SCT module places the strips at a stereo angle of 40 mrad, giving a resolution in  $z$  ( $R$ ) in the barrel (endcaps). The spatial resolution of the detector is  $17\mu\text{m}$  in  $R - \phi$  and  $580\mu\text{m}$  in  $z$ ,

while a similar performance is achieved in the endcap region.

## Transition Radiation Tracker (TRT)

The TRT is a straw drift tube tracker, that capitalises on transition radiation to help identify particles. The tracker's modules consist of 4 mm diameter straw bundles filled with a mixture of gas – 70% Xe, 27%  $CO_2$  and 3%  $O_2$ . A tungsten wire fills the centre of the tube and allows the tracker to collect charge. The straws run parallel with the beam axis in the barrel and are electrically divided into two at  $|\eta| = 0$ , with a readout at either end. The straws run radially in the endcaps, giving a total number of 351,000 readout channels. The resolution of the tracker in the  $R - \phi$  region is 130 $\mu$ m, with no measurement in the  $z$  direction.

The barrel and endcap straws are embedded with polypropylene fibres, that allow transition radiation photons to be emitted when charged particles cross between them. The photons are then absorbed by the straw tubes gas mixture and produce a large signal from ionising charged particles.

### 3.2.4 Calorimeter

The ATLAS calorimeter is the first detector outside the solenoid magnet and is designed to measure the energy of incoming particles through absorption. The coverage of the calorimeter is up to  $|\eta| = 4.9$  and uses different technologies throughout the pseudo-rapidity regions as shown in Figure 3.5. The calorimeter surrounding the inner detector (electromagnetic calorimeter) is finely segmented for precision measurements of electrons and photons. The electron or photon largely interacts through

bremsstrahlung and pair production, which produce a cascade of auxiliary electrons and photons. The other regions of the calorimeter are segmented more coarsely, since the objective of these regions is to reconstruct jets and measure missing transverse momentum.

One of the main design criteria of the calorimeter is to contain the electromagnetic and hadronic showers of the particles, as energy escaping results in a considerable reduction in energy resolution and contamination into the muon system. The total thickness of the EM calorimeter is measured in radiation lengths  $X_0$  and is greater than  $22X_0$  in the barrel and greater than  $24X_0$  in the end-caps. The total thickness of the hadronic calorimeter is approximately 11 nuclear interaction lengths ( $\lambda$ ), which is sufficient for accurate energy measurements of jets and reducing punch-throughs into the muon system.

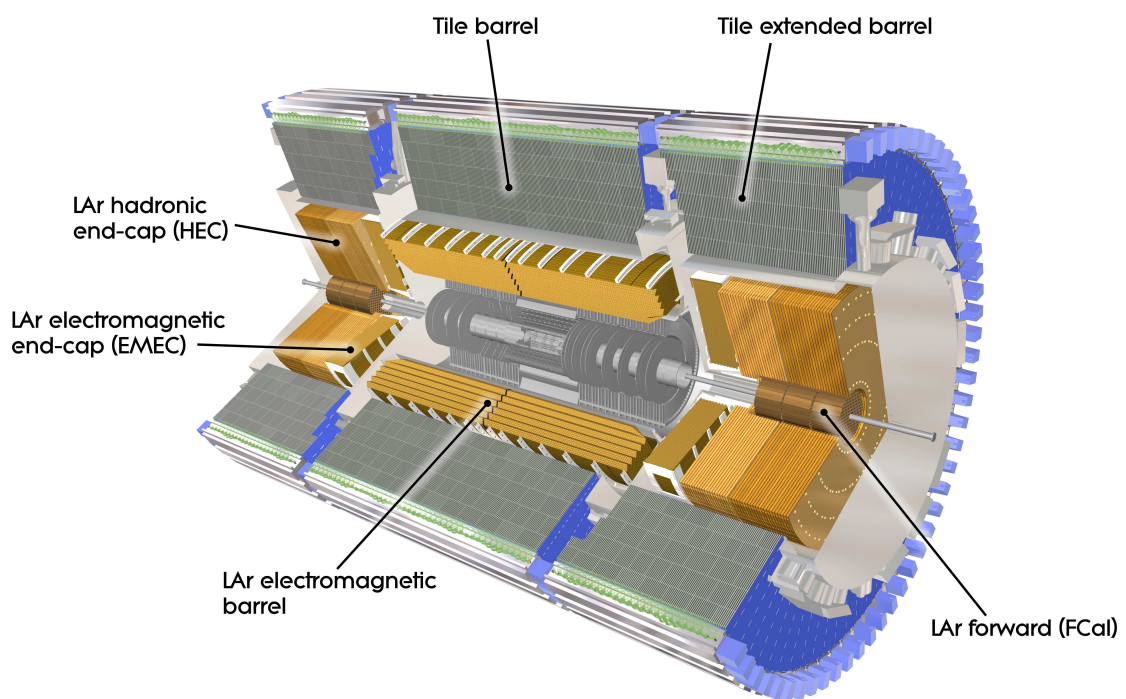


Figure 3.5: The schematic of the ATLAS Calorimeter

## LAr electromagnetic calorimeter

The EM calorimeter covers a pseudorapidity range of  $|\eta| < 3.2$  and is divided into a barrel (  $|\eta| < 1.475$  ) and two end-caps ( $1.375 < |\eta| < 3.2$ ). The EM calorimeter is a lead-LAr detector. The lead is used to absorb and produce particle showers, while the liquid argon is an active medium for particle detection. The barrel calorimeter is split into two identical calorimeters separated at  $z = 0$  by a 4 mm gap. The end-caps are divided into two coaxial wheels, which cover two separate regions of the detector ( $1.375 < |\eta| < 2.5$  and  $2.5 < |\eta| < 3.2$ ). The presampler detector, which is used to correct the energy lost in the solenoid before entering the calorimeter sits in a region  $|\eta| < 1.8$  and is built from an active LAr layer of 1.1 cm in the barrel.

Due to the precision measurement requirements of the EM calorimeter, both in energy and position, accordion-shaped kapton electrodes with lead absorber plates are used for full coverage. The accordion geometry allows for complete  $\phi$  symmetry of the detector without any azimuthal cracks, minimising the electromagnetic energy resolution. Over the region of  $|\eta| < 2.5$ , the EM calorimeter is segmented into three longitudinal sections. The first layer is called the eta-strip layer and is finely granulated in  $|\eta|$  to detect particles entry into the calorimeter and their shower shape. The shower shape is used for separating between photon (with a single energy deposition) and neutral pions, which have two very close energy deposits. The resolution achieved by the EM barrel calorimeter is shown in Equation 3.7 and was acquired with test beam data.

$$\frac{\sigma(E)}{E} = \frac{10\%}{\sqrt{E(GeV)}} \oplus 0.17\%, \quad (3.7)$$

where 10% is the stochastic term and 0.17% is the constant term. Similar results are also achieved for the endcap region of EM calorimeter. At the boundaries of the barrel and end-caps there are two cryostats ( $1.37 < |\eta| < 1.52$ ) which are excluded regions of the detector for precision measurements involving photons and electrons.

## Hadronic calorimeters

The hadronic calorimeter uses a number of technologies to maximise performance. The tile calorimeter, which uses scintillating tiles as the active material and steel as the absorber, is situated just outside the EM calorimeter envelope. The barrel covers a region of  $|\eta| < 1.0$ , while the two extended barrels cover a range of  $0.8 < |\eta| < 1.7$ . The LAr end-cap calorimeters, extend from  $|\eta| = 1.5$  up to  $|\eta| = 3.1$ , whilst the LAr forward calorimeter covers an  $\eta$  region up to 4.9. The combined LAr and tile calorimeter energy response from isolated charged pions was shown to be  $\frac{\sigma(E)}{E} = \frac{52\%}{\sqrt{E}} \oplus 3\%$ , which is very close to the design specifications. The forward detector, which uses LAr technology with a copper passive absorber for the first layer and tungsten for the second and third layer, has an energy response to pions of  $\frac{\sigma(E)}{E} = \frac{94\%}{\sqrt{E}} \oplus 7.5\%$  from test beam data. Lastly, the end-caps with similar LAr technology as the forward detector, but with only copper absorbers was shown to have an energy response of  $\frac{\sigma(E)}{E} = \frac{71\%}{\sqrt{E}} \oplus 1.5\%$  with test beam data.

### 3.2.5 Muon System

Muons can be cleanly detected in the muon system at ATLAS, due to the muons ability to pass through the calorimeter. The Muon Spectrometer measures the magnetic deflections of muon tracks with three large superconducting air-core toroid magnets (shown in figure 3.6). The barrel toroid, which is inline with the central solenoid magnet, has end-cap toroids at each end. The three toroids are made out of eight coils assembled radially and symmetrically around the beam axis, which cause muons to be bent outside the inner detector in the  $R - z$  plane. The magnetic field in the large barrel toroid spans a range of  $|\eta| < 1.4$ , while the two end-caps cover a region of  $1.6 < |\eta| < 2.7$ . The transition region in the muon system is a superposition of the three toroidal magnetic fields and has a lower bending power than the barrel and end-cap regions.

The muon detector is split up into two regions, one for triggering on muon events in a given bunch crossing and the other for high precision measurements, which determine the muon momenta. The precision measurements are performed by the Monitored Drift Tube chambers (MDTs), which constrain the muon track in the bending plane with an accuracy of 35  $\mu\text{m}$ . The MDT covers a region up to  $|\eta| = 2.7$ , whilst in the forward region ( $2 < |\eta| < 2.7$ ) Cathode-Strip Chambers (CSC) are used for their higher rate and time resolution measurements. The CSCs have an accuracy in the R direction of 40  $\mu\text{m}$  and 10 mm in  $\phi$ . The CSC can achieve these measurements due to the multiwire proportional chambers that have cathodes segmented into strips, which allow higher granularity in the innermost plane.

The trigger system in the muon detector consists of Resistive Plate Chambers

(RPG) in the barrel, and Thin Gap Chambers (TGC) in the end-cap region, which cover a pseudorapidity range  $|\eta| < 2.4$ . The RPG is a gaseous detector with a rate capability of 1 KHz/cm<sup>2</sup> and a space-time resolution of 1 cm × 1 ns in the barrel region ( $|\eta| < 1.05$ ). The TGC that is situated in the end-cap region ( $1.05 < |\eta| < 2.4$ ) has a slightly worse space-time resolution than the RPG.

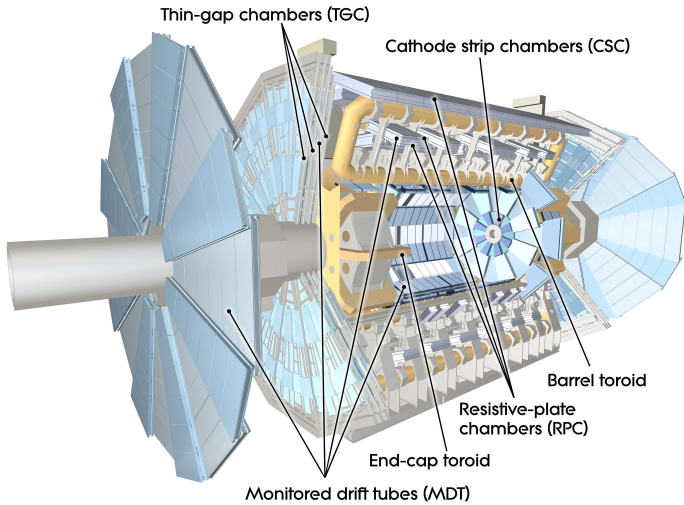


Figure 3.6: The schematic of the ATLAS Muon Spectrometer

### 3.2.6 Trigger System

The high interaction rate and complex event structure at ATLAS calls for an efficient and flexible trigger system design. The event selection used in the trigger system is composed of three different subsets: Level-1 (L1), Level-2 (L2) and Event Filter (EF).

The first level trigger provides a latency of  $\sim 2 \mu\text{s}$  and selects an event every 25 ns, during which time the data is processed and time stamped in the buffers of the front-

end circuits in a time of around  $2.5\ \mu\text{s}$ . The signatures that are selected by the L1 trigger are high- $p_T$  electrons, photons, muons, jets,  $\tau - \text{leptons}$  decaying into hadrons and missing transverse energy. Tracking information from the detector is not used in the L1 decision, due to the complex nature and computation time of the tracking algorithms. The signature decisions taken by the various parts of the detector are processed by the central trigger processor, which creates a trigger menu made of a combination of different trigger selections. The selected events from the L1 trigger are transmitted to the next stage of the detector specific readout chain, while the unsuccessful events are discarded. From the successful events the L1 defines Regions of Interest (RoI), which are coordinates in  $\eta$  and  $\phi$  of the detector where selections have identified interesting signatures. The RoI data is then used in the next stage of the trigger system. Based on the signature decisions taken by the L1 the rate is reduced from 1 GHz to approximately 75 KHz.

From the seeded RoIs and all available detector data within that region the L2 trigger reduces the rate to approximately 3.5 KHz, with an average event processing time of 40 ms.

The last stage of the trigger system is implemented using offline analysis and is called the Event Filter, which reduces the rate further to 20 Hz, with a processing time per event of around 4 seconds.

### 3.2.7 Luminosity Measurements

The delivered luminosity in the LHC varies over time and is closely monitored by measurements taken from the Inner Detector, Beam Condition Monitor (BCM) and

LUCID detector. The luminosity is used to determine the cross sections of the physics processes in the ATLAS detector by recording a luminosity block of data about once ever minute. The integrated luminosity is calculated by summing over all blocks in a data run period. A more detailed description of the luminosity measurement can be found in [64].

The ATLAS detector measures the luminosity by monitoring the interaction rate per bunch crossing using beam separation scans [67, 68], while the Inner Detector counts the number of reconstructed primary vertices from the interactions of charged particle tracks (see Section 4.3). The distribution of the vertex multiplicity is shown to be proportional to the delivered luminosity in the LHC.

The LUCID detector uses the quantity of Cherenkov photons to calculate the luminosity per-bunch. The number of Cherenkov photons is found to be proportional to the number of charged particles produced. An independent luminosity is also measured by the BCM, which uses fast readout counts to estimate the number of collisions per bunch crossing.

### 3.2.8 Simulation of the ATLAS Detector

The *GEANT4* software [69] within the simulation framework [70] is used to simulate particle interactions in the detector material. The simulated active detector materials convert the energy deposited by the particles into signals that are in the same format as the detector read-out, which allows the same reconstruction software to be used as the data. The *GEANT4* model can specify various types of particle interactions within the detector material at various energy ranges. Hadronic interactions are

simulated using two models, the Quark Gluon String model [71], which is used for the fragmentation of the nucleus and the Bertini cascade model, [72] which is used for interactions of hadrons in a nuclear medium.

The *GEANT4* simulation has been rigorously tested with test-beam measurements to prove the validity of the software. Such validation has seen agreement within a few percent for inclusive measurements of single hadron response, using isolated tracks and identified single particles [73]. While tests identifying pions and protons from the decay products of kaon and lambda particles have also shown agreement between Monte Carlo simulation and data [74]. An overview of the Monte Carlo used in this analysis was discussed in Section 2.3.4.

### 3.2.9 Summary

The ATLAS detector is designed to give physicists the ability to observe new physics phenomena, by taking the output from the trigger and reconstructing the events of interest. A review of the detectors components and performance has been shown in this chapter. The following chapter will review how the data taken from the trigger is reconstructed and processed into analysis quality data and Monte Carlo.

# Chapter 4

## Event Reconstruction

Physics events passing the online trigger selection at ATLAS are processed from raw data (energy deposits, timings and hits) obtained by the numerous sub-detectors and then reconstructed using the ATHENA software framework. The various algorithms used at each stage of the reconstruction allow the event to be interpreted from raw data to a set of charged tracks, photons, electrons, jets and muons. The complexity of the physics environment at ATLAS has proven this task to be non-trivial and there is continual development on the reconstruction algorithms to improve performance.

The analyses shown in Chapter 5 strongly rely on the numerous reconstruction algorithms presented in the following chapter and provide accurate information about the final state objects: electrons, muons, jets,  $b$ -jets, missing transverse energy and trigger.

## 4.1 Data Quality

Data quality is the most integral component to the analysis process. Events containing errors due to subdetector effects are not included in the physics analysis dataset. Each subsystem has its own individual data quality and integrity procedure, allowing each Luminosity Block (LB)<sup>1</sup> to be appropriately assigned a condition state. A list of LB's are created for each run and are used to create a Good Run List (GRL), which is used to reject events affected by issues that arise during the data taking period in the subdetectors.

During the 2011 data taking period there was an issue with the LAr calorimeter's front-end boards that affected  $\sim 948.6 \text{ pb}^{-1}$  of data. The damage had an effect on the accuracy of the simulation to data. Release 16 of the ATLAS software did not model the change to the detector, which led to mis-modelling between Monte Carlo and data. However, in release 17 the ATLAS software was modified to include the damage to the LAr calorimeter's front-end boards and no correction for the acceptance loss is needed in the presented analysis.

## 4.2 Reconstruction of Charged Track Particles

Charged particle tracks are reconstructed in the inner detector by a series of Inner Detector (ID) hits (see Section 3.2.3 for further details). The ID hits are reconstructed into particle tracks using a tracking algorithm called the New ATLAS Track Reconstruction (NEWT) [75]. The NEWT algorithm can be summarised in two main

---

<sup>1</sup>A Luminosity Block is defined by a unit of time during data taking, and is approximately two minutes long.

stages:

- The pre-processing stage, which consists of raw data from the pixel and SCT detectors, which are converted into clusters, while TRT timings are transformed into calibrated drift circles.
- Secondly, the track-finding stage, which uses an array of methods for track pattern recognition and algorithms to recover energy losses due to bremsstrahlung.

## Inside-out Tracking

During the track-finding stage, the first three pixel layers and the first SCT layer are used to find and seed tracks, which are then extended throughout the rest of the SCT to form track candidates using the Kalman fitter-smoother [76]. The Kalman fitter extrapolates the track parameters into the adjacent layer of the detector and progressively updates the track information and their covariances. The tracks are ranked to ensure the most optimised collection of tracks are used in the physics event. Track candidates that are found to have fake or overlapping tracks are negatively scored, while tracks with a large number of hits from the pixel detector are looked at more favourably. On top of the scoring scheme a global  $\chi^2$  refit of the track is also considered when determining the quality of the track. A quality threshold for the tracks is applied and tracks that score below the threshold are discarded from the collection.

The remaining collection of quality tracks are then used to match TRT hits in the detector, while keeping the silicon-only tracks unchanged. The silicon-track is extended into the TRT only if the combined refit scores higher than the original score,

thus ensuring the quality of the tracks is maintained.

## Outside-in Tracking

The backward tracking approach taken by the outside-in tracking algorithm recovers many of the track segments that were overlooked by the inside-out tracking sequence. The inside-out sequence discards tracks that fail the scoring scheme mainly due to a lack of silicon hits. The outside-in sequence recovers tracks originating from secondary decaying vertices, photon conversions and large energy losses, that were neglected by the inside-out tracking due to insufficient silicon hits.

The outside-in algorithm follows a two-step procedure, starting from the TRT segments (that are not associated with the already discovered silicon tracks) and working inward, towards the SCT and pixel detectors. A Hough transform [77] is used to find a hit pattern from the TRT segments by resolving missing hit information along the drift tube. The hit pattern from the Hough transform is then fitted using the same Kalman fitter technique used in the inside-out sequence and allows drift-time measurements to be included. From here the track can be extended into the SCT and pixel detectors.

The two algorithms improve the efficiency of track identification, while maintaining a low fake rate of misidentification of tracks. During high detector occupancy the possibility of having incorrect hit assignments and fake tracks from random hit combinations increases. Therefore, there is still motivation to increase the current set of algorithms used and improve track reconstruction.

## 4.3 Reconstruction of the Primary Vertex

During identification and reconstruction of physics objects ( $b$ -jets,  $\tau$ -jets and leptons) it is vitally important to determine the position of the primary vertex. The convoluted physics environment in the ATLAS detector makes it a non-trivial procedure when distinguishing the true primary vertex from other background vertices. The position of the hard scattered event of interest in the ATLAS detector is tightly constrained in the transverse plane, while being virtually unconstrained in the longitudinal direction. The accuracy of reconstructing the primary vertex is largely dependent on the accurate measurement of the position and size of the interaction point (beam spot), which is averaged over a large number of events. The algorithms that are responsible for the reconstruction of the primary vertex can be categorised into two groups - vertex finding and vertex fitting [78].

The vertex finding algorithms associate reconstructed tracks to a vertex candidate, while the vertex fitting algorithms reconstruct the vertex position by quantifying the quality of tracks associated with the vertex. Challenges faced by the algorithms include distinguishing between primary and secondary vertices and consideration of the optimal separation of tracks positioned between different vertices. The vertex finding algorithm first allocates a primary vertex (PV) seed to the vertex with the maximum probability of being closest to the beam spot. An iterative  $\chi^2$  fit is then applied to the surrounding tracks. Tracks that are incompatible with the chosen PV are used to seed a new PV. The procedure is continued until no unassociated tracks are left or no more additional vertices can be found. The reconstructed PVs must have two associated tracks. The hard-scatter PV is chosen to be the vertex with the

greatest sum of squared transverse momenta  $\sum p_T^2$  of the tracks.

Figures 4.1 and 4.2 show the performance of the ATLAS inner detector when reconstructing tracks and vertices from inner detector hits. From Figure 4.1 you can see there is a mis-modelling in the  $\eta$  distribution between MC and data of  $\sim 2\%$ , when comparing pixel, SCT, and TRT hits. The same can be said for the impact parameters shown in Figure 4.2, where the tails of the distributions show mis-modelling between MC and data. In a high pile-up environment, the number of fake tracks and vertices increases, due to the higher probability of more interactions between objects in the detector. The PV reconstruction efficiency has been shown to be directly affected by the increase in pile-up [79].

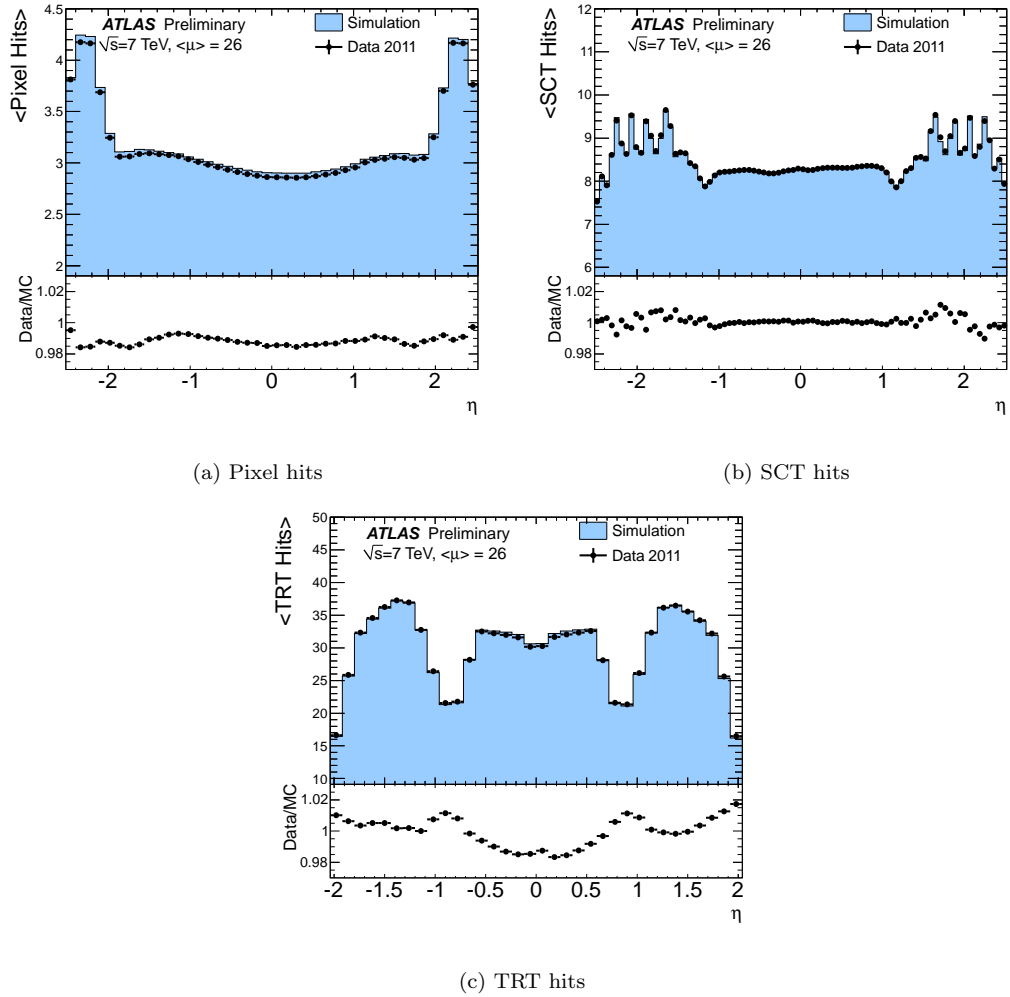


Figure 4.1: The number of pixel, SCT and TRT hits as a function of  $\eta$  from the 2011 A1 dataset and corresponding simulation sample. Taken from [79].

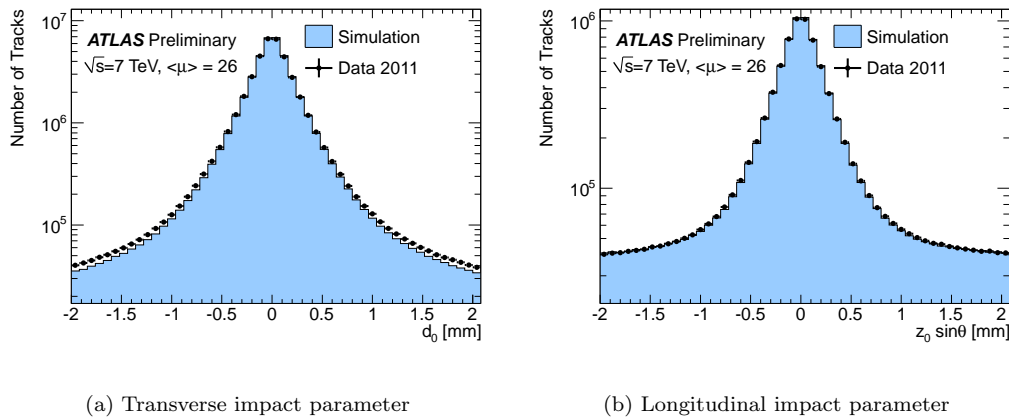


Figure 4.2: The impact parameter distribution with respect to the primary vertex of the tracks from the 2011 A1 dataset and corresponding simulation sample. Taken from [79].

## 4.4 Electrons

#### 4.4.1 Electron Reconstruction

Electrons in the ATLAS detector are reconstructed by combining calorimeter and ID hits. The curved tracks from the ID shower into narrow columns when entering the EM calorimeter. During electron reconstruction and identification strict constraints are applied to the energy deposits and associated tracks, which improves the probability of finding a true electron candidate. Electrons in the central region of the detector ( $\eta < 2.47$ ) are reconstructed using an algorithm that combines information from the EM calorimeter and the inner detector [80]. Reconstruction of electrons in the forward region use an algorithm that takes advantage of data readings from the EM calorimeter only [81].

Electron reconstruction in the central region applies a sliding window algorithm

to identify all candidates [80]. Energy clusters are seeded in the middle layer of the EM calorimeter with an  $E_T > 2.5$  GeV and a cluster size of  $3 \times 5$  cell units ( $\Delta\eta \times \Delta\phi = 0.025 \times 0.025$ ). The seeded clusters are used to match track pairs originating from the inner detector, which are tagged as electron candidates. If a seeded cluster is matched to a pair of tracks originating from a reconstructed photon conversion vertex, the cluster is tagged as a converted photon. Matching of paired tracks and clusters in a window of  $\Delta\eta \times \Delta\phi = 0.05 \times 0.10$  is chosen to account for the loss in electron energy due to bremsstrahlung. The matched tracks require a momentum compatible with the cluster energy and hits in the silicon and TRT detectors, which reduce fake electron candidates from pions. Final clusters are re-calibrated to the EM energy scale, which accounts for energy losses through interactions with the detector. The energy scale is derived from MC based on measurements from the test-beam and  $Z \rightarrow ee$  decays [82].

#### 4.4.2 Electron Identification

The electrons distinguishing features are used to identify electrons from other particles in the ATLAS detector. Electrons can be separated from hadrons due to the EM shower depositing a large proportion of its energy in the second layer of the EM calorimeter. Figures from 4.3 show the hadronic leakage  $(R_{had})^2$  and  $(\frac{E}{p})^3$  distributions. The difference in the distributions for electrons and hadrons can be used to

---

<sup>2</sup>The ratio of transverse energy reconstructed in the first layer of the hadronic calorimeter compared with the transverse energy reconstructed in the EM calorimeter.

<sup>3</sup>The ratio of energy reconstructed in the EM calorimeter to track momentum.

increase electron acceptance within the event.

Separating electrons from neutral pions is also a challenging task in the ATLAS detector, as neutral pions decaying into two photons produce indistinguishable EM showers in the second layer of the EM calorimeter. However, due to the high granularity in the first layer of the EM calorimeter, differences can be seen in the shower shapes between the corresponding electrons and neutral pions.

To achieve a higher rate of fake electron rejection, the ATLAS experiment currently classifies six different sets of cuts. These cuts provide good separation between real and fake electrons with varying degrees of accuracy. The proceeding sets of cuts are ordered in degrees of accuracy and are described below for loose, loose++, medium, medium++, tight and tight++ [83]:

- **Loose** electrons are defined in the  $\eta < 2.47$  region of the calorimeter. Using information from the first and second layers of the calorimeter, electrons are selected by requiring low hadronic leakage and a range of cuts on the shower shape. Loose electrons benefit from a high identification efficiency of  $\sim 95\%$ . However, the looser cuts achieve a larger expected background rejection, leading to 1 in 500 jets passing the loose electron selection (rejection factor of 500).
- **Loose++** electrons add additional cuts to the loose selection. Information from matched tracks are used to identify higher quality electrons, by requiring at least 1 hit from the pixel detector and at least 7 hits from the pixel and SCT detector. The  $|\eta|$  between the cluster and tracks must also be less than 0.015 when taking these cuts into account. The additional cuts lead to a slightly lower identification efficiency of  $\sim 93\%$ , with a higher expected rejection of 5000.

- **Medium** electrons again build on the loose++ criteria by adding additional cuts that help discriminate against neutral pions. These cuts occur in the first EM layer and require the transverse impact parameter of the track,  $|d_0|$ , to be less than 5mm. Comparisons between energy deposits are also considered when discriminating between electrons and neutral pions. The identification efficiency of the medium electron is estimated at  $\sim 88\%$  with a rejection factor that exceeds that of the loose++ electron.
- **Medium++** electrons require an additional B-layer hit to reject electrons from photon conversion and apply additional TRT track hits to reduce the effect of contamination from charged hadrons. The  $|\Delta\eta|$  between the cluster and tracks in the first EM layer is also reduced to less than 0.005 mm to achieve a rejection factor of 50000. However, the tighter cuts lead to an identification efficiency of  $\sim 85\%$ .
- **Tight** electrons have additional requirements in the fiducial region of the detector, requiring cluster and matched tracks to be in an area less than  $\Delta\phi \times \Delta\eta = 0.02 \times 0.005$ . A tightened  $|d_0| < 1$  mm requirement and higher threshold on the TRT hits also contribute to decreasing the identification efficiency to  $\sim 75\%$  with an increase in the background rejection.
- **Tight++** electrons are currently the cleanest, most probable electron candidate in the ATLAS detector, with additional cuts coming from asymmetric  $\Delta\phi$  matching between tracks and clusters, leading to a greater efficiency selection and background rejection.

Additional cuts are also recommended by the Egamma Performance Group to suppress backgrounds from decaying hadrons producing jets. The additional cuts take advantage of the high granularity of the calorimeter and require isolation cuts on the track and energy of the cluster. A calorimeter isolation is estimated by calculating the fraction of energy in a cone of  $\Delta R = 0.2$  centred on the electron and compared with the energy of the electron candidate. Similarly, track isolation is calculated by comparing the scalar sum of the tracks  $p_T$  in a cone of  $\Delta R = 0.3$  centred on the electron and compared with the electrons  $p_T$ .

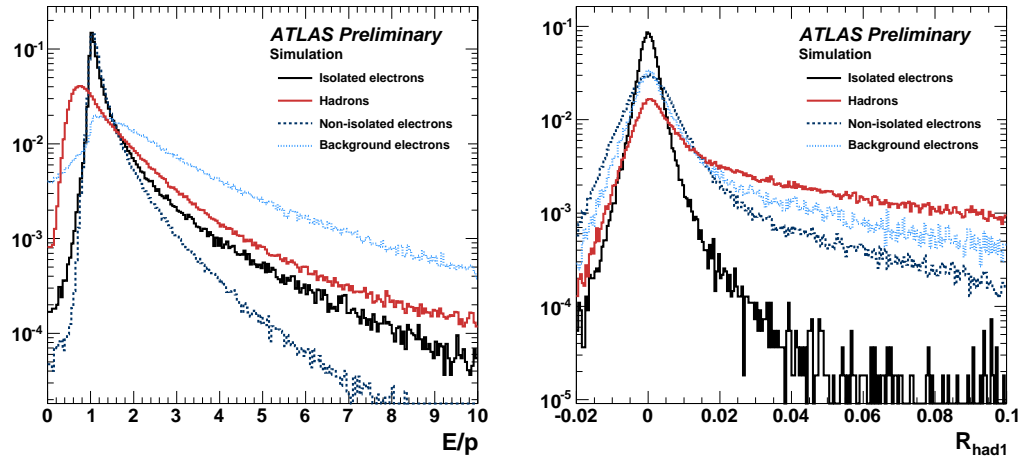


Figure 4.3: The number of events as a function of hadronic leakage  $R_{had1}$  and  $\frac{E}{p}$  for electrons and hadrons. Taken from [83].

### 4.4.3 Scale Factors and Energy Corrections

Electron scale factors and energy corrections have been derived by the Egamma Performance Group to correct for the mis-modelling of the MC and detector effects. Electron identification scale factors were derived as a function of  $\eta$ -cluster and  $E_T$ . These weights are applied to the simulation and take into account the differences between the data and simulation. The impact of the electron identification scale factors is close to  $\sim 1$  with an uncertainty of  $\sim 2\%$  [84].

An energy correction is also applied to the electron to match the Z boson peak from  $Z \rightarrow ee$  and  $J/\Psi \rightarrow ee$  events, with a systematic uncertainty of  $\pm 1 - 1.5\%$  [84]. The correction is applied by smearing the energy distribution of the electron using a Gaussian random number generator, which represents the uncertainty of the electrons energy. The derived energy scale correction from the EM electron cluster energy in data is then applied to the Gaussian expectation and electron energy.

## 4.5 Muons

### 4.5.1 Muon Reconstruction and Identification

Muon reconstruction in the ATLAS detector relies on accurate information from the MS, IN and Calorimeter. To efficiently reconstruct muons in a wide  $p_T$  spectrum, muons have been categorised into four optimum groups, each with their own analysis requirements:

- **Standalone Muons (SA)** are reconstructed by collecting information from the MS and using fitting algorithms to reconstruct muon tracks. The

algorithms reconstruct muon tracks by using back extrapolation from the MS to the interaction point in the ID. The energy losses in the calorimeter are taken into account and SA muons are reconstructed in a large  $\eta$  region ( $\eta < 2.7$ ). However, due to design inefficiencies in the MS at  $\eta = 0$  and  $n \sim 1.2$ , reconstruction efficiencies suffer, leading to an efficiency of  $\sim 97\%$ .

- **Combined Muons (CB)** are defined by combining SA muons with inner detector tracks. The tracks are matched using information from  $p_T$ ,  $\eta$  and  $\phi$  of the SA muon and inner detector tracks. The CB muon benefits from greater precision during reconstruction, due to the accurate resolution calculated from two independent measurements and additional information from the vertex. This results in a high reconstruction efficiency of  $\sim 92\%$ .
- **Tagged Muons (ST)** maximise the reconstruction efficiency of the muon in the low- $p_T$  region. Due to the muon having a lower probability of reaching the spectrometer middle station and the outermost calorimeter layers, the SA and CB algorithms are seldomly used. The ST muons instead use an inside-out method to extrapolate ID tracks to the entrance of the MS, by looking for nearby hits in the first layer of the muon chambers. The ST muons have a reconstruction efficiency of  $\sim 98\%$  for a muon with a  $p_T > 40$  GeV.
- **Calorimeter Muons** are also reconstructed using the inside-out algorithm, by using the ID track to match calorimeter deposits compatible with a muon signature. The calorimeter muons are predominately used to compensate for losses endured in the  $\eta = 0$  region of the MS detector.

In the ATLAS experiment muons can be reconstructed using two algorithms, STACO [85] and MuID [86]. Both algorithms provide similar performance when reconstructing the muons from detector hits and also provide algorithms to reconstruct all four muon categories. In this analysis the MuID algorithm was chosen along with the Muon Performance Groups (MCP) hit requirements in the inner detector. A summary of the MCP hit requirements is shown below:

- The number of pixel hits plus the number of crossed dead pixel sensors must be greater than 0.
- The number of SCT hits plus the number of crossed dead SCT sensors must be greater than 4.
- The number of pixel holes plus the number of SCT holes must be greater than 3.
- TRT hits on the muon track and TRT outliers on the muon track must be greater than 5 in a region of  $0.1 < |\eta| < 1.9$ .
- The number of TRT outliers on the muon track must not equal more than 90% of all TRT hits.

The performance of the muons in the 2012 data set are shown in Figure 4.4, where there is good agreement between data and Monte Carlo in both the  $p_T$  and  $\eta$  spectra. The  $\eta$  inefficiencies are predominately due to the barrel and End-Cap transition, with  $\eta = 0$  suffering from the junction of the two MS detectors.

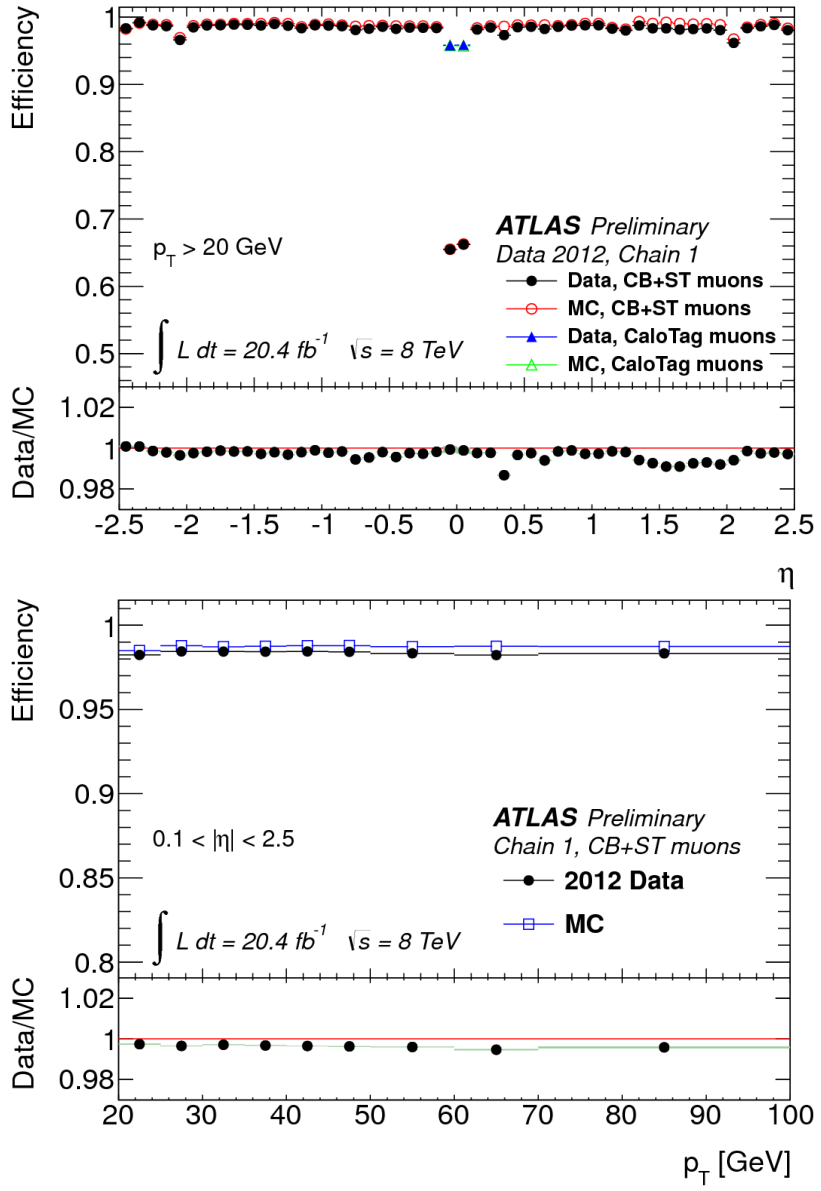


Figure 4.4: Muon reconstruction efficiency for Chain 1 CB+ST muons as a function of the  $p_T$  and  $\eta$ . The panel at the bottom shows the ratio between the measured and predicted efficiencies. Taken from [87].

### 4.5.2 Muon Scale Factors and Energy Corrections

Reconstruction and identification efficiency scale factors have been derived using  $Z \rightarrow \mu\mu$  events. The scale factors have a dependency as a function of  $\eta$ ,  $\phi$  and  $p_T$ . The muon reconstruction efficiency is measured to be greater than 98% with a systematic uncertainty of  $\sim 2\%$ . Energy scale shifting and resolution smearing is applied to correct for reconstruction muon momentum inefficiencies in MC. The corrections are applied to match the energy scale and resolution of the  $Z \rightarrow \mu\mu$  decay mass spectrum. A muon momentum scale measured to correct the mis-modelling is calculated at  $\sim 0.1\%$  [87].

## 4.6 Jets

The ATLAS detector experiences large volumes of  $p\bar{p}$  collisions during each event. The partons in the event hadronise and produce tracks in the ID and energy deposits throughout the calorimeter. Jets are defined either by track information (track jets) or calorimeter information (calorimeter jets). The analysis presented makes use of calorimeter jets. This section will discuss the reconstruction process of calorimeter jets and define the steps involved during reconstruction, calibration and selection of an analysis jet.

### 4.6.1 Jet Reconstruction

During reconstruction of calorimeter jets, cells from the calorimeter are combined into clusters for inputs into the jet reconstruction algorithms. The ATLAS experiment currently defines two cell clustering algorithms:

- **Topological Clusters (Topoclusters)** are formed dynamically from a combination of cells around a seeded cell that exceeds a given signal-to-noise ratio threshold. The threshold is defined to be  $|E_{cell}/\sigma_{cell}^{noise}| > 4$ , where  $E_{cell}$  is the cell energy and  $\sigma_{cell}^{noise}$  is the root mean squared (RMS) of the cell noise distribution. The surrounding cells must also satisfy a signal-to-noise ratio of their own to be considered. Each surrounding cell must exceed a threshold of  $|E_{cell}/\sigma_{cell}^{noise}| > 2$ . The formed cells that have passed the two thresholds are then defined as a topocluster and are added to other neighbouring topoclusters. A topocluster has no mass and the energy of the cluster is defined by the sum of all cell energies in the cluster. The direction of the topocluster is derived from the cell energy weighted averages of the pseudorapidity and azimuthal angles relative to the nominal ATLAS coordinate system. Due to noise fluctuations in the calorimeter, clusters can obtain negative energies. The negative clusters are rejected from the jet reconstruction since they having no physical meaning [88].
- **Noise Suppressed Towers** are constructed in a grid of calorimeter cells with a tower bin size  $\Delta\eta \times \Delta\phi = 0.1 \times 0.1$ . In the ATLAS detector there are cells larger than the  $0.1 \times 0.1$  resolution required by the noise suppressed towers. The larger cells are split proportionally between the opposing towers along with their energies. The towers are built using topological clusters and have the same noise suppression and topology [88].

Jet reconstruction algorithms are used after the clustering stage to yield a stable and accurate description of the QCD interaction in the pp collision. To produce an

accurate account of the interaction the jet must meet a number of requirements before it is deemed eligible for a physics analysis:

- During the splitting of a particle into two collinear particles, there should be no resulting effect on the reconstruction of the jet (collinear safety).
- The presence of soft particles between jet components should not effect reconstruction of the jet (infrared safety).
- The resolution of the detector and other effects such as noise should impose little or no effect on the reconstruction of the jet.
- There should be invariance under Lorentz boosts along the z-coordinate.
- The algorithm should be efficient enough to be used within an analysis framework.

Once an algorithm is chosen that meets the requirements above, reconstruction of the clusters into a jet can begin. The anti- $k_T$  algorithm [89] is one such algorithm and is used in the presented analysis. The algorithm sequentially recombines topoclusters or towers into jets according to a distance parameter  $d_{ij}$ , which is defined in Equation 4.1.

$$d_{ij} = \min(p_{T,i}^{2p}, p_{T,j}^{2p}) \frac{\Delta R_{ij}^2}{R^2}, \quad (4.1)$$

$$d_i = p_{T,i}^{2p}, \quad (4.2)$$

where  $p_{T,i}$  is the transverse momentum of the input  $i$  and  $p_{T,j}$  is the transverse momentum of the input  $j$ . The  $\Delta R_{ij} = \sqrt{(y_i - y_j)^2 + (\phi_i - \phi_j)^2}$  parameter is the distance between the pair of inputs in  $y-\phi$  space, while  $R$  characterises the size of the jet and  $p$  defines the type of algorithm used. The distance parameter  $d_{ij}$  represents the distance between the inputs  $i$  and  $j$ , while  $d_i$  represents the distance between input  $i$  and the beam axis in momentum space. The anti- $k_T$  algorithm calculates the distance between the two objects  $i$  and  $j$  ( $d_{ij}$ ). If the  $i$ 'th object is closer to the  $j$ 'th object than the beamline ( $\min(d_i, d_{ij})$ ), then the two objects are combined using the (E-scheme)<sup>4</sup>. Once the two objects have been combined they are removed from the event and stored in a list. The process is repeated until all matched objects are in the list and no objects are left. The list of combined objects is then used to reconstruct a jet. The anti- $k_T$  algorithm has  $p = -1$  and works in the inverse transverse momentum space. It begins by clustering nearby particles, which ensures infrared safety. The softer particles also prefer to cluster with the harder inputs instead of with other soft particles, while all hard particles within a  $\Delta R_{ij} < R$  will be combined into one jet, ensuring collinear safety.

To overcome jets reconstructed from pile-up interactions, ID track information is used to define a jet vertex fraction:

$$JVF = \frac{\sum_{track,PV} p_T}{\sum_{track} p_T}, \quad (4.3)$$

---

<sup>4</sup>The sum of the objects four-momentum are added together

where  $\sum_{track,PV} p_T$  is the sum of the track  $p_T$  from the primary vertex (PV) associated to the jet and  $\sum_{track} p_T$  is the sum of tracks associated to the jet. The JVF is found to be close to one when tracks in a jet originate from the hard scatter, while jets from pile-up events have a much smaller JVF value. The JVF is only defined in the ID coverage ( $|\eta| < 2.5$ ), while the jet reconstruction takes place in a region of up to  $|\eta| < 4.5$

#### 4.6.2 Jet Calibration

Reconstructed jets in the ATLAS detector are initially calibrated to the electromagnetic (EM) scale, where calorimeter signals are calibrated to take into account energy losses in the calorimeter by an electron. The EM scale is obtained by using test-beam measurements for electrons in  $Z \rightarrow ee$  events from the barrel and endcap regions of the calorimeter [82]. The results have also been validated for muons using test-beams and cosmic-rays, which have been found to be compatible with the EM scale. The EM scale calibration describes accurately the energy deposits produced by electrons and photons, but does not successfully describe processes from hadronic particles, such as protons, neutrons, pions and kaons. There are a number of points to take into account when calibrating hadronic particles:

- There are partial measurements taken of the hadrons deposited energy in the calorimeter.
- There are energy losses in the dead regions of the detector.
- There are inaccurate energy deposit readings that are not fully contained in the calorimeter.

- There are energy losses due to out of cone effects during jet reconstruction.
- There are signal losses due to threshold effects in calorimeter clustering and jet reconstruction.

The ATLAS experiment uses several calibration schemes with varying degrees of complexity. These schemes help tackle the issues discussed above and calibrate the hadronic particles in the event. The schemes currently available in the ATLAS experiment are EM+JES, global sequential, global cell energy density weighting and local cluster weighting calibration schemes, which are discussed below [88, 90]:

- **EM+JES** calibration applies a jet-by-jet correction to each reconstructed jet energy to match that of a particle jet energy<sup>5</sup>. The calibration is derived in MC, where each jet that is at the EM scale is further scaled by a correction factor, which is dependent on the jets energy and  $\eta$  position in the detector. In addition to the correction factor pile-up and jet origin, corrections are applied to further improve jet reconstruction [88].
- **Global Sequential (GS)** calibration is another MC derived jet calibration, where longitudinal and transverse properties of the jet are used to improve the jet resolution. During the GS calibration the jet energy remains unchanged until the EM+JES calibration is applied on top of the GS calibrated jet.
- **Global Cell Energy-Density Weighting (GCW)** calibrates jets by weighting each cell in the calorimeter by the energy response of hadronic and electromagnetic particles. The weights are dependent on the cell energy

---

<sup>5</sup>A jet reconstructed from a stable particle produced by hadronisation.

density in the calorimeter layer and are calculated by minimising the energy fluctuations between the reconstructed EM scale jets and particle jets in MC simulation [90].

- **Local Cluster Weighting (LCW)** calibration takes advantage of properties from topoclusters to calculate weights. The weights are derived by cluster classification (electromagnetic or hadronic), cluster energy and cell density. The correction weights are then applied to the cluster energy for deposits just outside the cluster and also deposits found in dead material [90].

The EM+JES scheme was applied to the jets in the analysis presented using corrections derived from pp collisions at a centre-of-mass energy of  $\sqrt{s} = 7$  TeV [88].

#### 4.6.3 Jet Selection

Due to noise in the ATLAS calorimeter, fake energy deposits can be produced, which result in fake reconstructed jets. Additional requirements on the recorded pulses in the calorimeter must be applied to discriminate between real and fake jets. In the ATLAS experiment, jets are categorised into four groups, each group having varying degrees of quality jets. The four categories are Looser, Loose, Medium and Tight [91].

The Looser selection is efficient at rejecting most of the noise in the calorimeter, with a jet selection efficiency of  $\sim 99\%$  for jets with  $p_T > 20$  GeV.

Loose selection applies additional cuts from the Looser selected jets and removes fake jets from beam induced backgrounds, leading to a similar jet selection efficiency and higher rejection rate.

Medium and Tight selection further reduces the fake background by further rejecting beam induced backgrounds. However, the large number of cuts leads to a lower jet selection efficiency of  $\sim 98\%$  for medium and  $88 - 96\%$  for the tight selection.

Figures 4.5 show the distribution of jet selection efficiency as a function of jet  $p_T$  for the various  $\eta$  ranges. At smaller  $p_T$  values the efficiencies for the Medium and Tight criteria are more affected than that of the Looser and Loose criteria. Also, as  $|\eta|$  is increased we can see there is little effect on the Looser and Loose jet selection efficiency. However, the Medium and Tight criteria selection efficiency are badly effected, particularly in the  $1.2 \leq |\eta| \leq 2.5$  region, where the efficiency drops to  $\sim 88\%$  at low  $p_T$ .

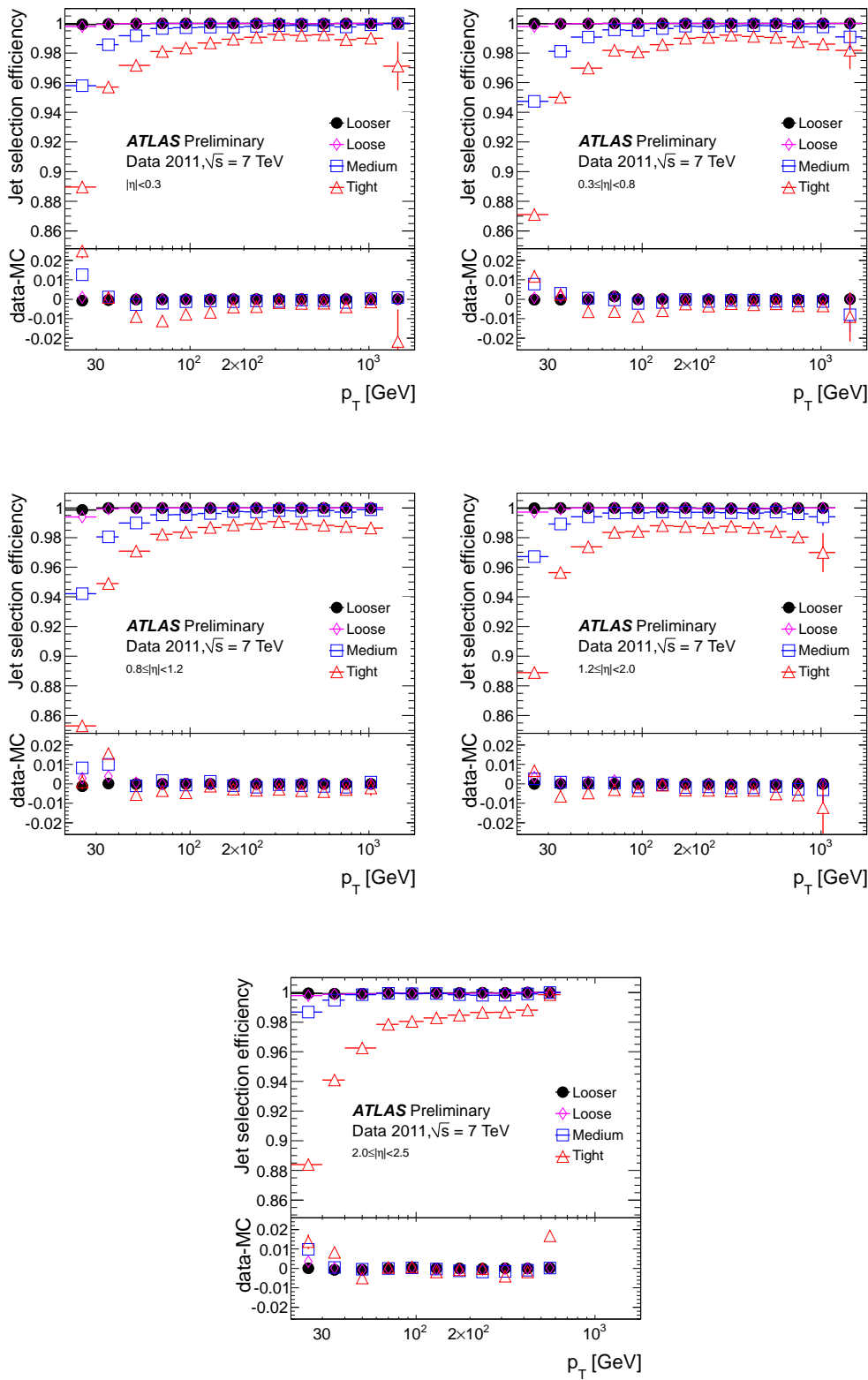


Figure 4.5: Jet quality selection efficiency for anti- $k_T$  jets with  $R = 0.4$  measured with a tag-and-probe technique as a function of  $p_T$  in  $\eta$  ranges, for the four sets of selection criteria. Differences between data and Monte Carlo simulation are also shown. Taken from [91].

#### 4.6.4 Jet Energy Resolution

Jet energy resolution (JER) is also corrected to improve agreement between data and simulation. The correction is calculated using events containing only two jets [92]. The correction exploits the assumption of the two jets transverse momentum's being balanced, due to the conservation of momentum in the transverse plane. From this presumption the jet energy resolution can be measured by studying the asymmetry observed in the jet's  $p_T$  spectra. Jets are chosen to be within the same rapidity  $y$  space in order to reduce secondary effects that may enhance the resolution correction. The fractional jet energy resolution is calculated over  $p_T \times \eta$  bins and shown below:

$$\frac{\sigma_{p_T}}{p_T} = \frac{N}{p_T} \oplus \frac{S}{\sqrt{p_T}} \oplus C, \quad (4.4)$$

where N, S and C are the noise, stochastic and constant terms respectively. Figure 4.6 shows the jet energy resolution as a function of  $p_T$  measured in data and MC for the EM+JES scheme. The di-jet balance technique produces a jet resolution with an uncertainty of  $\sim 20\%$  for jets with a  $p_T < 20$  GeV. Jets with a  $p_T$  between 20 and 80 GeV in a rapidity range  $|y| < 2.8$  are found to have an uncertainty of 14%. The jet energy resolution uncertainty is found to be one of the major uncertainties that affect the presented analysis (see Section 5.7 for more details).

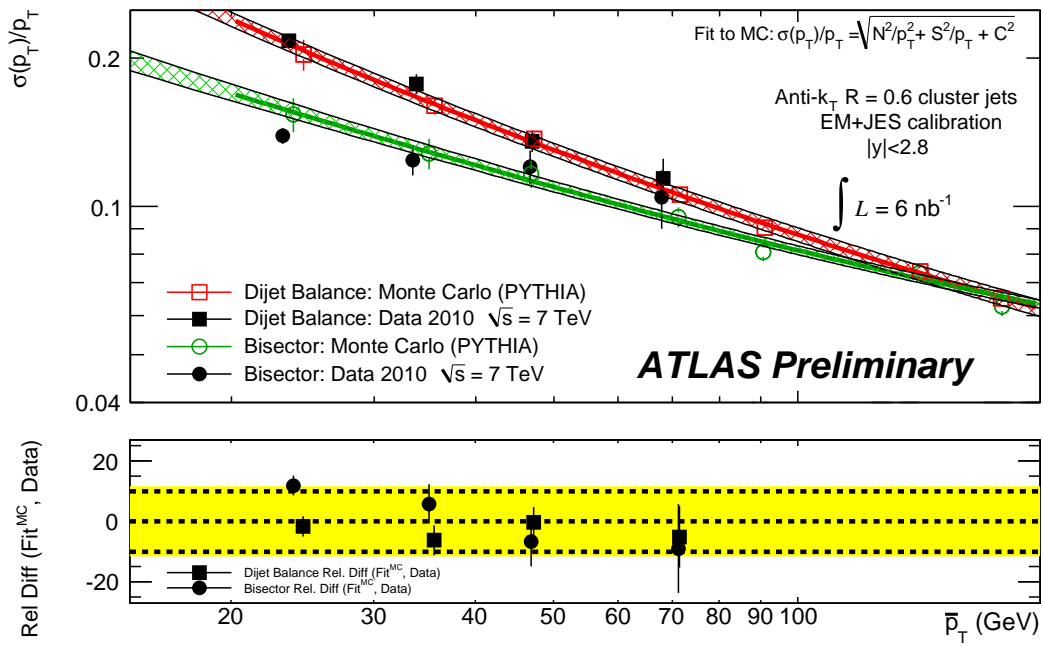


Figure 4.6: Jet energy resolution for the di-jet balance and bi-sector techniques as a function of the average jet transverse momenta. The lower plot shows the relative difference between the Monte Carlo fit and the data results. The yellow band indicates a relative uncertainty of  $\pm 10\%$ . Taken from [92].

## 4.7 b-tagging

*b*-tagging in the ATLAS detector is a complex procedure plagued by a convoluted and over populated detector environment. The B-hadron however has a unique signature that helps separate itself from other jets. Bottom quarks decaying into B-hadrons have a relatively long lifetime when compared to other particles ( $\sim 1 \times 10^{-12}$ s). The B-hadrons can travel  $\sim 3$  mm in the detector before decaying, which helps discriminate the B-hadrons from the lighter particles. Identification of *b*-jets is an instrumental part of many analyses at the ATLAS experiment and in particular the analysis presented, where identification of *b*-jets decaying from a Higgs boson candidate must be successfully identified to maximise signal acceptance. *b*-tagging algorithms are used to exploit the decay length of the B-Hadron by requiring a certain number of tracks to arrive at a secondary vertex.

### 4.7.1 b-tagging Algorithms

A number of *b*-tagging algorithms currently exist in the ATLAS experiment that are based on the discriminating features of the B-hadron decay. The algorithms take advantage of various secondary vertex properties that allow each jet to be given a weight that reflects the probability of the jet originating from a *b*-quark. The MV1 tagging algorithm used in the presented analysis combines three different algorithmic methods using an artificial neural network. The three algorithms that are used in the neural network are based on information from the track impact parameters (IP3D algorithm), secondary vertex (SV1 algorithm) and reconstruction of the B meson decay chain (JetFitterCombNN algorithm) [93]. Figure 4.7 shows stacked plots for

the IP3D, IP3D+SV1, JetFitter and MV1 weights compared to data. The figures show that the higher the  $b$ -tagging weight, the more likely we are of selecting a  $b$ -jet. However, for larger weights the figures also show larger disagreement between data and MC. The IP3D, SV1 and JetFitter weights are used to produce an MV1 weight. Figure 4.7d shows the number of expected MC and truth events as a function of MV1 weight compared to data. Light jets in the distribution will have their  $b$ -weights closer to 0, while more  $b$ -like-jets will have their  $b$ -weight closer to 1. On Figure 4.7d there is also an additional peak at  $w \sim 0.15$ . The peak can be explained by the affect of the  $c$ -quark hadronising. The choice of the value of weight  $\hat{w}$  depends greatly on the desired  $b$ -tagging efficiency and mistag rate. Ideally we would have the greatest amount of fake  $b$ -jet rejection, with the highest amount of  $b$ -tagging efficiency and low mistagging rate.

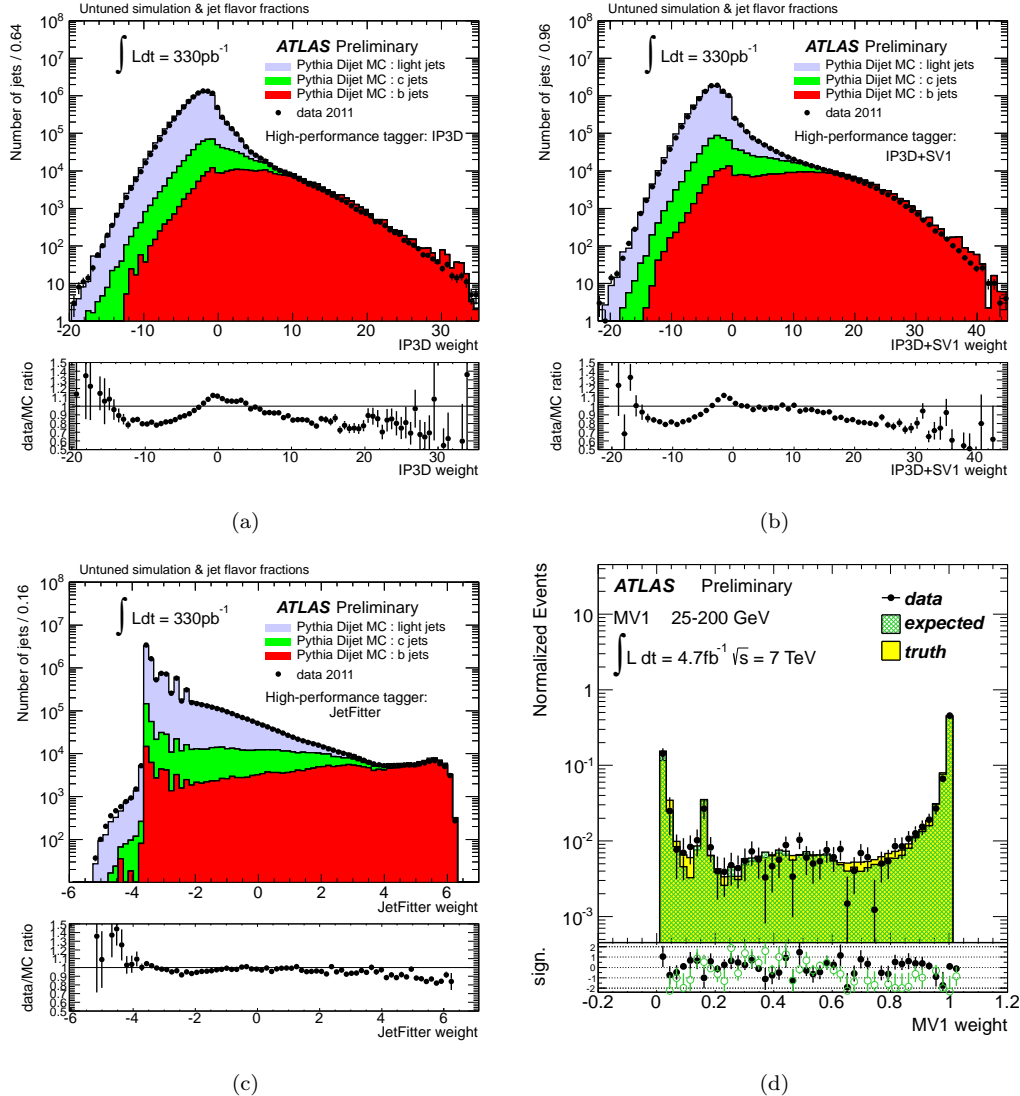


Figure 4.7: Data and MC comparison for the  $b$ -tagging weights: IP3D, IP3D+SV1, JetFittCombNN and MV1. Taken from [93].

### 4.7.2 b-tagging Uncertainty

The performance of the  $b$ -tagging algorithms are determined by the efficiency of the tagger  $\epsilon_{b\text{-}tag}$ , which is defined as the fraction of correctly tagged  $b$ -jets, as a function of the mistag rate (the fraction of falsely tagged non- $b$ -jets). The analysis presented uses a working point of  $\epsilon_{b\text{-}tag} = 70\%$ .

The  $b$ -tagging efficiency and the mistag rate have been measured in data and compared to simulation [94]. Good agreement has been shown in these studies, but scale factors to correct simulation are needed [95, 96, 97]. The scale factors used in the analysis are shown to be close to 1 and depend on the  $p_T$  of the  $b$ -tagged jet. Uncertainties on these scale factors are also applied in the analysis and have been shown to have a significant affect (see Section 5.7 for more details).

## 4.8 Missing Transverse Energy Reconstruction

The missing transverse energy  $E_T^{miss}$  is defined as the vector sum of the transverse momenta in a partially reconstructed event. For a completely reconstructed event such as  $ZH \rightarrow l^+l^-b\bar{b}$  the expected missing transverse momenta should be zero. However, due to inefficiencies in measurements the missing transverse momenta is not negligible. Undetected particles, such as neutrinos and other weakly interacting particles are not accurately recorded by the detector and lead to non-zero values of missing transverse energy. To accurately reconstruct the events four-vector, reconstruction of the missing transverse energy must be derived. The missing transverse energy is calculated by considering all physics objects in the event (see [98, 99]).

The missing transverse energy relies on energy deposits from the calorimeter, muon

track information and inner detector tracks for reconstruction. The calorimeter cells are used to associate particles to each cell in a specific order (electrons, photons, hadronically decaying  $\tau$ -leptons, jets and muons), cells that are not associated to an object are included in a CellOut term, which is used in the missing transverse energy reconstruction. The calorimeter cells associated to particles are calibrated and the negative sum energy of the calibrated cell is used in the missing transverse energy reconstruction. The  $x$  and  $y$  components of the missing transverse energy vector is defined as follows:

$$E_T^{miss} = - \sum p_T = \sqrt{(E_x^{miss})^2 + (E_y^{miss})^2}, \quad (4.5)$$

such that:

$$E_{x(y)}^{miss} = E_{x(y)}^{miss,e} + E_{x(y)}^{miss,\gamma} + E_{x(y)}^{miss,\tau} + E_{x(y)}^{miss,jets} + E_{x(y)}^{miss,softjets} + E_{x(y)}^{miss,calo,\mu} + E_{x(y)}^{miss,CellOut} + E_{x(y)}^{miss,\mu}, \quad (4.6)$$

where  $E_{x(y)}^{miss,*}$  terms, except  $E_{x(y)}^{miss,calo,\mu}$ , are the negative sums of the calibrated cell energies associated to the object projected onto the  $x$  and  $y$  axis. The  $E_{x(y)}^{miss,calo,\mu}$  term is determined using the momenta calculated from the muon tracks. The energy loss of muons in the calorimeter is also included in the  $E_{x(y)}^{miss}$  calculation with the term  $E_{x(y)}^{miss,calo,\mu}$ . The jet component of the  $E_{x(y)}^{miss}$  is separated in low ( $10 \text{ GeV} < p_T < 20 \text{ GeV}$ ) and high ( $p_T > 20 \text{ GeV}$ ) transverse momenta contributions, with the terms  $E_{x(y)}^{miss,softjets}$  and  $E_{x(y)}^{miss,jets}$  respectively (see [98] for more details).

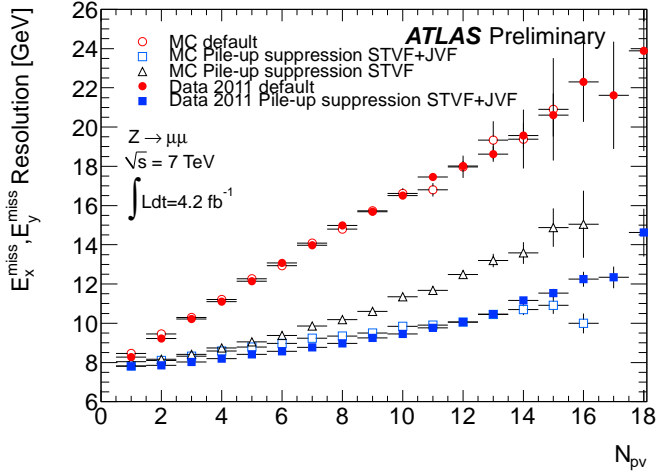


Figure 4.8:  $E_T^{miss}$  resolution in data and simulation for  $Z \rightarrow \mu\mu$  events, as function of the primary vertex multiplicity  $N_{PV}$ . Taken from [99].

Studies using the  $Z$  and  $W$  boson have shown the performance of the missing transverse energy reconstruction [99]. Events from  $W \rightarrow lv$ , where  $E_T^{miss} > 40$  GeV have shown to be within 5% and 3% of the data for  $W \rightarrow ev$  and  $W \rightarrow \mu v$  decays respectively. Events from  $Z \rightarrow ee/\mu\mu$  decays are expected to show no genuine  $E_T^{miss}$  and are therefore used to estimate the resolution of  $E_T^{miss}$ , which is limited by the calorimeters response and energy reconstruction. Figure 4.8 shows the resolution measured in data and simulation from  $Z \rightarrow \mu\mu$  events as a function of primary vertices  $N_{PV}$  for the standard and pile-up suppressed definitions of the missing transverse energy [99]. From Figure 4.8 the  $E_T^{miss}$  resolution deteriorates with an increase in pile-up.

The missing transverse energy CellOut and soft-jet term are particularly sensitive to pile-up in the event and are combined into a soft term

$$E_{x(y)}^{miss} = E_{x(y)}^{miss,softjets} + E_{x(y)}^{miss,CellOut}. \quad (4.7)$$

The soft term is then scaled using the soft term vertex fraction (STVF) to suppress the impact of pile-up

$$STVF = \sum p_{Ttrack,PV} / \sum p_{Ttrack} \quad (4.8)$$

where  $\sum p_{Ttrack,PV}$  is the sum over all tracks not matched to a physics object and the associated primary vertex and  $\sum p_{Ttrack}$  is the sum over all tracks matched to a physics object. Figure 4.8 shows the reduced effect pile-up has on the  $E_T^{miss}$  resolution when applying the STVF scaling. Further improvements are achieved in reducing the pile-up dependence from the jet term by scaling each jet with the jet vertex fraction (JVF) explained in Section 4.6.1.

Systematic uncertainties in  $E_T^{miss}$  reconstruction come predominately from the electron, jet and soft term reconstruction uncertainties. The contribution to the  $E_T^{miss}$  uncertainties are shown in Figure 4.9 as a function of the total transverse energy measured in the calorimeter. Figure 4.9 shows that there is an increase in uncertainty with an increase in the total transverse energy from  $\sim 1\%$  to  $\sim 10\%$  in a total transverse energy range of  $0 - 800\text{GeV}$ . The main contributing term in the  $E_T^{miss}$  uncertainty comes from the  $E_T^{miss,JES}$  and  $E_T^{miss,JER}$ .

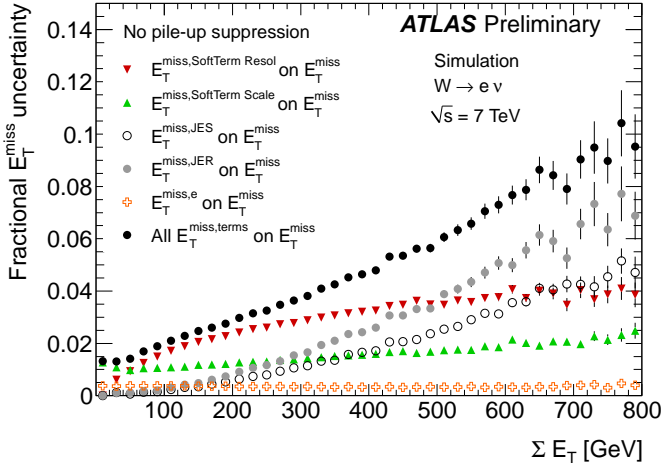


Figure 4.9: Relative systematic uncertainty of  $E_T^{miss}$  and its contributing terms as a function of the total transverse energy  $\sum E_T$ . Taken from [99].

## 4.9 Trigger

An overview of the ATLAS trigger system is presented in Section 3.2.8. In this chapter the muon and electron triggers used in the analysis are presented. A more detailed description can be found in [100, 101].

The ATLAS trigger system is configured over three stages. The Level-1 (L1) trigger selects Regions of Interest (RoI) in the detector, which in turn reduces the event rate to  $\sim 100$  kHz. The High Level Trigger (HLT) consists of the Level-2 (L2) Trigger, that uses fast reconstruction algorithms on detector hits and the Event Filter, which uses the full ATLAS event reconstruction to identify and reconstruct physics objects.

Trigger efficiencies are derived by a tag-and-probe method [100, 101], where they were found to be 90% for electrons and 90% and 65% for muons in the barrel and endcaps respectively. The efficiency difference shown in data and simulation are

corrected using per-event weights that are applied to the simulation.

### 4.9.1 Muon Trigger

The L1 muon trigger uses information from the muon trigger chambers, which cover 80% of the Muon Spectrometer barrel and 99% of the endcaps. The tracks in the different layers of the Muon Spectrometer allow the L1 muon algorithms to estimate transverse momentum and RoI information, which is passed on to the L2 trigger. The RoI reduce the search area of the detector to 2 – 6%, allowing the L2 triggers algorithms to work effectively in the given time frame.

The L2 trigger uses a fast track algorithm to reconstruct stand-alone muons and improves on the muon transverse momentum estimated by the L1 muon trigger. The stand-alone muons are combined with Inner Detector tracks in the RoIs, with a muon being classified as isolated if no tracks or energy deposits are found around the muon. The L2 muon trigger is found to accept one in every thirty events, these events are then passed on to the Event Filter.

The Event Filter uses full muon reconstruction (described in Section 4.5) to discriminate the muon from other particles in the event. The Event Filter applies several muon quality cuts to improve muon acceptance and also keeping the trigger at a low rate.

### 4.9.2 Electron Trigger

The L1 electron trigger defines RoI trigger towers of  $\Delta\eta \times \Delta\phi = 0.1 \times 0.1$  with the calorimeters fine granularity. Each calorimeter cell that is contained in a trigger tower

is found by a sliding window algorithm based on a grid of  $4 \times 4$  in  $\eta - \phi$ . The energy at the centre of the window is required to exceed a given threshold.

The L2 trigger reconstructs electrons and photon clusters in the RoI regions that are provided by the L1 trigger. Due to the triggers requirement of having a low latency, only the second layer of the EM calorimeter is used to identify pre-seeded cells with large transverse energy deposits within the RoI. Track reconstruction in the Inner Detector and cluster-to-track matching algorithms are used in the RoIs to estimate the position and transverse energy of the cluster more accurately. The electron identification uses energy deposit shower shapes in the EM calorimeter to improve the quality of the electron candidates, without sacrificing signal acceptance.

The Event Filter uses full reconstruction algorithms that are explained in Section 4.4. Electron trigger requirement based on transverse momentum, isolation and electron quality are applied to the reconstructed electron candidate to improve electron acceptance and keep the trigger rate low.

## 4.10 Summary

Event reconstruction allows us to understand the ATLAS physics event in terms of real physics objects. This chapter has outlined the importance of event reconstruction in the final physics result and the steps needed in turning raw data output into accurately modelled physics objects. With the information provided in this and previous chapters, we are now ready to understand the full analysis chain. The next chapter presents the main focus of this thesis, with the analysis of  $ZH \rightarrow l^+l^-b\bar{b}$  production.

# Chapter 5

**$H \rightarrow b\bar{b}$  in Associated Production**

**with a  $Z \rightarrow l^+l^-$  Vector Boson**

## 5.1 Introduction

In the following chapter the methodology used to analyse the 2012, 8 TeV,  $13 \text{ fb}^{-1}$  dataset when searching for associated  $ZH$  production of the Standard Model Higgs boson decaying to  $b\bar{b}$  is discussed. The analysis will focus searches on events containing two charged leptons (electrons or muons), where  $Z \rightarrow e^+e^-$  or  $Z \rightarrow \mu^+\mu^-$  are the allowed decaying modes of the  $Z$  vector boson. A  $b$ -tagging algorithm is used to identify  $H \rightarrow b\bar{b}$  decays in the event, while the addition of topological selection increases identification of leptons and  $b$ -jets, leading to an increase in the signal to background ratio.

Section 5.2 presents the data samples used for the signal and background processes, including PDFs and techniques used for overlap removal of events. Sections 5.3

and 5.4 present the analysis selection and its impact. Section 5.5 presents analysis of the background estimation and shape derivation of the *multi-jet* background. While, Section 5.6 discusses the control regions used to measure the accuracy of the background estimations. The systematic uncertainties and how they affect the outcome of the analysis are discussed in Section 5.7. Lastly, the results and outcome of the analysis is presented in Section 5.8.

## 5.2 Simulation and Data Samples

The analysis presented takes advantage of the LHC 2012 data taking period up to E4, where  $13 \text{ fb}^{-1}$  at 8 TeV of data was recorded by the ATLAS detector. The data satisfy a number of requirements before it is used in the analysis. These requirements are summarised below:

- The data are only collected using leptonic triggers
- The beam condition of the LHC is in a stable state
- The detector performance is in line with data quality checks and events pass a standardised good run list.

Monte Carlo (MC) event samples are used to simulate the data collected in the ATLAS detector using GEANT4 [102]. All known detector effects were included when producing the MC datasets, allowing the events to accurately model the Higgs signal and the majority of the background processes. A full list of MC datasets and their corresponding cross sections can be found on Table 5.1.

## Signal Samples

The  $ZH \rightarrow l^+l^-b\bar{b}$  signal samples, where  $l = e, \mu$  and  $\tau$  have been generated for a number of Higgs boson mass points ( $m_H = 110 - 130$  GeV) and are modelled using the *Pythia* 8 generator, with the CTEQ6L1 leading order parton distribution functions and the AUET2B tune. The AUET2B tune has been optimised for the ATLAS environment and in particular, parton showers, hadronisation and multiple parton interactions [44]. The Higgs boson cross sections and uncertainties have been calculated by the LHC Higgs Cross Section Group using comparisons from different generators and parton distribution functions [28, 34]. An overview of the results are presented in Table 5.2, along with  $H \rightarrow b\bar{b}$  decay branching ratios calculated using *HDECAY* [36].

## Background Samples

A number of background processes have similar signatures to the Higgs boson signal and are produced by various event generators. The main background contribution comes from the  $Z + jets$  processes that are simulated using the *SHERPA* generator tuned with the CTEQ6L1 parton distribution functions [43]. The samples are split into  $Z \rightarrow e^+e^-$ ,  $Z \rightarrow \mu^+\mu^-$  and  $Z \rightarrow \tau^+\tau^-$  events, where the jets can either come from *SHERPA Z + Heavy* ( $b$  and  $c$  quarks) or *SHERPA Z + Light* (everything other than  $b$  and  $c$  quarks) samples. To avoid overlapping events in the two samples, truth hadron matching<sup>1</sup> is required:

- $Z + \geq 1b - jet$  events occur when at least one  $b$  hadron matches a signal jet.

---

<sup>1</sup> $\Delta R = \sqrt{\Delta\phi^2 + \Delta\eta^2} \leq 0.4$ , where the difference in distance is between the quark and the truth hadron in the  $\Delta R$  region.

- $Z+ \geq 1c-jet$  events occur when no  $b$  hadron is matched to a signal jet and at least one  $c$  hadron is matched to a signal jet.
- $Z+ \geq 1light-jet$  events occur when no  $b$  or  $c$  hadron is matched to either of the signal jets.

Background samples for  $W+ \geq 1b-jet$ , where  $W \rightarrow e\nu$ ,  $W \rightarrow \mu\nu$  and  $W \rightarrow \tau\nu$  are produced by the *POWHEG* generator [103] using the CT10 NLO PDFs, interfaced with *Pythia 6* for the parton shower and hadronisation. For events with no  $b$ -jets,  $W+ \geq 1c$  and  $W+ \geq 1light-jet$  the *ALPGEN* generator [41] along with *HERWIG* [45] are used to simulate the events. Again, to remove double counting between  $b$ ,  $c$  and light quark events, the same overlap removal procedure is applied to the samples:

- $W+ \geq 1b-jet$  events occur when at least one  $b$  hadron matches a signal jet.
- $W+ \geq 2c-jets$  events occur when two  $c$  hadrons are matched to two signal jets.
- $W+ \geq 1c-jet$  events occur when no  $b$  hadron is matched to a signal jet and at least one  $c$  hadron is matched to a signal jet.
- $W+ \geq 1light-jet$  events occur when no  $b$  or  $c$  hadron is matched to either of the signal jets.

The  $t\bar{t}$ ,  $t$ -channel single top,  $s$ -channel single top and  $Wt$ -channel processes are generated using a number of generators and tunes. The  $t\bar{t}$ ,  $s$ -channel single top and

$Wt$  processes are simulated using *HERWIG* at *MC@NLO* with CT10 NLO PDFs [25] and the AUET2B tune, whilst the  $t$ -channel single top process is simulated using *AcerMC* [42] with *Pythia 6* and AUET2B for the parton shower, hadronisation and multiple parton interactions. Lastly, the simulated diboson processes  $WW$ ,  $WZ$  and  $ZZ$  are modelled using the *HERWIG* generator using the CTEQ6L1 PDFs with the AUET2 tune [104].

Table 5.1: MC background samples used in the  $ZH \rightarrow l^+l^-b\bar{b}$  analysis. For each sample the cross-section, k-factor (scale factor from leading order to next-to-leading order) and total cross-section are shown.

<b>Sample Name</b>	<b>Sample Number</b>	<i>LO</i> $\sigma(pb)$	<b>k-factor</b>	$\sigma_{total}(pb)$
ttbarLeptonFilter	105200	112	1.14	129
ttbarallhad	105204	95.1	1.14	108
SingleTopSChanWenu	108343	0.56	1.07	0.6
SingleTopSChanWtaunu	108345	0.56	1.07	0.6
SingleTopSChanWmunu	108344	0.56	1.07	0.6
SingleTopWtChanIncl	108346	20.6	1.08	22.3
singletoptchane	117360	8.6	1.1	9.46
singletoptchanmu	117361	8.6	1.1	9.46
singletoptchantau	117362	8.6	1.1	9.46
WenuNp0	107680	8037	1.2	9,645
WenuNp1	107681	1579	1.2	1,895
WenuNp2	107682	477	1.2	572
WenuNp3	107683	133	1.2	160
WenuNp4	107684	35.6	1.2	42.7
WenuNp5	107685	10.5	1.2	12.6

Table 5.1: Continued. MC background samples used in the  $ZH \rightarrow l^+l^-b\bar{b}$  analysis. For each sample the cross-section, k-factor (scale factor from leading order to next-to-leading order) and total cross-section are shown.

<b>Sample Name</b>	<b>Sample Number</b>	<i>LO</i> $\sigma(pb)$	<b>k-factor</b>	$\sigma_{total}(pb)$
WmunuNp0	107690	8040	1.2	9,645
WmunuNp1	107691	1580	1.2	1,895
WmunuNp2	107692	477	1.2	572
WmunuNp3	107693	133.9	1.2	160
WmunuNp4	107694	35.6	1.2	42
WmunuNp5	107695	10.5	1.2	12.6
WtaunuNp0	107700	8035	1.2	9,645
WtaunuNp1	107701	1579	1.2	1,895
WtaunuNp2	107702	477	1.2	572
WtaunuNp3	107703	133	1.2	160
WtaunuNp4	107704	35.5	1.2	42.7
WtaunuNp5	107705	10.5	1.2	12.6
WccNp0	117284	150	1.2	180
WccNp1	117285	132	1.2	159
WccNp2	117286	71.8	1.2	86.1
WccNp3	117287	30.2	1.2	36.3

Table 5.1: Continued. MC background samples used in the  $ZH \rightarrow l^+l^-b\bar{b}$  analysis. For each sample the cross-section, k-factor (scale factor from leading order to next-to-leading order) and total cross-section are shown.

<b>Sample Name</b>	<b>Sample Number</b>	<i>LO</i> $\sigma(pb)$	<b>k-factor</b>	$\sigma_{total}(pb)$
WcNp0	117293	807	1.52	1,227
WcNp1	117294	267	1.52	406
WcNp2	117295	69.8	1.52	106
WcNp3	117296	20.5	1.52	31.2
WcNp4	117297	4.3	1.52	6.54
Wpennubb	167000	27.5	1.0	27.5
Wpmunubb	167001	27.7	1.0	27.7
Wptaunubb	167002	27.4	1.0	27.4
Wmenubb	167003	17.6	1.0	17.6
Wmmunubb	167004	17.7	1.0	17.7
Wmtaunubb	167005	17.5	1.0	17.5
ZmumuLightJets	146821	1052	1.2	1,262
ZeeLightJets	146820	1051	1.2	1,261
ZtautauLightJets	146822	1051	1.2	1,261
ZnunuLightJets	146823	5679	1.2	6,815

Table 5.1: Continued. MC background samples used in the  $ZH \rightarrow l^+l^-b\bar{b}$  analysis. For each sample the cross-section, k-factor (scale factor from leading order to next-to-leading order) and total cross-section are shown.

<b>Sample Name</b>	<b>Sample Number</b>	<i>LO</i> $\sigma(pb)$	<b>k-factor</b>	$\sigma_{total}(pb)$
ZeeHeavyJets	128975	58.7	1.2	70.5
ZmumuHeavyJets	128976	58.7	1.2	70.5
ZtautauHeavyJets	128977	58.7	1.2	70.5
ZnunuHeavyJets	128979	315	1.2	378
WWNoLeptonFilter	161995	55.4	1.0	55.4
WZNoLeptonFilter	161996	22.6	1.0	22.6
ZZNoLeptonFilter	161997	7.69	1.0	7.69

Table 5.2: MC signal samples used in the  $ZH \rightarrow l^+l^-b\bar{b}$  analysis. For each signal sample the cross-section, branching fraction of the Higgs, branching fraction of the  $Z$  boson and total cross-section are shown.

<b>Sample Name</b>	<b>Sample Number</b>	$\sigma(pb)$	$HBr$	$ZBr$	$\sigma_{total}(pb)$
ZH110llbb	161824	0.59	0.74	0.1	0.04
ZH115llbb	161825	0.51	0.7	0.1	0.04
ZH120llbb	161826	0.45	0.65	0.1	0.03
ZH125llbb	161827	0.39	0.58	0.1	0.02
ZH130llbb	161828	0.35	0.49	0.1	0.02

## 5.3 Object Selection

Analysis selection starts with requirements on the basic physics objects in the event. These objects have gone through a process of smearing and calibration corrections (see chapter 4 for details) before selection has taken place.

### 5.3.1 Muons

Muons at the ATLAS experiment have four defined categories of possible candidates in the detector (see Section 4.5.1 for details). These are categorised depending on how each muon has been reconstructed. The analysis considers all four flavours of muons (stand-alone, combined, segment tagged and calorimeter tagged) using the MuID algorithm to identify the muons in the detector, while the muon tracks are reconstructed using the Muonboy algorithm [105]. The analysis further separates the muons into two more categories. These categories are defined as loose and medium for the two lepton analyses. A loose muon will satisfy kinematic cuts, where  $p_T > 10 \text{ GeV}$  and  $|\eta| < 2.5$ . However, if the muon has no inner detector tracks and is only reconstructed in the Muon Spectrometer (stand-alone muon) a requirement of  $2.5 < |\eta| < 2.7$  is required. Muons that are reconstructed as calorimeter tagged are further required to be within an  $|\eta| < 0.1$  with  $p_T > 20 \text{ GeV}$ , while all muons must pass the tight MuID criteria (see Section 4.5.1 for details).

The ATLAS Muon Combined Performance (MCP) group quality criteria (see Section 4.5.1 for details) has also been included to improve the identification of muons. These improvements are achieved by requiring inner detector tracks associated with the muon to pass a number of additional cuts that are applied to the various layers

of the inner detector. These cuts have been summarised in Table 5.3.

Additional cuts to help suppress muons from cosmic rays are required on the impact parameter with respect to the primary vertex, where  $|d_0| < 1$  mm and  $|z_0| < 10$  mm is applied to the muon. The contamination from muons associated with jets is also considered by requiring the sum of the inner detectors track momenta in a cone of  $\Delta R = \sqrt{\Delta\eta^2 + \phi^2} < 0.2$  around the muon to be less than 10% of the muon's momentum. In addition to the loose requirements above, medium combined and segment-tagged muons are required to pass an additional kinematic cut of  $p_T > 25$  GeV. This further improves the identification of the Z bosons in the event.

Table 5.3: Summary of selection for loose and medium muons.  $N_{hits}(N_{holes})$  represents the number of hits (missing hits) in an area of the inner tracker.  $N_{dead}$  refers to the number of dead sensors the muon has crossed in a particular subdetector

<b>Muon Selection</b>	
	Combined (CB) or segment-tagged (ST) MuID muons
Identification	Calorimeter tagged (CaloTag) MuID muons
	Standalone (SA) MuID muons
<b>Loose:</b>	
	MuID CB + ST muons $p_T > 10$ GeV and $ \eta  < 2.5$
Kinematic cuts	MuID CaloTag muons $p_T > 20$ GeV and $ \eta  < 0.1$
	MuID SA muons $p_T > 10$ GeV and $2.5 <  \eta  < 2.7$
<b>Medium:</b>	
	MuID CD + ST muons $p_T > 25$ GeV and $ \eta  < 2.5$
Inner Detector	$N_{hits}^{b-layer} > 0$ (except in dead area)
	$N_{hits}^{pixel} + N_{dead}^{pixel} > 0$
	$N_{hits}^{SCT} + N_{dead}^{SCT} \geq 5$
	$N_{holes}^{pixel} + N_{holes}^{SCT} < 3$
	$ \eta  < 1.9$ : $N_{tot}^{TRT} > 5$ and $N_{outliers}^{TRT} < (0.9xN_{tot}^{TRT})$
	$ \eta  \geq 1.9$ : if $N_{tot}^{TRT} > 5$ , require $N_{outliers}^{TRT} < (0.9xN_{tot}^{TRT})$
	where $N_{tot}^{TRT} = N_{hits}^{TRT} + N_{outliers}^{TRT}$
Cosmic Ray Rejection	$ d_0  < 1$ mm
	$ z_0  < 10$ mm
Jet Mis-ID Rejection	$\sum_{tracks} p_T(\Delta R < 0.2)/p_T^\mu < 0.1$

### 5.3.2 Electrons

Electron identification begins with the electromagnetic calorimeter clusters found in the Electromagnetic Calorimeter (EM). The clusters are reconstructed using the ATLAS sliding window algorithm (described in Section 4.4.1) along with tracks matched from the inner detector. Similarly with the muon selection, electrons are split into loose and medium electrons. The electron candidates that pass the loose criteria must satisfy the standard ATLAS Loose++ quality requirements (see Section 4.4.1), while the medium electron candidates must satisfy the Medium++ quality requirements, which are inclusive of the Loose++ requirements (see Section 4.4.1). To ensure greater reconstruction and identification efficiency, electron candidates are required to be within  $\eta_{cluster} < 2.47$ , which is in the precision region of the EM measurement, and have an  $E_T > 10$  GeV. Medium electrons are required to have an  $E_T > 25$  GeV. Electrons are also required to have an isolation requirement to reduce the misidentification rate between electrons and jets. An electron is required to have the sum of the inner detector tracks transverse momenta in a cone of  $\Delta R < 0.2$  around the electron to be less than 10% of the electron's transverse momentum. To avoid fake electrons from final state muons, electron candidates that fall within a  $\Delta R < 0.2$  of selected muons are rejected. The cuts are summarised in Table 5.4.

Table 5.4: Summary of selection for loose and medium electrons.

<b>Electron Selection</b>	
	IsEM:
Identification	Leading Electron: Medium++ Second Electron: Loose++
	Loose:
Kinematic cuts	$p_T > 10 \text{ GeV}$ and $ \eta  < 2.47$
	Medium:
	$p_T > 25 \text{ GeV}$
Jet Mis-ID Rejection	$\sum_{tracks} p_T(\Delta R < 0.2)/p_T^\mu < 0.1$
Muon Mis-ID Rejection	$\Delta R_{elec,muon} < 0.2$

### 5.3.3 Jets

Jets used in the analysis come from topological clusters using the anti- $k_T$  algorithm [89] with a distance parameter  $\Delta R = 0.4$  (see Section 4.6.1 for further details). The jet candidates are split up into two categories, Veto and Signal jets. Veto jets are used to clean the event from bad conditions in the detector over the different run periods (.i.e. holes in the Liquid Argon Calorimeter), while Signal jets are used to reconstruct the potential Higgs boson candidates. The Veto jets are required to have a  $p_T > 20 \text{ GeV}$  and are within an  $|\eta| < 4.5$ . Jets originating from pile-up are identified and removed by requiring at least 50% of all associated tracks to the jet originate from the primary vertex. This cut is achieved by requiring a jet vertex fraction ( $JVF$ )  $< 0.5$ , which corresponds to the fraction of track momentum associated to the jet. Jets that do

not have associated tracks that arise from hadronisation of the quark and come from the signal process are included in the event, these jets have a  $JVF = -1$ . To account for misidentification of electrons as jets, an overlap removal requirement is applied to the jet. The jet is removed from the event if an electron is found within an  $\Delta R < 0.4$  around the jet axis. Signal jets are required to pass the requirements of the Veto jet with the addition of  $|\eta| < 2.5$ , while the leading  $b$ -weighted jet has a  $p_T > 45$  GeV and the subleading jet has a  $p_T > 20$  GeV. The jets are also matched to a truth hadron by requiring the jets to match either a  $b$ -hadron,  $c$ -hadron or light-hadron (neither  $a$   $b$  or  $c$  hadron) within a cone of 0.4 around the jet axis. The truth matching is applied to recognise overlapping events in the  $Z + jets$  background MC.

### 5.3.4 $b$ -jets

To exploit the long lifetime of the  $b$  hadron the MV1 algorithm discussed in Section 4.7 is used to identify jets originating from  $b$  quarks. The MV1 tagger [93] uses information from the impact parameter and the secondary vertex, along with a  $b \rightarrow c$  hadron chain fit to produce a signal neural network discriminant,  $w$ , that scores higher when a jet is more likely to be from a  $b$  quark. The weight  $> 0.795$  chosen in the analysis, results in  $\sim 70\%$  efficiency (from semi-leptonic  $t\bar{t}$  events) for  $b$ -jets, while a rejection factor of  $\sim 5$  and  $\sim 150$  for  $c$  and light jets respectively [94].

Table 5.5: Summary of selection for Veto and Signal jets.

Jet Selection	
Identification	Anti- $k_T$ R = 0.4 topological jets
Veto:	
	$p_T > 20 \text{ GeV}$ and $ \eta  < 4.5$
Kinematic cuts	Signal:
	b-weight leading jet: $p_T > 45 \text{ GeV}$ and $ \eta  < 2.5$
	b-weight subleading jet: $p_T > 20 \text{ GeV}$ and $ \eta  < 2.5$
Quality	Looser quality cuts
Electron Mis-ID Rejection	$\Delta R_{jet_{elec}} < 0.2$
b-Tagging	MV1 weight $> 0.795$ ( $\sim 70\%$ efficiency)

### 5.3.5 Missing transverse energy

Missing transverse energy,  $E_T^{miss}$ , can be used to discriminate against events with neutrinos in the final state. Since  $ZH \rightarrow l^+l^-b\bar{b}$  channel does not have a final state neutrino, a small  $E_T^{miss}$  is associated with the event. An upper limit of  $E_T^{miss} < 60 \text{ GeV}$  is placed on the event. This results in a reduction of events from  $t\bar{t}$ , single  $t$  and  $Wt$ , due to the presence of neutrinos in the top quark and W decay. The  $E_T^{miss}$  is reconstructed using the RefFinal algorithm which was explained in Section 4.8.

## 5.4 Event Selection

The event selection is summarised in Table 5.6. Events containing two leptons are required to satisfy the medium criteria for the leading lepton and the loose criteria for

the subleading lepton. These definitions are explained in Section 5.3. A lepton veto is also applied to the event, where each lepton must be of the same flavour i.e. events from  $Z \rightarrow e^+e^-$  and  $Z \rightarrow \mu^+\mu^-$  are selected. Events are also required to contain exactly two  $b$ -tagged jets, which are ordered according to their  $b$ -weight. The two  $b$ -tagged jets are used to reconstruct the mass of the Higgs boson candidate. Further topological cuts are applied to increase the signal to background ratio. A dilepton mass window cut is applied to the event between  $83 < m_Z < 99$  GeV, which increases the signal acceptance of the analysis by reducing the  $t\bar{t}$ , single-top (s-top),  $Wt$  and  $W + jets$  backgrounds – due to the background events not having a leptonic  $Z$  boson in their final state. A  $E_T^{miss} < 60$  GeV is also applied to the event which again further reduces the background contribution from  $t\bar{t}$ , s-top,  $Wt$  and  $W + jets$  events due to the presence of neutrinos in the top quark and  $W$  decay. Additional cuts applied to the angular distribution of the two  $b$ -jets are used to remove background from the  $V+jets$  processes, due to the increase in collimation in jets at greater transverse momenta. A cut of  $\Delta R(j_1, j_2) \geq 0.7$  is applied to the event when the  $Z$  vector bosons transverse momentum is between  $0 < p_T^Z < 150$  GeV. However, while the jets are in the region of  $150 < p_T^Z < 200$  GeV they are required to be within  $0.7 < \Delta R(j_1, j_2) < 1.8$ . For high  $p_T$   $Z$  bosons with a  $p_T^Z > 200$  GeV a requirement of  $\Delta R(j_1, j_2) \geq 1.6$  must be satisfied for the event to pass. The number of events for the signal and background after the event selection is shown for the dijet mass range  $80 < m_{b\bar{b}} < 150$  GeV in Table 5.7.

Table 5.6: Summary of Event Selection

Cut	Definition
Event quality	Require the reconstructed objects are of good quality and that the detector is fully operational.
Trigger	lowest- $p_T$ unprescaled triggers for both single and double leptons are selected.
Vertex	There must be at least one vertex with 3 associated tracks in the event
Leptons	1 Medium lepton + 1 Loose lepton
Jets	$N_{b-jets} = 2$ $N_{jets} \geq 2$
MET	$E_T^{miss} < 60$ GeV
Dilepton Mass	$83 < m_z < 99$ GeV
	Topological Cuts $\Delta R(j_1, j_2)$
$0 < p_T^Z < 150$ GeV	$\Delta R(j_1, j_2) \geq 0.7$
$150 < p_T^Z < 200$ GeV	$0.7 < \Delta R(j_1, j_2) < 1.8$
$p_T^Z > 200$ GeV	$\Delta R(j_1, j_2) \geq 1.6$

Table 5.7: The number of selected events in the  $N_{b-jets} = 2$  region for signal (S) and background (B) samples. The data and MC ratio is also shown, along with the significance ( $S/\sqrt{B}$ ). The numbers are taken from a mass range  $80 < m_{b\bar{b}} < 150$  GeV.

Process	$e^+e^-b\bar{b}$	$\mu^+\mu^-b\bar{b}$
<i>data</i>	$1291 \pm 36$	$1129 \pm 34$
<i>ZH125 (S)</i>	$7.48 \pm 0.09^{+0.76}_{-0.64}$	$7.59 \pm 0.09^{+0.80}_{-0.70}$
<i>Zb</i>	$919 \pm 13^{+107}_{-99}$	$862 \pm 12^{+113}_{-92}$
<i>Zc</i>	$60.7 \pm 27.2^{+7.2}_{-6.6}$	$0.044 \pm 0.031^{+0.012}_{-0.000}$
<i>Zl</i>	$11.3 \pm 7.9^{+1.4}_{-1.2}$	$36.7 \pm 18.4^{+4.6}_{-4.1}$
<i>Wb</i>	$0 \pm 0$	$0 \pm 0$
<i>Wcc</i>	$2.82 \pm 2.82^{+0.35}_{-0.32}$	$0 \pm 0$
<i>Wc</i>	$0 \pm 0$	$0 \pm 0$
<i>Wl</i>	$0 \pm 0$	$0 \pm 0$
<i>t\bar{t}</i>	$199 \pm 4^{+19}_{-29}$	$183 \pm 4^{+21}_{-23}$
<i>s - top</i>	$3.94 \pm 0.39^{+0.37}_{-0.77}$	$3.04 \pm 0.33^{+0.45}_{-0.27}$
<i>ZZ</i>	$28.9 \pm 1.1^{+3.7}_{-3.1}$	$31.4 \pm 1.2^{+3.9}_{-3.5}$
<i>WZ</i>	$0.64 \pm 0.18^{+0.08}_{-0.07}$	$1.87 \pm 0.40^{+0.23}_{-0.22}$
<i>WW</i>	$0 \pm 0$	$0 \pm 0$
<i>bkg (B)</i>	$1227 \pm 13^{+135}_{-161}$	$1118 \pm 12^{+128}_{-96}$
$\frac{\textit{data}}{S+B}$	$1.05 \pm 0.14$	$1.0 \pm 0.1$
$\frac{S}{\sqrt{B}}$	$0.21 \pm 0.11$	$0.23 \pm 0.11$

## 5.5 Background Estimation

Background estimation is a critical part of the analysis when trying to model the data. Care was taken not to bias the MC when calculating the discrepancies in the modelling. The backgrounds studied in the analysis have their shapes predominantly taken from MC with the normalisation shapes estimated from control regions in data. The *multi-jet* background has however been derived by using a data-driven approach to estimate the shape and normalisation. Estimation of the *multi-jet* background has been achieved by deriving a template from data that is rich in *multi-jet* events. The *multi-jet* template is then normalised by fitting the template to the signal region. The control regions are defined by inverting or alternating some of the event selection cuts. The control region event selection has been carefully chosen so that they contain a similar signature to the signal, while being rich in purity of the targeted background. The top control region has been selected by inverting the  $E_T^{miss}$  and  $m_{ll}$  cuts, while the flavour composition of the  $Z + jets$  is estimated by requiring a specific number of  $b$ -jets in the event.

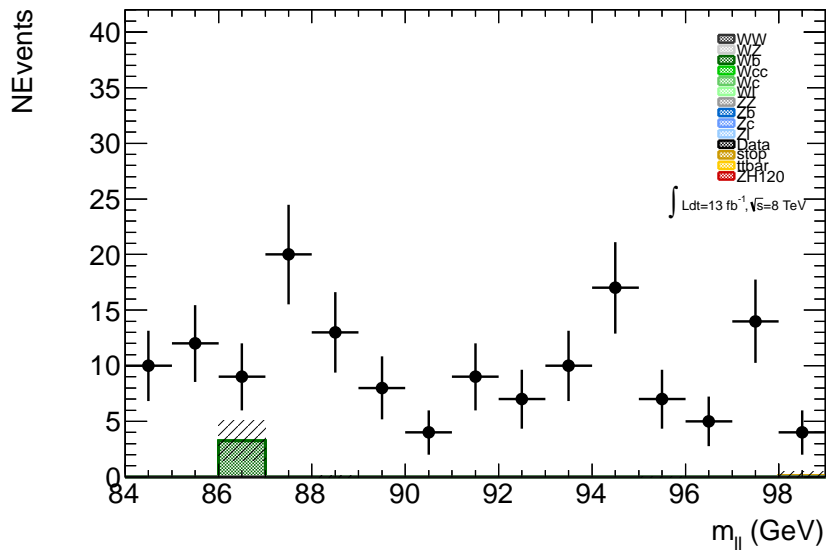
### 5.5.1 Estimation of the Multijet Background

*multi-jet* events in the  $ZH \rightarrow l^+l^-b\bar{b}$  channel are jets that have either faked two oppositely charge electrons or muons. In previous analyses [106] the *multi-jet* process has been shown to be a small contribution to the overall background, as the two jets would be required to have a combined mass in the range of the  $Z$  boson.

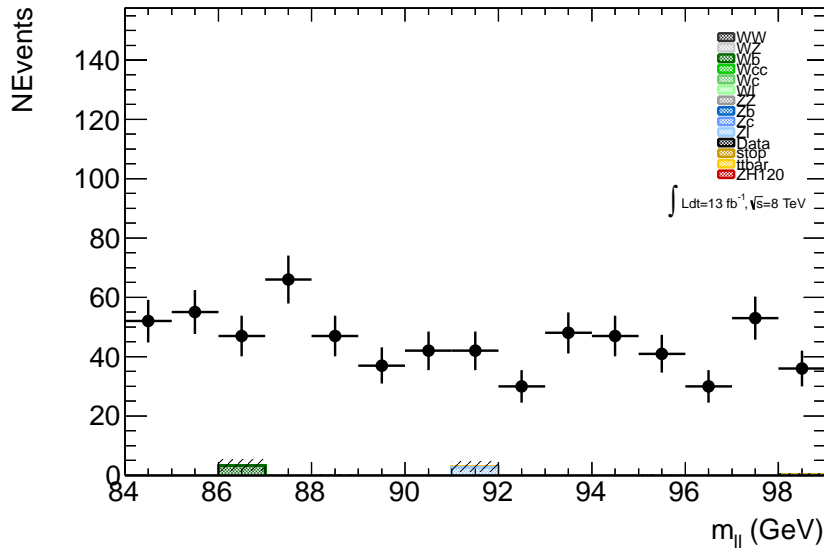
The  $ZH \rightarrow e^+e^-b\bar{b}$  channel is used to derive a shape template from the data in a region where *multi-jet* events are the dominant process. The shape template is

obtained by changing some of the selection criteria in the signal region. The two lepton requirement of one Medium++ electron and one Loose++ electron in the final state is loosened to require two Loose++ electrons, while the track isolation requirement of the electron has been inverted from  $\frac{\sum_{\text{tracks}} p_T (\Delta R < 0.2)}{p_T^e} < 0.1$  to  $\frac{\sum_{\text{tracks}} p_T (\Delta R < 0.2)}{p_T^e} \geq 0.1$ . The event is triggered using an un-prescaled trigger with the lowest threshold and no track isolation requirement. The trigger was chosen due to the signal region trigger requiring an isolation cut, which would have biased the event. The remaining signal selection criteria are also applied and histograms from this region are used as a shape template for the *multi-jet* background. Figures 5.2 and 5.3 show the corresponding *multi-jet* region in the  $m_{ll}$  distribution. We can see that the region is pure in *multi-jet* background, with a purity of  $\sim 99\%$ , while there is a negligible contamination from the  $Zb$ ,  $ZZ$  and  $s - top$  processes (see table 5.8 for more detail).

The *multi-jet* template was also normalised to the signal region to take into account the differences in efficiency in the electron selection. The normalisation is estimated by fitting the dielectron invariant mass distribution to the signal region within a mass window of  $84 < m_{ll} < 99$  GeV. The  $Z \rightarrow e^+e^-$  distribution is chosen in the fit, as it is both well modelled in data and MC as shown in Figures 5.2 and 5.3.



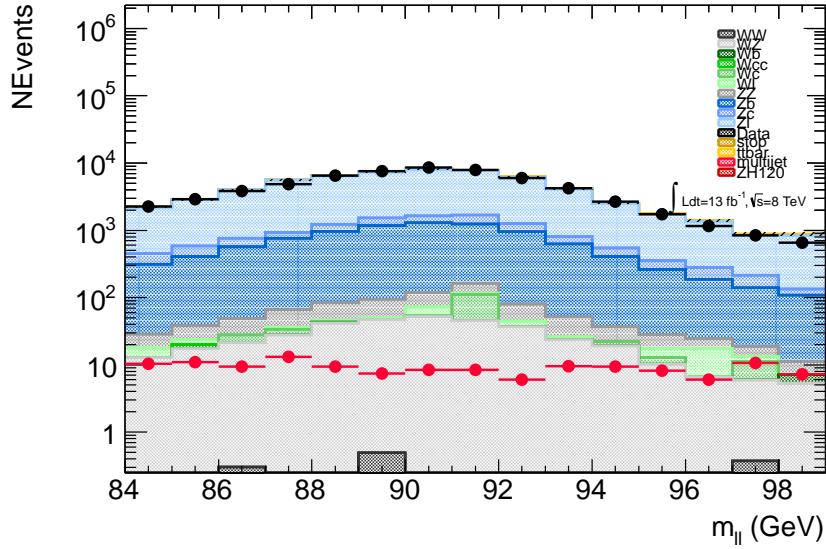
(a) The *multi-jet* background in the  $multi-jet\ N_{b-jets} \geq 1$  region is represented by the data and there is a small background contamination from the  $s-top$ ,  $t\bar{t}$  and  $Zb$  backgrounds.



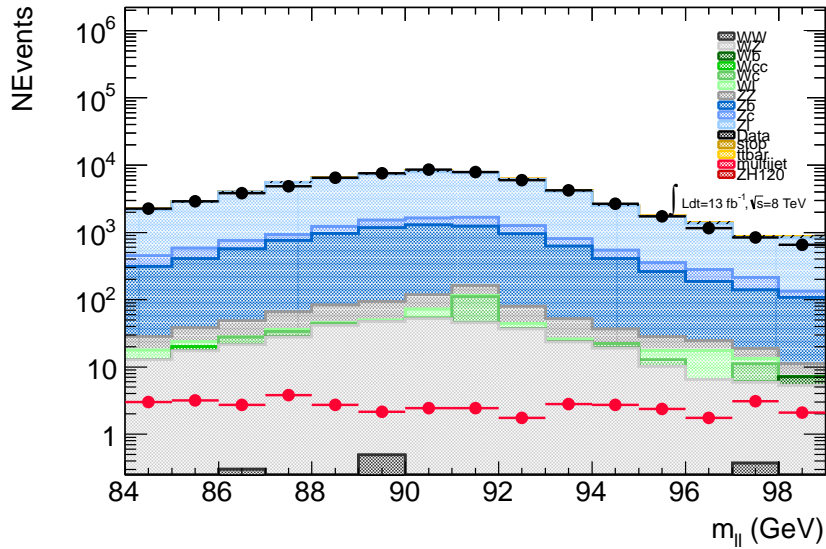
(b) The *multi-jet* background in the  $multi-jet\ N_{jets} \geq 1$  region is represented by the data and there is a small background contamination from the  $s-top$ ,  $t\bar{t}$  and  $Zb$  backgrounds.

Table 5.8: The number of selected signal (S), background (B) and data events from the *multi-jet* region, where  $Nb - jets \geq 1$ . The statistical uncertainties are only shown.

Process	$e^+e^- b\bar{b}$
$ZH125$ (S)	$0 \pm 0$
$Zb$	$0.26 \pm 0.26$
$Zc$	$0 \pm 0$
$Zl$	$0 \pm 0$
$Wb$	$0 \pm 0$
$Wcc$	$0 \pm 0$
$Wc$	$0 \pm 0$
$Wl$	$0 \pm 0$
$t\bar{t}$	$0.26 \pm 0.05$
$stop$	$0.30 \pm 0.10$
$ZZ$	$0.034 \pm 0.034$
$WZ$	$0 \pm 0$
<i>multi-jet (data)</i>	$160 \pm 13$

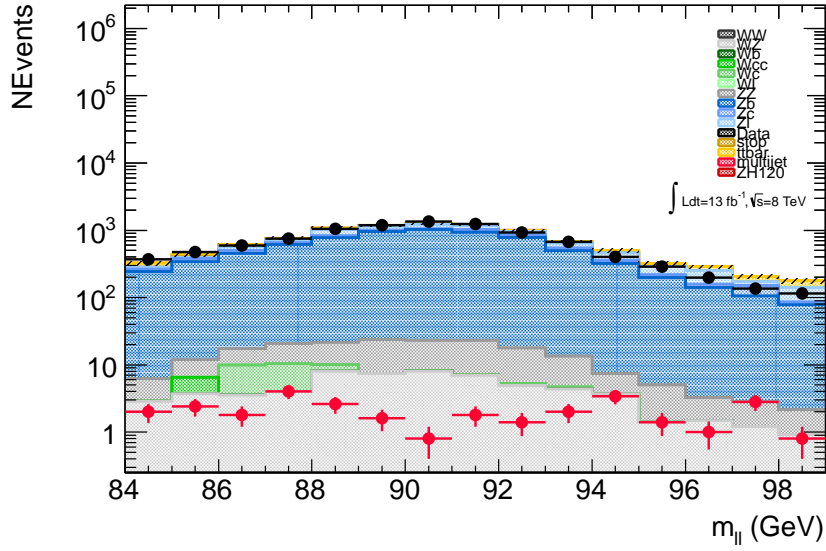


(a)  $m_{ll}$  distribution in the signal region  $N_{b-jets} = 2$  before log-likelihood fit is applied to the multijet sample (red).

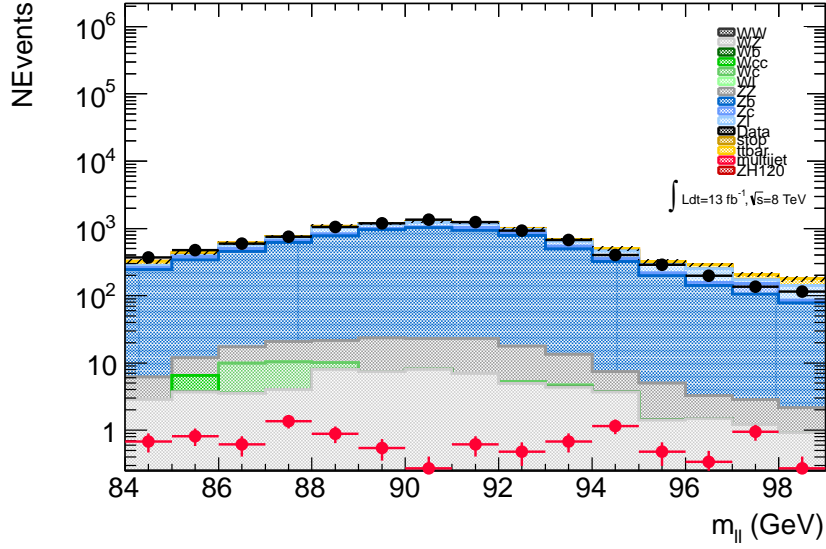


(b)  $m_{ll}$  distribution in the signal region  $N_{b-jets} = 2$  after log-likelihood fit is applied to the multijet sample (red).

Figure 5.2:  $m_{ll}$  distribution in the signal region  $N_{b-jets} = 2$  before and after the log-likelihood fit is applied to the multi-jet  $N_{b-jets} \geq 2$  background (red).



(a)  $m_{ll}$  distribution in the signal region  $N_{b-jets} = 2$  before log-likelihood fit is applied to the multijet sample (red).



(b)  $m_{ll}$  distribution in the signal region  $N_{b-jets} = 2$  after log-likelihood fit is applied to the multijet sample (red).

Figure 5.3:  $m_{ll}$  distribution in the signal region  $N_{b-jets} = 2$  before and after the log-likelihood fit is applied to the multi-jet  $N_{b-jets} \geq 1$  background (red).

However, the statistics in the two  $b$ -tagged region was insufficient to perform a fit and the  $b$ -tagged requirement was relaxed to only require 1  $b$ -jet or more within the event. The fit was carried out allowing the  $ZH \rightarrow e^+e^-j\bar{j}$  processes to vary unconstrained, while keeping the other backgrounds fixed by their statistical error. A scale factor of  $0.34 \pm 0.03$  (*stat.*) was achieved in the signal region fit and was used to scale the *multi-jet* template.

To verify the consistency between the control regions, the same procedure was carried out for the inclusive  $N_{jets} \geq 2$  region, which yielded a scale factor of  $0.29 \pm 0.02$  (*stat.*). Taking into account the statistical uncertainties, the two scale factors are comparable, however a conservative systematic of 100% uncertainty is assigned to the scale factors due to uncertainties in the other processes that effect the fit.

### 5.5.2 Estimation of the Top Background

Top production contributes significantly in the tagged regions of the analysis and also constitutes a small proportion of the untagged regions. The background is predominately dominated by leptonic  $t\bar{t}$  decays, where the originating leptons either decay from a  $W$  boson or a  $b$ -jet from a top quark decay. Neutrinos in the leptonic decay of  $t\bar{t}$  contribute to a large missing transverse energy in the event. A control region with  $E_T^{miss} > 60$  GeV and  $60 < m_{ll} < 76$  GeV or  $106 < m_{ll} < 150$  GeV is therefore chosen with a top process purity of  $\sim 97\%$ . From Table 5.9 we can see that the pre-fit process event numbers underestimate the data yield. A binned maximum log-likelihood fit is applied to the invariant mass distribution of the two  $b$ -jet candidates in the MC processes to match the data. The top process is allowed to freely float in the fit, while the

contamination from the remaining processes are constrained by their statistical and systematic uncertainties. Scale factors of  $1.59 \pm 0.21$  (*stat + sys.*) for the electron channel and  $1.54 \pm 0.19$  (*stat + sys.*) for the muon channel are obtained. The scale factors are then applied to the histograms shown in Figures 5.4 to 5.9, which obtain histograms shown in Figures 5.6 to 5.11. When taking the statistical and systematics uncertainties into account the data and MC are within good agreement over all of the distributions shown.

Table 5.9: The number of selected signal (S), background (B) and data events for the top,  $N_{b-jets} \geq 2$  region before and after the log-likelihood fit. The data over MC (data/S+B) for the top region is also shown before and after the fit.

	<b>Process</b>	$e^+e^-b\bar{b}$	$\mu^+\mu^-b\bar{b}$
	<i>data</i>	$762 \pm 28$	$726 \pm 28$
<i>MC Signal</i>	$ZH125$	$0.032 \pm 0.005^{+0.001}_{-0.001}$	$0.031 \pm 0.004^{+0.001}_{-0.001}$
	$Zb$	$2.44 \pm 0.49^{+0.30}_{-0.26}$	$2.56 \pm 0.53^{+0.32}_{-0.30}$
	$Zc$	$0 \pm 0$	$0 \pm 0$
	$Zl$	$0 \pm 0$	$0 \pm 0$
	$Wb$	$0 \pm 0$	$0 \pm 0$
	$Wcc$	$0 \pm 0$	$0 \pm 0$
Constrained background	$Wc$	$0 \pm 0$	$0 \pm 0$
	$Wl$	$0 \pm 0$	$0 \pm 0$
	$stop$	$13.5 \pm 0.7^{+1.2}_{-2.2}$	$11.5 \pm 0.6^{+1.1}_{-1.8}$
	$ZZ$	$0.049 \pm 0.049^{+0.012}_{-0.013}$	$0 \pm 0$
	$WZ$	$0 \pm 0$	$0 \pm 0$
	$t\bar{t}$	$467 \pm 5^{+51}_{-56}$	$462 \pm 5^{+50}_{-60}$
Non-constrained pre-fit	$\frac{data}{S+B}$	$1.58 \pm 0.1$	$1.52 \pm 0.1$
	$t\bar{t}$	$743 \pm 8^{+81}_{-90}$	$711 \pm 8^{+78}_{-93}$
Non-constrained post-fit	$\frac{data}{S+B}$	$1.0 \pm 0.3$	$1.0 \pm 0.3$

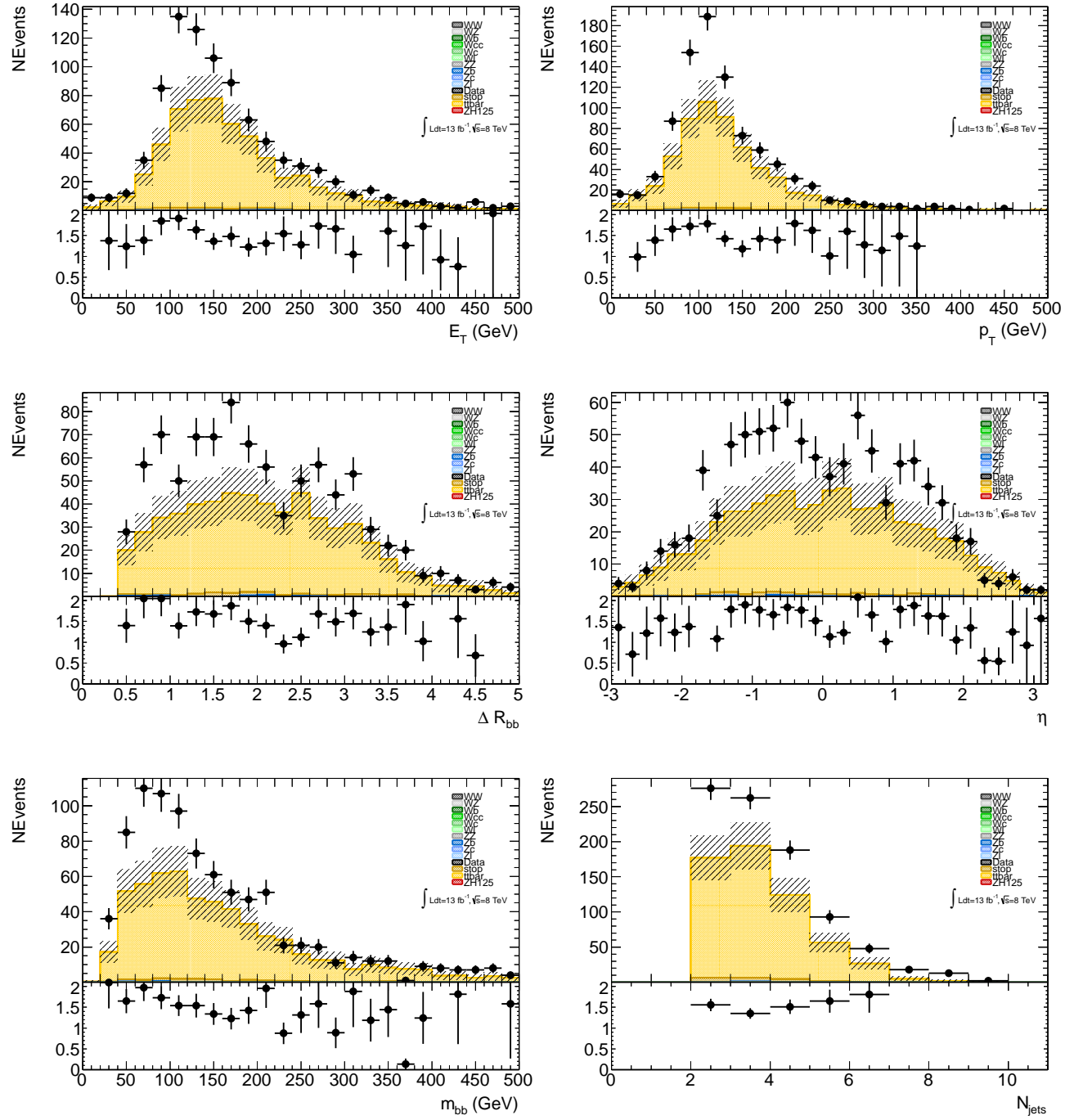


Figure 5.4: Distributions of the Higgs boson candidate in the top  $N_{b-jets} \geq 2$  and  $N_{electrons} = 2$  region, before applying scale factors from the log-likelihood fit.

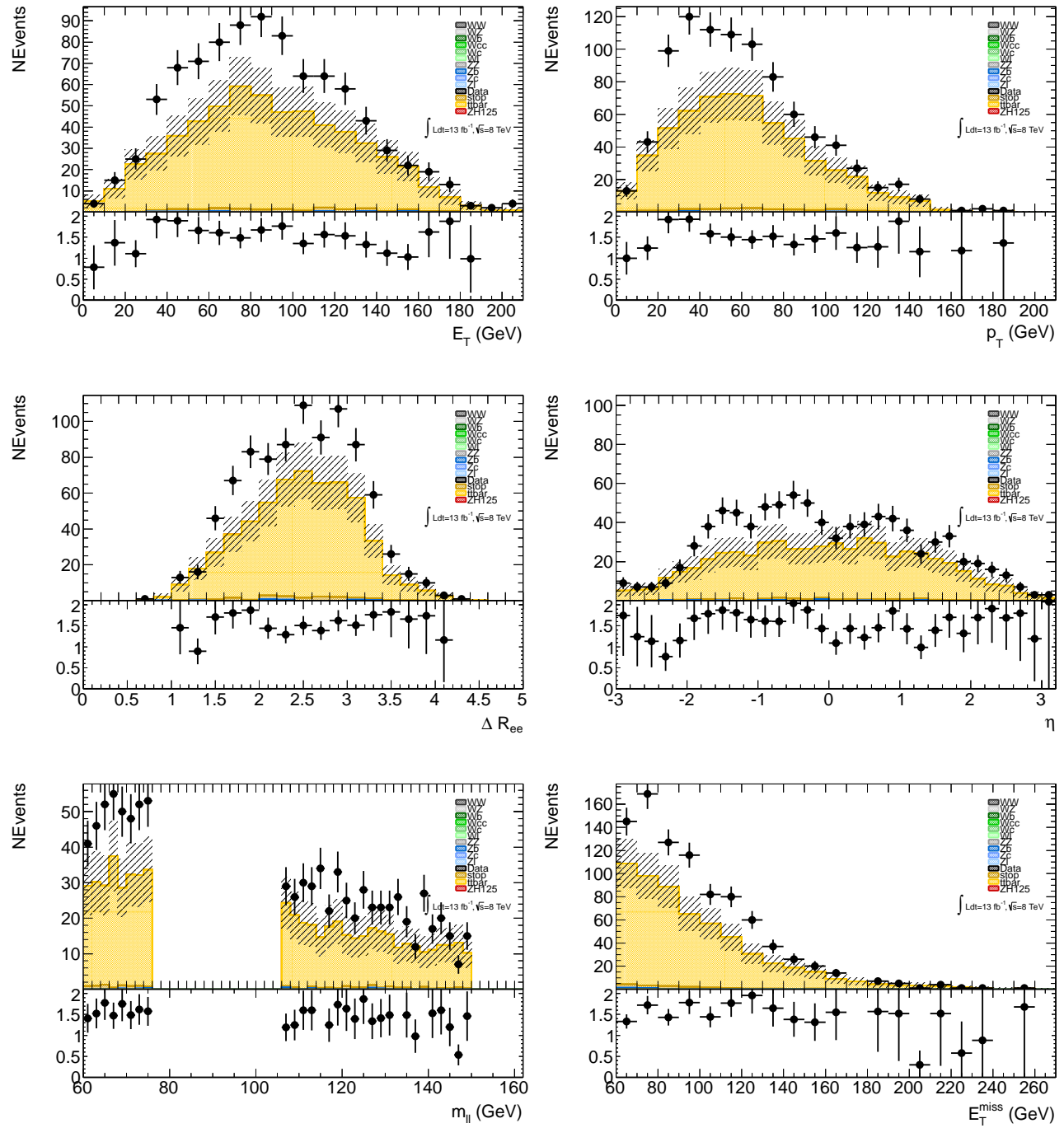


Figure 5.5: Distributions of the  $Z$  boson candidate in the top  $N_{b-jets} \geq 2$  and  $N_{electrons} = 2$  region before applying scale factors from the log-likelihood fit.

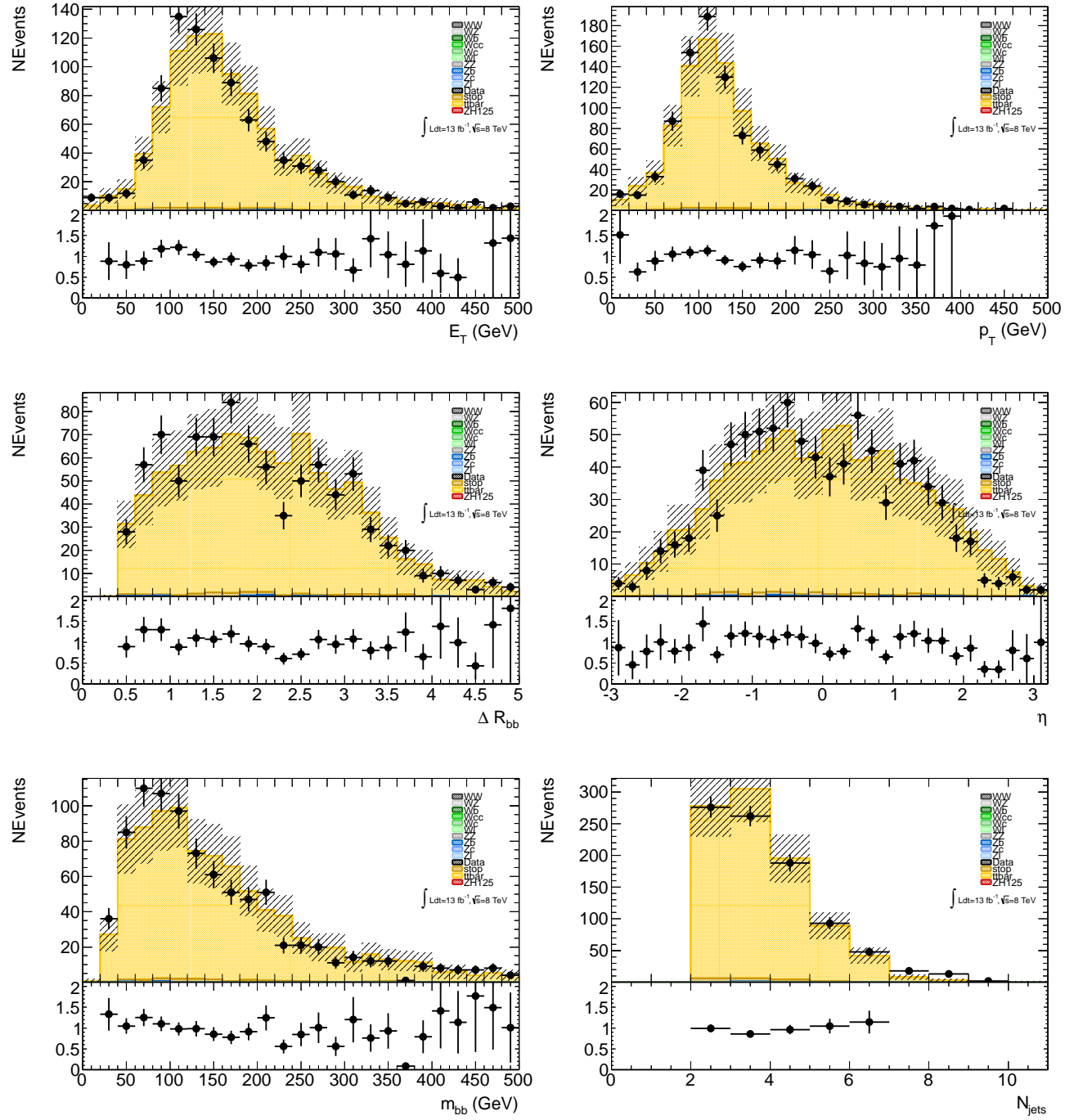


Figure 5.6: Distributions of the Higgs boson candidate in the top  $N_{b-jets} \geq 2$  and  $N_{electrons} = 2$  region after applying scale factors from the log-likelihood fit.

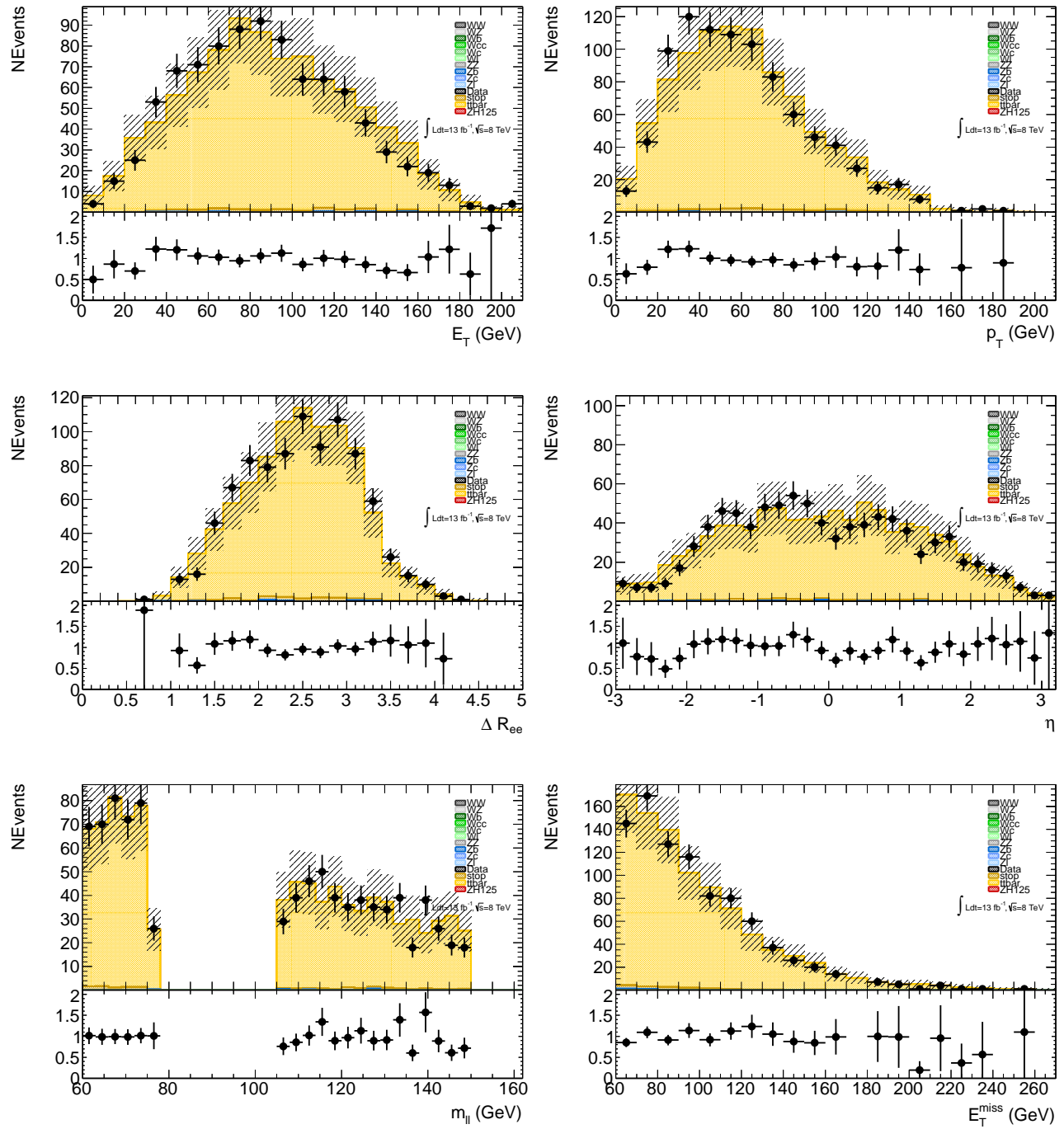


Figure 5.7: Distributions of the  $Z$  boson candidate in the top  $N_{b-jets} \geq 2$  and  $N_{electrons} = 2$  region after applying scale factors from the log-likelihood fit.

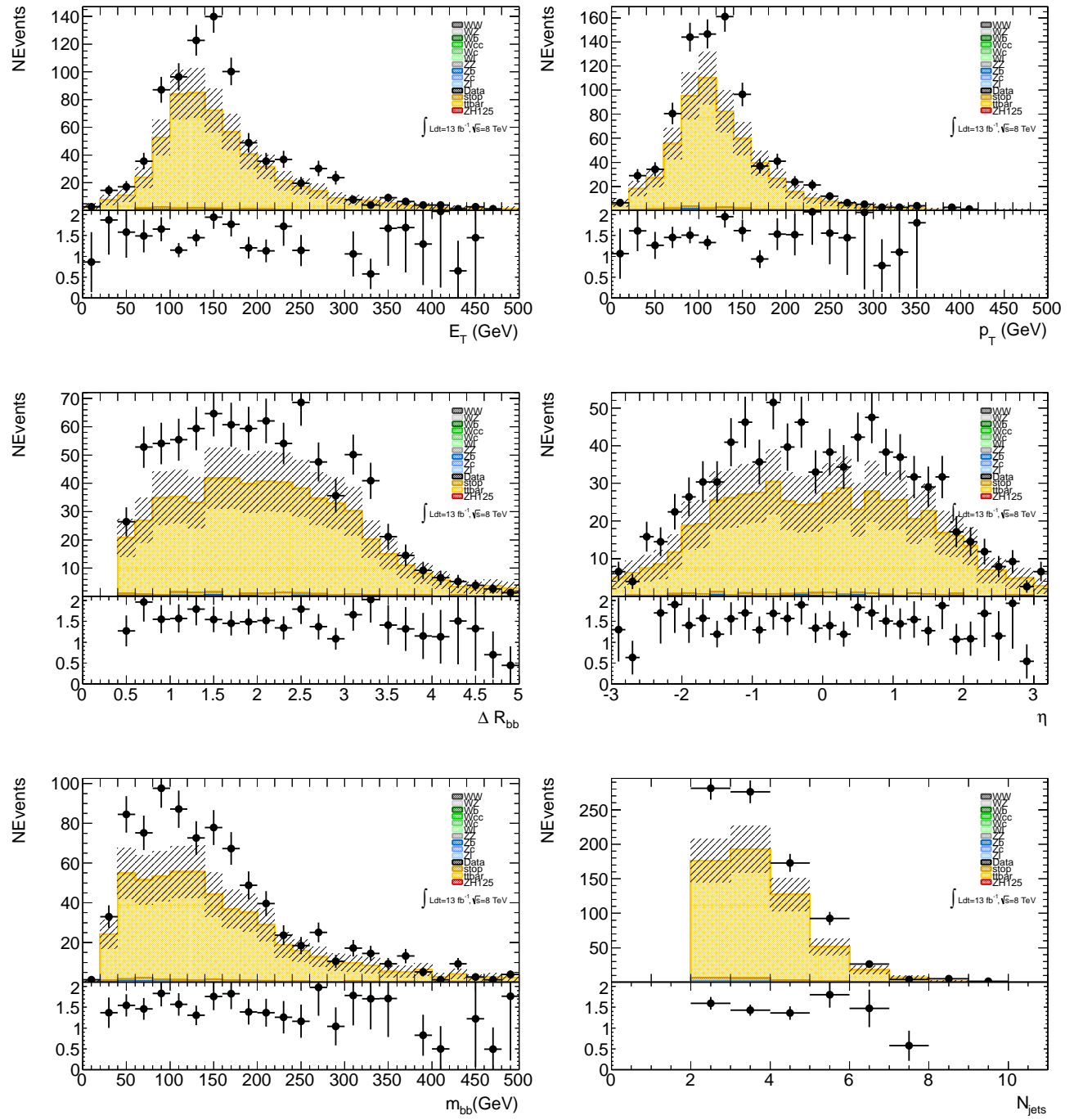


Figure 5.8: Distributions of the Higgs boson candidate in the top  $N_{b-jets} \geq 2$  and  $N_{muons} = 2$  region before applying scale factors from the log-likelihood fit.

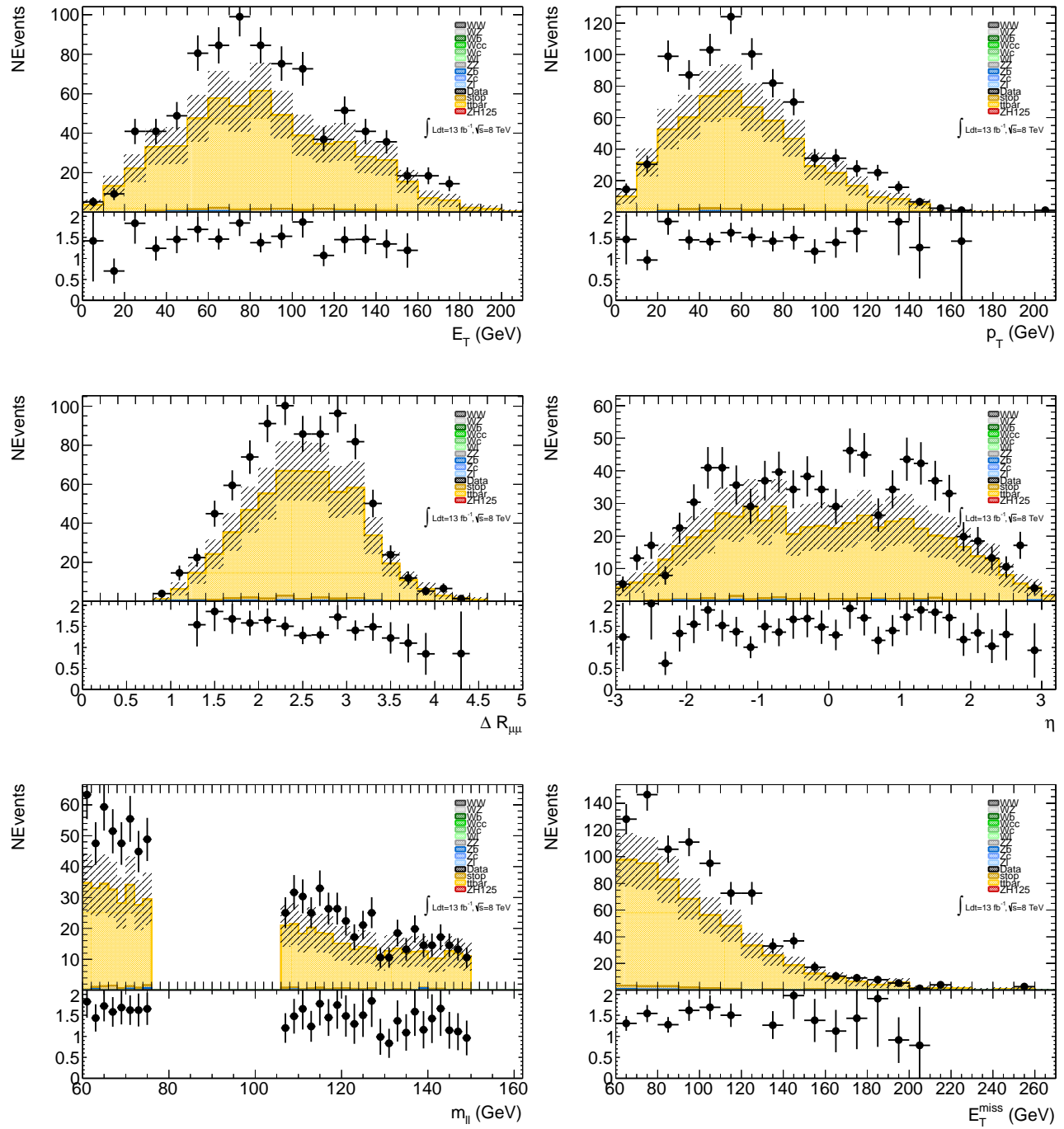


Figure 5.9: Distributions of the  $Z$  boson candidate in the top  $N_{b-jets} \geq 2$  and  $N_{muons} = 2$  region before applying scale factors from the log-likelihood fit.

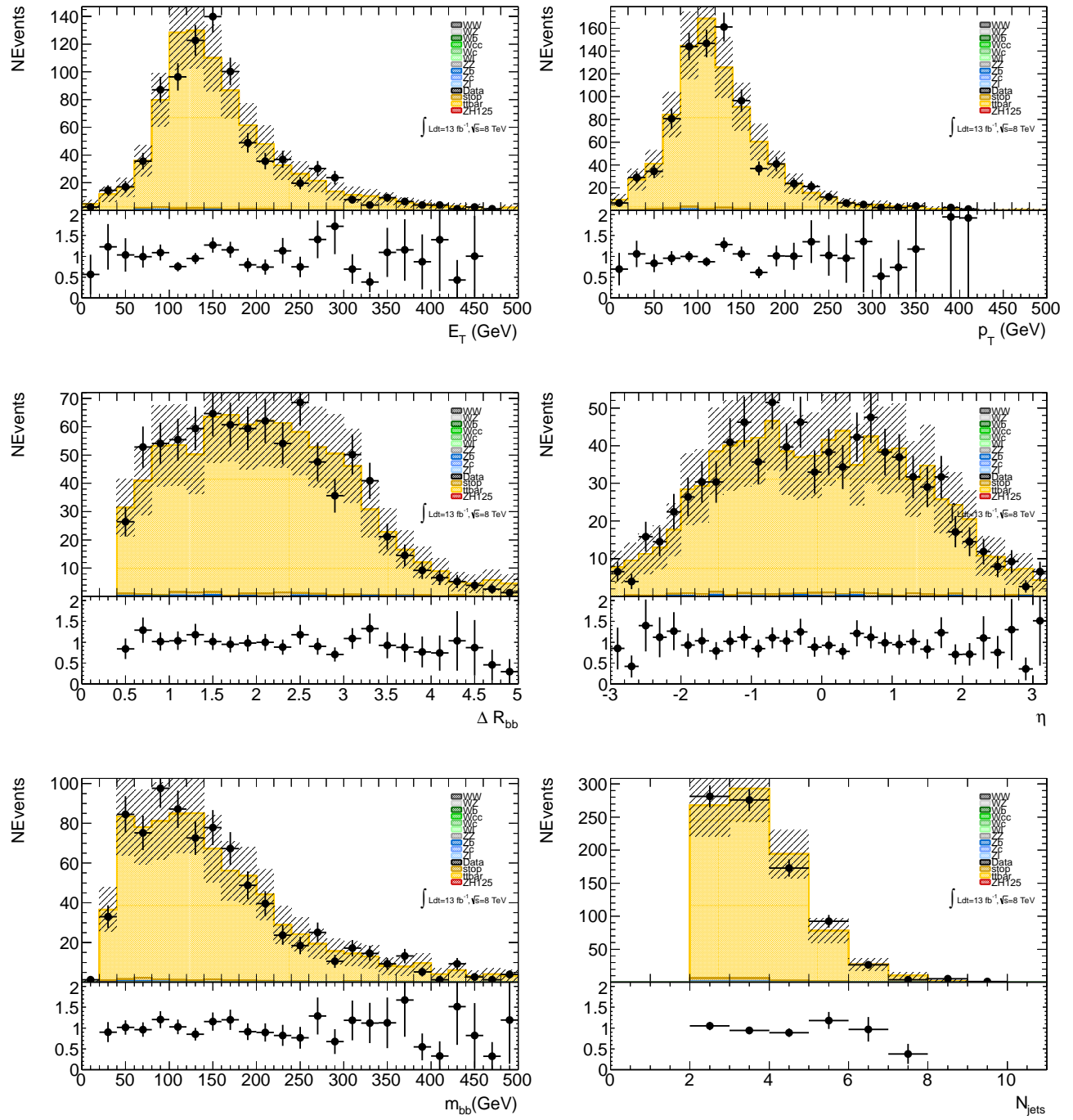


Figure 5.10: Distributions of the Higgs boson candidate in the top  $N_{b-jets} \geq 2$  and  $N_{muons} = 2$  region after applying scale factors from the log-likelihood fit.

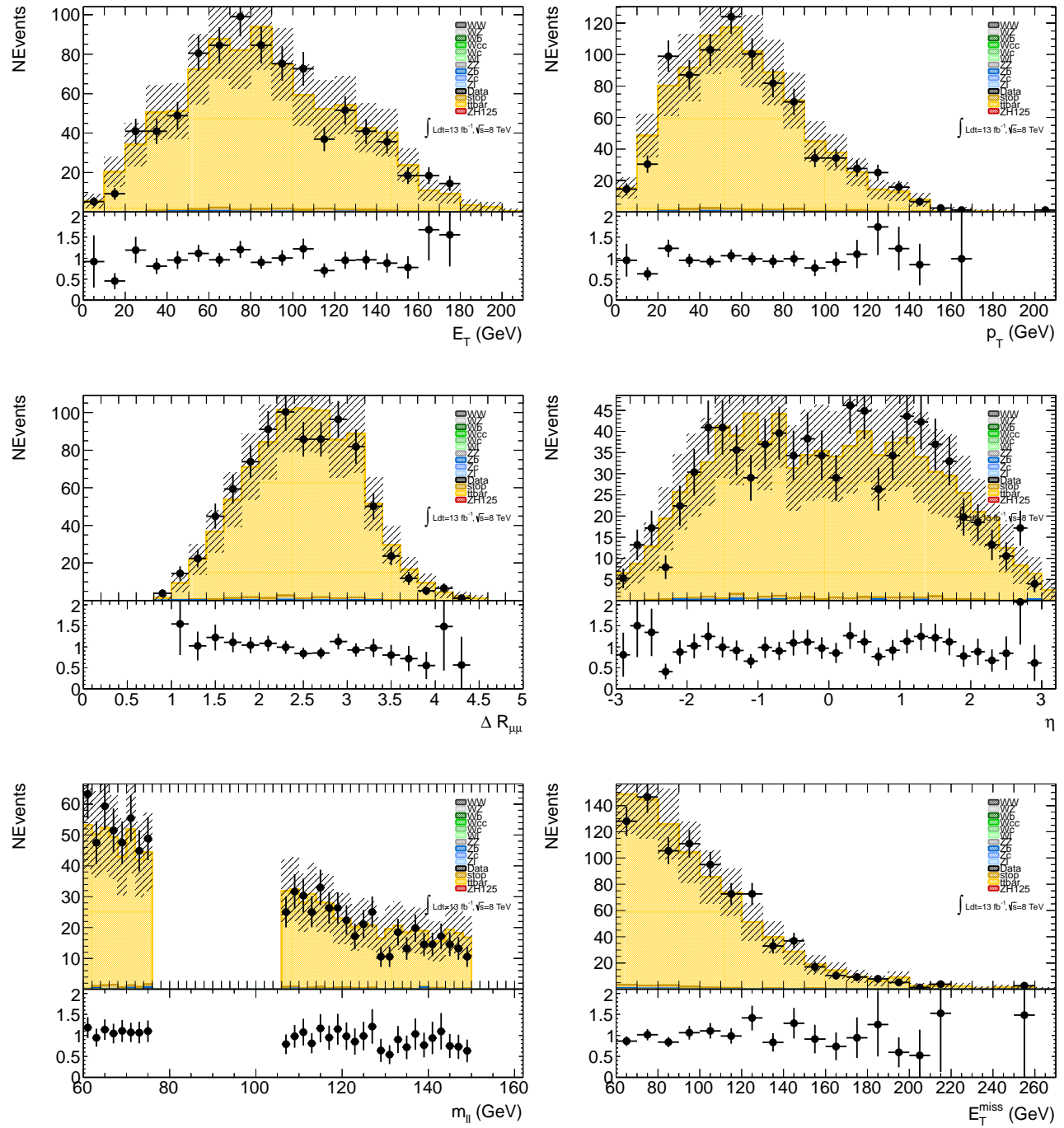


Figure 5.11: Distributions of the  $Z$  boson candidate in the top  $N_{b-jets} \geq 2$  and  $N_{muons} = 2$  region after applying scale factors from the log-likelihood fit.

### 5.5.3 Estimation of the $Z + jets$ Background

The  $Z + jets$  and Drell-Yan processes are the dominant backgrounds in the untagged region of the analysis, while the Drell-Yan and  $Z + heavy-jets$  processes are the main contributors to the tagged region. The background events are modelled using the *SHERPA* event generator and each jet is matched to a truth hadron –  $b$ -jets are matched within a  $\Delta R < 0.4$  to B-Hadrons,  $c$ -jets are matched within a  $\Delta R < 0.4$  to C-Hadrons and light jets are matched within  $\Delta R < 0.4$  to a hadron that is not a B or C hadron. The cross sections of the  $Z + light-jets$ ,  $Z + c-jets$  and  $Z + b-jets$  processes are not well modelled in the MC and therefore have large uncertainties. The normalisation of the Drell-Yan/ $Z + jets$  backgrounds are therefore constrained using control regions in data to obtain an accurate value for the cross sections. The control regions that have been defined for the Drell-Yan and  $Z + jets$  backgrounds take advantage of the number of  $b$ -jets in the event and truth matching of the jets to a hadron. The two regions selected are events containing only  $N_{b-jets} = 1$  and  $N_{b-jets} = 0$  in the  $m_{b\bar{b}}$  distribution. A simultaneous maximum log-likelihood fit is applied to the  $m_{b\bar{b}}$  distribution on both the  $N_{b-jets} = 1$  and  $N_{b-jets} = 0$  events, where  $Z + c-jets$  and  $Z + b-jets$  processes are allowed to freely float in  $N_{b-jets} = 1$  events and are constrained by their systematics in  $N_{b-jets} = 0$  events. Similarly,  $Z + light-jets$  and  $Z + c-jets$  processes are allowed to freely float in  $N_{b-jets} = 0$  events and are constrained by their systematics in  $N_{b-jets} = 1$  events. The fits are separated into the electron and muon channels and the corresponding scale factors are compared to each other to validate consistency between the two channels. The  $N_{b-jets} = 1$  region from Table 5.10 shows the purity of  $Z + light-jets$ ,  $Z + c-jets$

and  $Z + b$ -*jets* of 12.4%, 9% and 75.6% respectively, while the  $N_{b-jets} = 0$  region from Table 5.12 shows a purity of  $Z + light$ -*jets*,  $Z + c$ -*jets* and  $Z + b$ -*jets* of 12.4%, 9% and 75.6% respectively. The corresponding scale factors and the statistical and systematic uncertainties derived from the fit for the electron and muon channels are shown on Table 5.11. The scale factors are consistent between the electron and muon channels, with the  $t\bar{t}$  background acquiring the largest scale factor followed by the  $Zb$ ,  $Zc$  and  $Zl$  backgrounds. The scale factors are applied to the pre-fit Figures 5.12, 5.13, 5.20, 5.21, 5.16, 5.17, 5.24 and 5.25. From the applied scale factors we see improved modelling between MC and data, which is shown in Figures 5.14, 5.15, 5.22, 5.23, 5.18, 5.19, 5.26 and 5.27. Uncertainties placed on the scale factors show the degree of uncertainty due to statistical and systematic limits on the analysis. In conclusion the electron and muon channels are consistent in the  $N_{b-jets} = 1$  and  $N_{b-jets} = 0$  regions.

Table 5.10: The number of selected signal (S), background (B) and data events for the control region  $N_{b-jets} = 1$  before and after the log-likelihood fit.

	<b>Process</b>	$e^+e^-b\bar{b}$	$\mu^+\mu^-b\bar{b}$
	<i>data</i>	$7159 \pm 85$	$6210 \pm 79$
<i>MC Signal</i>	<i>ZH125</i>	$10.8 \pm 0.1^{+1.0}_{-1.0}$	$10.8 \pm 0.1^{+1.1}_{-1.1}$
	<i>Wb</i>	$0 \pm 0$	$0 \pm 0$
	<i>Wcc</i>	$0 \pm 0$	$0 \pm 0$
	<i>Wc</i>	$9.16 \pm 4.10^{+1.07}_{-1.19}$	$0 \pm 0$
	<i>Wl</i>	$0 \pm 0$	$0 \pm 0$
Constrained background	<i>stop</i>	$13.6 \pm 0.7^{+1.7}_{-1.4}$	$12.9 \pm 0.7^{+1.4}_{-2.7}$
	<i>ZZ</i>	$85.2 \pm 2.1^{+9.7}_{-10.0}$	$81.3 \pm 2.1^{+11.6}_{-10.6}$
	<i>WZ</i>	$58.2 \pm 2.1^{+6.7}_{-6.6}$	$57.7 \pm 2.0^{+7.0}_{-6.9}$
	<i>WW</i>	$0.47 \pm 0.21^{+0.05}_{-0.05}$	$0.56 \pm 0.23^{+0.07}_{-0.07}$
	<i>t̄t</i>	$180 \pm 4^{+18}_{-27}$	$154 \pm 3^{+15}_{-25}$
	<i>Zb</i>	$3930 \pm 26^{+470}_{-430}$	$3330 \pm 21^{+400}_{-410}$
Non-constrained pre-fit	<i>Zc</i>	$446 \pm 49^{+51}_{-50}$	$494 \pm 51^{+60}_{-59}$
	<i>Zl</i>	$645 \pm 57^{+77}_{-71}$	$728 \pm 62^{+72}_{-131}$
	$\frac{\text{data}}{S+B}$	$1.33 \pm 0.07$	$1.27 \pm 0.08$
	<i>t̄t</i>	$285 \pm 5^{+28}_{-42}$	$236 \pm 5^{+24}_{-38}$
	<i>Zb</i>	$5420 \pm 36^{+630}_{-620}$	$4434 \pm 28^{+530}_{-550}$
Non-constrained post-fit	<i>Zc</i>	$437 \pm 48^{+51}_{-50}$	$489 \pm 50^{+60}_{-59}$
	<i>Zl</i>	$812 \pm 72^{+95}_{-93}$	$880 \pm 75^{+85}_{-156}$
	$\frac{\text{data}}{S+B}$	$1.0 \pm 0.1$	$1.0 \pm 0.9$

Table 5.11: Scale factors for the  $t\bar{t}$ ,  $Z+light-jets$ ,  $Z+c-jets$  and  $Z+b-jets$  processes.

<b>Process</b>	$e^+e^-b\bar{b}$ <b>Scale Factors</b>	$\mu^+\mu^-b\bar{b}$ <b>Scale Factors</b>
$t\bar{t}$	$1.59 \pm 0.21$	$1.54 \pm 0.19$
$Zb$	$1.38 \pm 0.18$	$1.33 \pm 0.17$
$Zc$	$0.98 \pm 0.12$	$0.99 \pm 0.12$
$Zl$	$1.26 \pm 0.17$	$1.21 \pm 0.16$

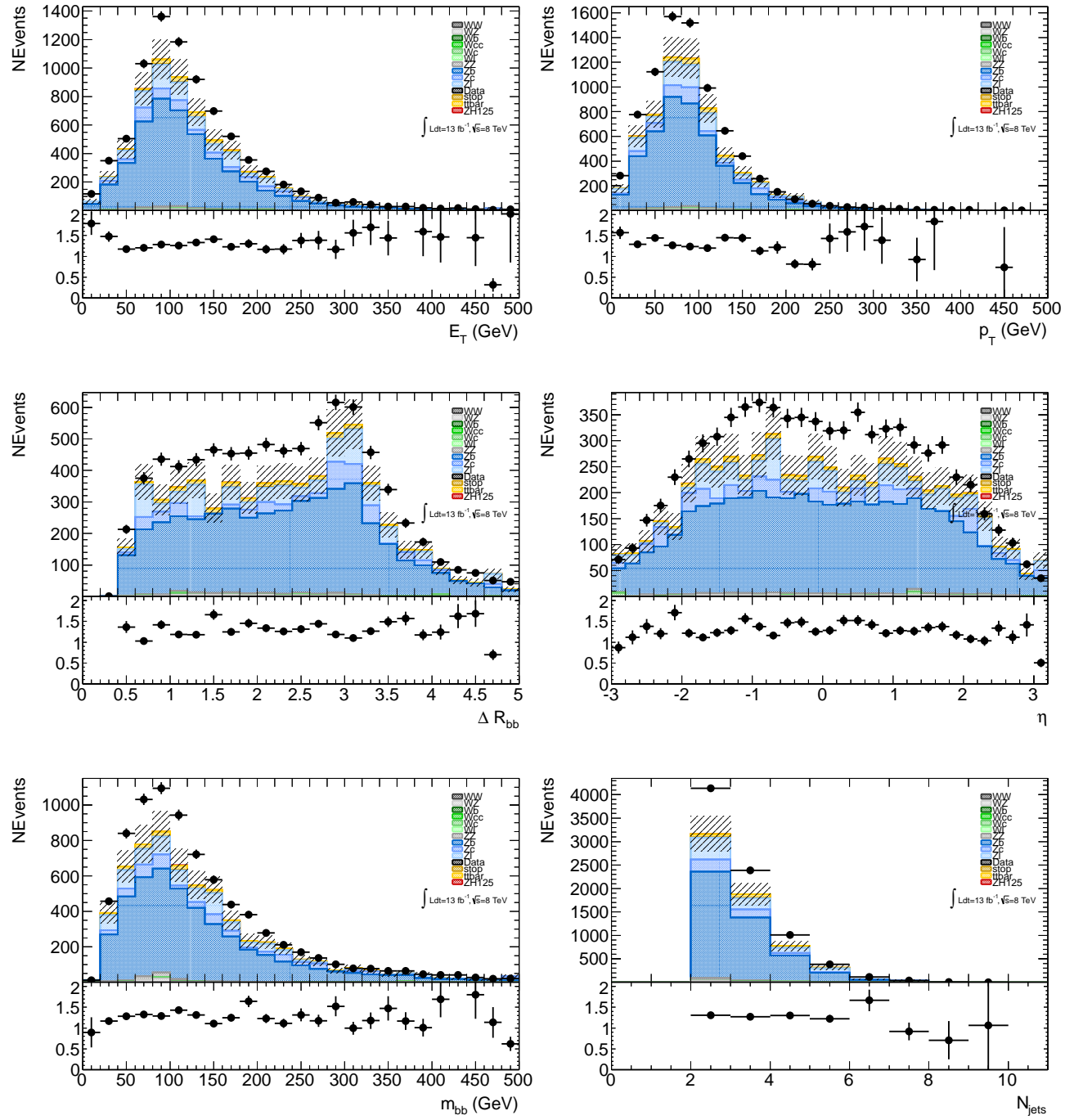


Figure 5.12: Higgs boson candidate distributions in the control  $N_{b-jets} = 1$  and  $N_{electrons} = 2$  region before applying scale factors from the log-likelihood fit.

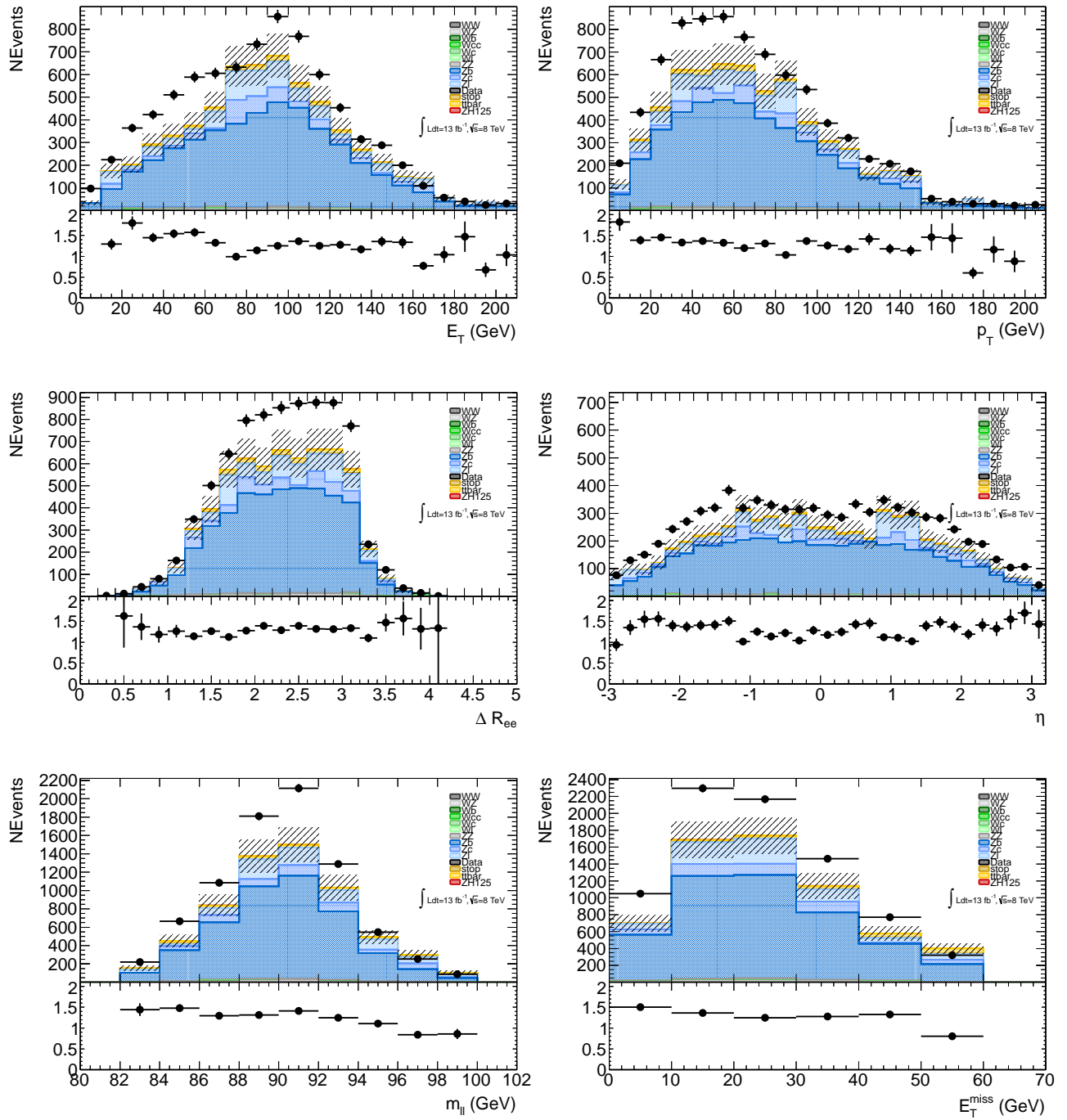


Figure 5.13:  $Z$  boson candidate distributions in the control  $N_{b-jets} = 1$  and  $N_{electrons} = 2$  region before applying scale factors from the log-likelihood fit.

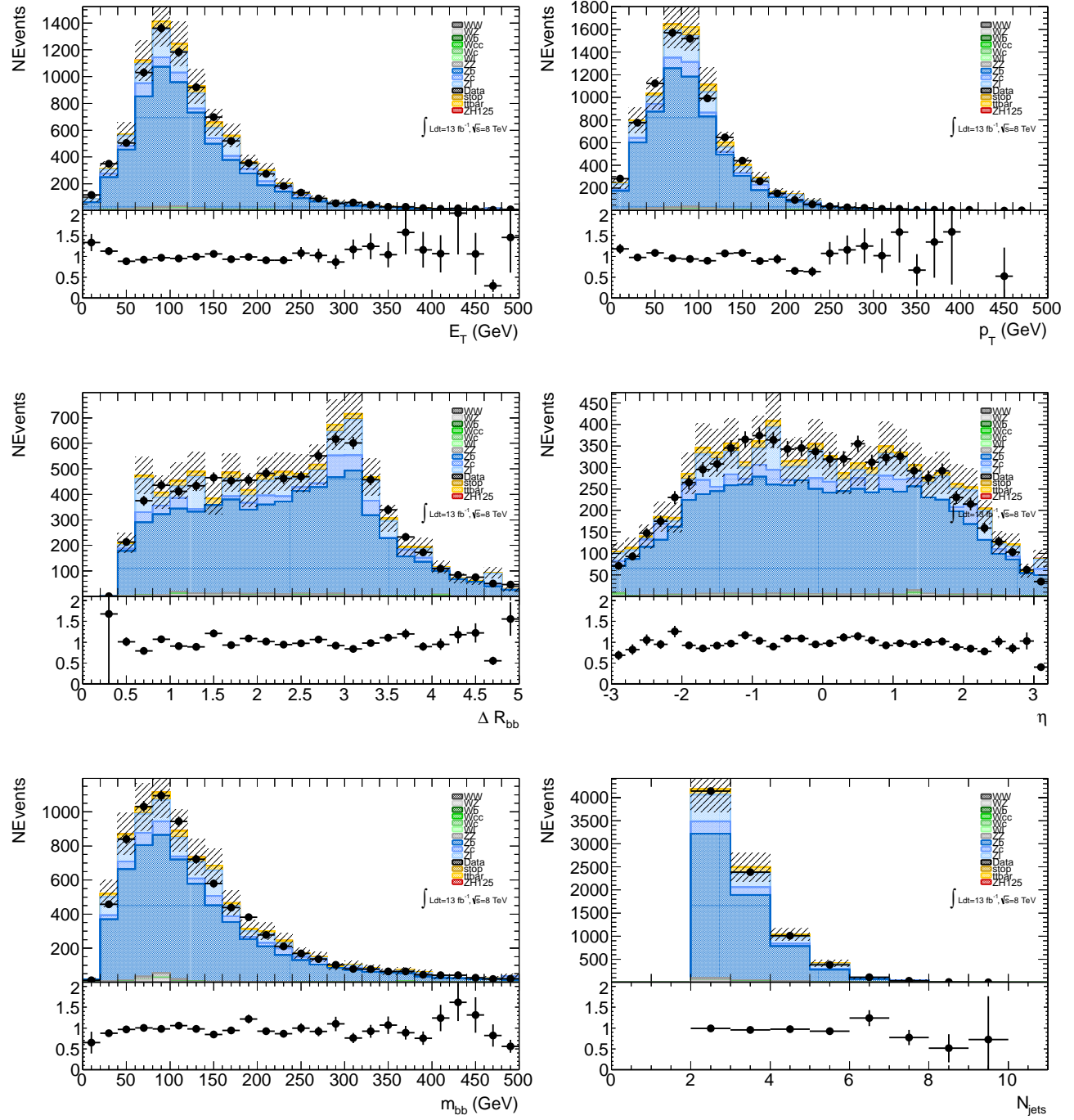


Figure 5.14: Higgs boson candidate distributions in the control  $N_{b-jets} = 1$  and  $N_{electrons} = 2$  region after applying scale factors from the log-likelihood fit.

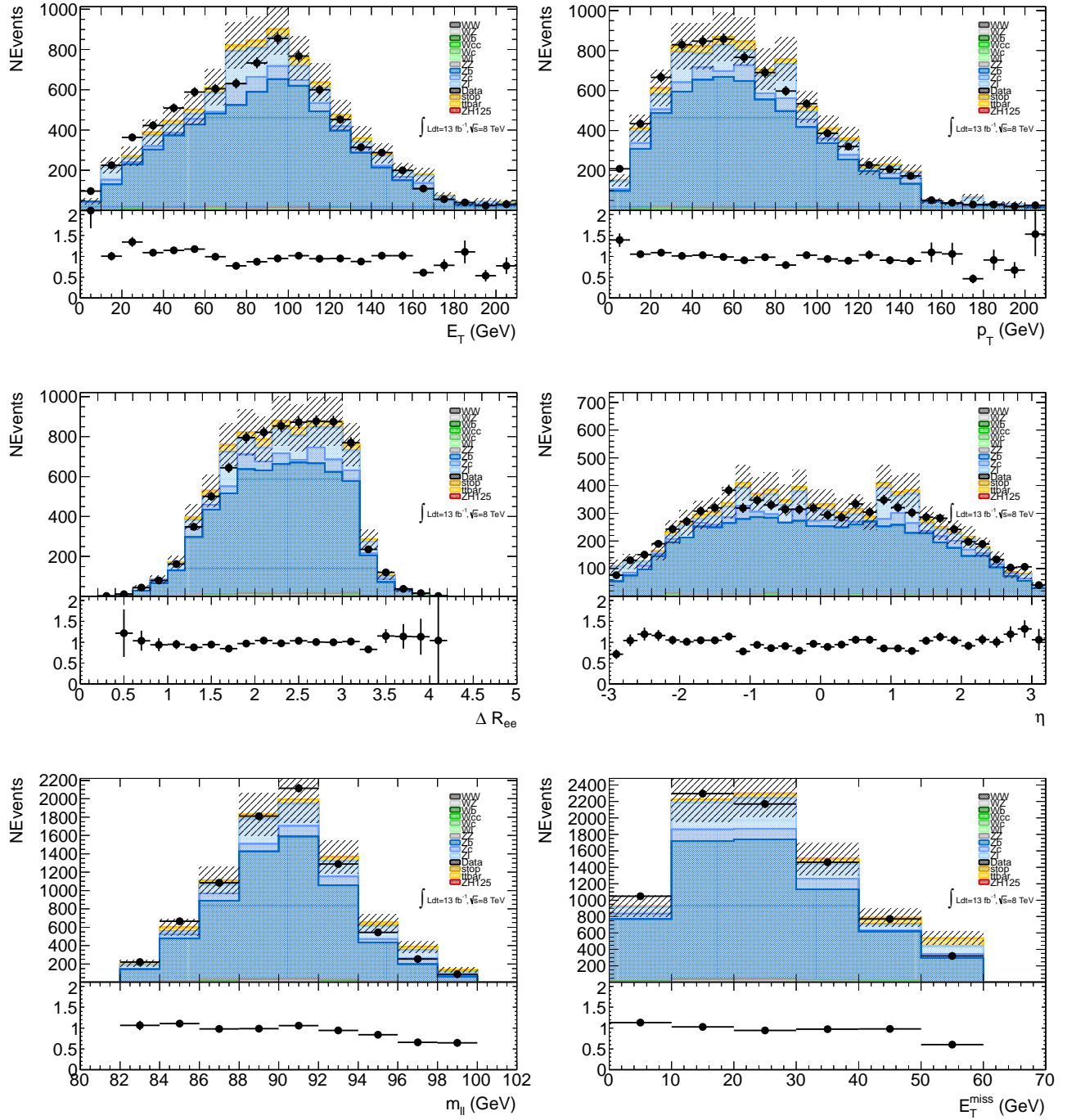


Figure 5.15:  $Z$  boson candidate distributions in the control  $N_{b-jets} = 1$  and  $N_{electrons} = 2$  region after applying scale factors from the log-likelihood fit.

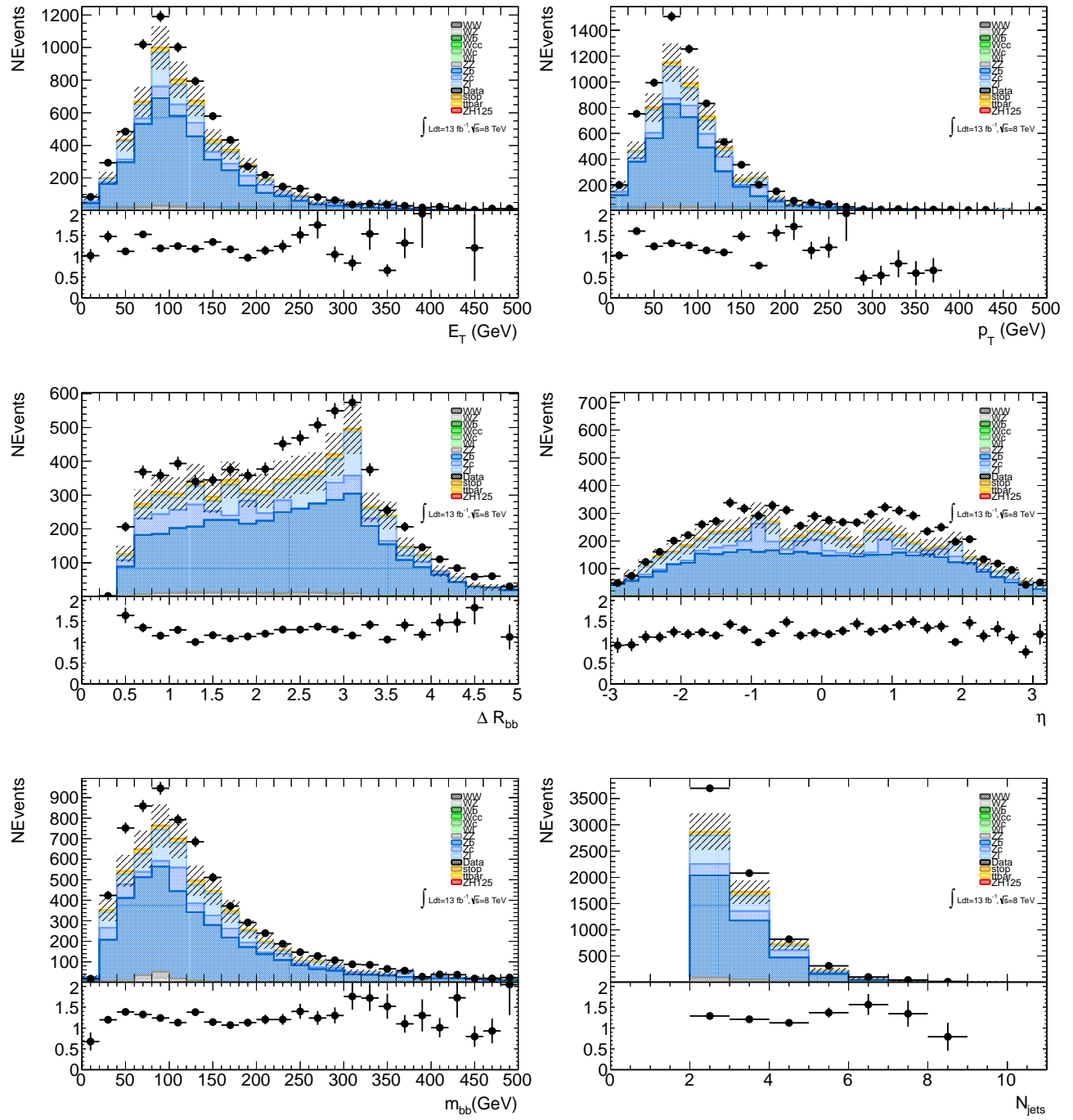


Figure 5.16: Higgs boson candidate distributions in the control  $N_{b-jets} = 1$  and  $N_{muons} = 2$  region before applying scale factors from the log-likelihood fit.

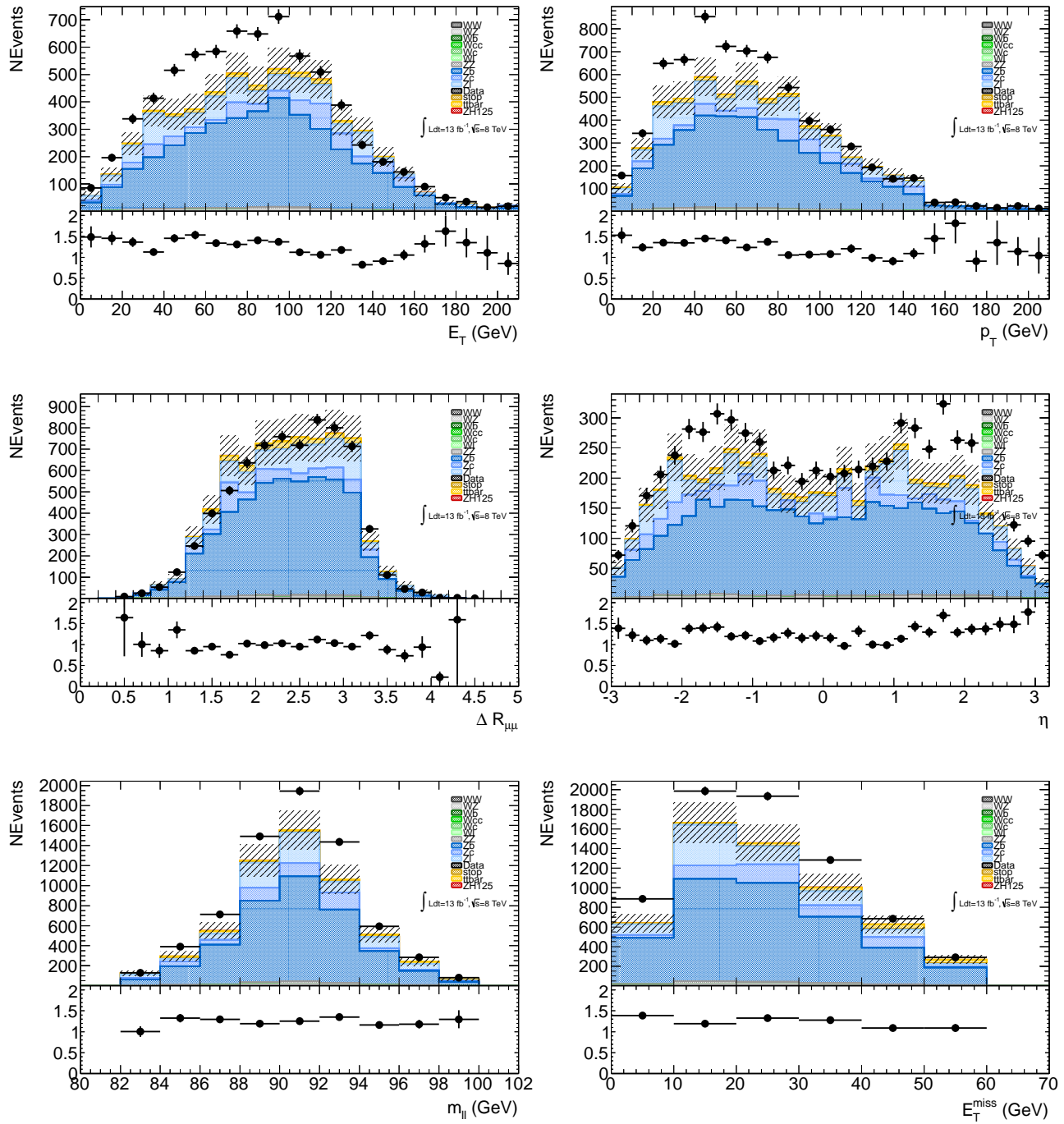


Figure 5.17:  $Z$  boson candidate distributions in the control  $N_{b-jets} = 1$  and  $N_{muons} = 2$  region before applying scale factors from the log-likelihood fit.

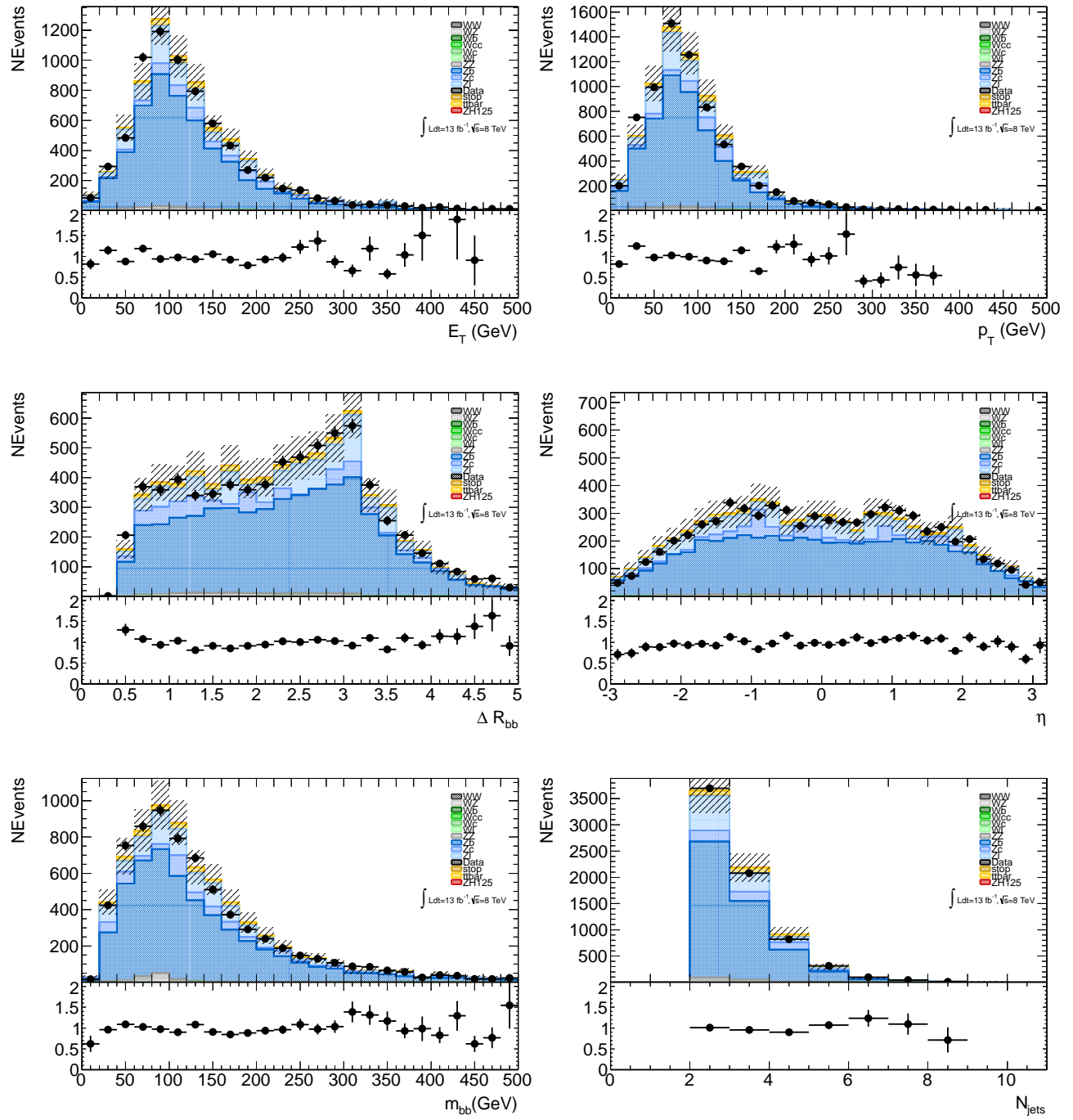


Figure 5.18: Higgs boson candidate distributions in the control  $N_{b-jets} = 1$  and  $N_{muons} = 2$  region after applying scale factors from the log-likelihood fit.

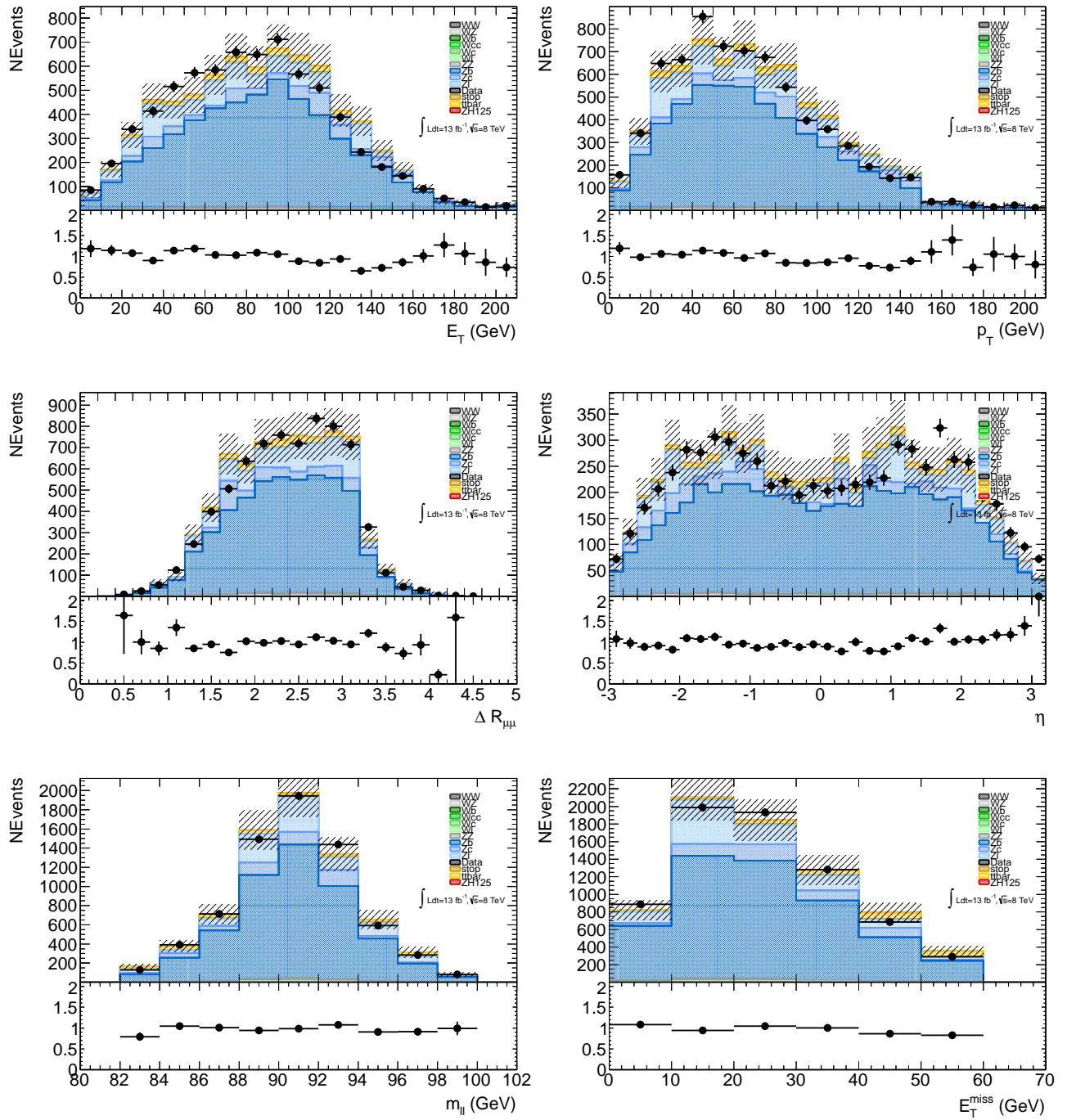


Figure 5.19:  $Z$  boson candidate distributions in the control  $N_{b-jets} = 1$  and  $N_{muons} = 2$  region after applying scale factors from the log-likelihood fit.

Table 5.12: The number of selected signal (S), background (B) and data events for the control region  $N_{b-jets} = 0$  before and after the log-likelihood fit. The data and MC ratio is also shown for the  $N_{b-jets} = 0$  region before and after the fit.

	<b>Process</b>	$e^+e^-b\bar{b}$	$\mu^+\mu^-b\bar{b}$
	<i>data</i>	$36809 \pm 192$	$43610 \pm 209$
<i>MC Signal</i>	$ZH125$	$2.54 \pm 0.06^{+0.21}_{-0.21}$	$2.65 \pm 0.06^{+0.24}_{-0.23}$
Constrained background	$Wb$	$1.8 \pm 1.8^{+0.19}_{-0.17}$	$0 \pm 0$
	$Wcc$	$0 \pm 0$	$0 \pm 0$
	$Wc$	$74.7 \pm 23.6^{+8.0}_{-7.5}$	$0 \pm 0$
	$Wl$	$67.8 \pm 12.4^{+7.3}_{-6.6}$	$1.34 \pm 0.95^{+0.14}_{-0.14}$
	$stop$	$3.87 \pm 0.39^{+0.66}_{-1.04}$	$5.32 \pm 0.55^{+0.54}_{-0.82}$
	$ZZ$	$226 \pm 3^{+24}_{-22}$	$251 \pm 4^{+27}_{-26}$
	$WZ$	$291 \pm 5^{+30}_{-30}$	$328 \pm 5^{+34}_{-35}$
Non-constrained pre-fit	$t\bar{t}$	$40.4 \pm 1.8^{+4.0}_{-4.9}$	$41.0 \pm 1.9^{+5.7}_{-2.9}$
	$Zb$	$980 \pm 13^{+110}_{-110}$	$1100 \pm 13^{+120}_{-110}$
	$Zc$	$1950 \pm 110^{+180}_{-280}$	$2410 \pm 120^{+300}_{-200}$
	$Zl$	$25800 \pm 370^{+2580}_{-2685}$	$32200 \pm 440^{+3550}_{-3530}$
Non-constrained post-fit	$\frac{data}{S+B}$	$1.25 \pm 0.06$	$1.20 \pm 0.06$
	$t\bar{t}$	$64.2 \pm 2.9^{+6.2}_{-7.7}$	$63.2 \pm 2.9^{+8.8}_{-4.4}$
	$Zb$	$1350 \pm 20^{+150}_{-140}$	$1440 \pm 20^{+160}_{-150}$
	$Zc$	$1911 \pm 108^{+177}_{-282}$	$2386 \pm 119^{+300}_{-200}$
	$Zl$	$32500 \pm 470^{+3270}_{-3370}$	$37960 \pm 530^{+4300}_{-4270}$
	$\frac{data}{S+B}$	$1.01 \pm 0.08$	$1.04 \pm 0.08$

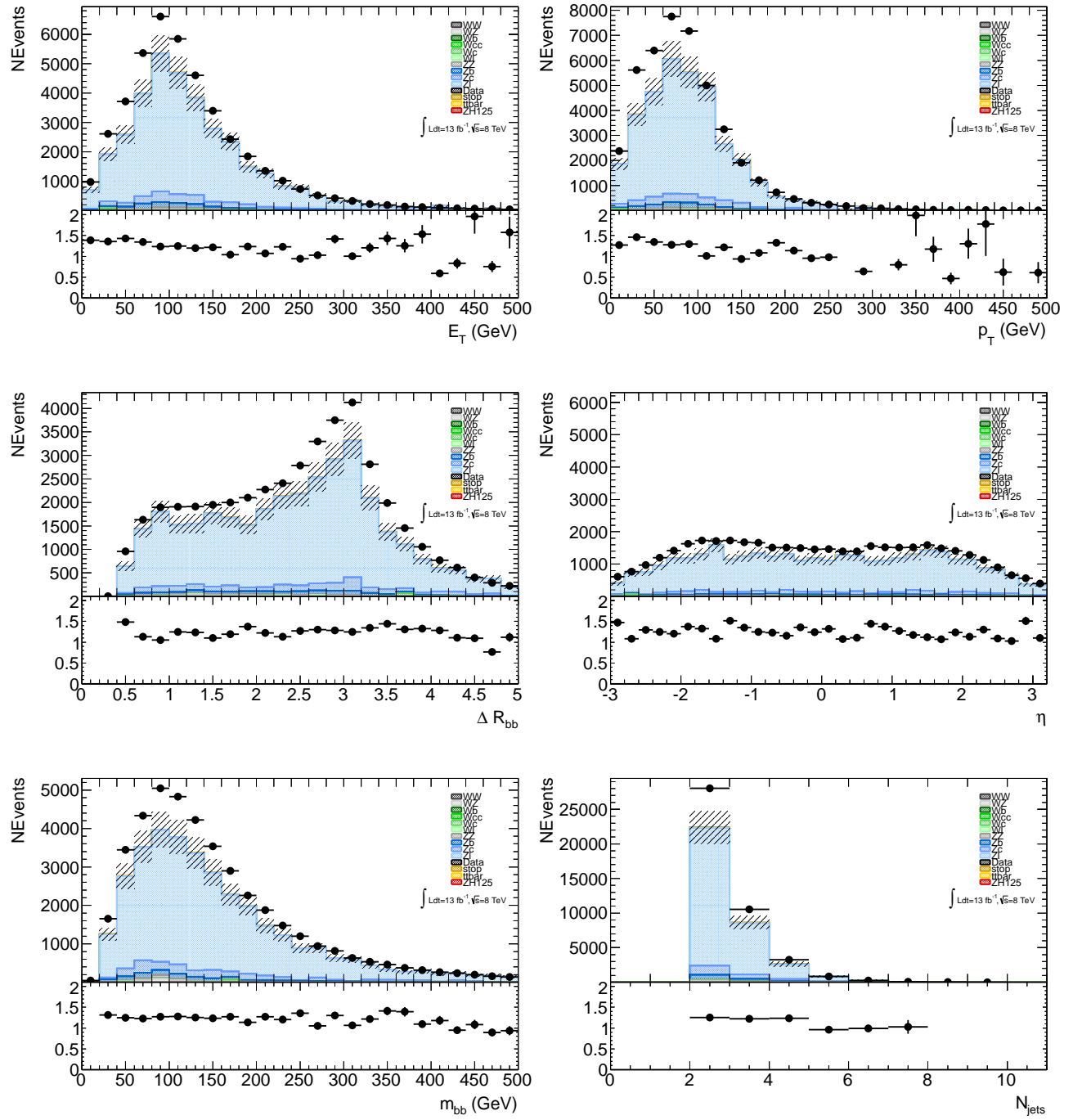


Figure 5.20: Higgs boson candidate distributions in the control  $N_{b-jets} = 0$  and  $N_{electrons} = 2$  region before applying scale factors from the log-likelihood fit.

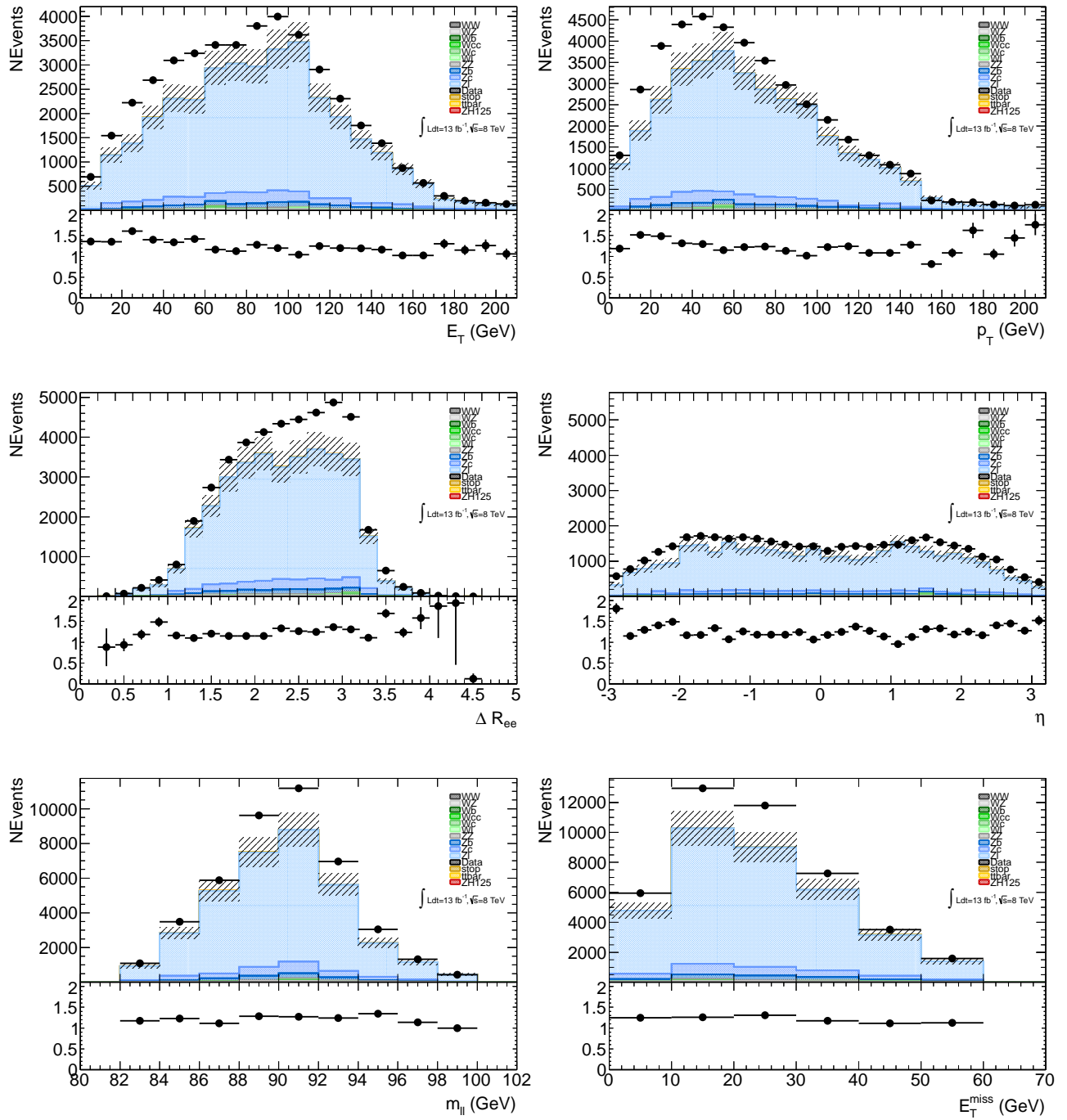


Figure 5.21:  $Z$  boson candidate distributions in the control  $N_{b-jets} = 0$  and  $N_{electrons} = 2$

region before applying scale factors from the log-likelihood fit.

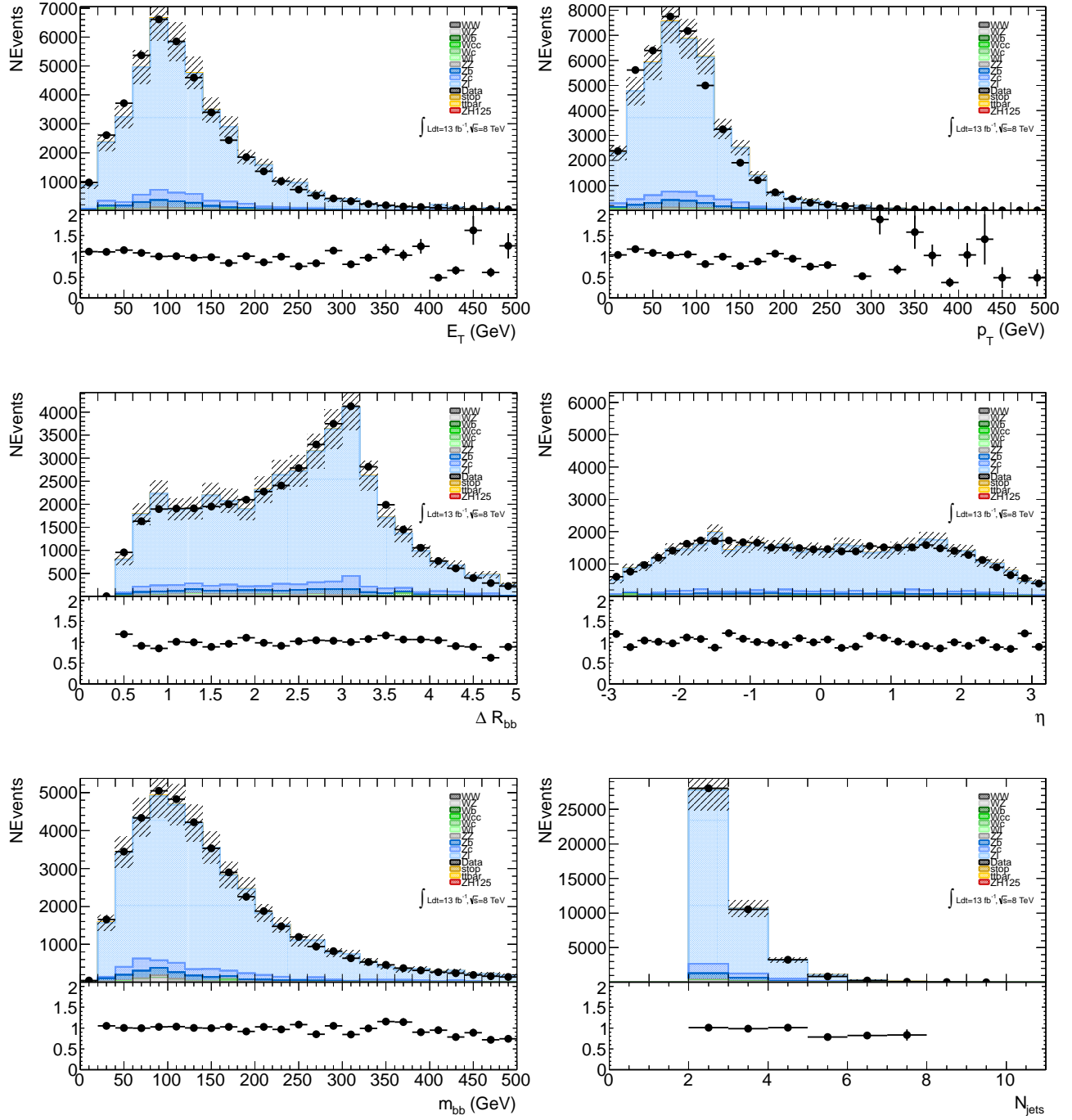


Figure 5.22: Higgs boson candidate distributions in the control  $N_{b-jets} = 0$  and  $N_{electrons} = 2$  region after applying scale factors from the log-likelihood fit.

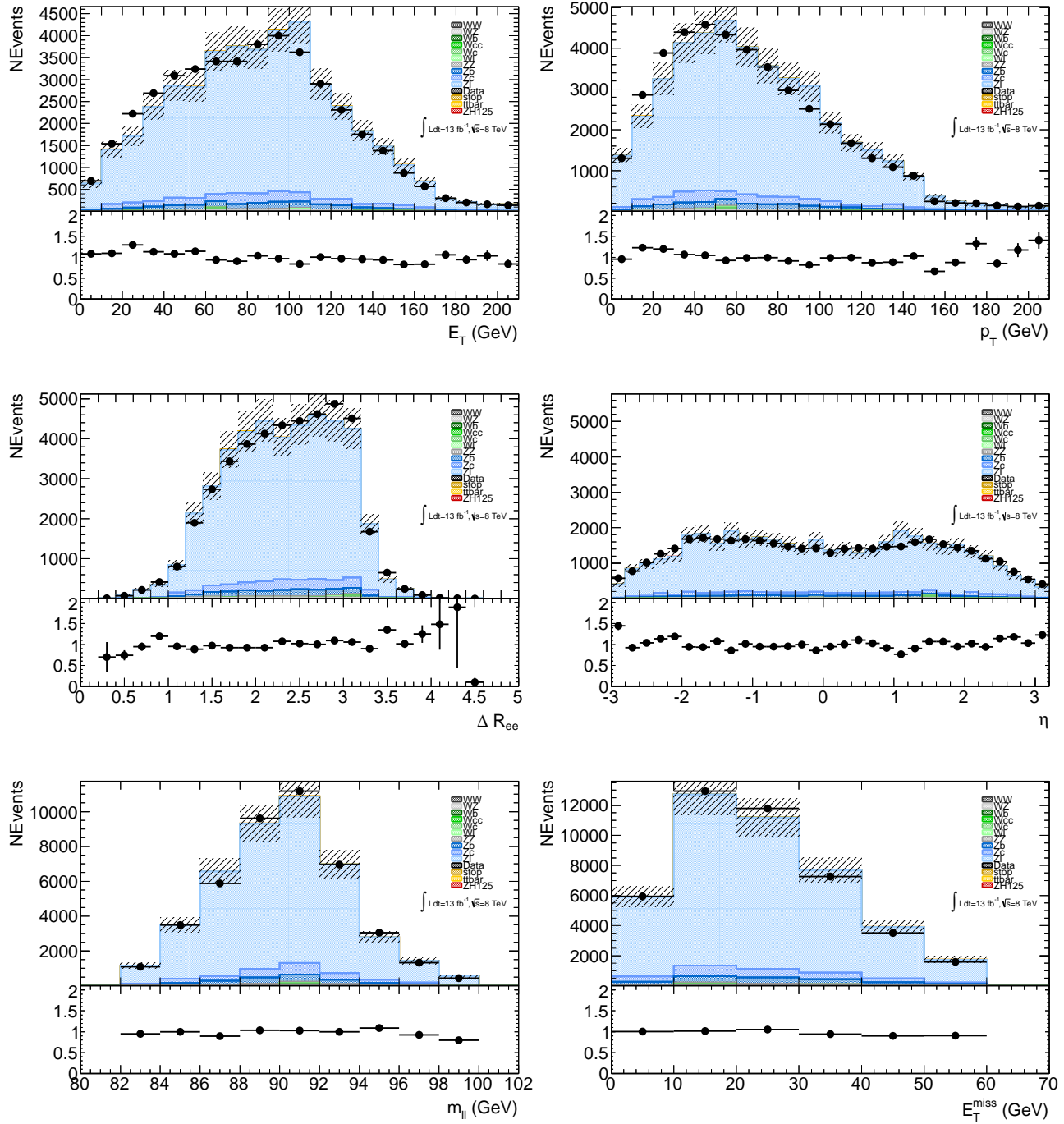


Figure 5.23:  $Z$  boson candidate distributions in the control  $N_{b-jets} = 0$  and  $N_{electrons} = 2$

region after applying scale factors from the log-likelihood fit.

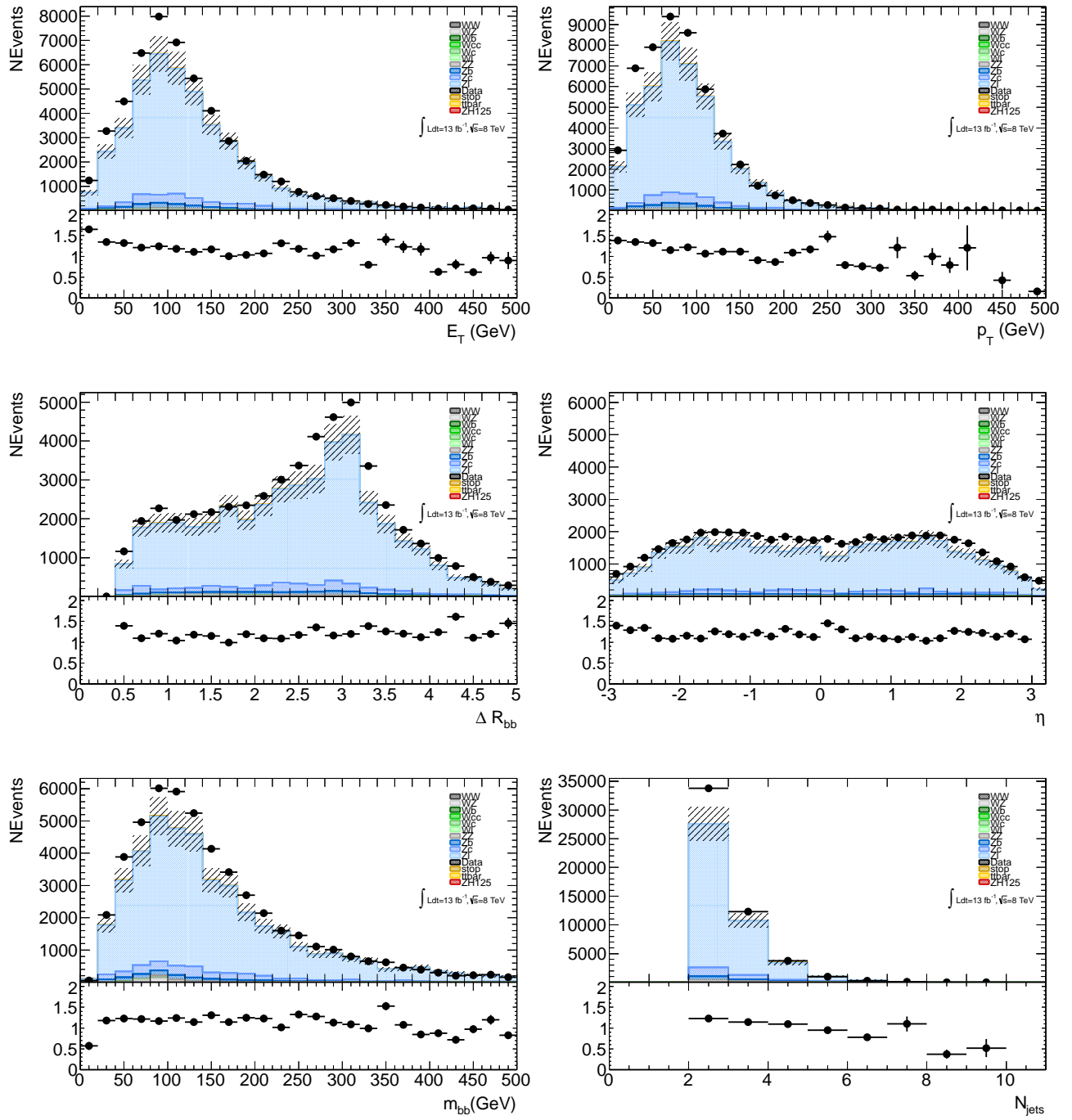


Figure 5.24: Higgs boson candidate distributions in the control  $N_{b-jets} = 0$  and  $N_{muons} = 2$  region before applying scale factors from the log-likelihood fit.

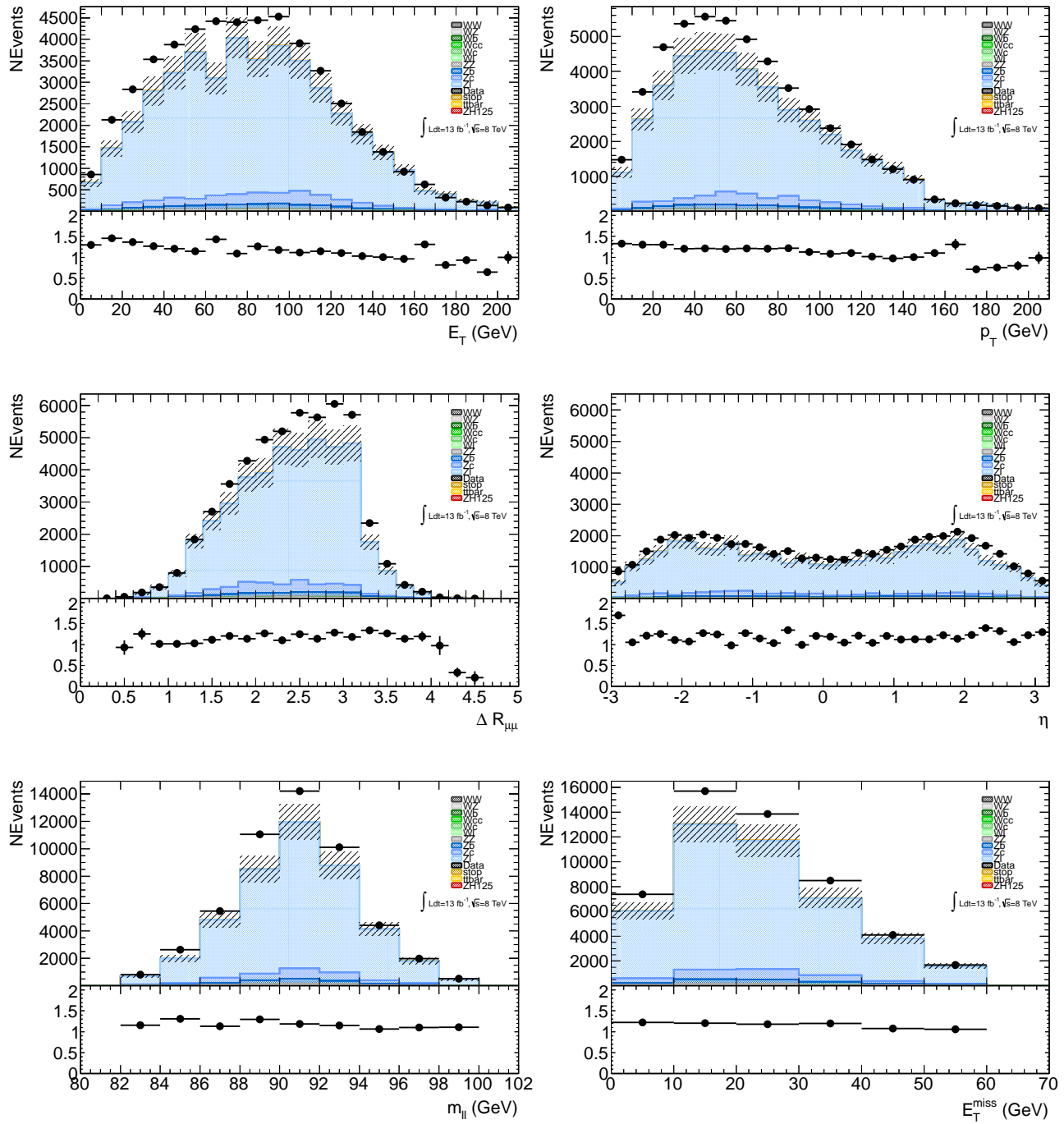


Figure 5.25:  $Z$  boson candidate distributions in the control  $N_{b-jets} = 0$  and  $N_{muons} = 2$  region before applying scale factors from the log-likelihood fit.

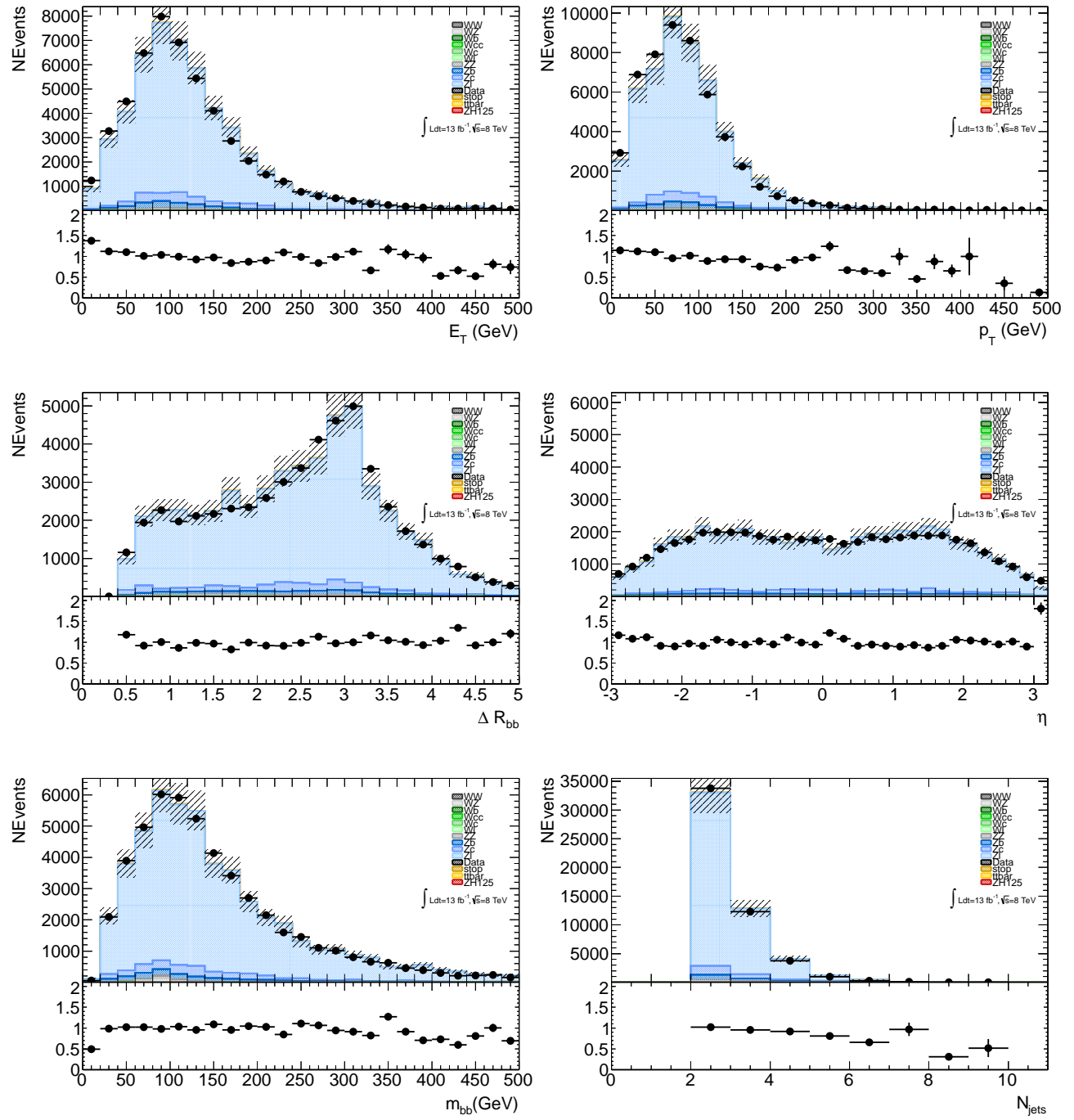


Figure 5.26: Higgs boson candidate distributions in the control  $N_{b-jets} = 0$  and  $N_{muons} = 2$  region after applying scale factors from the log-likelihood fit.

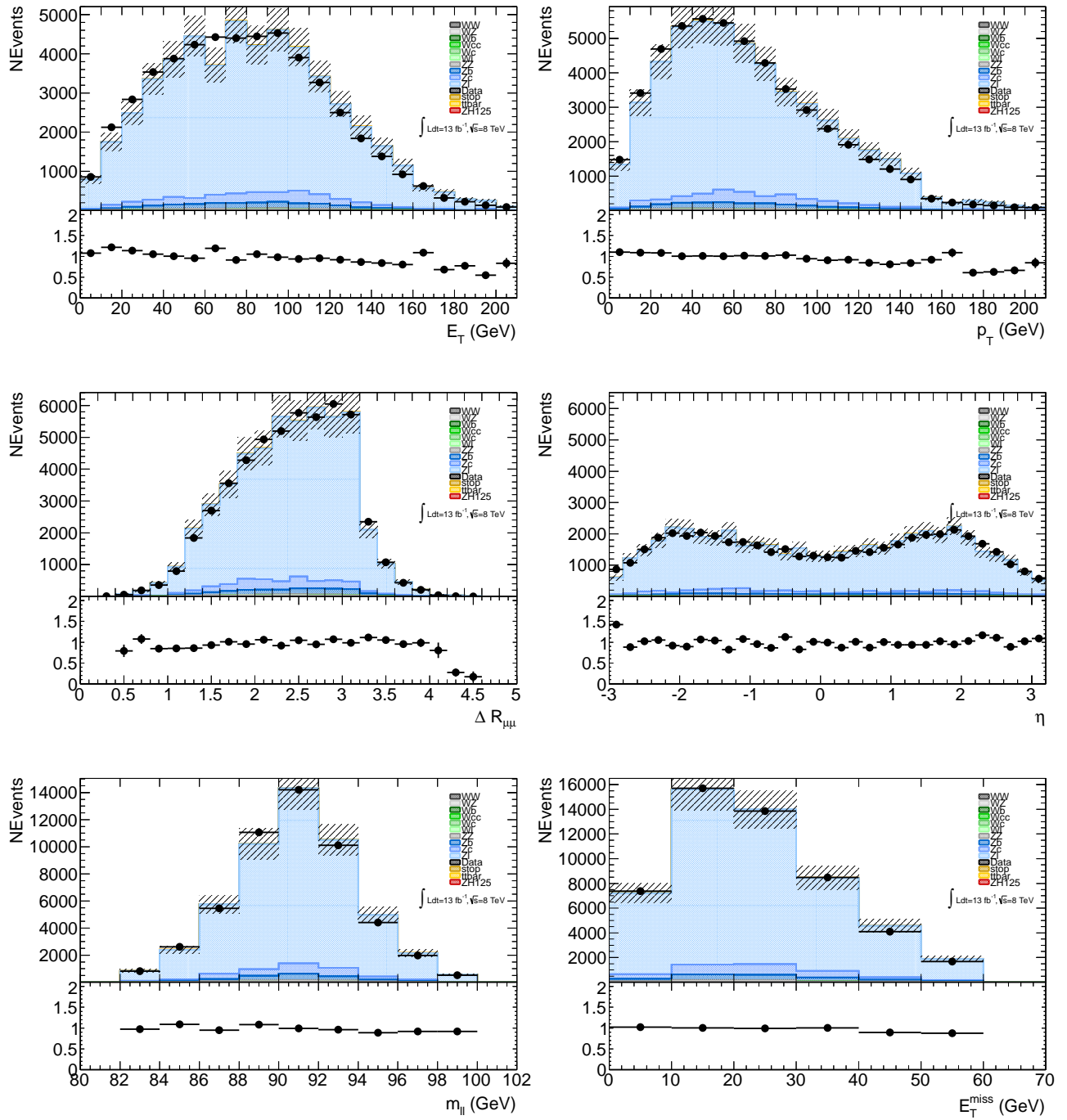


Figure 5.27:  $Z$  boson candidate distributions in the control  $N_{b-jets} = 0$  and  $N_{muons} = 2$  region after applying scale factors from the log-likelihood fit.

## 5.6 Control Regions

Control regions in the analysis are used to determine flavour composition of the  $Z + jets$  background in the  $N_{b-jets} = 0$  and  $N_{b-jets} = 1$  region, the top normalisation in the top region and the *multi-jet* contribution in the *multi-jet* data region (see Sections 5.5.3, 5.5.2 and 5.5.1 respectively for more details). The control regions are also used to determine the agreement between data and MC. This is achieved by first estimating the best fit between data and MC for the control regions stated above and then applying the derived scale factors and distributions to a new set of validation control regions. The validation control regions chosen are the pre-tagged  $N_{b-jets} \geq 0$  region and the 1-tagged  $N_{b-jets} \geq 1$  region. The control regions are chosen to be similar to the signal region to minimise the extrapolation from different analysis regions, which can add further uncertainties to the analysis. All distributions for the validation control regions are shown before and after scale factor normalisation. The full statistical and systematic uncertainties are also shown in the distributions to visually aid the agreement between data and MC.

### 5.6.1 Pretag Control Region

The events that have passed the pre-tag  $N_{b-jets} \geq 0$  control region, have also passed the selection cuts in Section 5.4, with exception to the requirement on the *b*-tagging, which has been relaxed. Figures from 5.28 to 5.35 and Table 5.13 show clearly that the pre-tag region is dominated by the  $Z + light-jet$  background (80% purity), while the  $Z + b-jets$ ,  $Z + c-jets$  and top background have a contribution of 13%, 6% and 1% respectively. Figures 5.30, 5.31, 5.34 and 5.35 show good agreement between data

and MC after the fit, when we take the statistical and systematic fluctuations into account. Due to the high statistics in the pre-tagged region the dominating factor for the uncertainty comes from the systematic fluctuations, which are discussed in Section 5.7.

Table 5.13: The number of selected signal (S), background (B) and data events for the control region  $N_{b-jets} \geq 0$  before and after the log-likelihood fit.

	<b>Process</b>	$e^+e^-b\bar{b}$	$\mu^+\mu^-b\bar{b}$
	<i>data</i>	$54458 \pm 233$	$51169 \pm 226$
<i>MC Signal</i>	<i>ZH125</i>	$20.9 \pm 0.2^{+1.9}_{-1.7}$	$21.2 \pm 0.2^{+2.0}_{-1.7}$
	<i>Wb</i>	$1.8 \pm 1.8^{+0.2}_{-0.2}$	$0 \pm 0$
	<i>Wcc</i>	$2.82 \pm 2.01^{+0.30}_{-0.27}$	$0 \pm 0$
	<i>Wc</i>	$83.9 \pm 21.7^{+9.1}_{-8.2}$	$0 \pm 0$
	<i>Wl</i>	$67.8 \pm 12.4^{+7.2}_{-6.9}$	$1.34 \pm 0.95^{+0.15}_{-0.13}$
Constrained background	<i>stop</i>	$21.4 \pm 0.9^{+2.1}_{-2.6}$	$21.4 \pm 1.0^{+2.1}_{-3.5}$
	<i>ZZ</i>	$340 \pm 4^{+35}_{-32}$	$373 \pm 4^{+40}_{-35}$
	<i>WZ</i>	$350 \pm 5^{+37}_{-33}$	$388 \pm 5^{+43}_{-42}$
	<i>WW</i>	$2.3 \pm 0.4^{+0.3}_{-0.2}$	$2.06 \pm 0.38^{+0.23}_{-0.21}$
	<i>t<bar>t</bar></i>	$348 \pm 5^{+35}_{-42}$	$315 \pm 5^{+32}_{-35}$
	<i>Zb</i>	$5590 \pm 30^{+580}_{-560}$	$5080 \pm 30^{+560}_{-510}$
Non-constrained pre-fit	<i>Zc</i>	$2470 \pm 120^{+240}_{-340}$	$2910 \pm 130^{+360}_{-250}$
	<i>Zl</i>	$34160 \pm 490^{+3420}_{-3760}$	$33110 \pm 450^{+3770}_{-3640}$
	$\frac{\text{data}}{S+B}$	$1.25 \pm 0.62$	$1.21 \pm 0.62$
	<i>t<bar>t</bar></i>	$553 \pm 8^{+54}_{-64}$	$485 \pm 7^{+51}_{-54}$
	<i>Zb</i>	$7710 \pm 40^{+780}_{-760}$	$6750 \pm 40^{+750}_{-650}$
Non-constrained post-fit	<i>Zc</i>	$2373 \pm 116^{+240}_{-340}$	$2852 \pm 128^{+360}_{-250}$
	<i>Zl</i>	$43040 \pm 610^{+4320}_{-4580}$	$40060 \pm 540^{+4340}_{-4300}$
	$\frac{\text{data}}{S+B}$	$1.0 \pm 0.7$	$1.0 \pm 0.7$

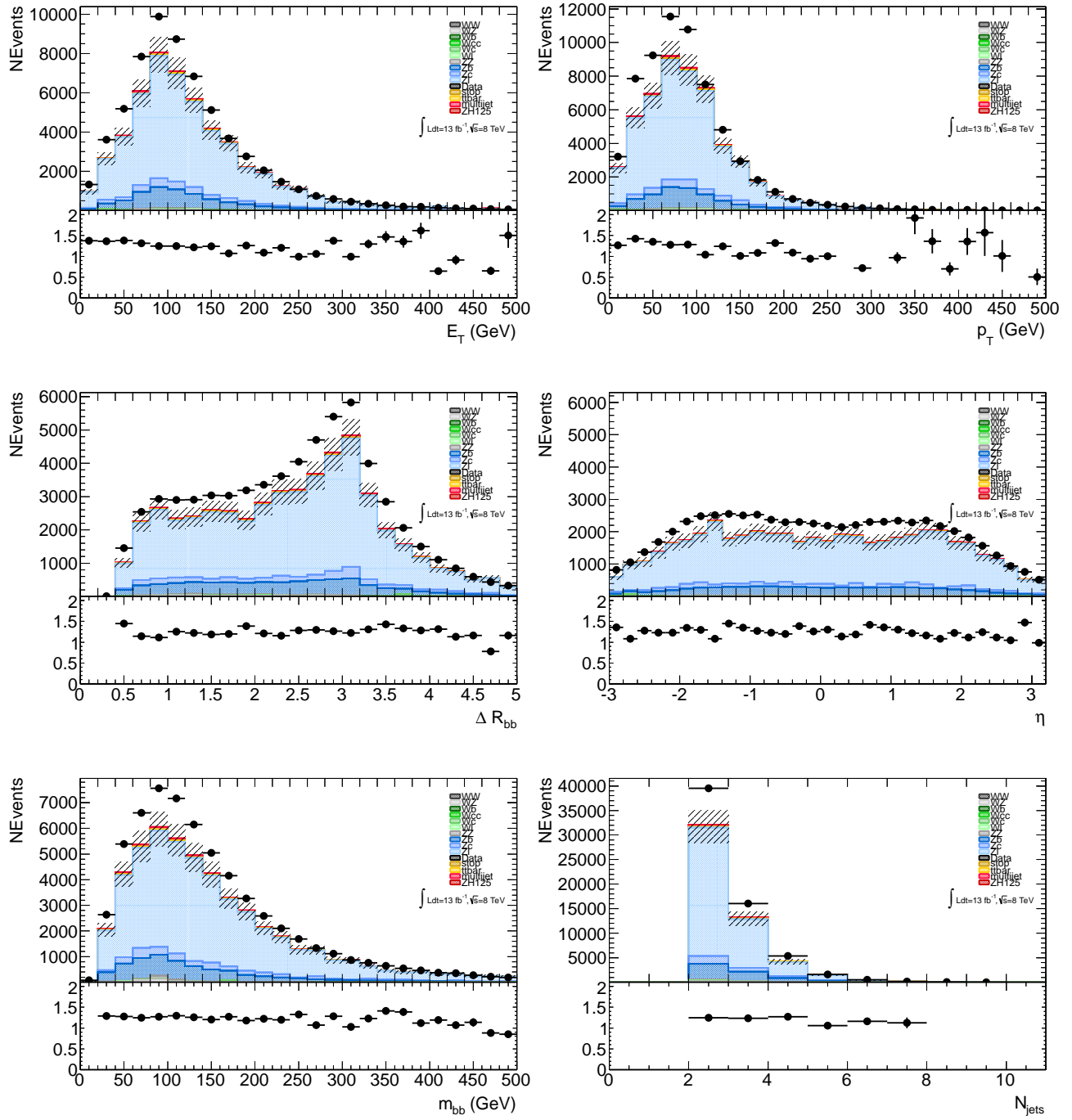


Figure 5.28: Higgs boson candidate distributions in the control  $N_{b-jets} \geq 0$  and  $N_{electrons} = 2$  region before applying scale factors from the log-likelihood fit.

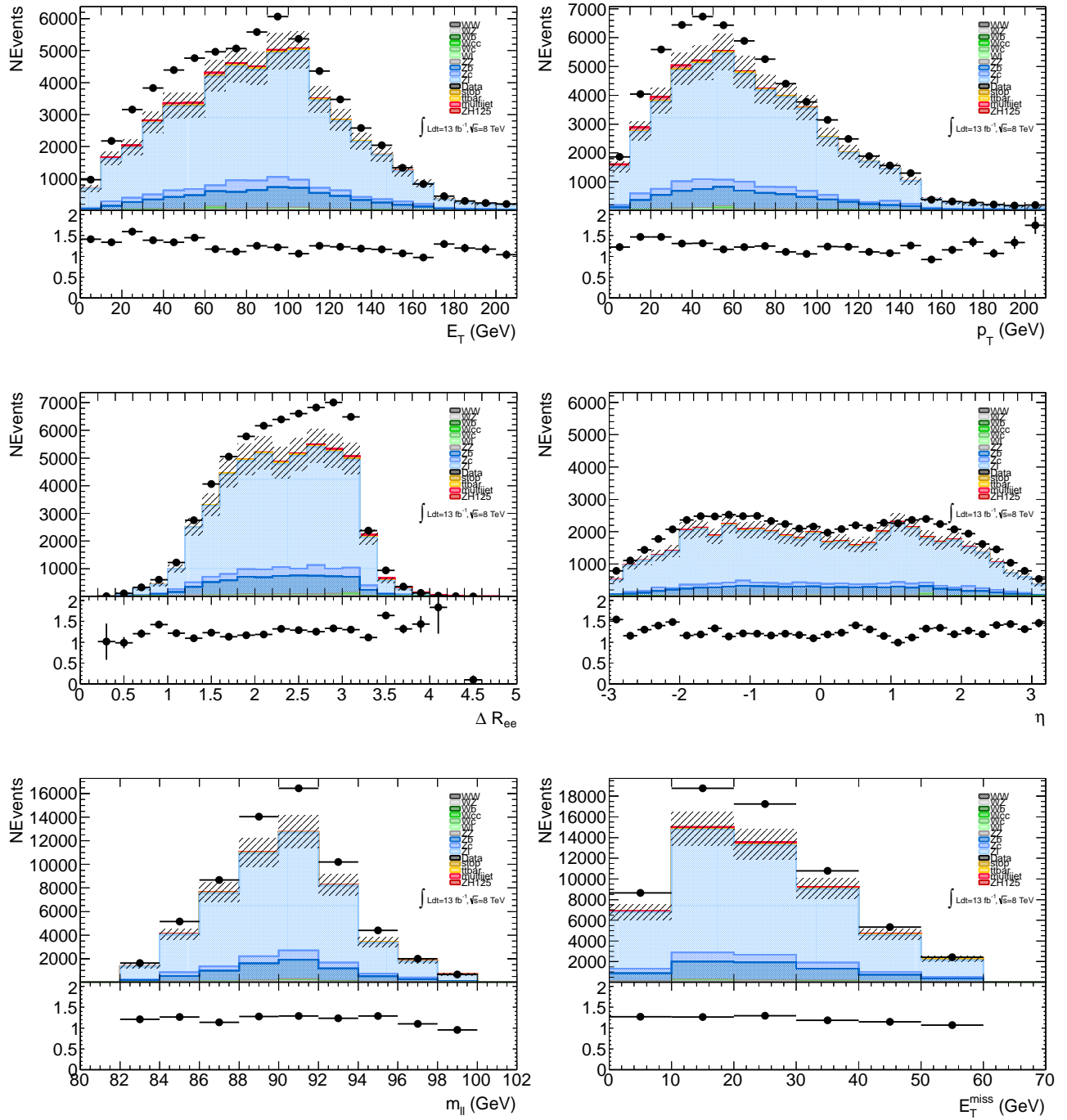


Figure 5.29:  $Z$  boson candidate distributions in the control  $N_{b-jets} \geq 0$  and  $N_{electrons} = 2$  region before applying scale factors from the log-likelihood fit.

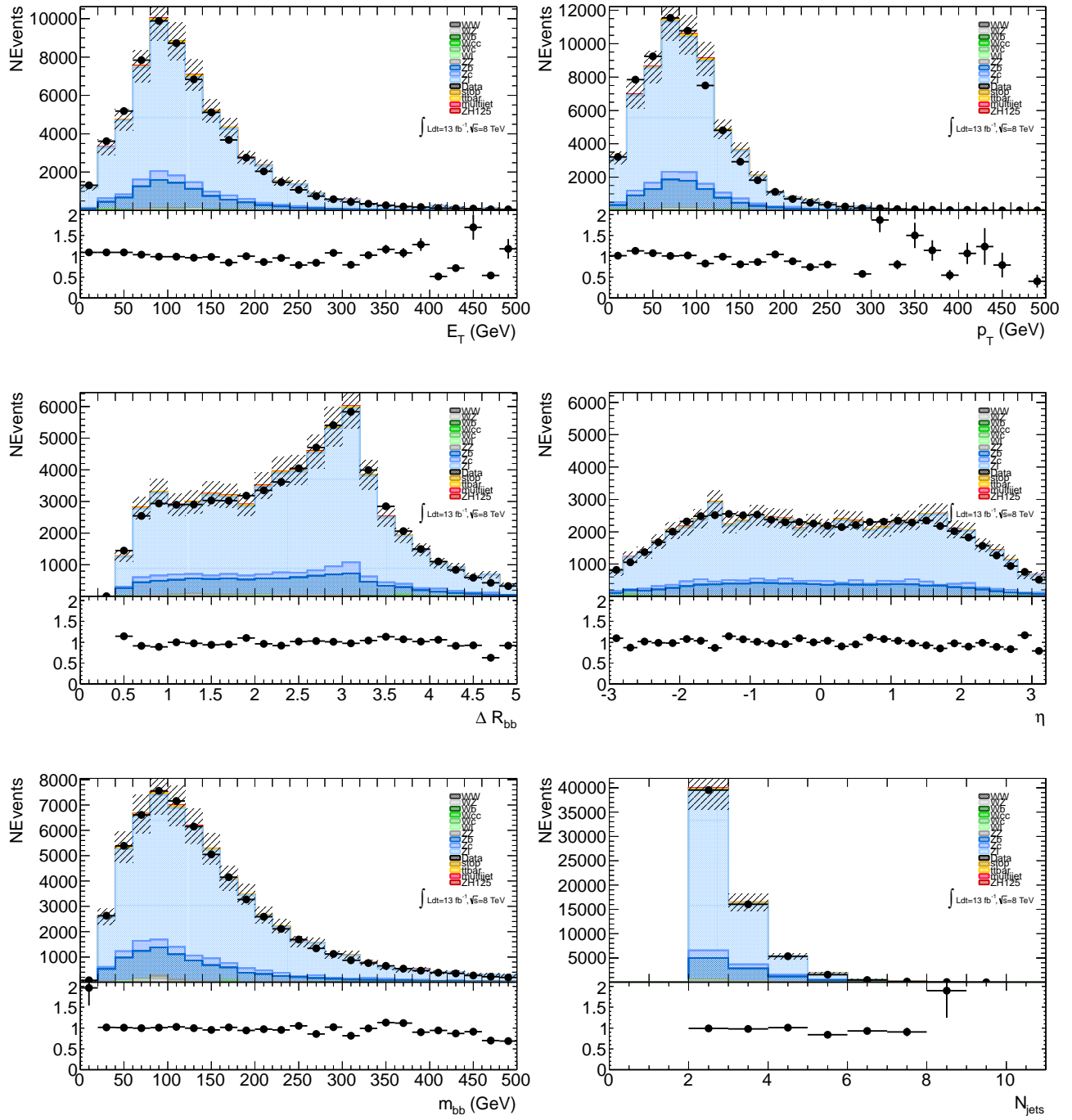


Figure 5.30: Higgs boson candidate distributions in the control  $N_{b-jets} \geq 0$  and  $N_{electrons} = 2$  region after applying scale factors from the log-likelihood fit.

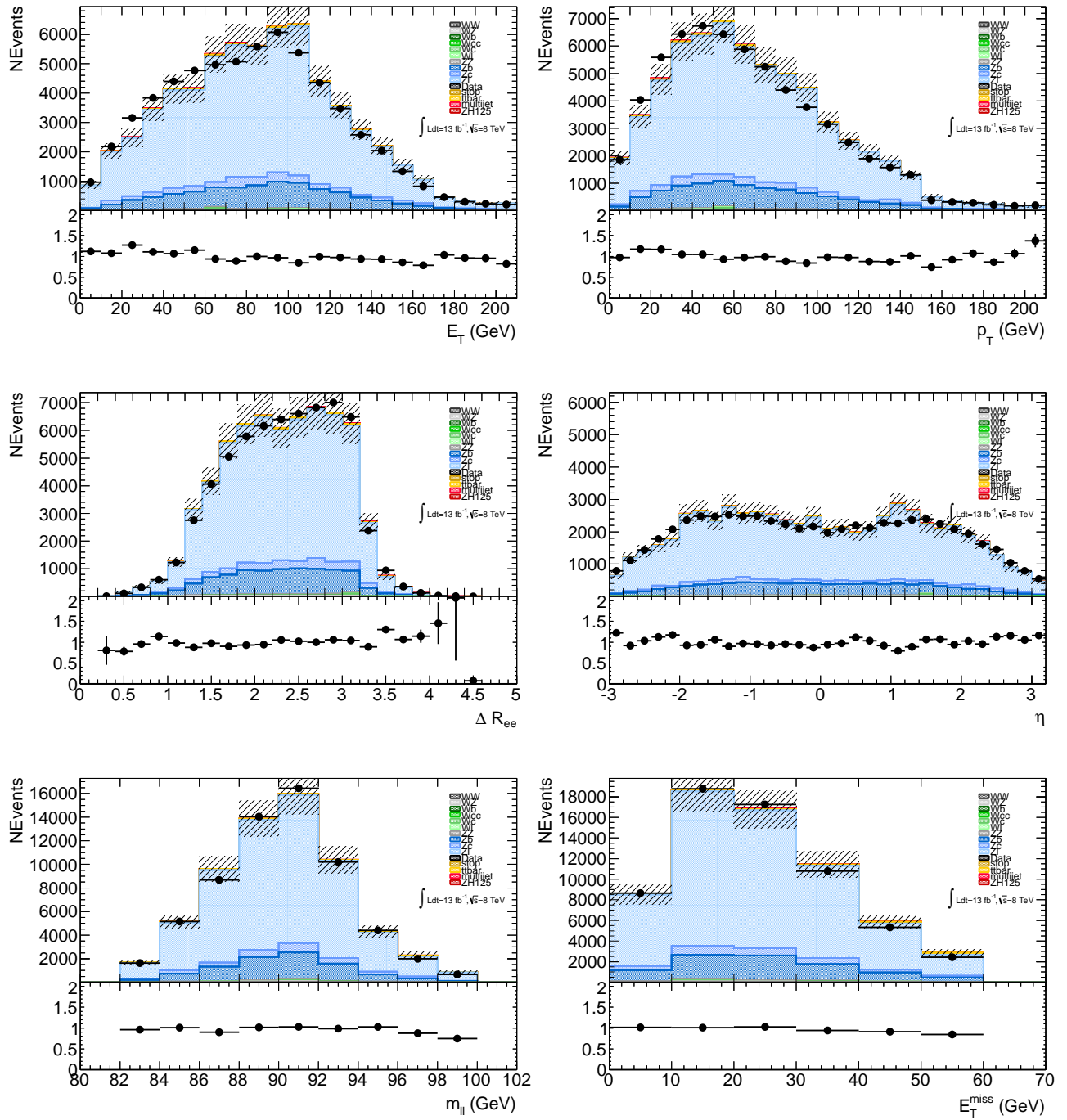


Figure 5.31:  $Z$  boson candidate distributions in the control  $N_{b-jets} \geq 0$  and  $N_{electrons} = 2$  region after applying scale factors from the log-likelihood fit.

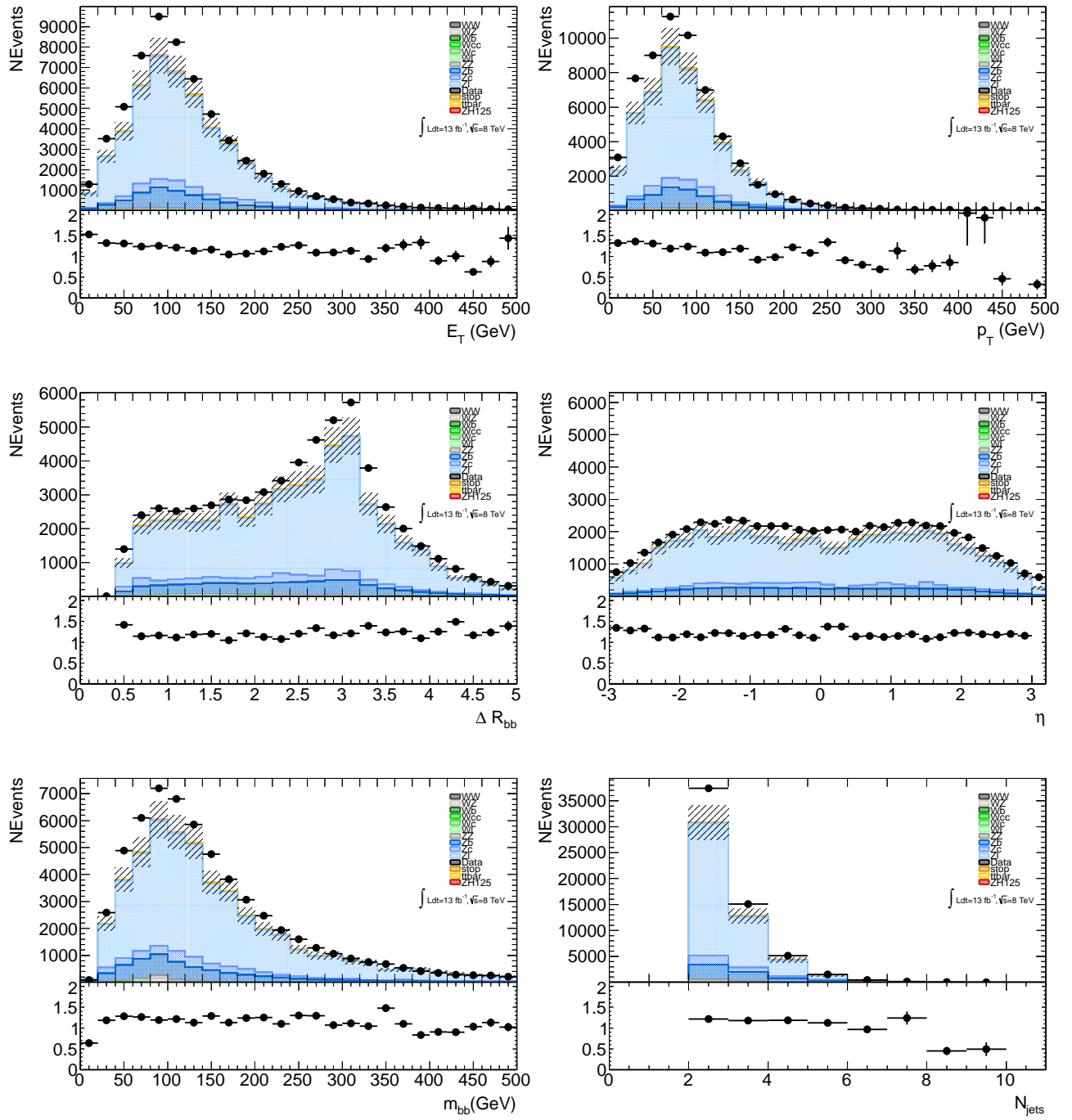


Figure 5.32: Higgs boson candidate distributions in the control  $N_{b-jets} \geq 0$  and  $N_{muons} = 2$  region before applying scale factors from the log-likelihood fit.

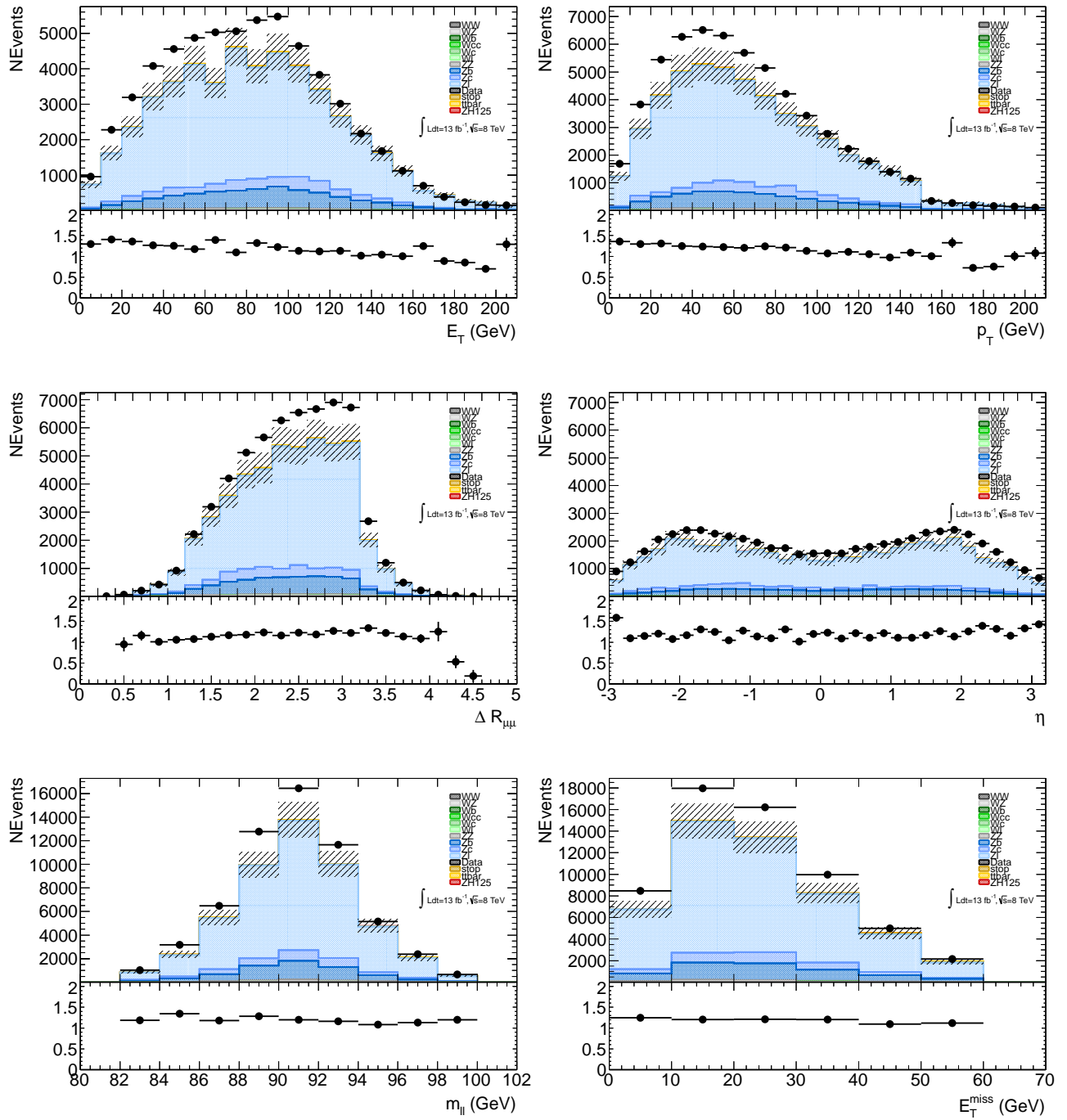


Figure 5.33:  $Z$  boson candidate distributions in the control  $N_{b-jets} \geq 0$  and  $N_{muons} = 2$  region before applying scale factors from the log-likelihood fit.

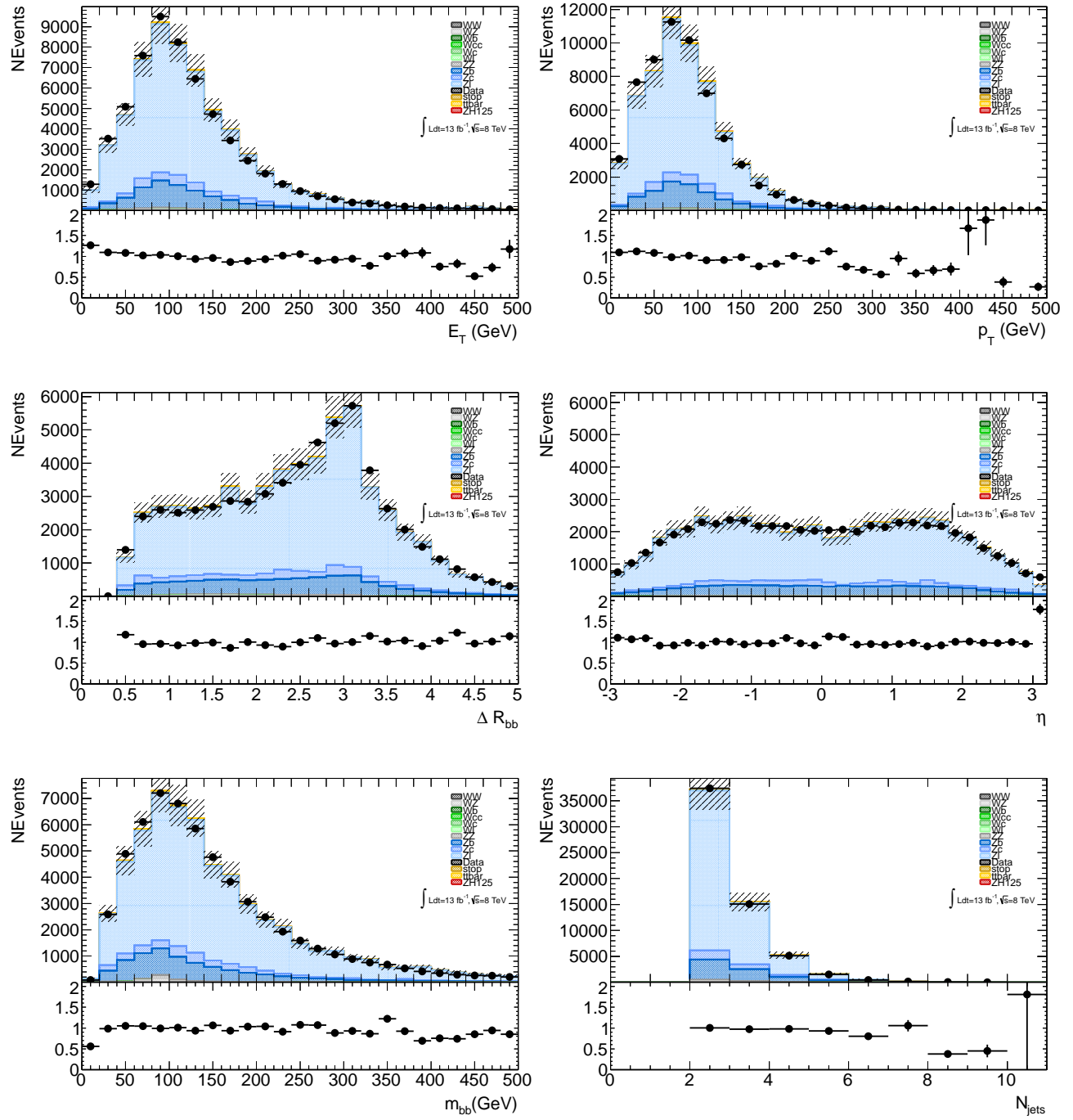


Figure 5.34: Higgs boson candidate distributions in the control  $N_{b-jets} \geq 0$  and  $N_{muons} = 2$  region after applying scale factors from the log-likelihood fit.

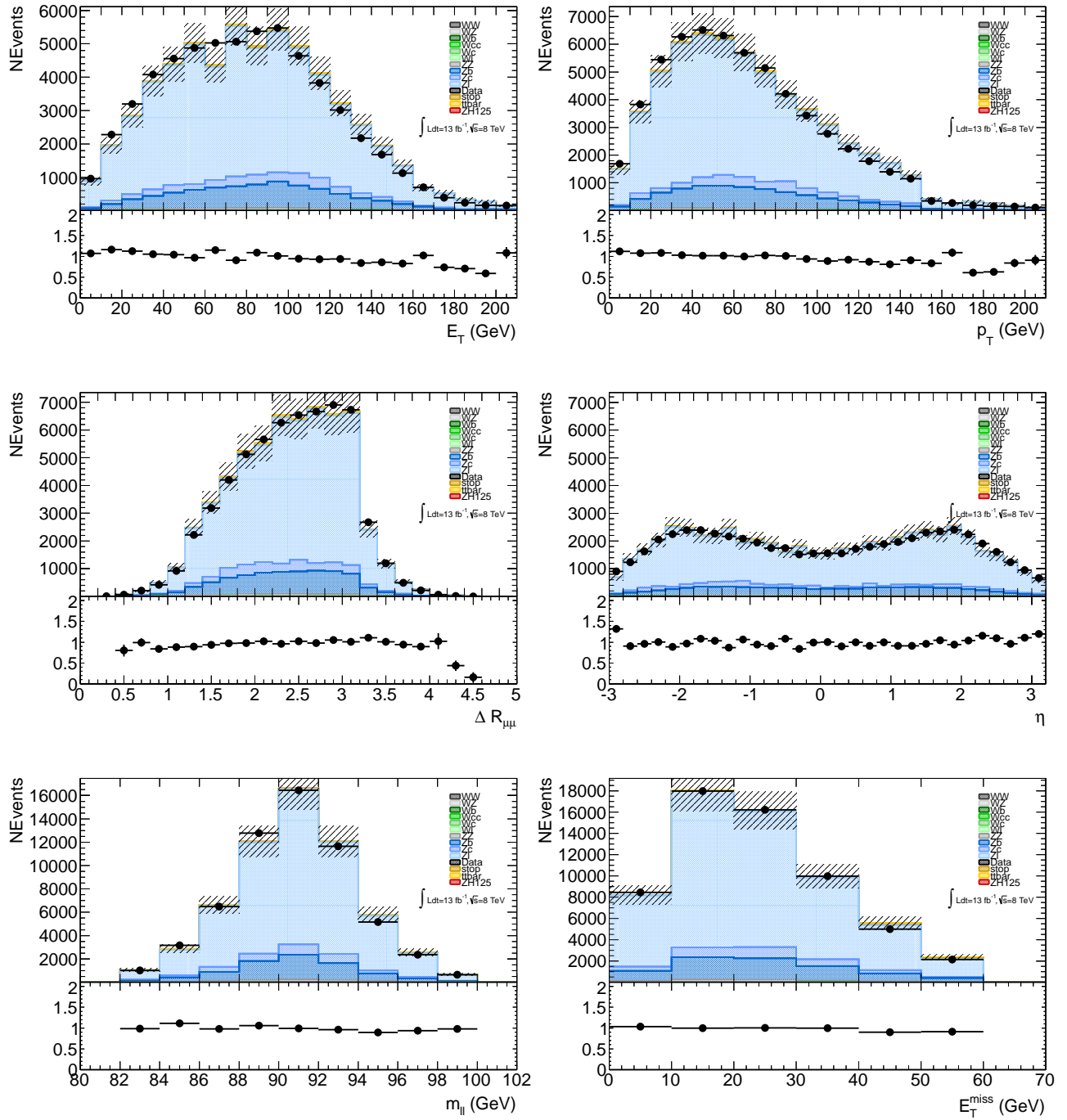


Figure 5.35:  $Z$  boson candidate distributions in the control  $N_{b-jets} \geq 0$  and  $N_{muons} = 2$  region after applying scale factors from the log-likelihood fit.

## 5.6.2 1-tag Control Region

The 1-tag  $N_{b-jets} \geq 1$  control region has also passed the selection cuts in Section 5.4, with exception to the requirement on the  $b$ -tagging, which has been relaxed to only require at least 1  $b$ -jet in the event. Figures from 5.36 to 5.43 and Table 5.14 show clearly that the 1-tag region is dominated by the  $Z + b\text{-jet}$  background (72% purity), while the  $Z + \text{light-jets}$ ,  $Z + c\text{-jets}$  and top background have a contribution of 15%, 6% and 5% respectively. Figures 5.38, 5.39, 5.42 and 5.43 again show good agreement between data and MC after the fit, when we take the statistical and systematic fluctuations into account.

Table 5.14: The number of selected signal (S), background (B) and data events for the control region  $N_{b-jets} \geq 1$  before and after the log-likelihood fit.

	<b>Process</b>	$e^+e^-b\bar{b}$	$\mu^+\mu^-b\bar{b}$
	<i>data</i>	$8919 \pm 94$	$7842 \pm 88$
<i>MC Signal</i>	<i>ZH125</i>	$18.4 \pm 0.2^{+1.8}_{-1.8}$	$18.6 \pm 0.2^{+1.9}_{-1.8}$
Constrained background	<i>Wb</i>	$0 \pm 0$	$0 \pm 0$
	<i>Wcc</i>	$2.80 \pm 2.82^{+0.33}_{-0.34}$	$0 \pm 0$
	<i>Wc</i>	$9.16 \pm 4.10^{+0.99}_{-0.99}$	$0 \pm 0$
	<i>Wl</i>	$0 \pm 0$	$0 \pm 0$
	<i>stop</i>	$17.5 \pm 0.8^{+2.0}_{-2.2}$	$16.0 \pm 0.8^{+1.6}_{-3.1}$
	<i>ZZ</i>	$114 \pm 2^{+13}_{-13}$	$122 \pm 2^{+15}_{-14}$
	<i>WZ</i>	$58.8 \pm 2.1^{+7.0}_{-6.8}$	$59.9 \pm 2.1^{+7.3}_{-7.2}$
	<i>WW</i>	$0.47 \pm 0.21^{+0.05}_{-0.05}$	$0.56 \pm 0.23^{+0.07}_{-0.07}$
	<i>t<math>\bar{t}</math></i>	$308 \pm 5^{+34}_{-43}$	$274 \pm 4^{+30}_{-36}$
	<i>Zb</i>	$4780 \pm 30^{+530}_{-570}$	$4150 \pm 20^{+520}_{-500}$
Non-constrained pre-fit	<i>Zc</i>	$520 \pm 60^{+60}_{-59}$	$490 \pm 50^{+58}_{-59}$
	<i>Zl</i>	$1070 \pm 90^{+130}_{-130}$	$930 \pm 80^{+90}_{-160}$
	$\frac{\text{data}}{S+B}$	$1.29 \pm 0.10$	$1.29 \pm 0.10$
	<i>t<math>\bar{t}</math></i>	$489 \pm 7^{+51}_{-67}$	$422 \pm 6^{+48}_{-54}$
	<i>Zb</i>	$6600 \pm 40^{+740}_{-770}$	$5530 \pm 30^{+670}_{-640}$
Non-constrained post-fit	<i>Zc</i>	$510 \pm 59^{+60}_{-60}$	$485 \pm 50^{+60}_{-60}$
	<i>Zl</i>	$1350 \pm 120^{+160}_{-160}$	$1120 \pm 90^{+110}_{-200}$
	$\frac{\text{data}}{S+B}$	$0.97 \pm 0.13$	$1.01 \pm 0.13$

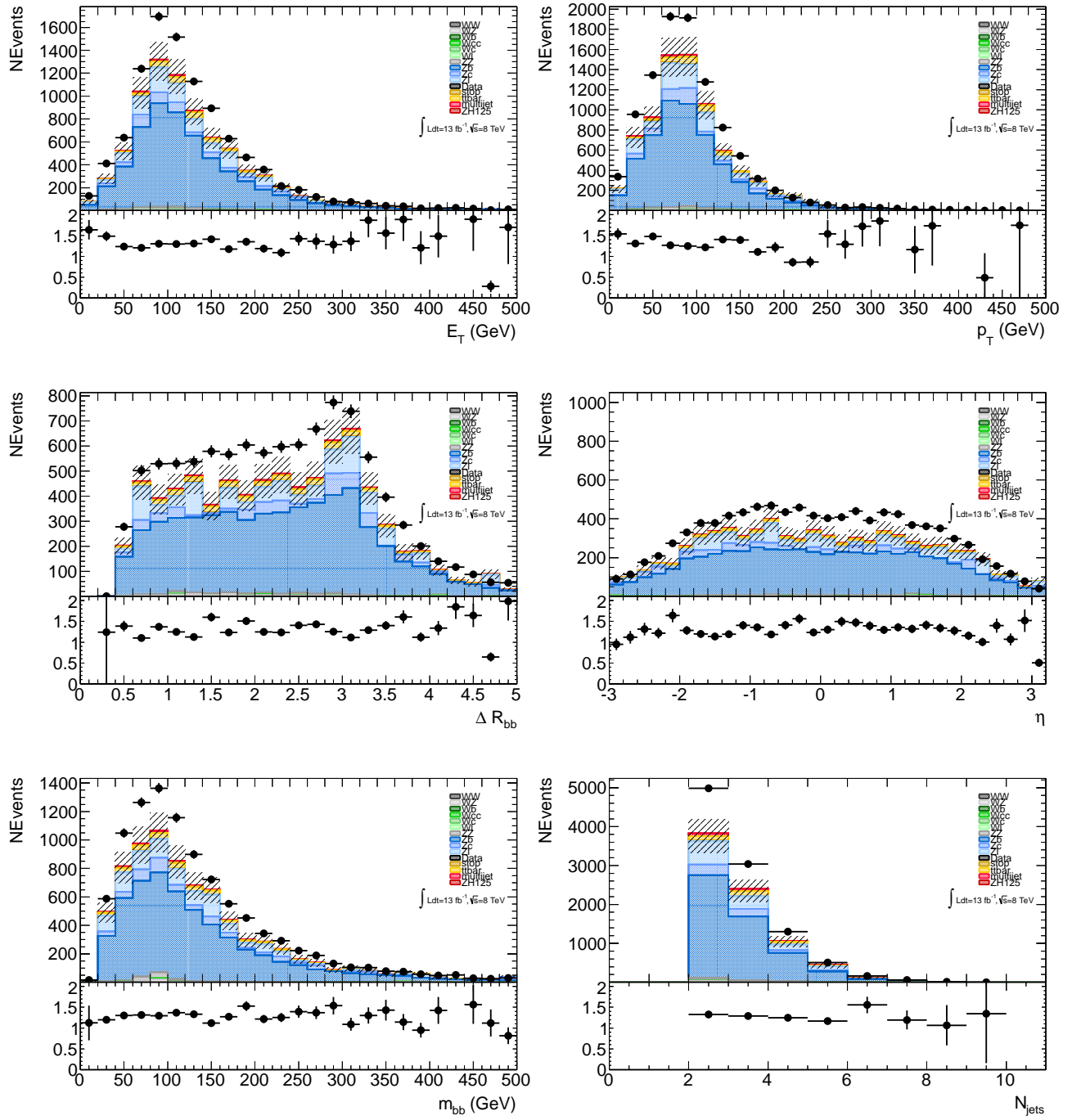


Figure 5.36: Higgs boson candidate distributions in the control  $N_{b-jets} \geq 1$  and  $N_{electrons} = 2$  region before applying scale factors from the log-likelihood fit.

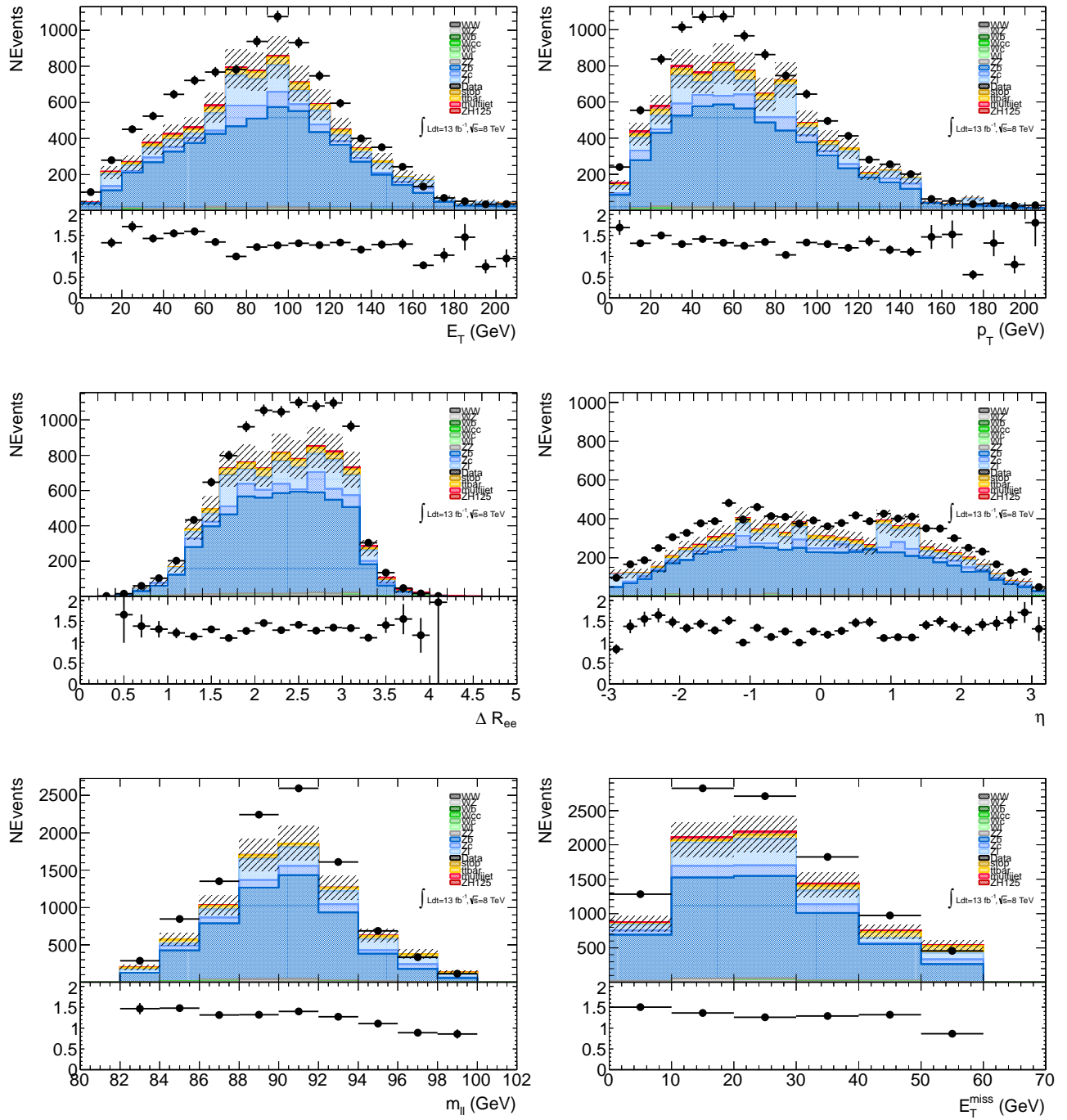


Figure 5.37:  $Z$  boson candidate distributions in the control  $N_{b-jets} \geq 1$  and  $N_{electrons} = 2$  region before applying scale factors from the log-likelihood fit.

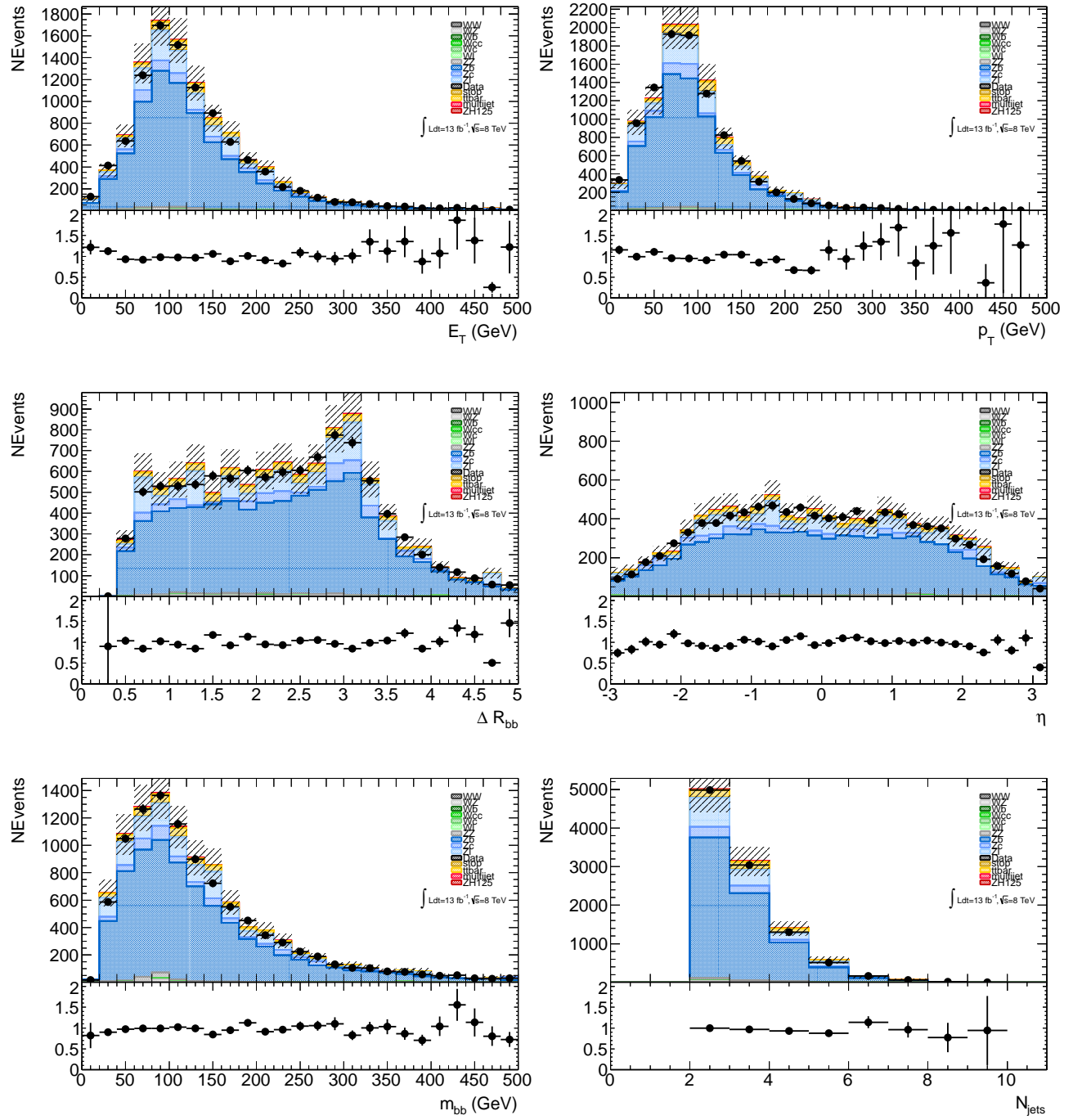


Figure 5.38: Higgs boson candidate distributions in the control  $N_{b-jets} \geq 1$  and  $N_{electrons} = 2$  region after applying scale factors from the log-likelihood fit.

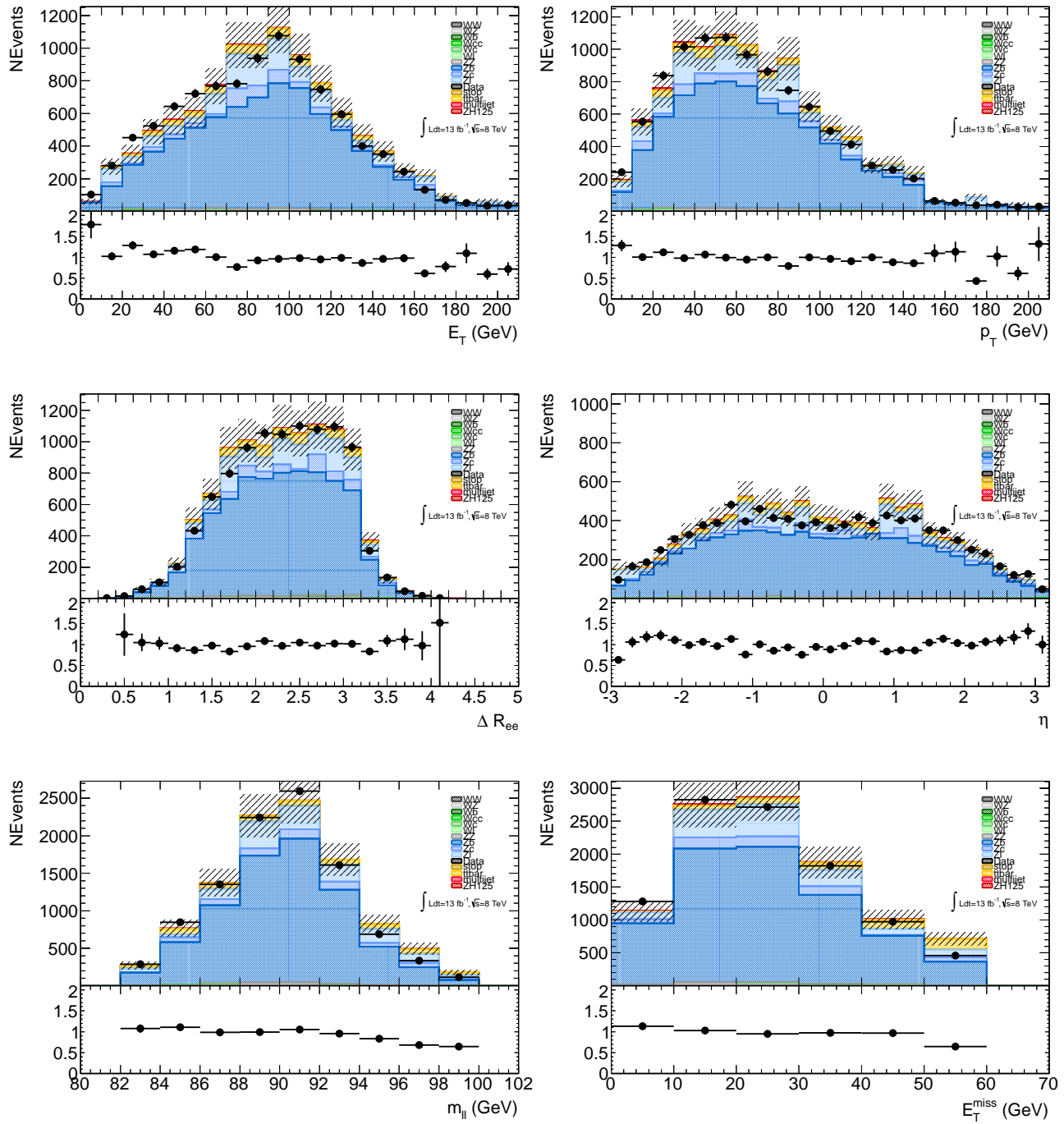


Figure 5.39:  $Z$  boson candidate distributions in the control  $N_{b-jets} \geq 1$  and  $N_{electrons} = 2$  region after applying scale factors from the log-likelihood fit.

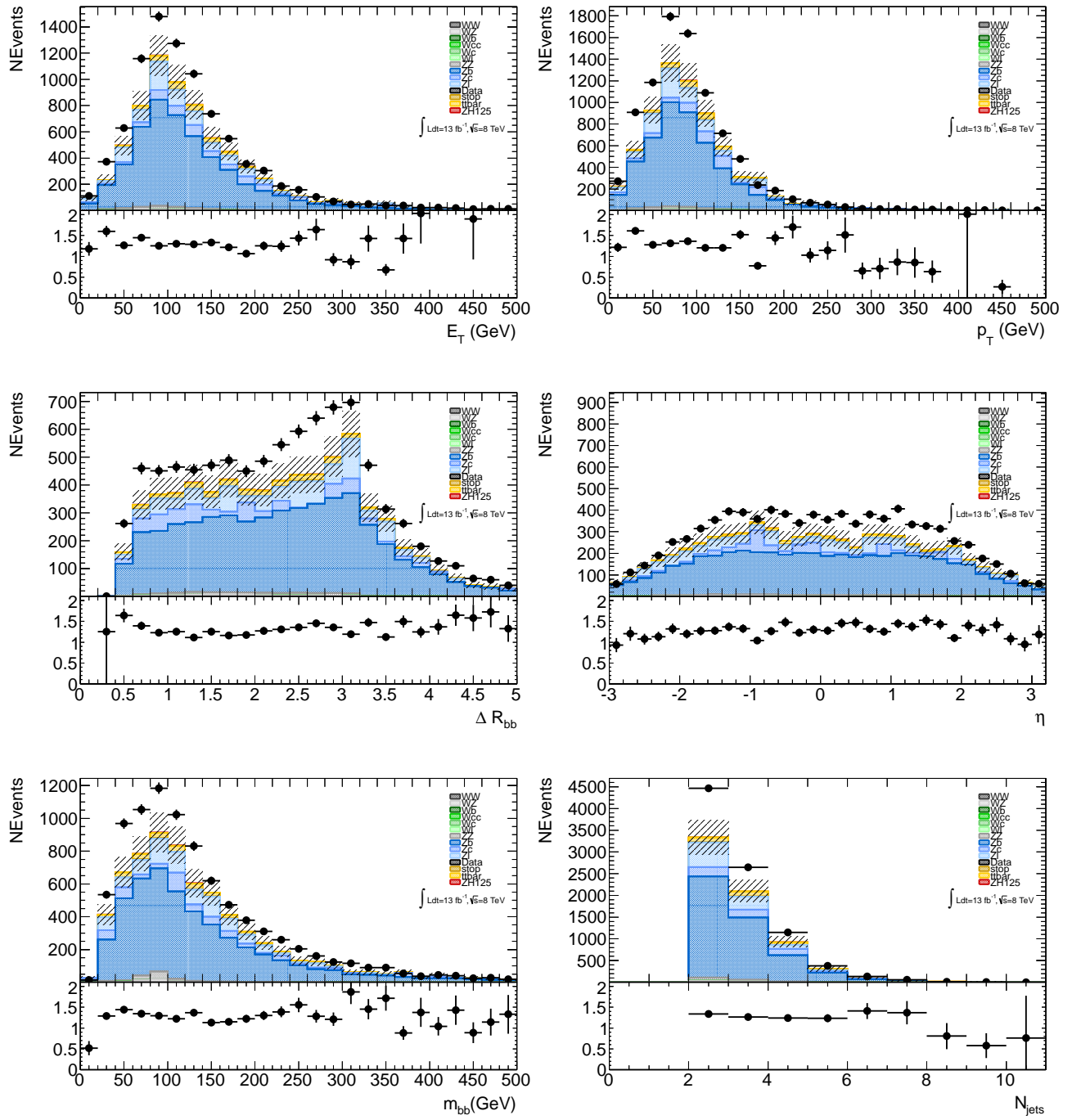


Figure 5.40: Higgs boson candidate distributions in the control  $N_{b-jets} \geq 1$  and  $N_{muons} = 2$  region before applying scale factors from the log-likelihood fit.

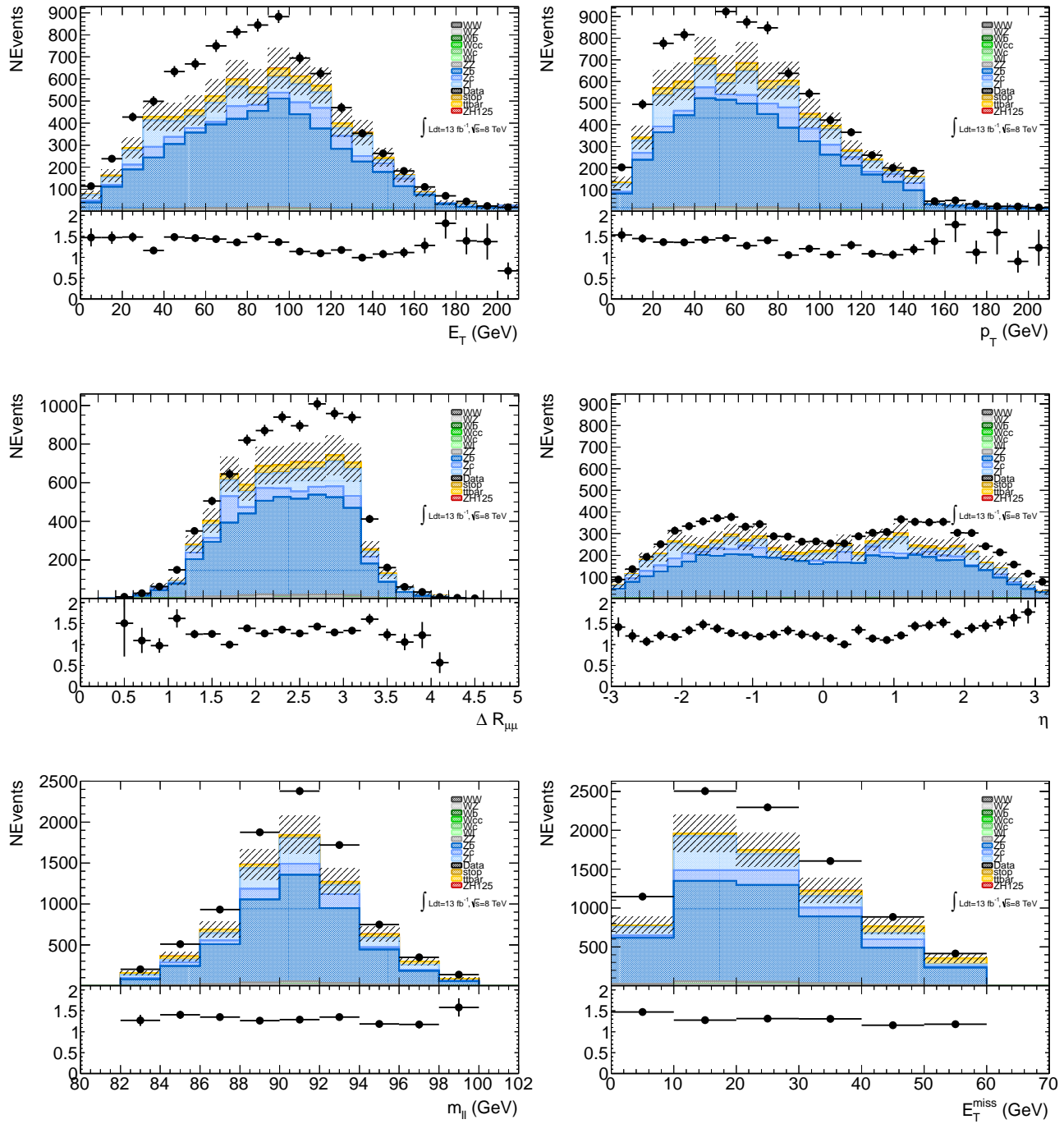


Figure 5.41:  $Z$  boson candidate distributions in the control  $N_{b-jets} \geq 1$  and  $N_{muons} = 2$  region before applying scale factors from the log-likelihood fit.

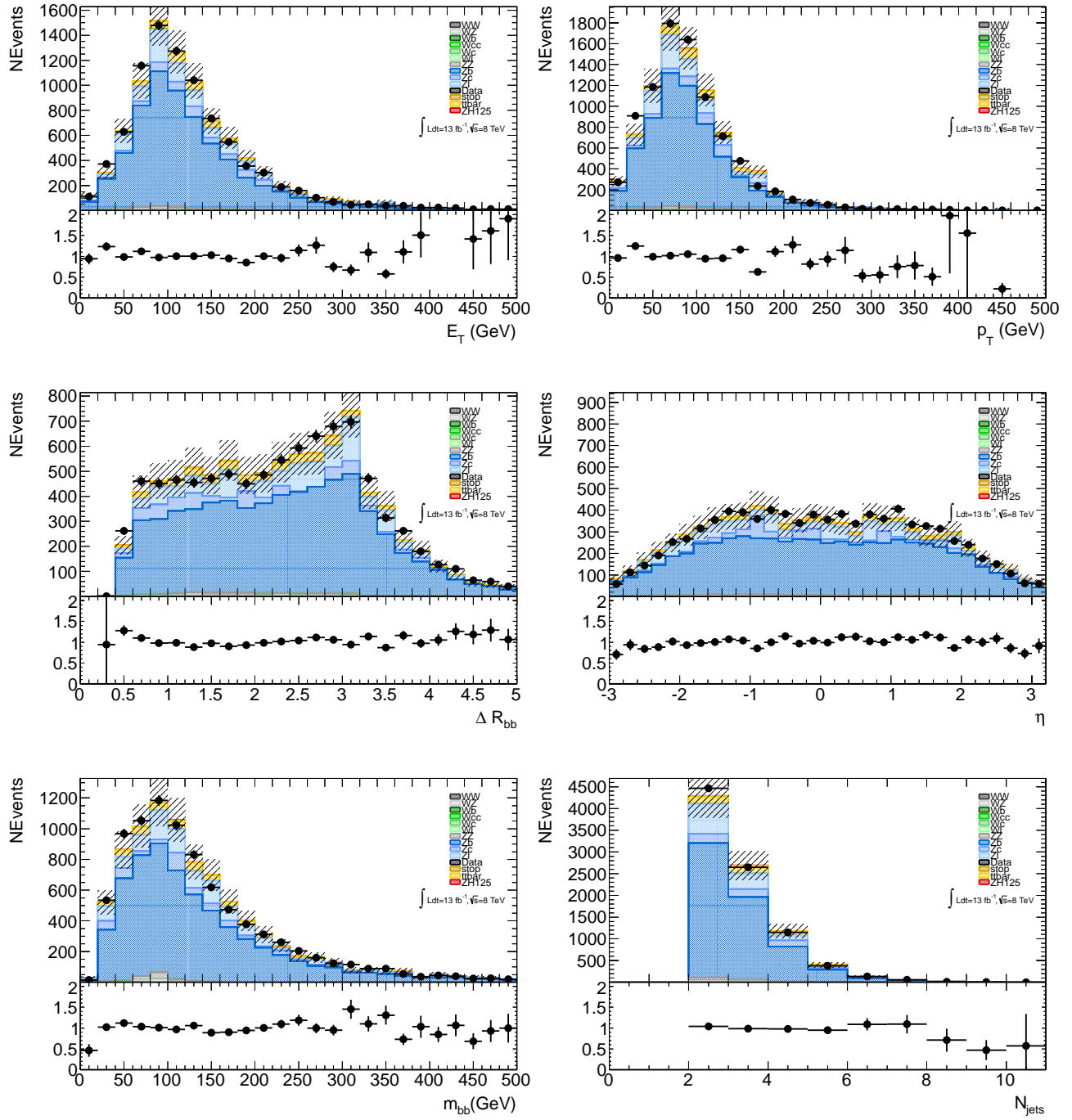


Figure 5.42: Higgs boson candidate distributions in the control  $N_{b-jets} \geq 1$  and  $N_{muons} = 2$  region after applying scale factors from the log-likelihood fit.

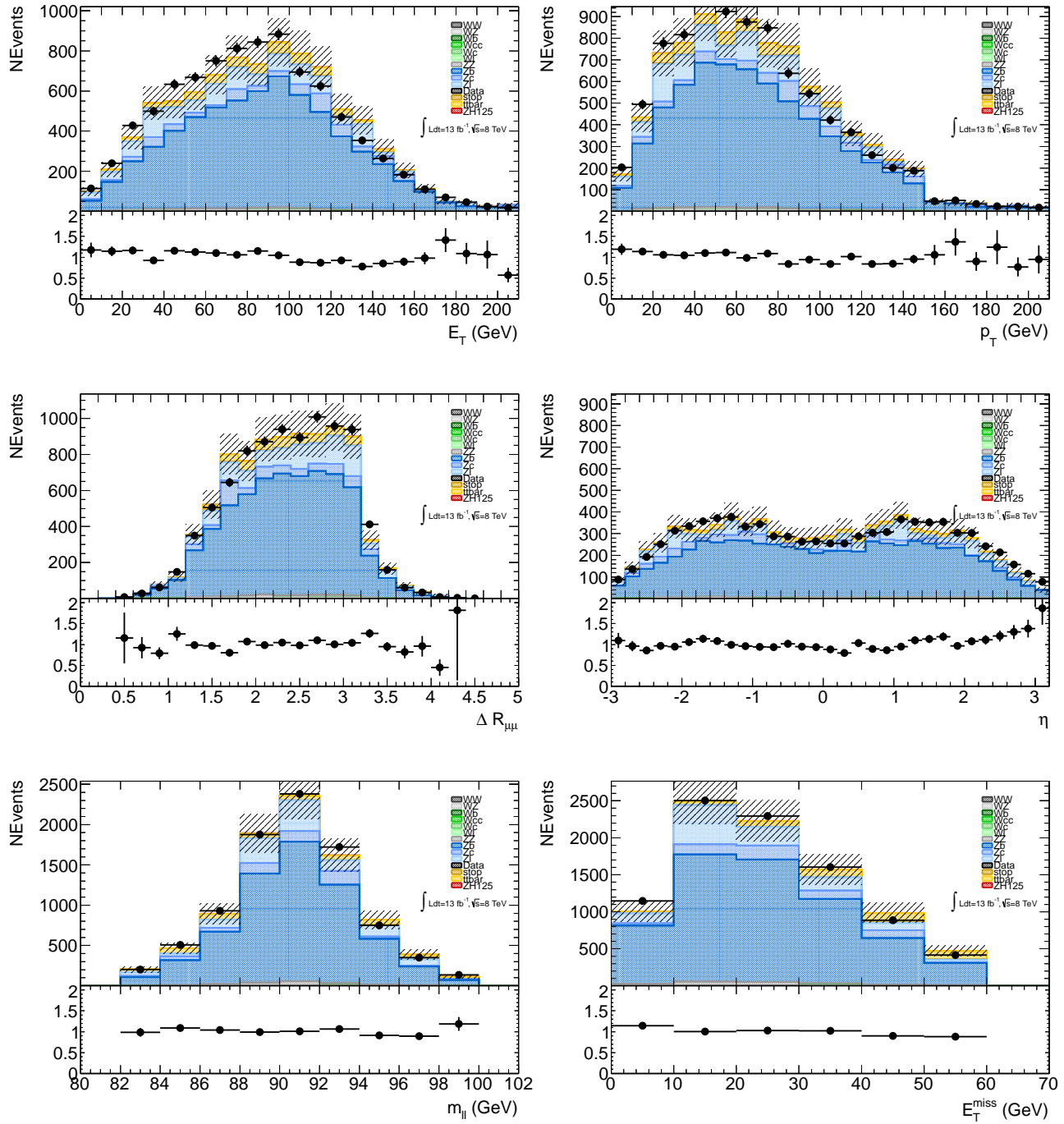


Figure 5.43:  $Z$  boson candidate distributions in the control  $N_{b-jets} \geq 1$  and  $N_{muons} = 2$  region after applying scale factors from the log-likelihood fit.

## 5.7 Systematic Uncertainties

Systematic uncertainties included in the  $ZH \rightarrow l^+l^-b\bar{b}$  analysis are taken from performance group studies that have derived efficiencies and associated uncertainties for reconstruction and identification of physics objects. Uncertainties have also been derived for momentum and energy corrections applied to a given particle (for more details see Section 4). While these uncertainties are dependent on each particle in the event, global uncertainties are applied to the luminosity and theoretical normalisation predictions for signal and background processes. In the following sections we take a closer look at these theoretical and instrumental uncertainties and how they affect the overall analysis.

### 5.7.1 Theoretical Uncertainties on the ZH Signal

The Higgs boson production cross sections have been studied in great detail by the LHC Higgs cross section working group. The  $ZH \rightarrow l^+l^-b\bar{b}$  signals are normalised to the inclusive cross sections reported in the Higgs cross section group report [28]. The Higgs boson branching ratio uncertainty for  $H \rightarrow b\bar{b}$  ranges from 2.5% to 4.3% for a mass range between 110 – 130 GeV, with an uncertainty of 3.3% at  $m_H = 125$  GeV. The  $ZH \rightarrow l^+l^-b\bar{b}$  inclusive cross section has been divided into Parton Distribution Function (PDF), renormalisation and factorisation uncertainties. The uncertainties are summarised in Table 5.15 for Higgs masses from 110 to 130 GeV. Due to the correlation between the PDF and the renormalisation/factorisation scale factors, the uncertainties are separated during the maximum likelihood fit, while the renormalisation and factorisation scale factors are considered uncorrelated and are

combined. The inclusive cross sections include electroweak correction factors  $\Delta_{EW}$  that have been integrated over the entire VH phase space and take into account the fully differential NNLO QCD + NLO EW cross sections.

Table 5.15: NNLO QCD + NLO EW inclusive cross sections for  $ZH$  and related uncertainties at 8 TeV, quoted in the CERN Yellow Report [28]. The  $Scale[\%]$  error indicates the uncertainty from factorisation and renormalisation scale variation. The  $PDF + \alpha_s$  error indicates uncertainty from PDF +  $\alpha_s$  variations. The  $\Delta_{EW}[\%]$  error indicates uncertainty from the electroweak correction factors.

$m_H$	$\sigma(ZH)[\text{pb}]$	$Scale[\%]$	$PDF + \alpha_s[\%]$	$\Delta_{EW}[\%]$
110 GeV	0.5117	$^{+1.4}_{-1.3}$	$\pm 4.2$	-5.1
115 GeV	0.4483	$^{+1.5}_{-1.4}$	$\pm 3.5$	-5.1
120 GeV	0.3943	$^{+1.6}_{-1.5}$	$\pm 3.5$	-5.1
125 GeV	0.3430	$^{+1.7}_{-1.6}$	$\pm 3.7$	-5.3
130 GeV	0.3074	$^{+1.8}_{-1.6}$	$\pm 3.6$	-5.3

### 5.7.2 Modelling of the $Z+jets$ Background

The most significant backgrounds in the analysis come from the  $Z + jets$  processes, which have been renormalised to data using techniques explained in Section 5.5.3. The modelling of the  $Z + jets$  background is a critical aspect of the analysis. A systematic uncertainty on the modelling of the backgrounds has been derived by directly comparing the differences in the modelling from *SHERPA* and *ALPGEN*

event generators. Figures 5.44 and 5.45 show the comparisons between both generators for the  $N_{b-jets} \geq 0$  region. We can see that there is varying agreement in the  $m_{b\bar{b}}$  distributions at the lower and higher mass regions for the  $Z+b-jets$ ,  $Z+c-jets$  and  $Z+light-jets$  processes. In the lower mass regions we can see that the *SHERPA* event generator has a bigger contribution of events, while in the higher mass regions the distribution is dominated by a lack of statistics. The larger number of events coming from the *SHERPA* event generator could be explained by the use of the full matrix element when calculating the cross section and decay rates. From Table 5.16 we can see good agreement between the  $Z+light-jets$  process of less than  $\sim 1\%$ , with more events coming from the *SHERPA* generator. While the  $Z+b-jets$  process has a larger uncertainty of  $\sim 6\%$  and  $Z+c-jets \sim 4\%$ , with more events coming from *SHERPA* in both processes. A shape and normalisation systematic is derived from the distributions of the  $Z+jets$  backgrounds generated by *ALPGEN*. The systematic is calculated by symmetrising the distributions and by taking into account a  $1\sigma$  fluctuation in the *ALPGEN* samples. This is then used to constrain the  $Z+jets$  backgrounds in the final fit.

Table 5.16: Comparison between event yields of the  $Z + jets$  backgrounds in the *SHERPA* and *ALPGEN* event generators for the  $N_{b-jets} \geq 0$  region. Statistical uncertainties are only shown.

Process	$e^+e^-b\bar{b}$		$\mu^+\mu^-b\bar{b}$	
	<i>SHERPA</i>	<i>ALPGEN</i>	<i>SHERPA</i>	<i>ALPGEN</i>
Zb	$7709 \pm 42$	$7177 \pm 39$	$6754 \pm 36$	$6294 \pm 33$
Zc	$2469 \pm 119$	$2348 \pm 77$	$2909 \pm 88$	$2785 \pm 88$
Zl	$43039 \pm 612$	$42591 \pm 577$	$40061 \pm 540$	$39716 \pm 512$

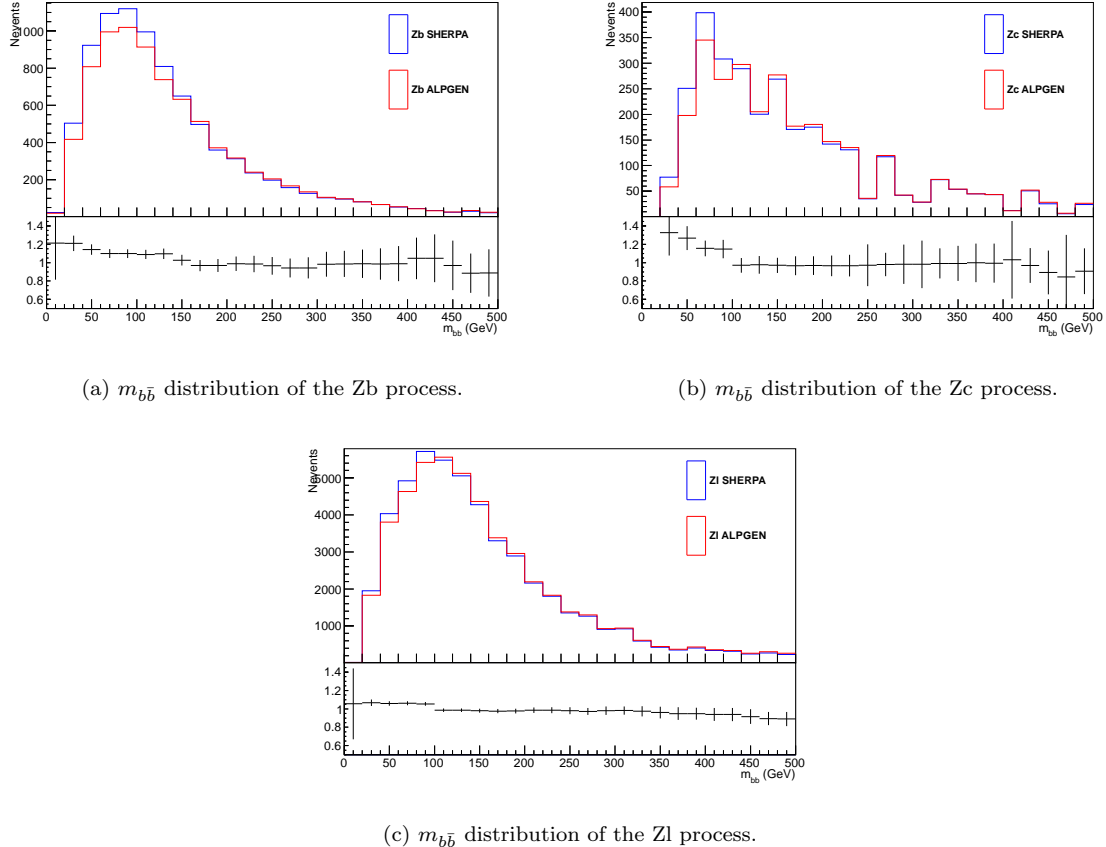


Figure 5.44:  $m_{b\bar{b}}$  distribution of the  $Z + jets$  backgrounds in the  $N_{b-jets} \geq 0$  and  $N_{electrons} = 2$  region for the *SHERPA* and *ALPGEN* event generators.

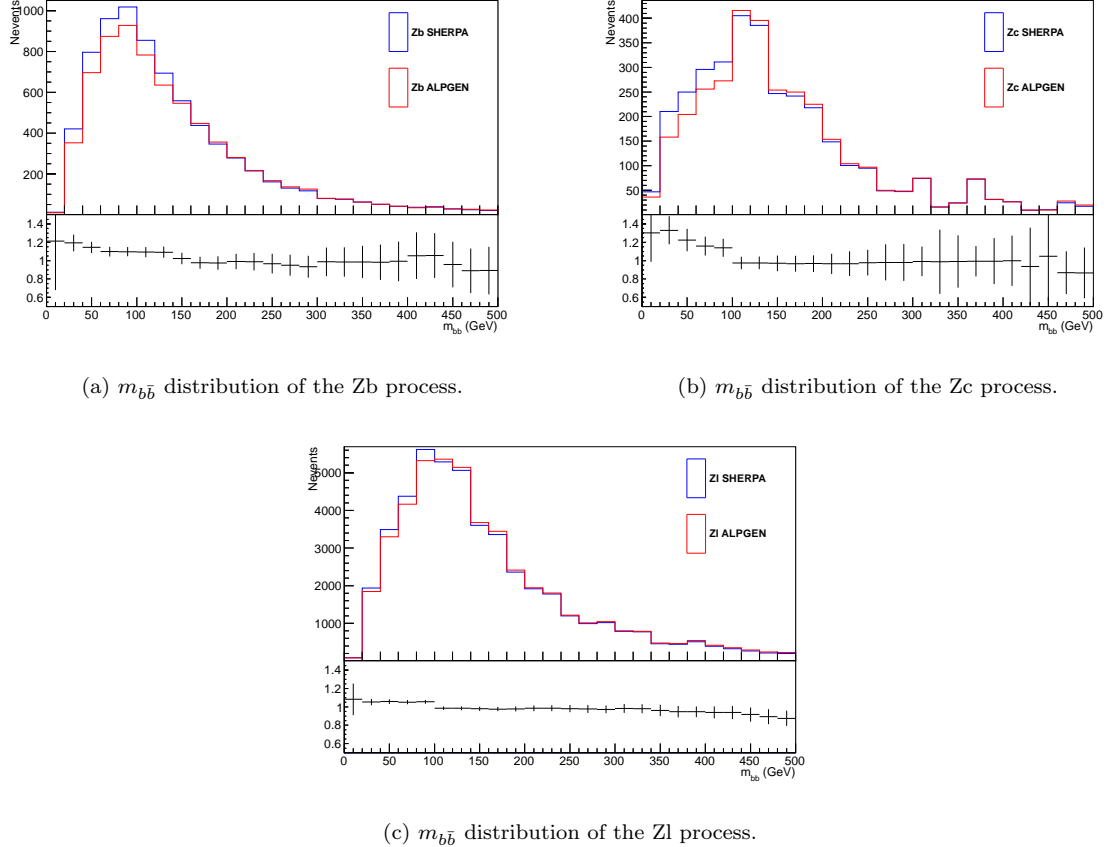


Figure 5.45:  $m_{b\bar{b}}$  distribution of the  $Z + jets$  backgrounds in the  $N_{b-jets} \geq 0$  and  $N_{muons} = 2$  region for the *SHERPA* and *ALPGEN* event generators.

### 5.7.3 Impact of Systematic Uncertainties

Several systematic uncertainties for the analysis have been considered, from theoretical uncertainties to experimental apparatus. The systematics determine the degree of accuracy we can take from the analysis and also direct future improvements. The main detector related contributions come from the jet reconstruction and identification efficiencies. The complex environment in which the jet candidates reside, cause large uncertainties in the energy scale, resolution, tagging and flavour of the jet. The largest uncertainty obtained in the analysis comes from the  $b$  and  $c$  tagging efficiencies, which have uncertainties of  $\sim 1 - 6\%$  and  $\sim 4.5\%$  respectively. The  $b$ -tagging efficiency is separated into several eigenvector variations to take into account the dependency of the  $p_T$  of the jet candidate, which is assumed to be 100% correlated with the  $b$ -tagging efficiency. Due to the  $p_T$  dependence of the  $b$ -tagging efficiency, jets with higher  $p_T$  in the event are found to have a higher tagging uncertainty ( $\sim 6\%$ ), while lower  $p_T$  jets have typically a lower uncertainty. The energy scale and resolution of the jet is also an area of large uncertainty, with an effect of  $\sim 4\%$  and  $\sim 3.5\%$  respectively. The main contributing theoretical uncertainty comes from the modelling of the  $Z + jets$  background, where we find a large contribution of  $\sim 5\%$  uncertainty coming from the  $m_{b\bar{b}}$  distribution. The  $Z + jets$  background is the dominant process in the  $N_{b-jets} = 2$  signal region, with a contribution of  $\sim 77\%$  of all processes in the event. Due to the large contribution of the  $Z + jets$  background the uncertainty has a large effect on the analysis, which can be shown by observing the effect on the  $\frac{S}{B}$  ratio. A complete list of the studied systematics and their percentage impact on the event yield can be seen in Tables 5.17 and 5.18.

Table 5.17: The impact of uncertainties in the  $N_{b-jets} = 2$  and  $N_{electrons} = 2$  region shown as a percentage for both upward and downward variations.

Uncertainty	Impact on Analysis (%)
<b>Global Event Uncertainties</b>	
Luminosity	$\pm 3.0$
Mu Scaling	$^{+1.7}_{-1.3}$
<b>Jet Uncertainties</b>	
Baseline Jet Energy Scale (JES)	$^{+4.0}_{-3.7}$
JES NPV	$^{+1.2}_{-1.0}$
JES Mu	$^{+2.3}_{-1.8}$
b-jet Energy Scale	$\pm 2.4$
Jet Energy Resolution (JER)	$\pm 3.5$
JES Flavour	$\pm 0.9$
JES Closeby	$^{+1.4}_{-1.0}$
JES PtReco	$^{+0.5}_{-1.6}$
JES Forward	$\pm 1.6$
b-tagging Efficiency 0	$^{-0.2}_{-0.4}$
b-tagging Efficiency 1	$^{+1.5}_{-0.9}$
b-tagging Efficiency 2	$^{+1.9}_{-1.7}$
b-tagging Efficiency 3	$^{+1.1}_{-0.7}$
b-tagging Efficiency 4	$^{+6.0}_{-4.6}$
b-tagging Efficiency 5	$^{+3.8}_{-4.0}$
c-tagging Efficiency	$^{+4.7}_{-2.6}$
l-tagging Efficiency	$^{+2.6}_{-3.1}$
<b>Lepton Uncertainties</b>	
Electron Energy Scale	$^{+0.7}_{-1.6}$
Electron Energy Resolution	$^{+1.3}_{-1.1}$
Electron Efficiency	$^{+2.0}_{-1.1}$
<b>MC Uncertainties</b>	
Diboson cross section	$\pm 0.3$
Z+b jets $m_{b\bar{b}}$	$\pm 4.7$
Z+c jets $m_{b\bar{b}}$	$\pm 0.6$
Z+l jets $m_{b\bar{b}}$	$\pm 0.1$

Table 5.18: The impact of uncertainties in the  $N_{b-jets} = 2$  and  $N_{muons} = 2$  region shown as a percentage for both upward and downward variations.

Uncertainty	Impact on Analysis (%)
<b>Global Event Uncertainties</b>	
Luminosity	$\pm 3.0$
Mu Scaling	$^{+1.9}_{-0.8}$
<b>Jet Uncertainties</b>	
Baseline Jet Energy Scale (JES)	$\pm 3.8$
JES NPV	$\pm 1.2$
JES Mu	$^{+2.3}_{-1.8}$
b-jet Energy Scale	$^{+2.4}_{-2.6}$
Jet Energy Resolution (JER)	$\pm 3.7$
JES Flavour	$^{+0.8}_{-0.9}$
JES Closeby	$^{+1.0}_{-0.6}$
JES PtReco	$^{+0.3}_{-1.3}$
JES Forward	$^{+1.6}_{-1.3}$
b-tagging Efficiency 0	$\pm 0.0$
b-tagging Efficiency 1	$^{+1.3}_{-0.6}$
b-tagging Efficiency 2	$^{+2.3}_{-1.8}$
b-tagging Efficiency 3	$^{+1.4}_{-0.9}$
b-tagging Efficiency 4	$^{+6.5}_{-4.7}$
b-tagging Efficiency 5	$^{+3.7}_{-4.0}$
c-tagging Efficiency	$^{+4.7}_{-2.8}$
l-tagging Efficiency	$^{+3.0}_{-3.5}$
<b>Lepton Uncertainties</b>	
Muon ID Energy Resolution	$^{+2.0}_{-2.3}$
Muon MS Energy Resolution	$^{+2.0}_{-2.1}$
Muon Efficiency	$^{+2.5}_{-2.1}$
<b>MC Uncertainties</b>	
Diboson cross section	$\pm 0.3$
Z+b jets $m_{b\bar{b}}$	$\pm 5.0$
Z+c jets $m_{b\bar{b}}$	$\pm 0.0$
Z+l jets $m_{b\bar{b}}$	$\pm 0.0$

## 5.8 Results

The following section presents the signal region used to produce the 95% CL limits set for the Higgs boson cross section using the  $CL_s$  test statistic [107]. The limits themselves are also shown for the  $ZH \rightarrow e^+e^-b\bar{b}$ ,  $ZH \rightarrow \mu^+\mu^-b\bar{b}$ , and inclusive  $ZH \rightarrow l^+l^-b\bar{b}$  channels in a Higgs mass range  $110 - 130$  GeV in 5 GeV bins.

### 5.8.1 Signal Region

Events with  $N_{b-jets} = 2$  and that have passed the selection criteria described in Section 5.4 are considered to be within the signal region of the analysis and are used to derive a limit on the  $ZH \rightarrow l^+l^-b\bar{b}$  production. Figures 5.48, 5.49, 5.52, 5.53 and Table 5.19 show the various event distributions and numbers in the signal region. The  $Z + b$ -jet background is the dominant process in the signal region, contributing  $\sim 75\%$  of all events. The signal  $ZH \rightarrow l^+l^-b\bar{b}$  production contributes  $\sim 1\%$  of all the events in the signal region, giving a signal over background ratio of  $\sim 0.006$ . The statistical and systematic effects are shown on the distributions below using a shaded area, which shows good agreement between MC and data. The event yields for both the electron and muon stream are also shown on Table 5.19, again showing good agreement between both streams when taking the statistical fluctuations into account.

Table 5.19: The number of selected events in the  $N_{b-jets} = 2$  region for signal (S) and background (B) samples. The data and MC ratio is also shown, along with the significance ( $S/\sqrt{B}$ ). The numbers are taken from a mass range  $80 < m_{b\bar{b}} < 150$  GeV.

Process	$e^+e^-b\bar{b}$	$\mu^+\mu^-b\bar{b}$
<i>data</i>	$1291 \pm 36$	$1129 \pm 34$
<i>ZH125 (S)</i>	$7.48 \pm 0.09^{+0.76}_{-0.64}$	$7.59 \pm 0.09^{+0.80}_{-0.70}$
<i>Zb</i>	$919 \pm 13^{+107}_{-99}$	$862 \pm 12^{+113}_{-92}$
<i>Zc</i>	$60.7 \pm 27.2^{+7.2}_{-6.6}$	$0.044 \pm 0.031^{+0.012}_{-0.000}$
<i>Zl</i>	$11.3 \pm 7.9^{+1.4}_{-1.2}$	$36.7 \pm 18.4^{+4.6}_{-4.1}$
<i>Wb</i>	$0 \pm 0$	$0 \pm 0$
<i>Wcc</i>	$2.82 \pm 2.82^{+0.35}_{-0.32}$	$0 \pm 0$
<i>Wc</i>	$0 \pm 0$	$0 \pm 0$
<i>Wl</i>	$0 \pm 0$	$0 \pm 0$
<i>t\bar{t}</i>	$199 \pm 4^{+19}_{-29}$	$183 \pm 4^{+21}_{-23}$
<i>s - top</i>	$3.94 \pm 0.39^{+0.37}_{-0.77}$	$3.04 \pm 0.33^{+0.45}_{-0.27}$
<i>ZZ</i>	$28.9 \pm 1.1^{+3.7}_{-3.1}$	$31.4 \pm 1.2^{+3.9}_{-3.5}$
<i>WZ</i>	$0.64 \pm 0.18^{+0.08}_{-0.07}$	$1.87 \pm 0.40^{+0.23}_{-0.22}$
<i>WW</i>	$0 \pm 0$	$0 \pm 0$
<i>bkg (B)</i>	$1227 \pm 13^{+135}_{-161}$	$1118 \pm 12^{+128}_{-96}$
$\frac{\textit{data}}{S+B}$	$1.05 \pm 0.14$	$1.0 \pm 0.1$
$\frac{S}{\sqrt{B}}$	$0.21 \pm 0.11$	$0.23 \pm 0.11$

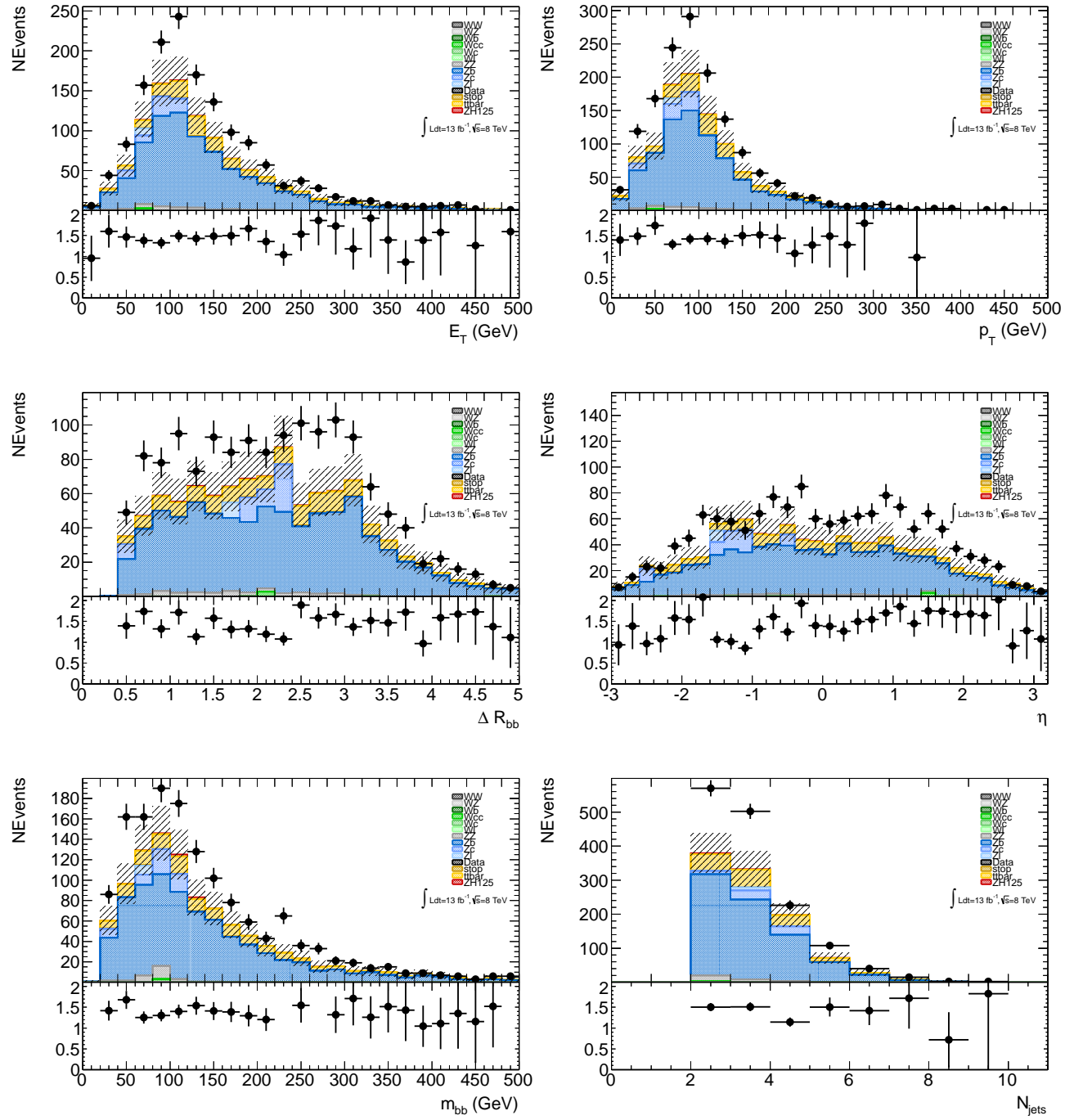


Figure 5.46: Higgs boson candidate distributions in the signal  $N_{b-jets} = 2$  and  $N_{electrons} = 2$  region before applying scale factors from the log-likelihood fit.

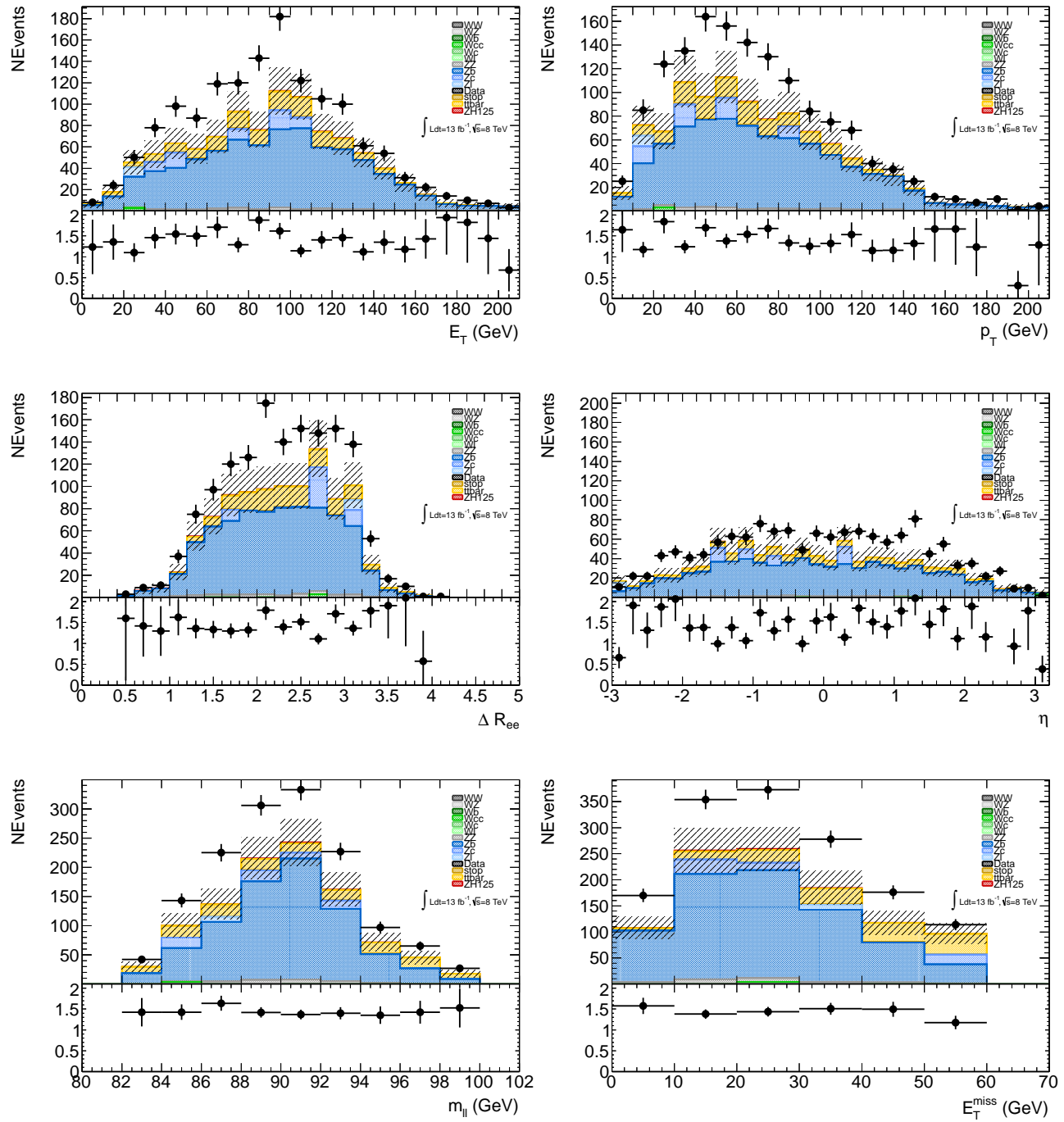


Figure 5.47:  $Z$  boson candidate distributions in the signal  $N_{b-jets} = 2$  and  $N_{electrons} = 2$  region before applying scale factors from the log-likelihood fit.

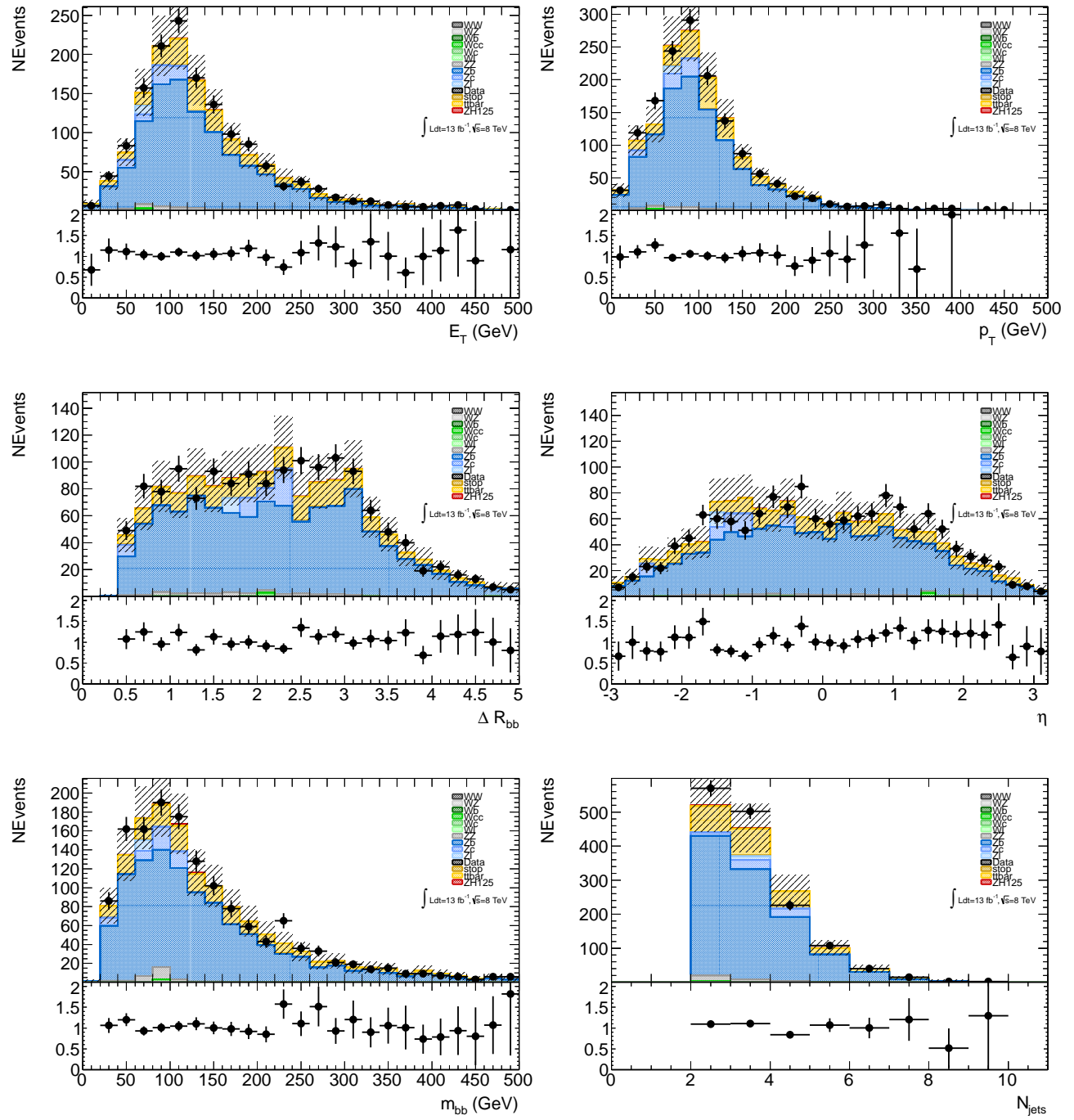


Figure 5.48: Higgs boson candidate distributions in the signal  $N_{b-jets} = 2$  and  $N_{electrons} = 2$  region after applying scale factors from the log-likelihood fit.

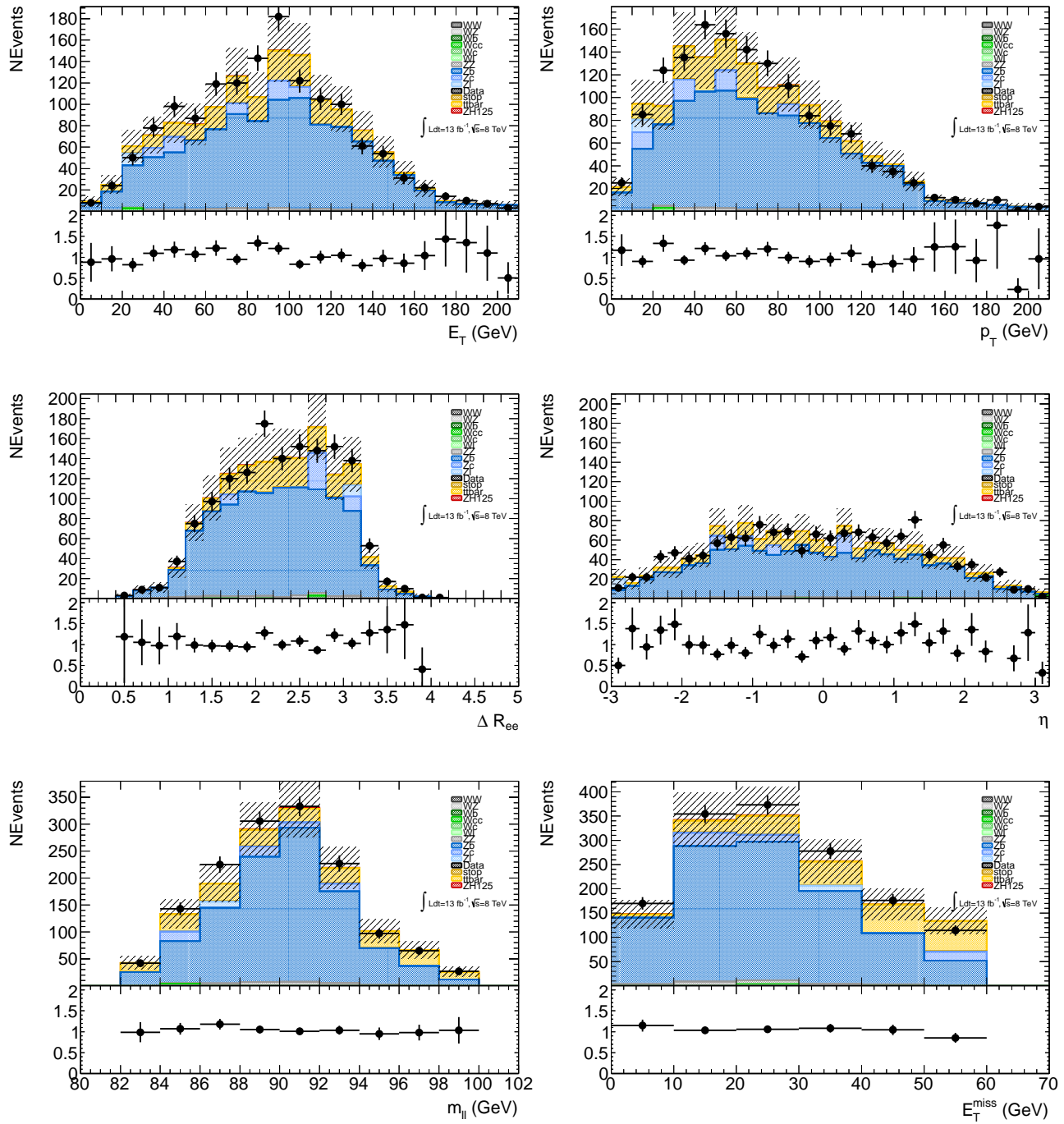


Figure 5.49:  $Z$  boson candidate distributions in the signal  $N_{b-jets} = 2$  and  $N_{electrons} = 2$  region after applying scale factors from the log-likelihood fit.

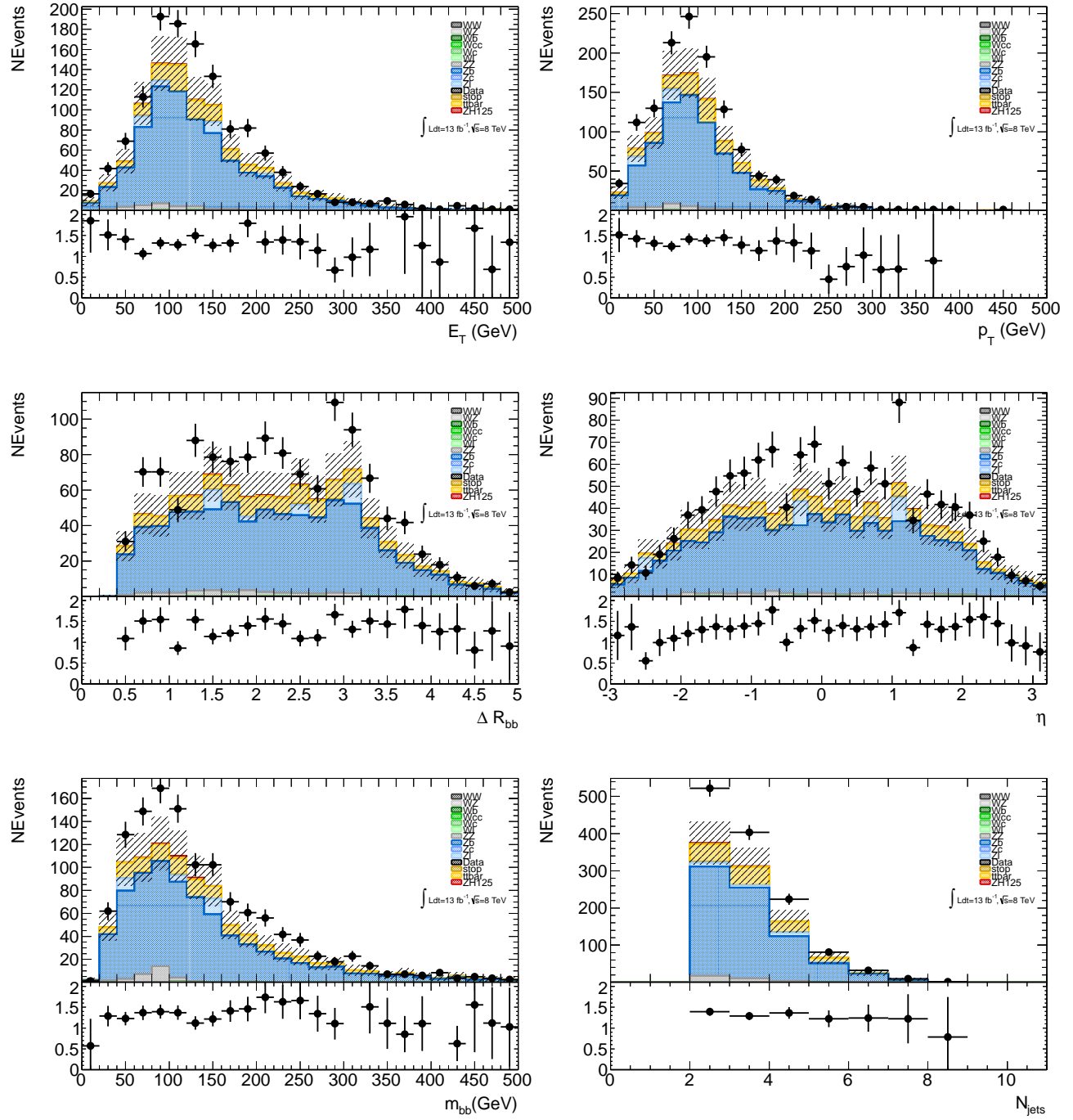


Figure 5.50: Higgs boson candidate distributions in the signal  $N_{b-jets} = 2$  and  $N_{muons} = 2$  region before applying scale factors from the log-likelihood fit.

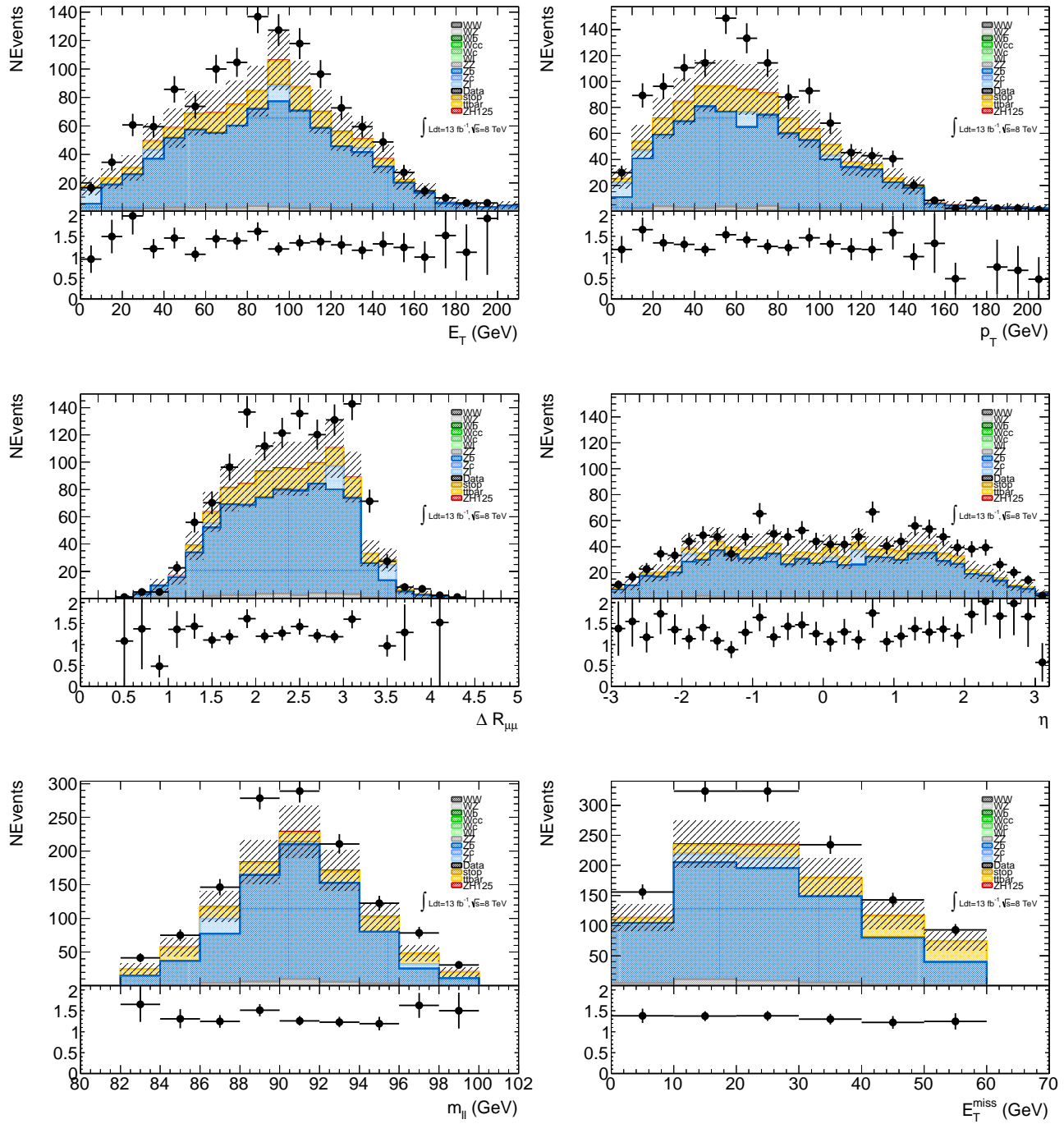


Figure 5.51:  $Z$  boson candidate distributions in the signal  $N_{b-jets} = 2$  and  $N_{muons} = 2$  region before applying scale factors from the log-likelihood fit.

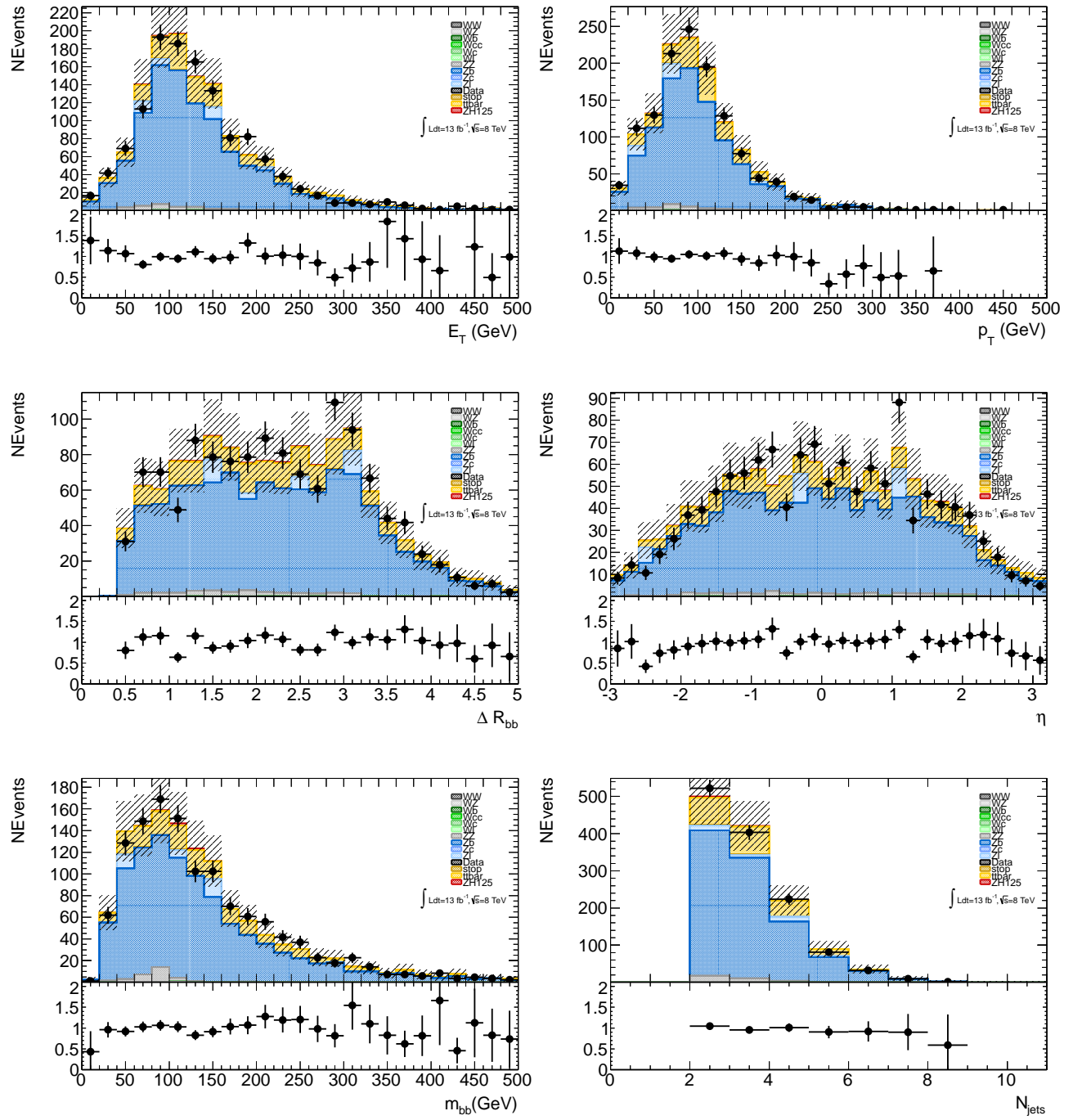


Figure 5.52: Higgs boson candidate distributions in the signal  $N_{b-jets} = 2$  and  $N_{muons} = 2$  region after applying scale factors from the log-likelihood fit.

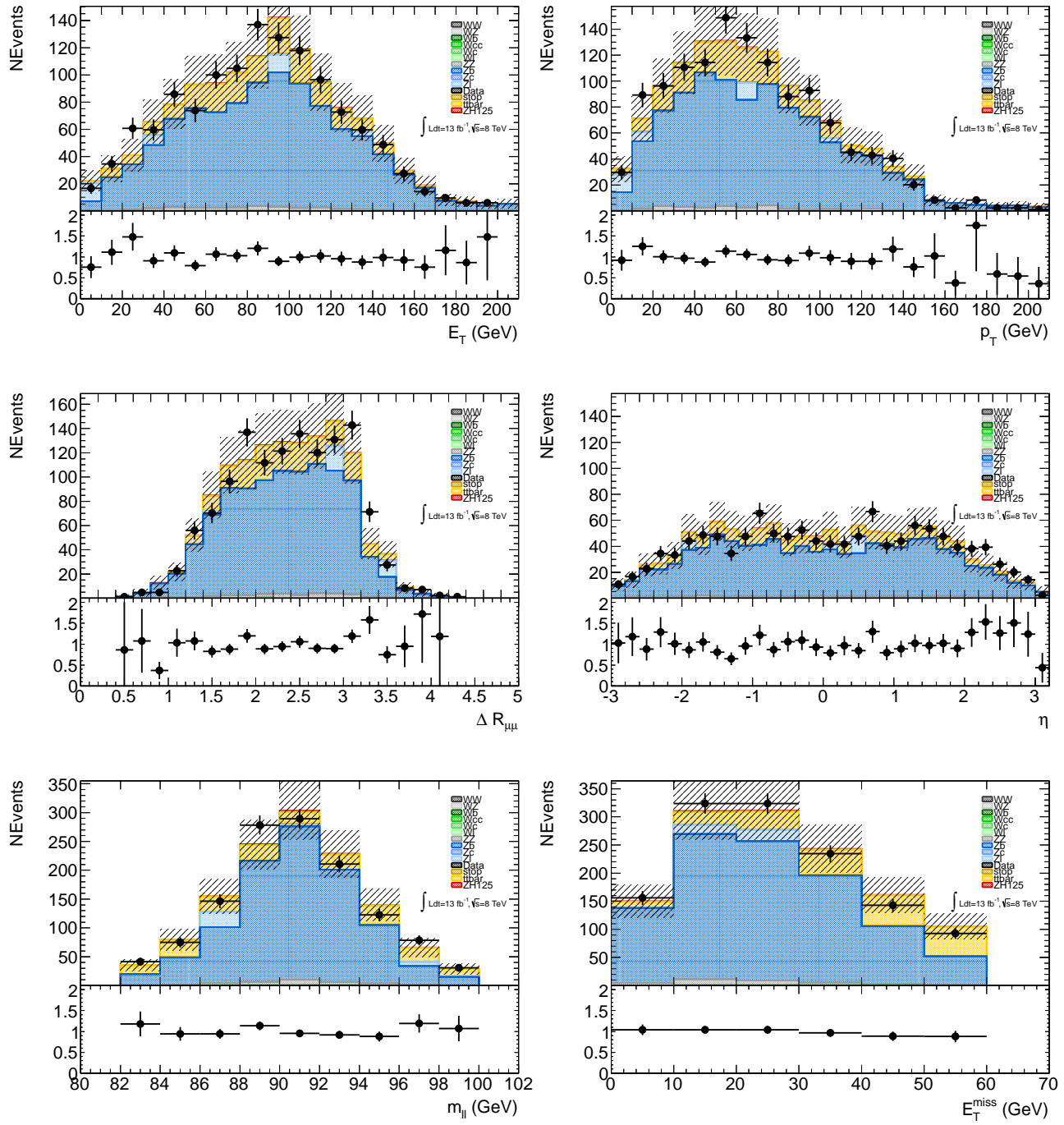


Figure 5.53:  $Z$  boson candidate distributions in the signal  $N_{b-jets} = 2$  and  $N_{muons} = 2$  region after applying scale factors from the log-likelihood fit.

### 5.8.2 Extraction of the Limit on $ZH \rightarrow l^+l^-b\bar{b}$ Production

The invariant mass distribution of the two signal  $b$ -jet candidates are used to test the presence of a significant Higgs signal in the analysis. A likelihood function is used to describe the binned  $m_{b\bar{b}}$  distribution for the signal and background processes, where the function is separated into two different categories coming from the  $Z \rightarrow e^+e^-$  and  $Z \rightarrow \mu^+\mu^-$  streams. Poisson terms are also included in the likelihood function, which allow the statistical uncertainties on the expected number of events compared to data to be fully described in the final fit.

The systematic uncertainties are included by producing Probability Density Functions (PDFs) of the  $m_{b\bar{b}}$  distributions for a given systematic. These additional parameters (nuisance parameters) allow the fit to not only be constrained by the normalisation of the signal and background uncertainties, but also the shape of those uncertainties in the distribution.

A maximum log-likelihood fit is applied to the constructed function  $-\log(\mathcal{L}(\mu, n_{bkg}, \vec{\theta}))$ , where  $\mu$  is the signal strength,  $n_{bkg}$  is the background normalisations obtained from data and  $\vec{\theta}$  represents all nuisance parameters. The signal strength is defined by the cross section over the standard model cross section ( $\frac{\sigma}{\sigma_{SM}}$ ), where  $\mu = 1$  defines the Standard Model hypothesis. The  $n_{bkg}$  parameters are allowed to float within the statistical uncertainties of their individual background normalisation's, while the nuisance parameters  $\vec{\theta}$  are allowed to freely float within their own constraints during the fit.

The signal hypothesis test uses a test statistic  $q_\mu$  to derive the limit. The test statistic is defined by the profile likelihood ratio,  $q_\mu = 2\ln(\mathcal{L}(\mu, n_{bkg}, \hat{\vec{\theta}}_\mu)/\mathcal{L}(\hat{\mu}, n_{bkg}, \hat{\vec{\theta}}))$ ,

where  $\hat{\mu}$  and  $\hat{\theta}$  are the parameters that maximise the likelihood with the constraint of  $0 \leq \hat{\mu} \leq \mu$  and  $\hat{\theta}_\mu$  are the nuisance parameters that maximise the likelihood for a given  $\mu$ . A one-sided upper limit is then placed on the ratio of the Higgs boson production cross section against its Standard Model value with a 95% confidence level (CL). An exclusion limit is then derived using  $CL_s$  and the test statistic above [107].

The RooStats framework [108] was used in the derivation of the exclusion limits for the Higgs boson production cross section in the mass range  $110 - 130$  GeV shown below in Figures 5.54 and 5.55. The expected  $CL_s$  limit for the SM backgrounds without a Higgs boson range from 6.3 to 11.4 times the Standard Model expectation over the full mass range for the statistical uncertainties only (see Figures 5.54). While the systematic constrained limits see an expectation from 9 to 17 times the Standard Model expectation over the full mass range (see Figures 5.55). The expected limit for  $m_H = 125$  GeV is 13.9 times the Standard Model expectation for a Standard Model Higgs, while the observed limit is 10.8 times the Standard Model expectations, which corresponds to a downward fluctuation of  $1\sigma$  between the expected and observed limit.

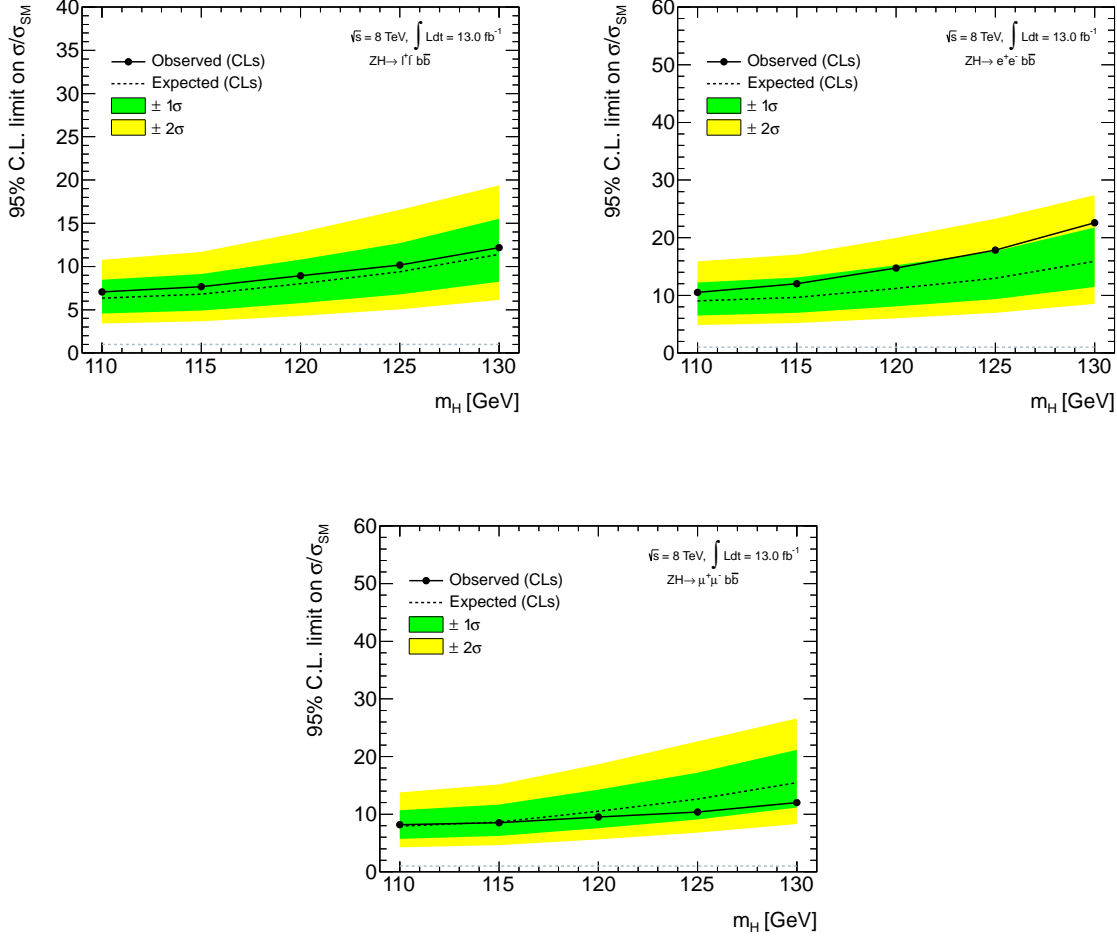


Figure 5.54: The expected (dashed line) and observed (solid line) upper limits on the total cross section divided by the expected Standard Model Higgs boson cross section, calculated using CLs at 95% for statistical errors only. The green ( $\pm 1\sigma$ ) and yellow ( $\pm 2\sigma$ ) bands, centred on the dotted line, indicate the range in which the statistical limit is expected to lie in the absence of a signal. The dotted grey line shows the Standard Model value of 1. Starting from the top left plot and moving round clock-wise, we have limits for the combined  $ZH \rightarrow l^+l^-$ ,  $ZH \rightarrow e^+e^-$  and  $ZH \rightarrow \mu^+\mu^-$  channels.

Table 5.20: The observed 95% CL upper limits with no systematics in the  $ZH \rightarrow l^+l^-b\bar{b}$  channel, as a multiple of the Standard Model rate, for an integrated luminosity of  $13 \text{ fb}^{-1}$ . The corresponding expected median upper limit, along with its  $\pm 1\sigma$  and  $\pm 2\sigma$  values, is also shown.

$m_H$ (GeV)	Observed		<u>Expected <math>\mu/\mu_{SM}</math></u>				
	$\mu/\mu_{SM}$		$-2\sigma$	$-1\sigma$	Median	$+1\sigma$	$+2\sigma$
<b>Inclusive</b>							
$m_H = 110$	7.1	3.4	4.6	6.3	8.5	11	
$m_H = 115$	7.7	3.7	4.9	6.8	9.1	12	
$m_H = 120$	8.9	4.3	5.8	9.0	11	14	
$m_H = 125$	10	5.0	6.8	9.4	13	17	
$m_H = 130$	12	6.1	8.2	11	16	20	
$ZH \rightarrow e^+e^-b\bar{b}$							
$m_H = 110$	11	4.9	6.5	9.0	12	16	
$m_H = 115$	12	5.2	7.0	9.7	13	17	
$m_H = 120$	15	6.0	8.0	11	15	20	
$m_H = 125$	18	7.0	9.3	13	18	23	
$m_H = 130$	23	8.5	11	16	22	29	
$ZH \rightarrow \mu^+\mu^-b\bar{b}$							
$m_H = 110$	8.2	4.3	5.7	7.9	11	14	
$m_H = 115$	8.5	4.6	6.2	8.6	12	15	
$m_H = 120$	9.5	5.6	7.6	11	14	19	
$m_H = 125$	10	6.8	9.1	13	17	23	
$m_H = 130$	12	8.3	11	15	21	28	

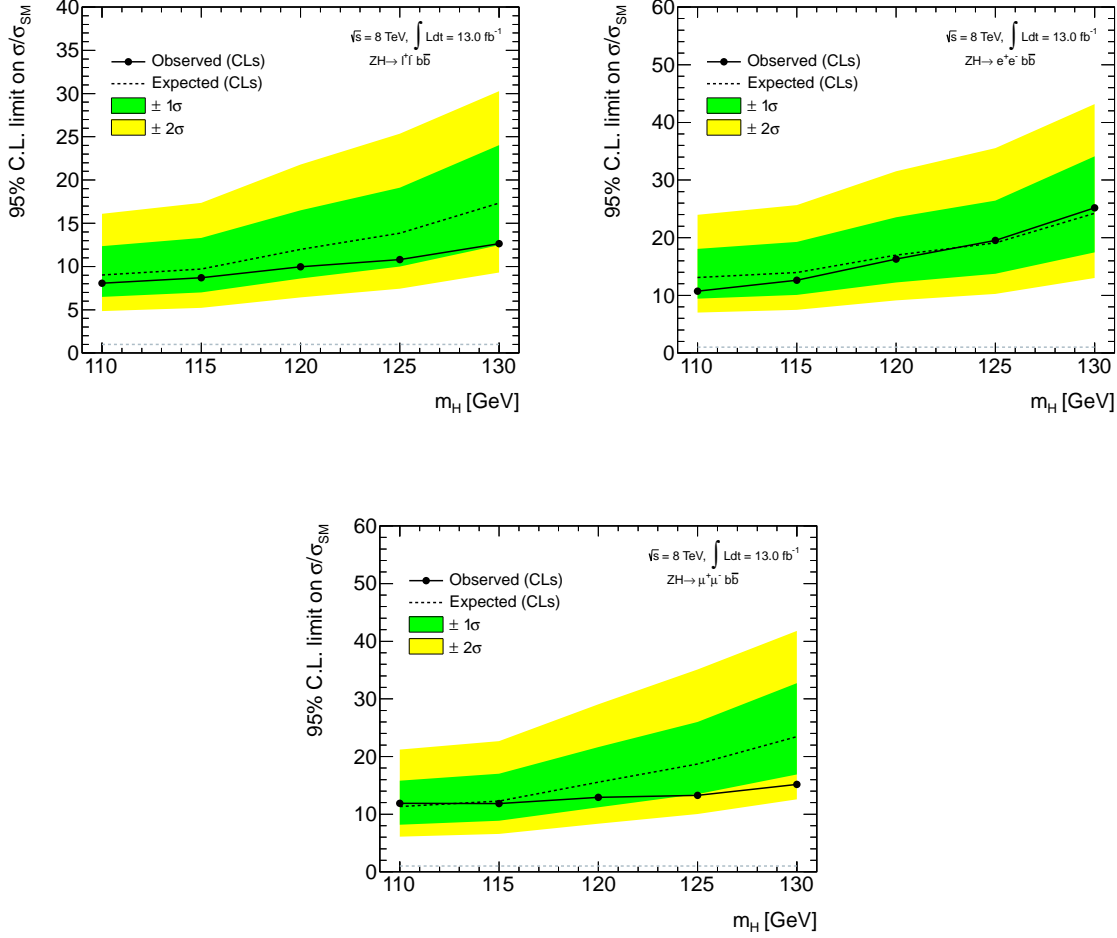


Figure 5.55: The expected (dashed line) and observed (solid line) upper limits on the total cross section divided by the expected Standard Model Higgs boson cross section, calculated using CLs at 95% for statistical and systematic errors. The green ( $\pm 1\sigma$ ) and yellow ( $\pm 2\sigma$ ) bands, centred on the dotted line, indicate the range in which the statistical limit is expected to lie in the absence of a signal. The dotted grey line shows the Standard Model value of 1. Starting from the top left plot and moving round clock-wise, we have limits for the combined  $ZH \rightarrow l^+l^-$ ,  $ZH \rightarrow e^+e^-$  and  $ZH \rightarrow \mu^+\mu^-$  channels.

Table 5.21: The observed 95% CL upper limits with full systematics in the  $ZH \rightarrow l^+l^-b\bar{b}$  channel, as a multiple of the Standard Model rate, for an integrated luminosity of  $13 \text{ fb}^{-1}$ . The corresponding expected median upper limit, along with its  $\pm 1\sigma$  and  $\pm 2\sigma$  values, is also shown.

$m_H$ (GeV)	Observed		Expected $\mu/\mu_{SM}$				
	$\mu/\mu_{SM}$		$-2\sigma$	$-1\sigma$	Median	$+1\sigma$	$+2\sigma$
<b>Inclusive</b>							
$m_H = 110$	8.1	4.8	6.5	9.0	12	16	
$m_H = 115$	8.7	5.2	7.0	9.1	13	17	
$m_H = 120$	10	6.4	8.6	12	16	22	
$m_H = 125$	11	7.4	10	14	19	25	
$m_H = 130$	13	9.3	12	17	24	32	
$ZH \rightarrow e^+e^-b\bar{b}$							
$m_H = 110$	11	7.0	9.4	13	18	24	
$m_H = 115$	13	7.5	10	14	19	26	
$m_H = 120$	16	9.1	12	17	24	32	
$m_H = 125$	20	10	14	19	26	36	
$m_H = 130$	25	13	17	24	34	47	
$ZH \rightarrow \mu^+\mu^-b\bar{b}$							
$m_H = 110$	12	6.1	8.2	11	16	21	
$m_H = 115$	12	6.6	8.9	12	17	23	
$m_H = 120$	13	8.3	11	16	22	29	
$m_H = 125$	13	10	13	19	26	35	
$m_H = 130$	15	13	17	23	33	44	

### 5.8.3 Summary

A measurement of the associated  $Z$  vector boson production rate into two  $b\bar{b}$  quarks, with the  $Z$  boson decaying to either an electron or muon pair has been performed from  $13\text{ fb}^{-1}$  of  $pp$  collision data at  $\sqrt{s} = 8\text{ TeV}$ . The event selection achieves a signal-to-background ratio of 0.006 and 0.007 for the electron pair and muon pair final states, respectively. The  $Zb$ ,  $t\bar{t}$ ,  $Zc$  and  $ZZ$  processes dominate the background. The yields of the backgrounds of the  $Zb$ ,  $Zc$ ,  $Zl$ ,  $t\bar{t}$  and *multi-jet* backgrounds are estimated from signal depleted control data, with the multi-jet background shape also taken from data. After event selection,  $1291 \pm 36$  ( $1129 \pm 34$ ) events are observed in the electron pair (muon pair) channel, where  $7.48 \pm 0.09^{+0.76}_{-0.64}$  ( $7.59 \pm 0.09^{+0.8}_{-0.7}$ ) signal and  $1227 \pm 14^{+135}_{-161}$  ( $1118 \pm 13^{+128}_{-96}$ ) background events are expected. The observed invariant mass of the Higgs candidate is interpreted in terms of a signal-plus-background hypothesis. The Standard Model Higgs boson production via associated  $ZH$  has been excluded at a 95% confidence level, for  $m_H = 125\text{ GeV}$  at  $14^{+11}_{-7}$  times the Standard Model cross section. The uncertainty in the measurement is dominated by statistical and systematic uncertainties, with the dominant systematic uncertainties coming from the jet energy scale, jet energy resolution and b-tagging, as well as from cross section predictions for the  $Z + jets$  background. The results show no significant observation of the Standard Model Higgs boson. However, more precise tests will be performed at the re-opening of the LHC at centre-of-mass energies of  $13 - 14\text{ TeV}$ , with a predicted integrated luminosity of  $300\text{ fb}^{-1}$  expected by the end of the decade. Assuming that the sensitivity scales with the statistical error and with the current integrated luminosity, we would expect a exclusion limit at  $\sim 2$  times the Standard Model cross

section. Therefore with the current analysis, it will not be possible to observe the Higgs boson with the  $ZH \rightarrow l^+l^-b\bar{b}$  channel.

# Chapter 6

## Conclusion

The Standard Model successfully describes the interactions between elementary particles using the principle of local gauge symmetry and has been experimentally verified with high precision. The discovery of a new massive vector boson of mass  $125.5 \pm 0.6$  GeV and  $125.7 \pm 0.4$  GeV from the ATLAS and CMS experiments respectively, has allowed for the verification of a Standard Model Higgs boson and completes the Standard Model particle content. While studies are still taking place to measure the properties of the Higgs boson candidate, such as the production and decay rates, initial studies [109] suggest the compatibility with the Standard Model.

In this thesis a measurement of the associated  $Z$  vector boson production rate into two  $b\bar{b}$  quarks, with the  $Z$  boson decaying to either an electron or muon pair has been performed. The associated  $ZH$  production has a characteristic signature, such that the decaying  $Z$  boson into electron and muon pairs can be accurately triggered upon. Further topological cuts are also applied to the accurately modelled  $Z$  boson mass, while a  $b$ -tagging algorithm is used to identify  $H \rightarrow b\bar{b}$  decays in the event. The event

selection achieves a signal-to-background ratio of 0.006 and 0.007 for the electron pair and muon pair final states, respectively. The  $Zb$ ,  $t\bar{t}$ ,  $Zc$  and  $ZZ$  processes dominate the background. The yields of the backgrounds of the  $Zb$ ,  $Zc$ ,  $Zl$ ,  $t\bar{t}$  and *multi-jet* backgrounds are estimated from signal depleted control data, with the *multi-jet* background shape also taken from data.

Proton-proton collision data from the ATLAS detector at a centre-of-mass energy of 8 TeV and corresponding to an integrated luminosity of  $13 \text{ fb}^{-1}$  has been analysed at the LHC. After event selection,  $1291 \pm 36$  ( $1129 \pm 34$ ) events are observed in the electron pair (muon pair) channel, where  $7.48 \pm 0.09^{+0.76}_{-0.64}$  ( $7.59 \pm 0.09^{+0.80}_{-0.70}$ ) signal and  $1227 \pm 14^{+135}_{-161}$  ( $1118 \pm 13^{+128}_{-96}$ ) background events are expected. The observed invariant mass of the Higgs candidate is interpreted in terms of a signal-plus-background hypothesis and is consistent with the Standard Model prediction. However, the Standard Model Higgs boson production via associated  $ZH$  has been excluded at a 95% confidence level, for  $m_H = 125 \text{ GeV}$  at  $14^{+11}_{-7}$  times the Standard Model cross section.

# References

- [1] F. Englert and R. Brout, *Broken Symmetry and the Mass of Gauge Vector Mesons*, Phys. Rev. Lett., 13, 321–323, URL <http://link.aps.org/doi/10.1103/PhysRevLett.13.321> (Aug 1964)
- [2] P. W. Higgs, *Broken Symmetries and the Masses of Gauge Bosons*, Phys. Rev. Lett., 13, 508–509, URL <http://link.aps.org/doi/10.1103/PhysRevLett.13.508> (Oct 1964)
- [3] G. S. Guralnik, C. R. Hagen and T. W. B. Kibble, *Global Conservation Laws and Massless Particles*, Phys. Rev. Lett., 13, 585–587, URL <http://link.aps.org/doi/10.1103/PhysRevLett.13.585> (Nov 1964)
- [4] G. Aad et al., *Observation of a new particle in the search for the Standard Model Higgs boson with the ATLAS detector at the LHC*, Phys.Lett., B716, 1–29 (2012)
- [5] S. Chatrchyan et al., *Observation of a new boson at a mass of 125 GeV with the CMS experiment at the LHC*, Phys.Lett., B716, 30–61 (2012)

- [6] G. Aad et al., *Measurements of Higgs boson production and couplings in diboson final states with the ATLAS detector at the LHC*, Phys.Lett., B726, 88–119 (2013)
- [7] *Combination of standard model Higgs boson searches and measurements of the properties of the new boson with a mass near 125 GeV*, Technical Report CMS-PAS-HIG-12-045, CERN, Geneva (2012)
- [8] M. Herrero, *The Standard model*, NATO Adv.Study Inst.Ser.C.Math.Phys.Sci., 534, 1–59 (1999)
- [9] *Standard Model elementary particles in the Standard Model*,  
<http://commons.wikimedia.org/wiki>
- [10] J. Beringer et al., *Review of Particle Physics (RPP)*, Phys.Rev., D86, 010001 (2012)
- [11] F. Halzen and A. Martin, *Quarks and Leptons: An introductory course in modern particle physics*, John Wiley and Sons (1984)
- [12] R. P. Feynman, *Mathematical Formulation of the Quantum Theory of Electromagnetic Interaction*, Phys. Rev., 80, 440–457, URL  
<http://link.aps.org/doi/10.1103/PhysRev.80.440> (Nov 1950)
- [13] A. Salam, *Weak and Electromagnetic Interactions*, Conf.Proc., C680519, 367–377 (1968)
- [14] H. Fritzsch, M. Gell-Mann and H. Leutwyler, *Advantages of the color octet gluon picture*, Phys. Lett., B47, 365–368 (1973)

- [15] R. P. Feynman, *The Theory of Positrons*, Phys. Rev., 76, 749–759, URL <http://link.aps.org/doi/10.1103/PhysRev.76.749> (Sep 1949)
- [16] P. A. Dirac, *The Quantum theory of electron*, Proc.Roy.Soc.Lond., A117, 610–624 (1928)
- [17] C.-N. Yang and R. L. Mills, *Conservation of Isotopic Spin and Isotopic Gauge Invariance*, Phys.Rev., 96, 191–195 (1954)
- [18] G. S. Guralnik, *The history of the Guralnik, Hagen and Kibble development of the theory of spontaneous symmetry breaking and gauge particles.*, Int. J. Mod. Phys. A, 24 (14), 2601–2627 (2009)
- [19] J. Goldstone, A. Salam and S. Weinberg, *Broken Symmetries*, Phys. Rev., 127, 965–970, URL <http://link.aps.org/doi/10.1103/PhysRev.127.965> (Aug 1962)
- [20] T. Hambye and K. Riesselmann, *Matching conditions and Higgs boson mass upper bounds reexamined*, Phys. Rev. D, 55, 7255–7262, URL <http://link.aps.org/doi/10.1103/PhysRevD.55.7255> (Jun 1997)
- [21] J. R. Ellis and G. L. Fogli, *New bounds on  $m(t)$  and first bounds on  $M(H)$  from precision electroweak data*, Phys.Lett., B249, 543–550 (1990)
- [22] J. F. Gunion, S. Dawson, H. E. Haber and G. L. Kane, *The Higgs hunter's guide*, Frontiers in Physics, Westview, Boulder, CO, later reprinted under the 'Frontiers in Physics' series from Perseus Publishing in 2000 (this edition also available in the library). (1990)

- [23] M. Botje et al., *The PDF4LHC Working Group Interim Recommendations* (2011)
- [24] R. K. Ellis, W. J. Stirling and B. Webber, *QCD and collider physics*, Press syndicate of the University of Cambringe (1996)
- [25] H.-L. Lai et al., *New parton distributions for collider physics*, Phys.Rev., D82, 074024 (2010)
- [26] P. M. Nadolsky et al., *Implications of CTEQ global analysis for collider observables*, Phys.Rev., D78, 013004 (2008)
- [27] J. M. Campbell, J. W. Huston and W. J. Stirling, *Hard interactions of quarks and gluons: a primer for LHC physics*, Reports on Progress in Physics, 70 (1), 89, URL <http://stacks.iop.org/0034-4885/70/i=1/a=R02> (2007)
- [28] S. Dittmaier et al., *Handbook of LHC Higgs Cross Sections: 1. Inclusive Observables* (2011)
- [29] V. Ravindran, J. Smith and W. L. van Neerven, *NNLO corrections to the total cross-section for Higgs boson production in hadron hadron collisions*, Nucl.Phys., B665, 325–366 (2003)
- [30] S. Actis, G. Passarino, C. Sturm and S. Uccirati, *NLO Electroweak Corrections to Higgs Boson Production at Hadron Colliders*, Phys.Lett., B670, 12–17 (2008)
- [31] K. Arnold et al., *VBFNLO: A Parton Level Monte Carlo for Processes with Electroweak Bosons – Manual for Version 2.5.0* (2011)

- [32] T. Han and S. Willenbrock, *QCD correction to the  $pp \rightarrow WH$  and  $ZH$  total cross-sections*, Phys.Lett., B273, 167–172 (1991)
- [33] D. A. Restrepo, *From hierarchical radiative quark mass matrices and mixing to FCNC in  $SU(2)_L \times U(1)_Y \times U(1)_H$* , Technical Report hep-ph/9607356. UDEA-PE-96-52, Antioquia Univ., Medelln (Jul 1996)
- [34] S. Dittmaier et al., *Handbook of LHC Higgs Cross Sections: 2. Differential Distributions* (2012)
- [35] *SM Higgs production cross sections at  $\sqrt{s} = 8$  TeV*,  
<https://twiki.cern.ch/twiki/bin/view/LHCPhysics/CERNYellowReportPageAt8TeV2012update>
- [36] A. Djouadi, J. Kalinowski and M. Spira, *HDECAY: A Program for Higgs boson decays in the standard model and its supersymmetric extension*, Comput.Phys.Commun., 108, 56–74 (1998)
- [37] M. Dobbs et al., *Les Houches guidebook to Monte Carlo generators for hadron collider physics*, Technical report (2004)
- [38] B. Andersson, G. Gustafson, G. Ingelman and T. Sjostrand, *Parton Fragmentation and String Dynamics*, Phys.Rept., 97, 31–145 (1983)
- [39] S. Alioli, P. Nason, C. Oleari and E. Re, *NLO Higgs boson production via gluon fusion matched with shower in POWHEG*, JHEP, 0904, 002 (2009)
- [40] S. Frixione and B. R. Webber, *Matching NLO QCD computations and parton shower simulations*, JHEP, 0206, 029 (2002)

- [41] M. L. Mangano et al., *ALPGEN, a generator for hard multiparton processes in hadronic collisions*, JHEP, 0307, 001 (2003)
- [42] B. P. Kersevan and E. Richter-Was, *The Monte Carlo event generator AcerMC versions 2.0 to 3.8 with interfaces to PYTHIA 6.4, HERWIG 6.5 and ARIADNE 4.1*, Comput.Phys.Commun., 184, 919–985 (2013)
- [43] T. Gleisberg et al., *Event generation with SHERPA 1.1*, JHEP, 0902, 007 (2009)
- [44] *ATLAS tunes of PYTHIA 6 and Pythia 8 for MC11*, Technical Report ATL-PHYS-PUB-2011-009, CERN, Geneva (Jul 2011)
- [45] G. Corcella et al., *HERWIG 6: An Event generator for hadron emission reactions with interfering gluons (including supersymmetric processes)*, JHEP, 0101, 010 (2001)
- [46] J. Butterworth, J. R. Forshaw and M. Seymour, *Multiparton interactions in photoproduction at HERA*, Z.Phys., C72, 637–646 (1996)
- [47] M. De Palma et al., *ALEPH: Technical Report 1983* (1983)
- [48] W. Bartl et al., *DELPHI: Technical Proposal* (1983)
- [49] M. Decamp, *The Opal Detector Technical Proposal* (1983)
- [50] R. Blair et al., *The CDF-II detector: Technical design report* (1996)
- [51] D. S. Denisov and S. Soldner-Rembold, *D0 Run IIB Silicon Detector Upgrade: Technical Design Report* (2001)

- [52] G. Bhattacharyya, *Electroweak Symmetry Breaking and BSM Physics (A Review)*, Pramana, 72, 37–54 (2009)
- [53] T. Aaltonen et al., *Higgs Boson Studies at the Tevatron*, Phys.Rev., D88 (5), 052014 (2013)
- [54] *Measurements of the properties of the Higgs-like boson in the two photon decay channel with the ATLAS detector using  $25 \text{ fb}^{-1}$  of proton-proton collision data*, Technical report (2013)
- [55] *Measurements of the properties of the Higgs-like boson in the four lepton decay channel with the ATLAS detector using  $25 \text{ fb}^{-1}$  of proton-proton collision data*, Technical Report ATLAS-CONF-2013-013, CERN, Geneva (Mar 2013)
- [56] S. Chatrchyan et al., *Measurement of the properties of a Higgs boson in the four-lepton final state*, Phys.Rev., D89, 092007 (2014)
- [57] *Measurements of the properties of the Higgs-like boson in the four lepton decay channel with the ATLAS detector using  $25 \text{ fb}^{-1}$  of proton-proton collision data*, Technical report (2013)
- [58] *Evidence for Higgs Boson Decays to the  $\tau^+\tau^-$  Final State with the ATLAS Detector*, Technical Report ATLAS-CONF-2013-108, CERN, Geneva (Nov 2013)
- [59] *Search for the  $b\bar{b}$  decay of the Standard Model Higgs boson in associated  $W/ZH$  production with the ATLAS detector*, Technical Report ATLAS-CONF-2013-079, CERN, Geneva (Jul 2013)

- [60] *Search for the b-bbar decay of the Standard Model Higgs boson in associated (W/Z)H production with the ATLAS detector*, Technical Report ATLAS-HIGG-2013-23-001, CERN, Geneva (Jul 2014)
- [61] T. S. Pettersson and P. Lefvre, *The Large Hadron Collider: conceptual design*, Technical Report CERN-AC-95-05 LHC, CERN, Geneva (Oct 1995)
- [62] C. Lefvre, *The CERN accelerator complex. Complexe des accélérateurs du CERN*, Technical report (Dec 2008)
- [63] K. Schindl, *The Injector Chain for the LHC; rev. version*, (CERN-PS-99-018-DI), 7 p (Mar 1999)
- [64] G. Aad et al., *Improved luminosity determination in pp collisions at  $\sqrt{s} = 7$  TeV using the ATLAS detector at the LHC*, Eur.Phys.J., C73, 2518 (2013)
- [65] *ATLAS luminosity measurements*,  
<https://twiki.cern.ch/twiki/bin/view/AtlasPublic/LuminosityPublicResults>
- [66] T. A. Collaboration, *The ATLAS Experiment at the CERN Large Hadron Collider*, Journal of Instrumentation, 3 (08), S08003, URL <http://stacks.iop.org/1748-0221/3/i=08/a=S08003> (2008)
- [67] S. van der Meer, *Calibration of the effective beam height in the ISR*, Technical Report CERN-ISR-PO-68-31. ISR-PO-68-31, CERN, Geneva (1968)
- [68] C. Rubbia, *Measurement of the luminosity of p-pbar collider with a (generalized) Van der Meer Method*, Technical Report CERN-p-pbar-Note-38, CERN, Geneva (Nov 1977)

- [69] S. A. et al, *Geant4a simulation toolkit*, Nuclear Instruments and Methods in Physics Research Section A: Accelerators, Spectrometers, Detectors and Associated Equipment, 506 (3), 250 – 303, URL <http://www.sciencedirect.com/science/article/pii/S0168900203013688> (2003)
- [70] G. Aad et al., *The ATLAS Simulation Infrastructure*, European Physical Journal C, 70, 823–874 (December 2010)
- [71] G. Folger and J. Wellisch, *String parton models in GEANT4*, eConf, C0303241, MOMT007, arXiv:nucl-th/0306007 (2003)
- [72] H. W. BERTINI, *Intranuclear-Cascade Calculation of the Secondary Nucleon Spectra from Nucleon-Nucleus Interactions in the Energy Range 340 to 2900 MeV and Comparisons with Experiment*, Phys. Rev., 188, 1711–1730, URL <http://link.aps.org/doi/10.1103/PhysRev.188.1711> (Dec 1969)
- [73] *ATLAS Calorimeter Response to Single Isolated Hadrons and Estimation of the Calorimeter Jet Scale Uncertainty*, Technical Report ATLAS-CONF-2011-028, CERN, Geneva (Mar 2011)
- [74] *Response of isolated particles identified using resonances in proton-proton collisions at  $\sqrt{s}=7$  TeV with the ATLAS detector*, Technical Report ATLAS-CONF-2011-019, CERN, Geneva (Mar 2011)
- [75] T. Cornelissen et al., *Concepts, Design and Implementation of the ATLAS New Tracking (NEWT)*, Technical Report ATL-SOFT-PUB-2007-007. ATL-COM-SOFT-2007-002, CERN, Geneva (Mar 2007)

- [76] R. Fruhwirth, *Application of Kalman filtering to track and vertex fitting*, Nucl. Instrum. Methods Phys. Res., A, 262 (HEPHY-PUB-503), 444. 19 p (Jun 1987)
- [77] R. O. Duda and P. E. Hart, *Use of the Hough transformation to detect lines and curves in pictures*, Commun. ACM, 15 (1), 11–15, URL <http://doi.acm.org/10.1145/361237.361242> (January 1972)
- [78] K. Prokofiev, *Reconstruction of primary vertices in pp collisions at energies of 900 GeV and 7 TeV with the ATLAS detector*, Technical report (2010)
- [79] *Performance of the ATLAS Inner Detector Track and Vertex Reconstruction in the High Pile-Up LHC Environment*, Technical Report ATLAS-CONF-2012-042, CERN, Geneva (Mar 2012)
- [80] G. Aad et al., *Electron performance measurements with the ATLAS detector using the 2010 LHC proton-proton collision data*, Eur.Phys.J., C72, 1909 (2012)
- [81] *ATLAS detector and physics performance: Technical Design Report, 1*, Technical Design Report ATLAS, CERN, Geneva, electronic version not available (1999)
- [82] E. Abat et al., *Combined performance studies for electrons at the 2004 ATLAS combined test-beam*, Journal of Instrumentation, 5 (11), P11006, URL <http://stacks.iop.org/1748-0221/5/i=11/a=P11006> (2010)
- [83] *Expected electron performance in the ATLAS experiment*, Technical Report ATL-PHYS-PUB-2011-006, CERN, Geneva (Apr 2011)

- [84] B. Acharya et al., *Object selection and calibration, background estimations and MC samples for the Winter 2012 Top Quark analyses with 2011 data*, Technical Report ATL-COM-PHYS-2012-224, CERN, Geneva (Feb 2012)
- [85] R. Nicolaïdou et al., *Muon identification procedure for the ATLAS detector at the LHC using Muonboy reconstruction package and tests of its performance using cosmic rays and single beam data*, Journal of Physics: Conference Series, 219 (3), 032052, URL <http://stacks.iop.org/1742-6596/219/i=3/a=032052> (2010)
- [86] T. Lagouri et al., *A Muon Identification and Combined Reconstruction Procedure for the ATLAS Detector at the LHC at CERN*, revised version number 1 submitted on 2003-10-30 18:34:15 (Oct 2003)
- [87] *Preliminary results on the muon reconstruction efficiency, momentum resolution, and momentum scale in ATLAS 2012 pp collision data*, Technical Report ATLAS-CONF-2013-088, CERN, Geneva (Aug 2013)
- [88] T. A. Collaboration, *Jet energy measurement with the ATLAS detector in proton-proton collisions at  $\sqrt{s} = 7 \text{ TeV}$* , Eur. Phys. J. C, 73 (arXiv:1112.6426. CERN-PH-EP-2011-191), 2304. 111 p, comments: 100 pages plus author list (111 pages total), 93 figures, 17 tables, submitted to European Physical Journal C (Dec 2011)
- [89] M. Cacciari, G. P. Salam and G. Soyez, *The Anti- $k(t)$  jet clustering algorithm*, JHEP, 0804, 063 (2008)

- [90] *Inputs to Jet Reconstruction and Calibration with the ATLAS Detector Using Proton-Proton Collisions at  $\sqrt{s} = 900$  GeV*, Technical Report ATLAS-CONF-2010-016, CERN, Geneva (Jul 2010)
- [91] *Selection of jets produced in proton-proton collisions with the ATLAS detector using 2011 data*, Technical Report ATLAS-CONF-2012-020, CERN, Geneva (Mar 2012)
- [92] *Jet energy resolution and selection efficiency relative to track jets from in-situ techniques with the ATLAS Detector Using Proton-Proton Collisions at a Center of Mass Energy  $\sqrt{s} = 7$  TeV*, Technical Report ATLAS-CONF-2010-054, CERN, Geneva (Jul 2010)
- [93] *Commissioning of the ATLAS high-performance b-tagging algorithms in the 7 TeV collision data*, Technical Report ATLAS-CONF-2011-102, CERN, Geneva (Jul 2011)
- [94] A. Coccaro, *Track Reconstruction and b-Jet Identification for the ATLAS Trigger System*, J.Phys.Conf.Ser., 368, 012034 (2012)
- [95] *b-jet tagging calibration on c-jets containing  $D^{*+}$  mesons*, Technical Report ATLAS-CONF-2012-039, CERN, Geneva (Mar 2012)
- [96] *Measurement of the Mistag Rate with  $5 \text{ fb}^{-1}$  of Data Collected by the ATLAS Detector*, Technical Report ATLAS-CONF-2012-040, CERN, Geneva (Mar 2012)

- [97] *Measurement of the b-tag Efficiency in a Sample of Jets Containing Muons with 5 fb<sup>1</sup> of Data from the ATLAS Detector*, Technical Report ATLAS-CONF-2012-043, CERN, Geneva (Mar 2012)
- [98] G. Aad et al., *Performance of Missing Transverse Momentum Reconstruction in Proton-Proton Collisions at 7 TeV with ATLAS*, Eur.Phys.J., C72, 1844 (2012)
- [99] *Performance of Missing Transverse Momentum Reconstruction in ATLAS with 2011 Proton-Proton Collisions at sqrt{s} = 7 TeV*, Technical Report ATLAS-CONF-2012-101, CERN, Geneva (Jul 2012)
- [100] *Performance of the ATLAS muon trigger in 2011*, Technical Report ATLAS-CONF-2012-099, CERN, Geneva (Jul 2012)
- [101] *Performance of the ATLAS Electron and Photon Trigger in p-p Collisions at sqrt{s} = 7 TeV in 2011*, Technical Report ATLAS-CONF-2012-048, CERN, Geneva (May 2012)
- [102] J. Allison et al., *Geant4 developments and applications*, Nuclear Science, IEEE Transactions on, 53 (1), 270–278 (Feb 2006)
- [103] C. Oleari and L. Reina, *W +- b-bar b production in POWHEG*, JHEP, 1108, 061 (2011)
- [104] *New ATLAS event generator tunes to 2010 data*, Technical Report ATL-PHYS-PUB-2011-008, CERN, Geneva (Apr 2011)
- [105] G. Aad et al., *Expected Performance of the ATLAS Experiment - Detector, Trigger and Physics*, Technical report (2009)

- [106] G. Aad et al., *Search for a standard model Higgs boson in the mass range 200 - 600-GeV in the  $H \rightarrow ZZ \rightarrow \ell^+\ell^-q\bar{q}$  decay channel with the ATLAS detector*, Phys.Lett., B717, 70–88 (2012)
- [107] A. L. Read, *Presentation of search results: The  $CL(s)$  technique*, J.Phys., G28, 2693–2704 (2002)
- [108] L. Moneta et al., *The RooStats Project*, PoS, ACAT2010, 057 (2010)
- [109] *Projections for measurements of Higgs boson cross sections, branching ratios and coupling parameters with the ATLAS detector at a HL-LHC*, Technical Report ATL-PHYS-PUB-2013-014, CERN, Geneva (Oct 2013)